Institut für Biochemie und Biologie,
Arbeitsgruppe für Physikalische Biochemie

Enzymatic Remodelling of the Exopolysaccharide Stewartan Network: Implications for the Diffusion of Nano-sized Objects

Dissertation

zur Erlangung des akademischen Grades
"doctor rerum naturalium" (Dr. rer. nat.)
in der Wissenschaftsdisziplin "Physikalische Biochemie"

eingereicht an der
Mathematisch-Naturwissenschaftlichen Fakultät
der
Universität Potsdam

von
Tobias Irmscher
Potsdam, Dezember 2019

Supervisor:
Dr. habil. Stefanie Barbirz

Date of final exam: 9 June 2020

https://doi.org/10.25932/publishup-47248
https://nbn-resolving.org/urn:nbn:de:kobv:517-opus4-472486

I. Abstract

In nature, bacteria are found to reside in multicellular communities encased in self-produced extracellular matrices. Indeed, biofilms are the default lifestyle of the bacteria which cause persistent infections in humans. The biofilm assembly protects bacterial cells from desiccation and limits the effectiveness of antimicrobial treatments. A myriad of biomolecules in the extracellular matrix, including proteins, exopolysaccharides, lipids, extracellular DNA and other, form a dense and viscoelastic three dimensional network. Many studies emphasized that a destabilization of the mechanical integrity of biofilm architectures potentially eliminates the protective shield and renders bacteria more susceptible to the immune system and antibiotics. *Pantoea stewartii* is a plant pathogen which infects monocotyledons such as maize and sweet corn. These bacteria produce dense biofilms in the xylem of infected plants which cause wilting of plants and crops. Stewartan is an exopolysaccharide which is produced by *Pantoea stewartii* and secreted as the major component to the extracellular matrix. It consists of heptasaccharide repeating units with a high degree of polymerization (2-4 MDa). In this work, the physicochemical properties of stewartan were investigated to understand the contributions of this exopolysaccharide to the mechanical integrity and cohesiveness of *Pantoea stewartii* biofilms. Therefore, a coarse-grained model of stewartan was developed with computational techniques to obtain a model for its three dimensional structural features. Here, coarse-grained molecular dynamic simulations revealed that the exopolysaccharide forms a hydrogel in which the exopolysaccharide chains arrange into a three dimensional mesh-like network. Simulations at different concentrations were used to investigate the influence of the water content on the network formation. Stewartan was further purified from 72 h grown *Pantoea stewartii* biofilms and the diffusion of bacteriophage and differently-sized nanoparticles (which ranged from 1.1 to 193 nm diameter) was analyzed in reconstituted stewartan solutions. Fluorescence correlation spectroscopy and single-particle tracking revealed that the stewartan network impeded the mobility of a set of differently-sized fluorescent particles in a size-dependent manner. Diffusion of these particles became more anomalous, as characterized by fitting the diffusion data to an anomalous diffusion model, with increasing stewartan concentrations. Further bulk and microrheological experiments were used to analyze the transitions in stewartan fluid behavior and stewartan chain entanglements were described. Moreover, it was noticed, that a small fraction of bacteriophage particles was trapped in small-sized pores deviating from classical random walks which highlighted the structural heterogeneity of the stewartan network. Additionally, the mobility of fluorescent particles also depended on the charge of the stewartan exopolysaccharide and a model of a molecular sieve for the stewartan network was proposed. The here reported structural features of the stewartan polymers were used to provide a detailed description of the mechanical properties of typically glycan-based biofilms such as the one from *Pantoea stewartii*.

In addition, the mechanical properties of the biofilm architecture are permanently sensed by the embedded bacteria and enzymatic modifications of the extracellular matrix take place to address environmental cues. Hence, in this work the influence of enzymatic degradation of the stewartan exopolysaccharides on the overall exopolysaccharide network structure was analyzed to describe relevant physiological processes in *Pantoea stewartii* biofilms. Here, the stewartan hydrolysis kinetics of the tailspike protein from the ΦEa1h bacteriophage, which is naturally found to infect *Pantoea stewartii* cells, was compared to WceF. The latter protein is expressed from the *Pantoea stewartii* stewartan biosynthesis gene cluster *wce I-III*. The degradation of stewartan by the ΦEa1h tailspike protein was shown to be much faster than the hydrolysis kinetics of WceF, although both enzymes cleaved the β-D-Gal^{III}(1→3)-α-D-Gal^{I} glycosidic linkage from the stewartan backbone. Oligosaccharide fragments which were produced during the stewartan cleavage, were analyzed in size-exclusion chromatography and capillary electrophoresis. Bioinformatic studies and the analysis of a WceF crystal structure revealed a remarkably high structural similarity of both proteins thus unveiling WceF as a bacterial tailspike-like protein. As a consequence, WceF might play a role in stewartan chain length control in *Pantoea stewartii* biofilms.

II. Zusammenfassung

In der Natur lagern sich Bakterien zu großen und komplexen Gemeinschaften zusammen, die als Biofilme bezeichnet werden. Diese multizellulären Biofilme sind der Ursprung vieler langlebiger und gefährlicher Infektionskrankheiten. Die bakteriellen Zellen produzieren und umgeben sich mit einen biofilm-spezifischen Schleim, der aus einer Unzahl von Biomolekülen, wie z.B. Exopolysaccharide, Lipide und extrazelluläre DNA, besteht. Diese Biofilmarchitektur schützt Bakterien vor Austrocknung und begrenzen die Wirksamkeit von antimikrobiellen Wirkstoffen (z.B. Antibiotika). Viele Studien haben gezeigt, dass die Destabilisierung der mechanischen Festigkeit des Biofilmapparates eine neue Behandlungsstrategie darstellt, in der das bakterielle Schutzschild eliminiert wird, sodass die Zellen wieder anfälliger gegenüber dem menschlichen Immunsystem oder Antibiotika werden.

Pantoea stewartii ist ein Pflanzenpathogen, welches Mais und Süßmais befällt. Diese Bakterien produzieren Biofilme im Inneren der Pflanze, sodass der freie Wassertransport gestört wird. Daraufhin verwelken die Blätter und Früchte. In dieser Arbeit wurde das Exopolysaccharid Stewartan untersucht, welches lange Ketten ausbildet und als häufigste Komponente in den Biofilmen von *Pantoea stewartii* vorkommt. Dabei wurden die mechanischen Eigenschaften von Stewartan untersucht, um zu verstehen, wie diese den Biofilm beeinflussen. Dafür wurde eine Lösung aus mehreren Stewartan Molekülen computergestützt simuliert. Hierbei konnte beobachtet werden, dass die Stewartan Ketten ein dreidimensionales Netzwerk ausbilden, welches Poren aufweist. Außerdem wurde Stewartan aus *Pantoea stewartii* Biofilmen isoliert und die Diffusion von verschieden großen Nanopartikeln in dem Exopolysaccharidnetzwerk untersucht. Je höher die Stewartankonzentration war, desto mehr wurde die Diffusion der Nanopartikeln abgebremst. Außerdem wurden große Partikel stärker von dem Netzwerk zurückgehalten. Diese Untersuchungen wurden auf die Diffusion von Bakteriophagen, das sind Viren, die spezifisch Bakterien infizieren, ausgeweitet. Infolgedessen wurde gezeigt, dass Bakteriophagen in kleine Stewartanporen feststecken können. Die Diffusion all dieser Partikeln war aber auch abhängig von der Oberflächenladung des Partikels. Folglich bildet Stewartan ein Netzwerk aus, welches ganz spezifisch den Transport von Molekülen mit bestimmten Eigenschaften unterbindet. Außerdem ist bekannt, dass die Bakterien in der Lage sind, die mechanischen Eigenschaften des Biofilms zu modulieren, um sie an Veränderungen in der Umgebung anzupassen. Dies geschieht über bakterielle Enzyme. Daher wurde in dieser Arbeit der enzymatische Abbau von Stewartan untersucht, der eine dramatische Änderung der Eigenschaften des Biofilms zufolge haben kann. Dabei wurde die Stewartan Spaltung durch das Enzym WceF untersucht, welches von *Pantoea stewartii* produziert

wird. Dieses Enzym spaltete die Stewartanketten nur sehr langsamen, sodass das Stewartannetzwerk erhalten blieb. Die Ergebnisse wurden mit dem *tailspike* Protein verglichen, welches von dem ΦEa1h Bakteriophagen produziert wird, dem natürlichen Feind des Bakteriums. Im Gegensatz zu WceF, baute das *tailspike* Protein Stewartan deutlich schneller ab und die gesamte mechanische Festigkeit des Netzwerkes wurde beseitigt. Beide Enzyme, trotz der unterschiedlichen Aktivität, besitzen eine sehr ähnliche Struktur, was vermuten lässt, dass sie von einem gleichen Vorgängerprotein abstammen. In dieser Arbeit wird vorgeschlagen, dass WceF möglicherweise in der Kettenlängekontrolle von Stewartan involviert ist.

III. Declaration of Authorship

I hereby declare, that I am the sole author and composer of my thesis and that no other sources or help than those listed, have been used. Wherever contributions of others are involved, this contribution is indicated, clearly acknowledged and due reference is given to the author and source. Furthermore, I declare that I have not submitted this thesis, either in its entirety or excerpts thereof, at any other institution.

(Place, Date) (Signature)

IV. Contributions to This Thesis

This work was done under the auspices of the International Max Planck Research School "Multiscale Bio-Systems". Experiments were carried out at the laboratory of the Physical Biochemistry (University of Potsdam, Head: Prof. Robert Seckler) under the supervision of PD Dr. habil. Stefanie Barbirz. Computational simulations were done at the Department of Theory and Bio-Systems (Max-Planck-Institute for Colloids and Interfaces, Head: Prof. Reinhard Lipowsky) under the supervision of Dr. Andrea Grafmüller.

The following contributions to this thesis work were obtained from experiments performed by other collaborators as listed below

Valentin Dunsing and Prof. Salvatore Chiantia, Physical Cellular Biochemistry, University of Potsdam:

- analysis of the diffusion studies of particles of different size using fluorescence correlation spectroscopy and single-particle tracking including the optimization of the microscope set-up and data processing
- bulk rheology viscosimetric analysis of differently concentrated stewartan solutions
- light-scattering experiments to determine size and zeta potential of nanoparticles

Igor Gayk, Physical Biochemistry, University of Potsdam:

- cloning of WceF and ΦEa1h TSP DNA constructs (plasmids: pET-23a(+)_ΦEa1hTSP_TEV_His6N and pET-23a(+)_WceF_tat_TEV_His6N)
- initial purification protocols for WceF, ΦEa1h TSP and stewartan which were further modified during this thesis work

Dr. Yvette Roske and Prof. Udo Heinemann, Crystallography group, Max-Delbrück Center for Molecular Medicine, Berlin:

- crystallization and structure refinement of WceF

V. Publications and Manuscripts

The contribution of Tobias Irmscher to each publication or manuscript is listed below:

1. Dunsing, V., Irmscher, T., Barbirz, S., Chiantia, S.
   Purely Polysaccharide-Based Biofilm Matrix Provides Size-Selective Diffusion Barriers for Nanoparticles and Bacteriophages, Biomacromolecules, 2019, 20(10):3842-3854

- *Pantoea stewartii* biofilm growth
- purification and resuspension of stewartan
- recombinant expression, purification and fluorescently labeling of the ΦEa1h TSP
- MBTH reducing end test for the determination of the activity of native and labeled ΦEa1h TSP
- labeling, separation from free dye and concentrating of P22 bacteriophage particles
- determination of the overall stewartan concentration in the *Pantoea stewartii* biofilm by the phenol-sulfuric acid method
- overall conceptualization of the diffusion experiments with Valentin Dunsing[1]
- proof-reading of the manuscript

2. Irmscher, T., Roske, Y., Gayk, I., Heinemann, U., Barbirz, S.
   Pantoea stewartii WceF is a glycan biofilm modifying enzyme with a bacteriophage tailspike-like parallel beta-helix fold. Manuscript.

- *Pantoea stewartii* biofilm growth
- purification and resuspension of stewartan
- recombinant expression and purification of WceF and ΦEa1h TSP
- analysis of the three dimensional crystal structure with Yvette Roske and Stefanie Barbirz
- MBTH reducing end test for the determination of the activity of WceF and ΦEa1h TSP under different pH and NaCl conditions
- SDS-PAGE experiments to analyse SDS-resistance of WceF, ΦEa1h TSP and P22 TSP
- purification and analysis of oligosaccharide fragments from the stewartan hydrolysis reactions with capillary electrophoresis
- preparation of the manuscript with Yvette Roske and Stefanie Barbirz

3. Irmscher, T., Singhal, A., Barbirz,S., Grafmüller, A.
   Coarse-grain modelling of the heteropolysaccharide biofilm matrix component stewartan for the description of its microviscosity properties. In preparation.

- all-atomistic and coarse-grain simulations of stewartan
- developing of a coarse-grain model of stewartan
- analysis of the intermolecular contacts, pore size distributions and diffusion dynamics of the stewartan network

VI. List of Abbreviations

CG	- coarse grain
CV	- column volume
DNA	- deoxyribonucleic acid
E. coli	- *Escherichia coli*
ExoPS	- exopolysaccharide
FCS	- fluorescence correlation spectroscopy
Gal	- galactose
Glc	- glucose
GlcA	- glucoronic acid
MBTH	- 3-Methyl-2-benzothiazolinon-hydrazon Hydrochlorid
MD	- molecular dynamics
PS	- polystyrene
P. stewartii	- *Pantoea stewartii*
RDF	- radial distribution function
RMSD	- root mean square deviation
RU	- repeating unit
SDS-PAGE	- dodecyl sulfate–polyacrylamide gel electrophoresis
SPT	- single-particle tracking
taMSD	- time-averaged mean square displacement
TSP	- tailspike protein

VII. List of Figures

VIII. List of Tables

IX. Table of Contents

1. Introduction

1.1 Biofilms – A Natural Bacterial Lifestyle

Bacteria are the oldest organisms on earth and first appeared over three billion years ago (Errington, 2013). Over millions of years, bacteria and archea shaped the global environment and formed suitable physicochemical conditions for globe spanning ecosystems on land, water and air (Jones *et al.*, 1994; Thomsen *et al.*, 2010; Flemming *et al.*, 2016). Nowadays, bacteria are highly appreciated for their atmospheric nitrogen fixation (Tao *et al.*, 2019), as decomposers of organic material (Sekhohola-Dlamini and Tekere, 2019) and lastly as indispensable biotechnological tools (McKay and Baldwin, 1990; Zhao *et al.*, 2019).

Nevertheless, sharing the world with bacteria comes at a price. Every multicellular organism is populated by a greatly diverse microbiota but disturbances in the balance of these associations can cause pathogenicity (Pfeilmeier *et al.*, 2016; Wang *et al.*, 2018). Apparently, bacteria account for economically damaging diseases in plant crops (Narayanasamy, 2011; Mansfield *et al.*, 2012) and provoke serious diseases in animals livestocks and humans (Guilbaud *et al.*, 2015; Ivana *et al.*, 2015). Pathogenesis is driven by an ensemble of various associations which determine the outcome of the invasion of the host, colonization, and evasion of the host defense (Kamoshida *et al.*, 2016; Koeppen *et al.*, 2016; Racicot *et al.*, 2016). Consequently, molecular interactions of bacteria with their host cells and bacterial strategies to proliferate and to survive in infected organisms are an immense research field.

Bacteria naturally form cellular communities encased in a self-produced slimy extracellular matrix (Donlan and Costerton, 2002; Hall-Stoodley *et al.*, 2004; Flemming *et al.*, 2016). These cellular assemblies were first described by van Leeuwenhoek who examined the plaque from his teeth: "Indeed all the people living in our United Netherlands are not as many as the living animals I carry in my own mouth this very day" (Gest, 2004). These biofilms gained a high attention over the past decades because they adhere to surfaces and account for persistent infections (Laganà *et al.*, 2015; Wessman *et al.*, 2015; Oliveira *et al.*, 2016; Høiby *et al.*, 2017; Lynch *et al.*, 2019). Consequently, 60-80 % of all microbial diseases are caused by opportunistic bacteria which form biofilms (Di Lorenzo *et al.*, 2005; Estrela *et al.*, 2009). Biofilm based infections are commonly associated with lung disease (Høiby *et al.*, 2017), otitis (Wessman *et al.*, 2015), periodontitis (Oliveira *et al.*, 2016) and endocarditis

(Laganà *et al.*, 2015; Lynch *et al.*, 2019). Likewise, many plant-associated biofilms infect crop plants and spoil fruits which cause high agricultural losses (Mansfield *et al.*, 2012; Bogino *et al.*, 2013).

Biofilm formation is the way to adopt to environmental conditions and to survive under harsh conditions (Mosier *et al.*, 2015; Charles *et al.*, 2017; Panitz *et al.*, 2019). It helps bacteria by a facilitated binding of ions and nutrients (Zhang *et al.*, 2015; Yu *et al.*, 2019), prevention of desiccation (Hansen and Vogel, 2011; Piercey *et al.*, 2017) and faster exchange of genetic material (Arias-Andres *et al.*, 2018; Olsen *et al.*, 2018a). The extracellular matrix therefore acts as a physical barrier against toxins, host defense substances and environmental stress factors (Birjiniuk *et al.*, 2014; Rybtke *et al.*, 2015; Sandai *et al.*, 2016; Singh *et al.*, 2016). Indeed, Bacteria embedded in a biofilm show a 1000-fold increase in tolerance to antibiotics when compared with their free living counterparts (Høiby *et al.*, 2011). Other factors also contribute to the resistance against antibiotics such as metabolically dormant persister cells and genetically acquired antibiotic resistances (Hall and Mah, 2017; Hughes and Webber, 2017). Data from the European Antimicrobial Resistance Surveillance Network was analyzed and estimated 671,689 infections by antibiotic resistant bacteria in 2015 in the European Economic Area (Cassini *et al.*, 2019). From these incidents a number of 33,110 led to death. Consequently antibiotic resistances are forecasted to be one of the most serious threats to the human society as conventional therapies are rendered ineffective.

As a consequence, alternative treatments of bacterial infections aim to develop strategies which effectively destabilize the integrity of these biofilm aggregates (Cavaliere *et al.*, 2014; Gordon *et al.*, 2017; Fleming and Rumbaugh, 2018). Hence, there is an immense interest in identifying the forces which hold a biofilm together and attaches it to a surface.

1.1.1 Formation of Biofilms

Biofilms were characterized as sticky cellular assemblies as they attach to a diverse set of surfaces. In addition to the colonization of human biotic surfaces, biofilms contaminate medical devices (catheters, pacemakers, dentures) (Percival *et al.*, 2015), technical equipment (Kim *et al.*, 2013) and food products (Shi and Zhu, 2009). Biofilms were also found to grow on ship hulls resulting in an increased fuel expenditure (Hunsucker *et al.*, 2018).

Surface-associated biofilm formation is usually characterized by a cycle of several stages (Figure 1) (Shi and Zhu, 2009; Toyofuku *et al.*, 2016; Santos *et al.*, 2018). The initial step is the attachment (1. Attachment) of a highly motile bacterium which will consequently produce large colonies by consecutive cell divisions (2. Microcolony Formation). The growth and physiology of biofilms strongly depend on environmental cues and the ability of cell-cell communications via quorum sensing (Koutsoudis *et al.*, 2006; Toyofuku *et al.*, 2016; Tseng *et al.*, 2016). This is of huge importance, as bacteria need to reach a critical cell density before a throughout infection can occur (Li and Tian, 2012). Here, bacteria regulate physiological processes by the production and response to small signal molecules including peptides or acyl-homoserine lactones. Subsequently, the production of the extracellular matrix is triggered in order to form the mature biofilm structures (3. Maturation). The whole process is underlined by a stage-specific microbiome and protein expression distinguishing the biofilm lifestyle from the planktonic state (Karatan and Watnick, 2009; Rodesney *et al.*, 2017). Nevertheless, biofilm formation is not necessarily irreversible and bacteria can escape from their sessile cellular community which leads to the dispersal of the biofilm and colonization of new surfaces (4. Dispersion) (Kim and Lee, 2016).

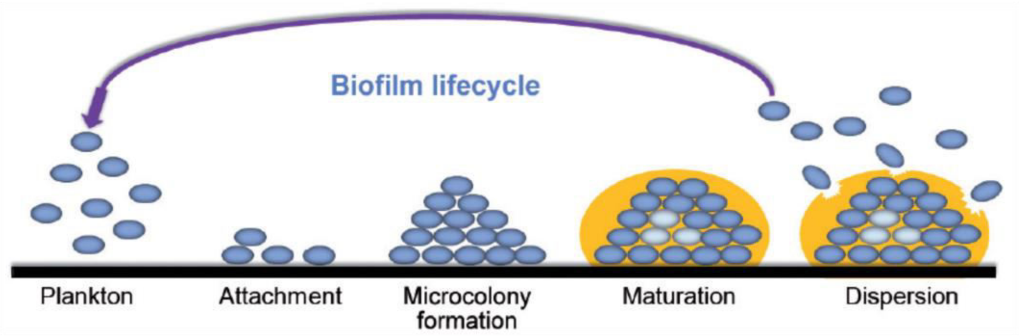

Figure 1: The Biofilm lifecycle, from Santos *et al.*, 2018
Biofilm formation is characterized by a circle of distinct steps: planktonic cells attach to a surface and initiate the assembly of microcolonies. The maturation of the biofilm includes the production of the extracellular matrix. Biofilm embedded bacteria can switch to the planktonic lifestyle again and are able to disperse from the biofilm in order to colonize new surfaces.

The ability to form biofilms is not only restricted to bacteria and has been also found in other organism such as archea and funghi (Sheppard and Howell, 2016; van Wolferen *et al.*, 2018). Indeed, in nature often mixed-species biofilms are found organized in physically enclosed microconsortia (Kay *et al.*, 2011; Chew *et al.*, 2014).

1.1.2 Mechanical Stability of the Three Dimensional Biofilm Architecture

Disruption of the biofilm renders bacteria more susceptible to antibiotics (Houry *et al.*, 2012; Cavaliere *et al.*, 2014; Fleming and Rumbaugh, 2018). Apparently, the increased tolerance against the host immune system and antimicrobials in biofilms is intimately linked to the structure and composition of the extracellular matrix. The highly hydrated extracellular space consist of a myriad of various kinds of biomolecules such as exopolysaccharides (ExoPSs), proteins, extracellular deoxyribonucleic acid (DNA) and phospholipids (Figure 2, A) (Karatan and Watnick, 2009; Flemming and Wingender, 2010). The amount and ratio of the extracellular materials differs greatly between bacterial species.

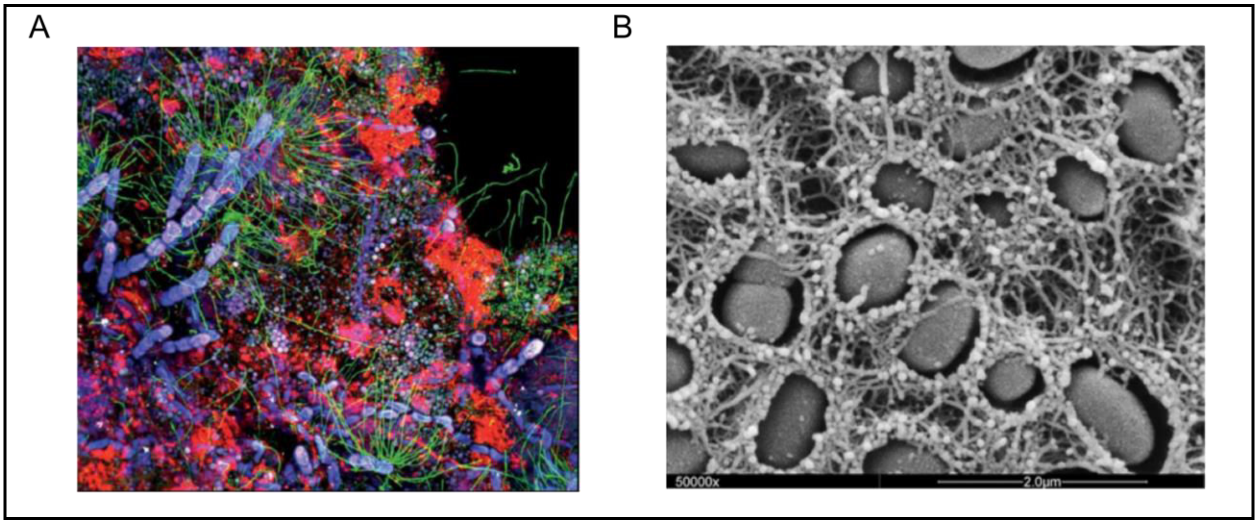

Figure 2: The extracellular space in biofilms, from Kamjunke *et al.*, 2015 and Serra *et al.*, 2013b
(A) Fluorescent stain of a river biofilm developed on a pebble stone to emphasize the high density of various extracellular biomolecules. Here, nucleic acids and polysaccharides are stained with SybrGreen (green) and AAL-Alexa568 (red), respectively (Kamjunke *et al.*, 2015). Algae and cyanobacteria are colored in blue and purple/ white due to their autofluorescence. (B) Electron microscopy image of *E. coli* cells which are embedded in a tightly packed extracellular matrix (Serra *et al.*, 2013b).

Elucidation of the physiochemical properties of the biofilm is highly difficult due to the heterogeneity of the extracellular matrix. In addition, biofilms may be investigated under unphysiological conditions with deviations in matrix compositions or genetic profile (Gordon *et al.*, 2017). Fluorescence based microscopy has been widely used to visualize the three dimensional biofilm assemblies (Bridier *et al.*, 2010; Guilbaud *et al.*, 2015; Oniciuc *et al.*, 2016). Nevertheless, despite the complex mixture in the extracellular matrix it could been shown that biofilms form large supracellular architectures with highly defined spatial organizations (Figure 2, B) (Wilking *et al.*, 2013; Birjiniuk *et al.*, 2014; Stewart *et al.*, 2015). The resulting biofilm morphology was shown to be flat, rough, filamentous or mushroom-like (Karatan and Watnick, 2009). Biofilms are permeated by fluid-like channels which guarantee the introduction of water and small molecules like ions (Wilking *et al.*, 2013; Birjiniuk *et al.*, 2014). In contrast, the extracellular matrix acts as a molecular filter that selectively determines which molecule are permitted to deeply penetrate the biofilm (Flemming and Wingender, 2010). Thus, diffusion strongly depends on the size and charge of the investigated diffusing agent. Especially ionic interactions or complexations with the matrix contributes to limiting the therapeutic effects of antimicrobials (Birjiniuk *et al.*, 2014; Singh *et al.*, 2016). In addition, biofilms might be shielded by a hydrophobic outer layer of proteins which also influence the diffusivity (Epstein *et al.*, 2011; Zeng *et al.*, 2015).

Particle tracking and cryo electron microscopy have revealed microscopic details of the extracellular biomolecules which form a tight mesh covering the bacteria cells (Figure 2, B) (Serra *et al.*, 2013a; Hart *et al.*, 2019). The density of the extracellular material increases with the depth of the biofilm (Birjiniuk *et al.*, 2014; Abedon, 2016). In addition, the biopolymers of the extracellular matrix account for the barrier function of the biofilms. Additionally, atomic force microscopy and rheological studies have shown that the overall biofilm material deforms in a viscoelastic gel-like manner (Stewart *et al.*, 2013; Gordon *et al.*, 2017; Vidakovic *et al.*, 2018). It is assumed that weak physiochemical interactions such as hydrogen bonds, van der Waals forces and other electrostatic interactions in the biofilm can be easily broken and reformed to ensure elastic deformation (Flemming and Wingender, 2010). This is supported by studies showing that the addition of sodium chloride and bivalent cations support the formation of the biofilm (Guvensen *et al.*, 2013; Tischler *et al.*, 2018; Dubois *et al.*, 2019). Especially Ca^{2+}-Ions chemically crosslink the ExoPS chains and therefore increase biofilm cohesiveness and stability (Seviour *et al.*, 2012; Chalykh *et al.*, 2017; Nakauma *et al.*, 2017).
Inherent to these viscoelastic mechanical processes is the sensing of mechanical inputs by the bacteria which are therefore able to respond to environmental stresses (Belas and Suvanasuthi, 2005; Hickman *et al.*, 2005; Rodesney *et al.*, 2017). Likewise, during the biofilm lifetime the extracellular matrix is constantly modified by the bacteria (Rochex *et al.*, 2008; Flemming, 2011; Peterson *et al.*, 2015). This includes alterations in the compositions of the extracellular matrix as well as enzymatic remodeling ultimately adjusting the physicochemical parameters of the biofilm architecture (Vuong *et al.*, 2004; Tielen *et al.*, 2010; Houry *et al.*, 2012). For example, bacteria respond to the experienced shear stress under fluid flow with an increased upregulation of biofilm-specific genes to form biofilms with higher mechanical cohesiveness (Rodesney *et al.*, 2017). Additionally, biofilm dispersion is initiated by the use of matrix-degrading enzymes (Houry *et al.*, 2012; Yu *et al.*, 2015; Jang *et al.*, 2016; Torelli *et al.*, 2017). Hence, the mechanical strength of the extracellular matrix and its flexible reconfiguration allow biofilms to survive and adapt to harsh environmental conditions.

1.2 Properties of Bacterial Exopolysaccharides

ExoPSs are the major constituents of biofilms and accounts for up to 90 % of the dry weight (Flemming and Wingender, 2010). ExoPSs exhibit a high degree of polymerization with high molecular weights (up to 10^5-10^9 Da) (Nwodo *et al.*, 2012). These glycans are secreted and accumulated in the extracellular space. Their biosynthesis pathway depends on the polysaccharide compositions (Nwodo *et al.*, 2012; Schmid *et al.*, 2015). Homopolymeric polysaccharides are often polymerized and secreted by a single synthase as part of a multimeric complex which spans the distance from the inner to the outer membrane. In contrast, heteropolymeric ExoPSs which show a large variety of combinations of different monosaccharides, are assembled into repeating units at the cytoplasmic face of the inner membrane. Translocation into the periplasm takes place in associations with a Wzx protein and they are then polymerized by a Wzy protein preceding the final secretion (Whitfield, 2006; Schmid *et al.*, 2015).

ExoPSs can be branched or unbranched and modified with acetyl, glycerol and phosphate groups (Ruas-Madiedo *et al.*, 2002; Nwodo *et al.*, 2012). They usually contain a mix of neutral and charged sugar residues, such as glucoronic acid. In concert with pyruvate and sulphate modifications these polysaccharides give rise to the polyanionic nature of the biofilm which maintains a proper hydration due to the binding capacity for water (Sutherland, 2001b).

ExoPSs form the mechanical scaffolds which confer a high stability and integrity to the biofilms (Chew *et al.*, 2014). Likewise, they are implicated in surface adhesion and in mediating the three-dimensional biofilm structure cohesiveness (Danese *et al.*, 2000; Borgersen *et al.*, 2018; Liu and Catchmark, 2018). Bacteria produce different types of ExoPSs which account for variations in the mechanical properties of the respective biofilms, such as cohesiveness and stiffness (Gordon *et al.*, 2017). They are also involved in cell-cell interactions (Ma *et al.*, 2009). Bacterial mutants in which ExoPS biosynthesis is disrupted are not able to form mature biofilms (Stewart *et al.*, 2015; Rodesney *et al.*, 2017; Vidakovic *et al.*, 2018). Similarly, ExoPSs play an important part in biofilm associated diseases and were found to be constantly produced by bacteria during chronic infections in human (Götz, 2002; Wang *et al.*, 2016a; Jean-Gilles Beaubrun *et al.*, 2017).

Similar or equivalent polysaccharides can be also found in plants and in humans (Freitas *et al.*, 2011; Nwodo *et al.*, 2012). Therefore, ExoPSs are of high biotechnological relevance for medical and pharmaceutical applications (Table 1). Additionally, they show anti-inflammatory and anti-metastatic properties. They have been used in cosmetics and as moisturizers due to their hygroscopic properties

(Freitas *et al.*, 2015; Petri, 2015; Ma and Suh, 2019). Furthermore, ExoPSs have been included as thickening and stabilizing agents in food products to alter the rheological properties (Ullah *et al.*, 2016; Baruah *et al.*, 2017; Qin *et al.*, 2018). Due to their environmental compatibility they are also considered for green thermoset coatings (Zheng *et al.*, 2015; Gandini *et al.*, 2016). The number of studies grow which concentrate on their usability in wastewater treatment (Mittal *et al.*, 2016) and oil recovery (Jang *et al.*, 2015). There is a demand for finding new polysaccharide-derived materials with complementing functionalities. Therefore, the composition and structure of the polysaccharides are engineered to achieve precisely tailored materials with superior properties (Schmid *et al.*, 2015; Schmid and Sieber, 2015).

Table 1: Overview of exopolysaccharides used in commercial applications

ExoPSs	Components	Bacterial host	Examples for applications	References
Alginate	Gluoronic acid Mannuronic acid Acetate	Pseudomonas aeruginosa Azotobacter vinelandii	Food thickening Cosmetics: Suspension stabilizer Wound dressings Controlled drug release Antiacid stomach protector Treatment of thromboembolic disorders	Peña *et al.*, 2008; Kamoun *et al.*, 2015; Chen *et al.*, 2018; Kozlowska *et al.*, 2019; Leon *et al.*, 2019; Wilkinson *et al.*, 2019
Cellulose	Glucose	Acetobacter species	Gelling Agent Drug Delivery/ coating Wound healing/ dressing	Hakkarainen *et al.*, 2016; Ullah *et al.*, 2016
Dextran	Glucose	Leuconostoc mesenteroides	Food Stabilizer Controls wound shock Chromatographic media	Kothari *et al.*, 2015; Yi *et al.*, 2015; Alibolandi *et al.*, 2017; Baruah *et al.*, 2017; Liu *et al.*, 2017
Hyaluronan	Glucoronic acid Acetylglucosamine	Streptococcus equisimilis/ zooepidemicus Bacillus subtilus	Cosmetics: Suspension stabilizer Cosmetics: Moisturizer Promote angiogenesis and inhibits tumor progression Tissue Engineering Vitreous substitute in eye surgery	Chanmee *et al.*, 2016; Wang *et al.*, 2016b; Zhang *et al.*, 2016; Januschowski *et al.*, 2019; Ma and Suh, 2019
Succinoglycan	Glucose Galactose Actetate Pyruvate Succinate 3-hydroxybutyrate	Alcaligenes faecalis subspecies myxogenes	Food thickening Cosmetics: Suspension stabilizer Oil drilling/ recovery	Halder *et al.*, 2017; Kavitake *et al.*, 2019; Pedroso *et al*, 2019; Yang *et al.*, 2019
Xanthan	Glucose Mannose Glucoronic acid Acetate Pyruvate	Xanthomonas species	Food thickening Cosmetics: Suspension stabilizer Oil drilling/ fracturing and pipeline cleaning Thermoset coatings Water-based paints	Jang *et al.*, 2015; Krstonošić *et al.*, 2015; Rwei *et al.*, 2015; Gandini *et al.*, 2016; Mittal *et al.*, 2016; Hasnain and Nayak, 2019; Singhvi *et al.*, 2019

1.3 Bacteriophages as an Alternative Treatment in Biofilm Infections

Bacteriophages have been used in the treatment of bacterial infections long before Alexander Fleming discovered antibiotics. In 1917 the Canadian microbiologist Felix d'Herelle isolated bacteriophages and termed them to be a bacteria-eating entity (Dublanchet and Bourne, 2007). Soon, first patients suffering from various diseases and injuries were treated with great success (Fruciano and Bourne, 2007; Moelling *et al.*, 2018). Nevertheless, as soon as antibiotics were shown to be fast and reliable in killing bacteria, the interest in phage therapy rapidly decreased (Bush, 2010). Nevertheless, scientists especially in the former Soviet Union carried on with the phage treatment either alone or in combination with antibiotics (Kutateladze and Adamia, 2008). Nowadays, due to the rise of the antibiotic crisis marked by multidrug-resistant bacteria, bacteriophage therapy has come back in focus.

Bacteriophages are viruses specifically infecting bacterial hosts which they use to replicate. They are described as the most abundant entity on earth with their weight in oceans estimated to be equal to the weight of human beings (Comeau *et al.*, 2008). *Caudovirales* are double-stranded DNA viruses which package their genome into an icosahedral capsid (Ackermann, 2003; Fokine and Rossmann, 2014). Here, the size of the genome ranges from 15 – 500 kilo base pairs. They are classified according to their tail morphology. Myoviridae are characterized by long contractile tails, Siphoviridae posses long non-contractile tails and Podoviridae have short non-contractile tails. The tail is connected to the head at one vertex of the capsid. It is responsible for host recognition and mediates the initiation of the infection process (Fernandes and São-José, 2018; Nobrega *et al.*, 2018). Tail fibers, spikes and tips serve as receptor-binding proteins and mediate the attachment of the phage to the bacterium which results in an essentially irreversible adsorption of the bacteriophage onto the bacterium's surface. The tail structure penetrates the host membrane and subsequently the phage's genetic material is injected into the host cytoplasm. A wide variety of bacterial surface polysaccharides have been studied as host cell receptors, including lipopolysaccharides with (smooth) or without (rough) O-antigens, teichoic acids and capsules (Chaturongakul and Ounjai, 2014; Nobrega *et al.*, 2018). A very well studied examples of a glycan-specific podoviridae is the P22 phage which recognizes the *Salmonella* O-antigen (Figure 3) (Steinbacher *et al.*, 1994; Andres *et al.*, 2010a; Andres *et al.*, 2013). In addition, proteinaceous structures have also been known to be recognized by bacteriophages (Nobrega *et al.*, 2018). Infection of bacteria embedded in biofilms poses another challenge for bacteriophages as they need to overcome this additional protective layer (Hughes and Webber, 2017;

Fernandes and São-José, 2018). The penetration and diffusion of bacteriophages into the biofilm assembly is reduced due to both steric constraints and tight binding events. Bacteriophages revealed a higher activity in less mature biofilms which displayed a lower density of extracellular material (Abedon, 2016; Vidakovic *et al.*, 2018). The genome of phages contains enzymes suitable for the degradation of matrix components. Bacteriophage polysaccharide depolymerases, endopeptidases and DNases have been shown to be involved in matrix digestion to render the biofilm more porous (Pires *et al.*, 2016; Fernandes and São-José, 2018).

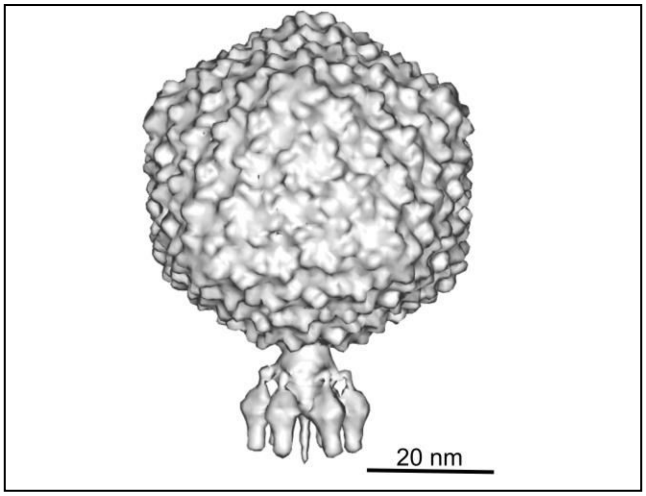

Figure 3: Reconstruction of the *Salmonella* P22 bacteriophage (emdb: 1222)
Bacteriophages consist of an icosahedral capsid structure and are classified according their tail morphology. Podoviridae, like the *Salmonella* P22 phage, exhibit short tails including tail fibers and spikes.

In vitro experiments and studies in infected patients have emphasized that phages can be used to eradicate biofilms, which were initially tolerant to antibiotics (Harper *et al.*, 2014). A set of commercially available phage cocktails are regularly used in agriculture to protect plants from bacterial biofilm infection and spread (Svircev *et al.*, 2018). Phages have also been approved for the use in food products against *Listeria monocytogenes* (Bren, 2007). Persister cells are infected by bacteriophages as soon as the cells switch to normal growth (Harms *et al.*, 2017; Di Luca *et al.*, 2018; Tkhilaishvili *et al.*, 2018). Due to their high host specificity, phage therapy reduces potential side effect, as for example the reduction of commensal bacteria. At the moment, a regulatory framework has to be devised for the use of bacteriophages as drugs against biofilm infections. This includes the systematic investigation of phage formulation administering, phage safety and other possible side effects such as a facilitated bacterial horizontal gene transfer (Hughes and Webber, 2017).

1.4 Conserved Folds in Bacteriophage Tailspike Proteins

Tailspike proteins (TSPs) are commonly used by the bacteriophage to recognize and enzymatically cleave exposed glycan structures on the bacterial surface to fulfill the infection process (Andres *et al.*, 2012; Lee *et al.*, 2017; Broeker *et al.*, 2018). Additionally, they are indispensable tools to overcome the biofilm barrier to permit access to the bacterial cell surface (Gutiérrez *et al.*, 2015; Majkowska-Skrobek *et al.*, 2016; Lee *et al.*, 2017). For example, TSPs administered to chicken were shown to reduce *Salmonella* typhimurium colonization of the cecum (Waseh *et al.*, 2010).

Until today, many crystal structures of TSPs have been published, among them, TSPs cleaving the O-antigen (*Salmonella* P22 TSP, Steinbacher *et al.*, 1994) or the biofilm ExoPS (*Acinetobacter* phage ΦAB6 TSP, Lee *et al.*, 2017). The studies visualized the cocrystallization of TSPs with digested polysaccharide fragments of one to three repeating units (RU) length. TSPs usually do not share any consensus sequences, but assemble into structurally similar elongated and tightly packed trimeric β-solenoids (Figure 4) (Barbirz *et al.*, 2008; Müller *et al.*, 2008; Lee *et al.*, 2017; Greenfield *et al.*, 2019). In addition, the monomeric subunits interdigitate to form highly thermostable and protease resistant units (Barbirz *et al.*, 2009; Broeker *et al.*, 2017). The hallmark of the three dimensional TSP structures is a central oligomeric parallel β-helix. The latter motif is often found in proteins from all kingdoms of life associated with polysaccharide modifications (Jenkins and Pickersgill, 2001; Cowen *et al.*, 2002; Kajava and Steven, 2006). Each monomeric β-helix is build from by coils composed of the three β-sheets B1, B2 and B3 which are connected by the turns T1, T2 and T3. The latter ones vary in their length and sometimes loops or helical elements are integrated. The coils of the β-helix have L- or kidney-shaped cross sections. The β-helix accommodates a hydrophobic interior which is sealed by an α-helix lying on top of the β-helix. Elongated and shallow grooves on the surface of the β-helix represent polysaccharide binding sites with high specificity (Kang *et al.*, 2016; Lee *et al.*, 2017; Greenfield *et al.*, 2019).

Preceding the β-helix, TSPs usually comprise an N-terminal particle-binding domain which connects the protein to the phage particle. However, attempts to crystallize the full-length TSPs were often hindered due to a flexible linker between the N-terminal domain and the protein. Therefore, often only N-terminal shortened constructs have been crystallized (Barbirz *et al.*, 2008; Müller *et al.*, 2008; Lee *et al.*, 2017). The C-termini of TSPs also differ between the bacteriophage species but usually display β-sheet motifs.

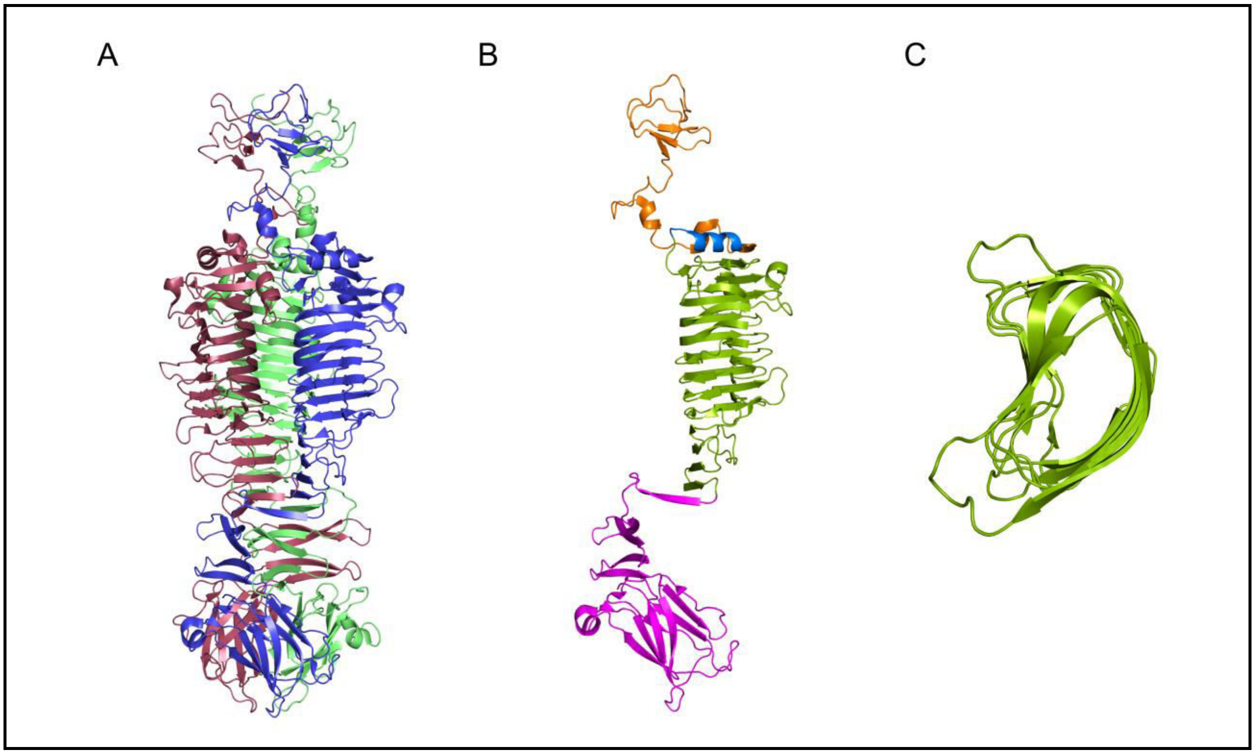

Figure 4: Structural overview of the ΦAB6 TSP
The three-dimensional structure of the ΦAB6 TSP (pdb: 5js4) is shown as an example of the β-solenoid TSP fold. (A) The trimer of the ΦAB6 TSP is given with each monomer to be depicted in cartoon representation in green, red and blue. (B) A single monomeric subunit of the ΦAB6 TSP is displayed with the N-terminus in orange, the α-helix in blue, the β-helix in green and the C-terminus in purple. (C) Cross-section of the β-helical structure revealed kidney-shaped coils.

1.5 *Pantoea stewartii* – A Biofilm Producing Plant Pathogen

Pantoea stewartii (P. stewarti) is a rod-shaped plant pathogen which was first reported in the 1890s (Stewart, 1897). It is the causative agent of the stewartas wilt disease in maize and sweet corn. Infected plants show characteristics of wilted leaves up to necrosis of crops which are deadly to seedlings and young plants (Braun, 1982; Pataky, 2003; Roper, 2011). Other hosts are dent, flint and flour (OEPP/EPPO). *P. stewartii* cells are transmitted to susceptible plants by the corn flee beetle (*Chaetocnema pulicaria*) via feeding wounds (Block *et al.*, 1998; Cook *et al.*, 2005). The bacterium immigrates into the intercellular spaces provoking water soaked lesions in leaves with green to yellow streaks and wavy margins (Figure 5, C) (Roper, 2011). It further colonizes the xylem of infected plants which allows the systemic spread of the disease (Koutsoudis *et al.*, 2006) (Figure 5, A,B). *P. stewartii* produces dense biofilms which account for blockage of the free water flow in the xylem which cause the wilt in infected plants (Bellemann *et al.*, 1994; Roper, 2011).

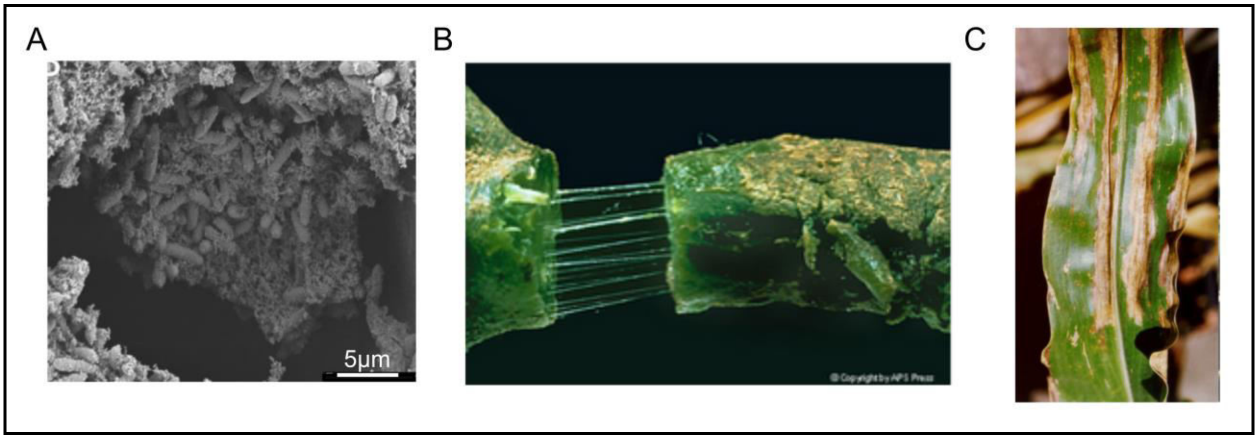

Figure 5: *P. stewartii* infects maize and sweet corn, from Koutsoudis *et al.*, 2006, Williams S.D., M.J., Hand, F.P., 2019 and Jeger *et al.*, 2018

(A) During the infection *P. stewartii* produces dense biofilms in the xylem of infected plants (Koutsoudis *et al.*, 2006). (B) When such a stem is cut, oozing of *P. stewartii* biofilm can be seen (Williams S.D., M.J., Hand, F.P., 2019). (C) Blockage of the free water flow leads to the characteristic wilting of leaves and crops (Jeger *et al.*, 2018).

Infection of susceptible plants led to substantial economic losses of corn in the 1930s and *P. stewartii* was therefore put under quarantine restrictions (OEPP/EPPO, 1978; Freeman and Pataky, 2001). Nowadays, resistant plant cultivars have diminished the threat of *P. stewartii* infections but this pathogen is still active in Europe, North and South America where susceptible plants grow (Jeger *et al.*, 2018). Furthermore import regulations on maize seeds has been set up to prevent further spread of the pathogen (Bragard *et al.*, 2019).

Pantoea species are highly diverse and have been isolated from diverse ecological sources (Walterson and Stavrinides, 2015). They carry out infections in rice, maize, eucalyptus, millet and pineapple all over the world. The closely related *Erwinia amylovora* spoils populations of rosaceous plants like apple and pear (Hinze *et al.*, 2016). The latter was put on place 7 on the list of the top ten most important plant pathogenic bacteria (Mansfield *et al.*, 2012). In addition, *Pantoea* species have appeared to be associated with inflammations in humans such as arthritis (Baere *et al.*, 2004; Cruz *et al.*, 2007). However, their implication in human infections is still under debate as *Pantoea* is not an opportunistic human colonizer (Dutkiewicz *et al.*, 2016). Still, studies have pointed towards a correlation of nosocomial infections in hospitals with the presence of *Pantoea* bacteria (Bicudo *et al.*, 2007). In addition, *Pantoea* species were found to be highly environmental versatile (Walterson and Stavrinides, 2015; Weller-Stuart *et al.*, 2017). They have been used for bioremediation and as biological control agents against insect pests and other plant pathogens.

During plant infection by *P. stewartii* high amounts of the ExoPS stewartan are secreted into the biofilm (Bellemann *et al.*, 1994; Nimtz *et al.*, 1996; Schollmeyer *et al.*, 2012). Stewartan is the most abundant component of the extracellular matrix and has consequently been shown to be the major *P. stewartii* virulence factor (Nimtz *et al.*, 1996; Herrera *et al.*, 2008). Stewartan also protects the bacterium from the host defense mechanisms (Koutsoudis *et al.*, 2006; Piqué *et al.*, 2015). Stewartan is a branched anionic heteropolymer consisting of repeating heptasaccharide units (Figure 6) (Nimtz *et al.*, 1996). The ExoPS backbone structure $[\rightarrow 3)\text{-}\alpha\text{-}\textsc{d}\text{-Gal}^{I}(1\rightarrow 6)\text{-}\beta\text{-}\textsc{d}\text{-Glc}^{II}(1\rightarrow 3)\text{-}\beta\text{-}\textsc{d}\text{-Gal}^{III}(1\rightarrow]_{n}$ is branched at Gal^{I} with $[(4\rightarrow 1)\text{-}\beta\text{-}\textsc{d}\text{-GlcA}^{IV}(4\rightarrow 1)\text{-}\alpha\text{-}\textsc{d}\text{-Gal}^{V}(6\rightarrow 1)\text{-}\beta\text{-}\textsc{d}\text{-Glc}^{VI}]$. Additionally, 90% of Gal^{I} is modified with $(6\rightarrow 1)\text{-}\beta\text{-}\textsc{d}\text{-Glc}^{VII}$. Stewartan chains are highly polymerized with sizes of 2-4 MDa (ca. 2000-4000 RUs) (Schollmeyer *et al.*, 2012).

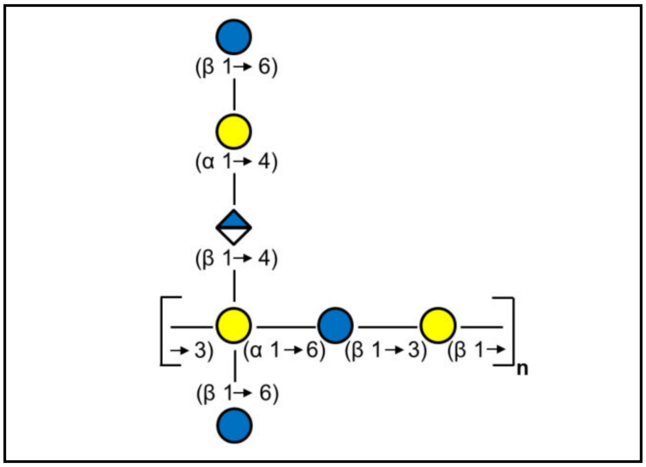

Figure 6: Structure of a single RU of the ExoPS stewartan from *P. stewartii*
The monosaccharides of stewartan are shown as blue (glucose) and yellow circles (galactose). The gluocoronic acid is depicted as a blue/ white diamond.

The genes encoding the biosynthesis of stewartan are organized on the three different loci *wce I-III* (Figure 7) (Bernhard, 1996; Carlier *et al.*, 2009). The *wce* gene cluster has been found to be cross-complementary to the *Erwinia pyrifoliae* and *Erwinia amylovora* ExoPSs loci. Therefore, the function of the proteins from the *wce* gene cluster were assigned by sequence homology (Bernhard, 1996; Langlotz *et al.*, 2011). In addition, mutational analysis in *P. stewartii* further revealed the roles of the *wce I-III* proteins (Carlier *et al.*, 2009; Wang *et al.*, 2012). This includes the characterization of the stewartan biosynthesis pathway as Wzx/Wzy dependent (Vanneste, 2000; Schmid *et al.*, 2015). Stewartan RU synthesis starts with the transfer of a galactose onto an undecaprenylphopshate-linker by WceG1 and 2 (Carlier *et al.*, 2009). The glycosyltransferases WceB, K, M, N and O add further monosaccharide units to complete the RU structure (Carlier *et al.*, 2009; Langlotz *et al.*, 2011). Subsequently, stewartan subunits are flipped by Wzx1 and 2 across the inner membrane and are polymerized in a Wzy-dependent manner using WceL

(Vanneste, 2000; Wang *et al.*, 2012). Finally, Wza,b and c take part in the export process of polymerized stewartan. WceJ was found to be a non-functional pyruvate-transferase which is not required for *P. stewartii* virulence (Wang *et al.*, 2012).

Figure 7: The biosynthesis of stewartan is encoded in the *P. stewartii wce I-III gene* cluster
The synthesis of stewartan RUs is accomplished by the glycosyltransferases WceB, G1, G2, K, M, N and O (orange). Afterwards RUs are flipped by Wzx1 and 2 (blue) to the periplasm and polymerized by WceL (green). Finally stewartan chains are secreted (Wza, b and c, purple). The gene *wceJ* (white) codes for a non-functional pyruvate-transferase. No function has yet been assigned to WceF (black).

1.6 Aims of this Study

The extracellular matrix is the key in understanding the assembly and integrity of biofilms. It controls the transport of drugs and antimicrobials. Consequently, bacterial biofilm assemblies are of high clinical relevance. Previous studies have rather concentrated on the macroscopic properties of biofilms but these bulk experiments are insufficient to obtain a detailed understanding of structural details at high spatiotemporal resolution. Therefore, reductionist approaches are needed to understand the contribution of single components of the extracellular matrix in constantly varying biofilm assemblies. In this study stewartan from *P. stewartii* was chosen as a model system for several reasons:

a. the extracellular matrix of the *P. stewartii* biofilm displays a comparatively well-defined composition with only one ExoPS species and

b. stewartan is the most abundant component in *P. stewartii* biofilms and consequently the leading factor that dominates *P. stewartii* biofilm function and integrity.

Just a few methods are capable of resolving polysaccharide nanostructures. In this work, the three dimensional structure of stewartan polymers was elucidated using Coarse-Grained Molecular Dynamics Simulations. For experimental investigations stewartan was purified from *P. stewartii* biofilms to further analyze the influence of the three dimensional stewartan network arrangement on the diffusion of fluorescently labeled model particles of varying size, bacteriophages and proteins. To derive a mathematical stochastic description of these processes fluorescence correlation spectroscopy and single particle tracking were used. It is of great interest to understand how bacteria and other biofilm interacting species modulate the mechanical properties of the biofilm. Likewise, it was the aim to find suitable enzyme candidates which are involved in the remodeling of the polysaccharide structure. Hence, the structure of WceF, from the *P. stewartii wce I* locus, and ΦEa1h TSP was biophysically characterized and their interaction with stewartan was investigated to give a description of the relevant underlying physiological processes.

2. Materials

2.1 Chemicals

Chemical		**Company**
Acetic acid	(CH_3COOH)	Carl Roth, Karlsruhe, Germany
Acetonitrile		VWR, Darmstadt, Germany
Agar-agar		Carl Roth, Karlsruhe, Germany
8-Aminopyrene-1,3,6-trisulfonic acid, trisodium salt	(APTS)	Biomol GmbH, Hamburg, Germany
Ammonium iron(III) sulfate dodecahydrate	($NH_4Fe(SO_4)_2 \cdot 12H_2O$)	Carl Roth, Karlsruhe, Germany
Ammoniumperoxodisulfat	(APS)	Carl Roth, Karlsruhe, Germany
Ampicillin		Carl Roth, Karlsruhe, Germany
ATTO 488 NHS-Ester		ATTO-TEC GmbH, Siegen, Germany
Bromophenol blue		Sigma-Aldrich, St. Louis, USA
Difco^{TM} Casamino Acids		Thermo Fisher Scientific, Waltham, USA
Calcium chloride dihydrate	($CaCl2 \cdot 2H_2O$)	Merck, Darmstadt, Germany
3-[(3-Cholamidopropyl)dimethylammonio]-1-propanesulfonate	(CHAPS)	Serva Feinbiochemica GmbH, Heidelberg, Germany
Coomassie Brilliant Blue R250		GE Healthcare, Chicago, USA
N-Cyclohexyl-2-aminoethanesulfonic acid	(CHES)	Serva Feinbiochemica GmbH, Heidelberg, Germany
Dihydroxybenzoic acid	(DHB)	Sigma-Aldrich, St. Louis, USA
Dimethyl sulfoxide	(DMSO)	Sigma-Aldrich, St. Louis, USA
Dithioerythritol	(DTE)	Carl Roth, Karlsruhe, Germany
Dithiothreitol	(DTT)	AppliChem GmbH, Darmstadt, Germany
di-Sodium hydrogen phosphate dihydrate	($Na_2HPO_4 \cdot 2H_2O$)	Carl Roth, Karlsruhe, Germany
Ethanol		VWR, Darmstadt, Germany
Ethylenediaminetetraacetic acid	(EDTA)	Carl Roth, Karlsruhe, Germany
D-(+)-Glucose		Sigma-Aldrich, St. Louis, USA
Glycerol		Carl Roth, Karlsruhe, Germany
Glycine		Carl Roth, Karlsruhe, Germany
Guanidine hydrochloride	(Gdm-HCl)	Thermo Fisher Scientific, Waltham, USA
Hydrochlorid acid	(HCl)	Carl Roth, Karlsruhe, Germany
4-(2-Hydroxyethyl)-1-piperazineethanesulfonic acid	(HEPES)	Carl Roth, Karlsruhe, Germany
Imidazole		Carl Roth, Karlsruhe, Germany
Isopropanole		VWR, Darmstadt, Germany
Isopropyl β-D-1-thiogalactopyranoside	(IPTG)	Carl Roth, Karlsruhe, Germany
Lithium acetate	(CH_3COOLi)	Carl Roth, Karlsruhe, Germany
Magnesium chloride hexahydrate	($MgCl_2 \cdot 6H_2O$)	Carl Roth, Karlsruhe, Germany

Magnesium sulfate heptahydrate	($MgSO_4 \cdot 7H_2O$)	Carl Roth, Karlsruhe, Germany
Manganese(II)-chloride tetrahydrate	($MnCl_2 \cdot 4H_2O$)	Carl Roth, Karlsruhe, Germany
Meat extract		Carl Roth, Karlsruhe, Germany
3-Methyl-2-benzothiazolinon-hydrazon Hydrochlorid	(MBTH)	Sigma-Aldrich, St. Louis, USA
2-(*N*-morpholino)ethanesulfonic acid	(MES)	Carl Roth, Karlsruhe, Germany
Nickel(II)-chloride hexahydrate	($NiCl_2 \cdot 6H_2O$)	Carl Roth, Karlsruhe, Germany
Phenol		Carl Roth, Karlsruhe, Germany
Polyethylene glycol 300	(PEG 300)	Carl Roth, Karlsruhe, Germany
Potassium chloride	(KCl)	Merck, Darmstadt, Germany
Potassium dihydrogen phosphate	(KH_2PO_4)	Carl Roth, Karlsruhe, Germany
Rotiphorese® Gel 30		Carl Roth, Karlsruhe, Germany
Sodium acetate trihydrate	($CH_3COONa \cdot 3H_2O$)	Merck, Darmstadt, Germany
Sodium chloride	(NaCl)	Carl Roth, Karlsruhe, Germany
Sodium cyanoborohydride	($NaBH_3CN$)	Carl Roth, Karlsruhe, Germany
Sodium dodecyl sulfate	(SDS)	AppliChem GmbH, Darmstadt, Germany
Sodium hydroxide	(NaOH)	Carl Roth, Karlsruhe, Germany
Sodium hydrogen carbonate	($NaHCO_3$)	Carl Roth, Karlsruhe, Germany
Sucrose		AppliChem GmbH, Darmstadt, Germany
Sulfamic acid	(H_3NSO_3)	Carl Roth, Karlsruhe, Germany
Sulfuric Acid	(H_2SO_4)	Carl Roth, Karlsruhe, Germany
Tetrahydrofuran	(THF)	
N,*N*,*N*′,*N*′-Tetramethylethylendiamin	(TEMED)	Carl Roth, Karlsruhe, Germany
Tris(hydroxymethyl)-aminomethan	(Tris)	Carl Roth, Karlsruhe, Germany
Trifluoroaetic acid	(TFA)	Merck, Darmstadt, Germany
tri-Sodium citrate		Merck, Darmstadt, Germany
tri-Sodium phosphate dodecahydrate	($Na_3PO_4 \cdot 12H_2O$)	Carl Roth, Karlsruhe, Germany
Tryptone/ peptone from casein		Carl Roth, Karlsruhe, Germany
Yeast extract		Carl Roth, Karlsruhe, Germany
YO-PRO-1 iodide (491/509)		Thermo Fisher Scientific, Waltham, USA

2.2 Buffers and Solutions

For the preparation of buffers and solutions pure water with a conductivity lower than 0.055 µS/cm (Purelab flex, ELGA LabWater, Celle, Germany) was used.

Buffer		Compounds
Benzonase buffer		50 mM Tris-HCl, 1 mM $MgCl_2$, pH 8
Capillary electrophoresis running buffer	(CE)	25 mM CH_3COOLi, 0.4 % (w/v) PEG 300
Casamino acid-peptone-glucose medium	(CPG)	1 g · L^{-1} Difco^{TM} Casamino Acids, 10 g · L^{-1} Tryptone, 10 g · L^{-1} Glucose, pH 6.7, if needed 17 g · L^{-1} Agar
Competent cells preparation buffer	(CCP)	9.8 % (v/v) Glycerol, 10 mM MES-NaOH, 38 mM $CaCl_2$, 45.5 mM $MnCl_2$
Denaturation buffer		50 mM Sodium phosphate, pH 7, 7 M Gdm-HCl
Immobilized metal affinity chromatography buffer A	(IMAC A)	50 mM HEPES-NaOH, 300 mM NaCl, 20 mM Imidazole, pH 8
Immobilized metal affinity chromatography buffer B	(IMAC B)	50 mM HEPES-NaOH, 300 mM NaCl, 500 mM Imidazole, pH 8
IMAC equilibration buffer		50 mM CH_3COONa, 300 mM NaCl, pH 4
IMAC regeneration buffer		20 mM Na_3PO_4, 1 M NaCl, 200 mM EDTA, pH 7.4
Liquid medium 1		0.5 % (w/v) Tryptone/ peptone, 0.3 % (w/v) Meat extract, pH 7
Lysogeny Broth	(LB)	10 g · L^{-1} Tryptone/ peptone, 5 g · L^{-1} Yeast extract, 10 g · L^{-1} NaCl, pH 7, if needed 20 g · L^{-1} Agar
MBTH Oxidizing solution		0.5 % $NH_4Fe(SO_4)_2$, 0.5 % H_3NSO_3, 0.5 % HCl
P. stewartii storage solution		65 % (v/v) Glycerin, 0.1 M $MgSO_4$, 25 mM Tris-HCl, pH 7
Phage buffer		50 mM Tris-HCl, 4 mM $MgCl_2$, pH 7.6
Phosphate-buffered saline	(PBS)	137 mM NaCl, 2.7 mM KCl, 10 mM Na_2HPO_4, 1.8 mM KH_2PO_4
Size-exclusion chromatography buffer	(SEC)	50 mM HEPES-NaOH, 200 mM NaCl, pH 8
SDS-PAGE gel stain		25 % (v/v) Isopropanol, 10 % (v/v) Acetic acid, 0.5 % (w/v) Coomassie Brilliant Blue R250
SDS-PAGE sample buffer		65 mM Tris-HCl, 10 % (v/v) Glycerol, 0.1 mg · mL^{-1} Bromophenol blue, 2 % (w/v) SDS, 2.5 mM DTE, pH 6.8
SDS-PAGE stacking gel buffer		0.125 M Tris-HCl, 0.2 % (w/v) SDS, pH 6.8
SDS-PAGE resolving gel buffer		0.75 M Tris-HCl, 0.4 % (w/v) SDS, pH 8.8
SDS-PAGE runing buffer		25 mM Tris-HCl, 192 mM Glycin, 0.1 % (w/v) SDS, pH 8.8
Storage buffer		50 mM MES-HCl, 50 mM NaCl, pH 5
Super optimal catabolite repression medium	(SOC)	20 g · L^{-1} Tryptone, 5 g · L^{-1} Yeast extract, 0.5 g · L^{-1} NaCl, 1 mM KCl, 10 mM $MgCl_2$, 20 mM Glucose
TEV protease buffer		50 mM HEPES-NaOH, 100 mM NaCl, 1 mM EDTA, 1 mM DTT, pH 8
Tris buffer		50 mM Tris-HCl, 50 mM NaCl, pH 8

2.3 Enzymes and Proteins

	Company
Benzonase® Nuclease	Merck, Darmstadt, Germany
Proteinase K	Sigma-Aldrich, St. Louis, USA
AEBSF (hydrochloride) protease inhibitor	Carl Roth, Karlsruhe, Germany

2.4 Kits and Standards

	Company
60 nm polystyrene microspheres	Bangs Laboratories, Inc., Fishers, USA
200 nm polystyrene microspheres	Bangs Laboratories, Inc., Fishers, USA
ACTH Fragment 18-39	Sigma-Aldrich, St. Louis, USA
Alexa Flour® 488 NHS-Ester	Thermo Fisher Scientific, Waltham, USA
Color Prestained Protein Standard, Broad Range	New England Biolabs, Ipswich, USA
Gel Filtration Calibration Kit	Serva Feinbiochemica GmbH, Heidelberg, Germany
Hexaacetyl-chitohexaose	Megazyme, Bray, Ireland
JBScreen JCSG crystallization screening matrix	Jena Bioscience, Jena, Germany
Mannohexaose	Megazyme, Bray, Ireland
Roti®-Prep Plasmid MINI	Carl Roth, Karlsruhe, Germany

2.5 Further Materials

	Company
N-CHO coated capillary, 50 µm · 65 cm	AB Sciex Germany GmbH, Darmstadt, Germany
Nunc-Immuno™ MicroWell™ PolySorp® 96 well plates	Sigma-Aldrich, St. Louis, USA
Amicon® Ultra-15, MW: 10 kDa	Merck, Darmstadt, Germany
IMAC Profinity™ IMAC Resin	GE Healthcare, Chicago, USA
MF-Millipore mixed cellulose ester, 0.45 µm pore size	Merck, Darmstadt, Germany
PD-10 Desalting Columns containing Sephadex G-25	GE Healthcare, Chicaco, USA
Superdex™ peptide 10/300	GE Healthcare, Chicaco, USA
Superdex™ 200 10/300	GE Healthcare, Chicaco, USA
Superdex™ 30 26/60	GE Healthcare, Chicaco, USA

2.6 Plasmids

Name	**Description**
pET-23a(+)	Merck, Karlsruhe, Germany: Provides a multiple cloning site under the control of a T7 promoter and a bla coding sequence
pET-23a(+)_ΦEa1hTSP_TEV_His6N	The plasmid contains the coding sequence of the ΦEa1h TSP as a construct with an N-terminal His_6 tag which precedes a TEV-protease cleavage site (Gayk, 2012)
pET-23a(+)_WceF_tat_TEV_His6N	The plasmid contains the coding sequence of WceF as a construct with an N-terminal His_6 tag which precedes a TEV-protease cleavage site (Gayk, 2012)

2.7 Bacteria

Name	**Company**
E. coli BL21 (DE3)	Merck, Darmstadt, Germany: F- *omp*T *hsdSB* (rB-mB-) *gal dcm*(DE3) (Dubendorf and Studier, 1991)
E. coli XL1 blue	Stratagene, La Jolla, USA: recA1 endA1 gyrA96 thi-1 hsdR17supE44 relA1 lac[F’ *proAB lacIq ZΔM15* Tn10 (Tetr)]c (Bullock *et al.*, 1987) Bullock, W.O., Fernandez, J.M. and Short J.M. (1987) XL1-Blue—a high-efficiency plasmid transforming recA *E. coli* strain with β-galactosidase selection, Biotechniques 5(3), 376-379.
P. stewartii DSM 30176	German Collection of Microorganisms and Cell Cultures (DSMZ), Braunschweig, Germany

2.8 Software

Software	Version
32 Karat	10.1
Blast	https://blast.ncbi.nlm.nih.gov/Blast.cgi
Coot	0.8.9.2
GROMACS	4.6.4 and 5.1.6
LabScan	4.0
LC solutions	1.03
mMass	5.5.0
Molprobity	molprobity.biochem.duke.edu
Phaser	2.8.3
Phenix	1.17.1
Phyre2	http://www.sbg.bio.ic.ac.uk/phyre2
PISA	https://www.ebi.ac.uk/pdbe/pisa/
PyMOL	2.2.3 and 2.3.2
Refmac	5.8.0238
SigmaPlot	11.0
TrackMate	3.8.0
Unicorn	6.0
VMD	1.9.3
VOTCA	1.4.1
XDSapp	2.99
ZEN	2.1

3. Methods

3.1 Microbiological and Molecular Biological Methods

3.1.1 Production of Bacterial Cell Media

P. stewartii bacteria were grown in Liquid medium 1, while *Escherichia coli* (*E. coli*) cultivation required LB medium which was supplemented with 100 µg · mL^{-1} ampicillin. All media were autoclaved at 120°C and the ampicillin was added to LBmedia after cooling. In case of agar plates, the agar was added right after the medium was autoclaved and poured into cell culture dishes under sterile conditions.

3.1.2 Production of Sub Cultures

Different volumes of LB medium (with 100 µg · mL^{-1} ampicillin) or 15 mL of Liquid medium 1 were inoculated with *E. coli* or *P. stewartii*, respectively, by either using the glycerol stock or by picking a colony from the respective agar plates. The sub cultures were afterwards shaken over night at 30°C (*P. stewartii*) or 37°C (*E. coli)*.

3.1.3 Cultivation and Storage of Bacterial Cells

Bacterial cells were cultivated in 50 mL sub cultures. In case of *P. stewartii* cells the OD_{600} of the subculture was adjusted to 0.5 by diluting the culture with autoclaved *P. stewartii* storage solution. *E. coli* cells were mixed with 87 % (v/v) glycerol to a final concentration of 20 % (v/v) glycerol. Afterwards the cultures were aliquoted to 1 mL and incubated for 2 h on ice. Finally, the aliqouts were snap-freezed in liquid nitrogen and stored at -80°C.

3.1.4 Preparation of Chemically Competent *E. coli* Cells

An *E. coli* 100 mL sub culture (in LB medium with 20 mM $MgSO_4$) was cooled in ice water for 2 min and incubated for further 28 min on ice. After centrifugation of the cells at 3,500 xg for 12 min at 4°C, the pellet was resuspended in 30 mL CCP buffer and again centrifuged. The final pellet was resuspended again in CCP buffer and 100 µL aliqouts were snap-freezed in liquid nitrogen and stored at -80°C.

3.1.5 Transformation of Chemically Competent *E. coli* Cells

100 µL of competent cells were thawed on ice for 3 min. After the addition of ca. 20 ng plasmid DNA the cells were further kept on ice for 30 min. The bacteria were heat shocked for 45 s at 42°C and 1 mL of prewarmed (37°C) SOC medium was added. Afterwards, the cells were incubated for 30 min at 37°C

and centrifuged for 5 min at 6200 xg. The pellet was resupended in 200 µL LB-medium and the cells were plated on LB agar, supplemented with 100 µg · mL^{-1} ampicillin.

3.1.6 Plasmid Preparation

Plasmids have been amplified in 4 mL *E. coli* XL1 blue subcultures and extracted using the plasmid isolation kit Roti®-Prep Plasmid MINI (Carl Roth, Karlsruhe, Germany). The final DNA concentration and purity was determined from the absorbance at 260 nm or absorbance ratio at 260 and 280 nm, respectively. The sequence from the 5' end of WceF and ΦEa1h TSP were validated using the LPP1 primer from GATC Biotech AG (Konstanz, Germany). Plasmid-DNA was stored at -20°C.

3.1.7 Recombinant Protein Expression in *E. coli* BL21 (DE3)

50 mL LB medium (with 100 µg · mL^{-1} ampicillin) were inoculated with glycerol cultures of *E. coli* BL21 (transformed with either pET-23a(+)_WceF_tat_TEV_His6N or pET-23a(+)_ΦEa1hTSP_ His6N) and shaken over night at 37°C. Four main cultures, each 1 L LB medium, were supplemented with 100 µg · mL^{-1} ampicillin and inoculated with the pre culture to a final OD_{600} of 0.055. The *E. coli* cells were then grown under shaking at 37°C to an OD_{600} of 0.9 to 1 and the protein expression was induced by the addition of 1 mM IPTG. Afterwards the flasks were shaken at 20°C over night and the cells harvested at 4248 xg for 15 min at 4°C. Finally, the biomass was weighted and stored at -20°C.

3.1.8 Biofilm Growth

CPG medium was poured into around ten cell culture dishes and allowed to solidify. 150 µL *P. stewartii* were plated on membrane filters (MF-Millipore mixed cellulose ester, 0.45 µm pore size, Merck, Darmstadt, Germany) which were beforehand placed on top of each dish. Biofilms were grown for 3 days at 28°C. After one day a mucoid yellowish biofilm was visible (Figure 22). After three days the biofilm embedded cells were scratched off from the membrane and suspended in 0.85 % (w/v) NaCl. Soluble components were removed from bacterial cells by centrifugation (13,000 xg for 1 h). Further separation of stewartan was accomplished by ultracentrifugation at 160,000 xg for 3 h. Afterwards, the supernatant was precipitated with 80 % absolute ethanol. The crude stewartan preparation was resuspended in Benzonase buffer and nucleic acid contaminations were removed with the addition of 50 U · mL^{-1} Benzonase® Nuclease (Merck, Darmstadt, Germany) over night. The stewartan solution was then adjusted to 800 mM guanidine hydrochloride and 50 mM EDTA before the addition of 15 µg · mL^{-1} proteinase K to clean off proteinaceous entities. After dialyses in 100 mM, 50 mM acetic acid and water, the stewartan preparation was lyophilized and the amount of pure stewartan determined from its mass. Usually, the yield was around 10^{-2} g stewartan per gramm crude biofilm.

3.2 Protein Biochemical Methods

3.2.1 Protein Purification

3.2.1.1 Cell Disruption

WceF and the ΦEa1h TSP were expressed as constructs with an N-terminal His_6 tag which precedes a TEV-protease cleavage site. One aliquot (around 1.5 g) of WceF or ΦEa1h TSP protein overexpressed *E. coli* BL21 (DE3) biomass was dissolved in 15 mL IMAC A buffer and 0.25 $mg \cdot mL^{-1}$ AEBSF hydrochloride protease inhibitor and subsequently the cells were disrupted in five French press passages (SLM-aminco, Polytec, Waldbronn) at 70 bar at 4 °C. Finally, the lysate was centrifuged at 38,000 xg for 1 h.

3.2.1.2 Column Equilibration and Regeneration

The IMAC Profinity^{TM} IMAC Resin (GE Healthcare, Chicago, USA) were initially equilibrated with three column volumes (CV) of IMAC equilibration buffer (2 $mL \cdot min^{-1}$) prior to loading with three CV of 0.1 M $NiCl_2$ (1 $mL \cdot min^{-1}$). Excess Ni-ions were washed with 3 CV IMAC equilibration buffer and 5 CV water, each with 2 $mL \cdot min^{-1}$. Before samples were loaded, the resin was equilibrated with IMAC A buffer for 3 CV with 2 $mL \cdot min^{-1}$. After the protein purification, Ni-ions were stripped with IMAC regeneration buffer and the material was stored at 4°C.

3.2.1.3 Immobilized Metal Affinity Chromatography Based Protein Purification

After the centrifugation, the supernatant of the cell lysate was loaded on 35 mL IMAC Profinity^{TM} IMAC Resin (GE Healthcare, Chicago, USA) with 1.5 $ml \cdot min^{-1}$ IMAC A buffer using an Äkta FPLC system (GE Healthcare, Chicago, USA). Purification of proteins was achieved by using standard immobilized metal affinity chromatography (IMAC) protocols and recording of the 280 nm absorbance. The resin was washed with IMAC A buffer until the 280 nm absorbance reached baseline level. The proteins eluted at around 75 % of IMAC buffer B in a 1 h gradient of 0 % to 100 % IMAC B buffer. Afterwards the His_6 tag was cleaved off by adding 0.51 mg/mL TEV Protease (which itself contained an N-terminal His_6 tag) and additional dialysis over night in TEV protease buffer at 4 °C. Proteins were separated from His_6 tag and TEV protease by an additional second IMAC. Here, the tag-free protein eluted in the flow-through of the column and was rebuffered in storage buffer. Throughout the protein purification process, the purity of the protein preparations was judged from sodium dodecyl sulfate–

polyacrylamide gel electrophoresis (SDS-PAGE). The final protein preparations exhibited homogeneities of more than 95 % with a yield of typically 20 - 35 mg (5.1 to 8.9 mg protein/ g cell wet weight). The C-terminal fragment of P22 TSP, which lacks the N-terminal head binding domain, has been cloned and purified as described earlier (Miller *et al.*, 1998a). TEV protease was purified using standard protocols (Doyle, 2009).

3.2.2 Oligomeric State Analysis

The degree of oligomerization of WceF and ΦEa1h TSP was analyzed on a Superdex^{TM} 200 10/30 (GE Healthcare, Chicago, USA) by loading 2 mL of a 1.5 mg · mL^{-1} protein solution with SEC buffer on an Äkta FPLC system (GE Healthcare, Chicago, USA). The molecular weight was determined from a calibration of globular proteins of different sizes (Figure S19) (Gel Filtration Calibration Kit, Serva Feinbiochemica GmbH, Heidelberg, Germany): Ferritin (Horse, 480 kDa), Aldolase (Rabbit, 147 kDa), Albumin (Bovine, 67 kDa), Albumin (chicken, 45 kDa) and Cytochrom C (Horse, 12.4 kDa).

3.2.3 Sodium Dodecyl Sulfate–Polyacrylamide Gel Electrophoresis

Discontinuous SDS-PAGE systems, according to (Laemmli, 1970), have been used to separate protein samples. Here, the gel is divided into a resolving and stacking gel. The composition of each gel type is shown in Table 2.

Table 2: Composition of the SDS-PAGE gels used in this work

	10 % (v/v) acrylamide stacking gel	**3 % (v/v) acrylamide resolving gel**
Rotiphorese® Gel 30	3.35 mL	0.5 mL
SDS PAGE Stacking gel buffer	-	1.5 mL
SDS PAGE Resolving gel buffer	2.5 mL	-
H_2O	4.15 mL	1.0 mL
10 % (w/v) APS	100 µL	60 µL
TEMED	6 µL	3.0 µL

The samples for the SDS-PAGE were mixed with 1x SDS-PAGE sample buffer and heated at 100°C for 5 min. Typically, 5 to 30 µL samples were loaded per lane and the protein molecular weight was estimated by comparing with the Color Prestained Protein Standard, Broad Range (New England Biolabs, Ipswich, USA). The electrophoretic separation was then conducted with SDS-PAGE running buffer at 200 V until the migration front reached the end of the gel. Afterwards, the gel was stained (SDS-PAGE gel stain) over night and migrated proteins were detected after destaining with 10 % (v/v) acetic acid.

3.2.4 Enzymatic Stewartan Hydrolysis

Stewartan solutions with the indicated concentrations were incubated with 1.2 µM WceF or 0.141 µM ΦEa1h TSP. The storage buffer was used as standard buffer throughout all kinetic experiments. Other buffer systems (50 mM of each buffer) with varying NaCl concentration (50-500 µM) were used in the pH and NaCl dependent activity tests: sodium phosphate-HCl buffer (pH 2), citrate-NaOH buffer (pH 3.5), acetate-NaOH buffer (pH 5), MES-NaOH (pH 6.5), Tris-HCl (pH 8), CHES-NaOH (pH 9.5), CHAPS-NaOH (pH 11).

3.2.5 Reducing End Quantification with the 3-Methyl-2-benzothiazolinon-hydrazon Hydrochlorid-Test

70 µL samples were taken from stewartan hydrolysis experiments at different time points and inactivated with 70 µL 0.5 M NaOH. The amount of reducing ends was measured using the 3-Methyl-2-benzothiazolinon-hydrazon Hydrochlorid (MBTH)-test as described by Anthon and Barrett, 2002. Briefly, 70 µL of 3 mg · mL MBTH were added to inactivated samples and heated for 15 min at 80°C. Afterwards, the samples were incubated with 140 µL of MBTH oxidizing solution and allowed to cool. 100 µL of each reaction was pipetted into 96-well plates and the absorbance at 655 nm was determined using a microplate reader (Epoch, BioTek, Winooski, USA). The concentration of reducing ends was calculated from a D-(+)-glucose calibration curve (Figure S4).

3.2.6 Kinetic Analysis of the Stewartan Degradation Process

The maximal enzymatic velocity $V_{max,app}$ of the stewartan hydrolysis was determined from the slope of the initial phase of the hydrolysis reaction with (Rigouin *et al.*, 2009; Zakariassen *et al.*, 2010):

$$V_{max,app} = \frac{\Delta c_{RE}}{\Delta t} \tag{1}$$

where c_{RE} is the concentration of reducing ends and t the reaction time. The apparent turnover number $k_{cat,app}$ of the reaction is then calculated with:

$$k_{cat,app} = \frac{V_{max,\,app}}{n_E} \tag{2}$$

with n_E the number of molecules of enzyme. To note, the turnover, measured as the production of reducing ends, is given in units ($\mu mol \cdot min^{-1}$).

In addition, the random degradation of polymers by acids and glycosyl-hydrolases has been described with zeroth order kinetics (Hjerde *et al.*, 1996; Tayal *et al.*, 1999; Tømmeraas and Melander, 2008):

$$-\frac{dp}{dt} = k_0 \tag{3}$$

$$p = p_0 - k_0 \cdot t \tag{4}$$

with k_0 to be the zeroth order rate constant of the stewartan degradation. The ExoPS is considered here as a polymer of N_0 repeating units. When no hydrolysis has occurred yet, the polymer contains N_0-1 bonds. Consequently, the total number of bonds is expressed in terms of the fraction of bonds p_0 at the time point zero (Gaylord and Gibbs, 1962). At the beginning of the reaction, the number of substrates, represented by the number of hydrolysable stewartan bonds, exceeds the number of molecules of the catalyzing agent. Hence, the reaction velocity is independent of the substrate concentration, which served as the explanation of the choice of a zeroth order reaction law (Tayal *et al.*, 1999; Li *et al.*, 2004). In addition, it is here assumed, that all bonds in stewartan are equally susceptible to hydrolysis and the ExoPS is cleaved at random position (random scission) (Gaylord and Gibbs, 1962; Tayal *et al.*, 1999; Staggs, 2002). As the degradation reaction proceeds, the fraction of intact bonds in equation 4 is expressed with p. The portion of hydrolyzed bonds q can then be calculated with:

$$q = p_0 - p \tag{5}$$

Substituting equation 5 with 3 yields:

$$q = k_0 \cdot t \tag{6}$$

The concentration of reducing ends c_{RE} formed during the reaction is proportional to q (Hjerde *et al.*, 1996). Hence, the apparent rate constants $k_{0,app}$ can be determined from the slope of:

$$c_{RE} = k_{0,app} \cdot t \tag{7}$$

3.2.7 Preparation of Fluorophore-Labeled Proteins

Proteins were dialyzed in PBS and labeled with ATTO 488 NHS-Ester according to manufacturer protocols (ATTO-Tec, Siegen, Germany). Briefly, 1820 µL protein was mixed with 131 µL $NaHCO_3$ to obtain a final pH of 8.4. Incubation of the protein with 2 µg · µL ATTO 488 NHS-Ester (dissolved in DMSO) was carried out for 1h at room temperature in the dark. The labeling reaction was stopped by subjecting the sample to size-exclusion chromatography with 1 mL · min^{-1} flow (eluent: PBS) using the

Superdex™ S200 10/300 (GE Healthcare, Chicago, USA) on a HPLC system equipped with SPD-10A absorption detector (Shimadzu, Kyoto, Japan) (Figure S2, A). The concentration of purified fluorescently labeled proteins was determined by comparing the absorption at 280 and 550 nm and an average labeling ratio of 1.59 and 1.67 dye molecules per protein for WceF and ΦEa1h TSP, respectively, was calculated (Figure S2, B).

3.2.8 Fluorescent Labeling of P22 *Salmonella* Phages

P22 phages were purified as described in (Andres *et al.*, 2010b). $2.15 \cdot 10^{12}$ P22 phage particles $\cdot$ mL^{-1} were incubated with 1 µM YO-PRO-1 iodide (491/509) (Thermo Fisher Scientific, Waltham, USA) in phage buffer for 2 h at room temperature. Labeled phages were purified using Sephadex G-25 in prepacked PD-10 Desalting Columns (GE Healthcare, Chicaco, USA). The material was equilibrated with 20 mL phage buffer and the solution of labeled phages was diluted to 100 µL with phage buffer prior to loading on the Sephadex G-25. 1 mL phage buffer was added in 200 µL steps on top of the column. The absorbance at 260 nm was used to determine elution fractions which contained labeled phage particles (Figure S1). The latter were afterwards concentrated to $1.63 \cdot 10^{12}$ particles $\cdot$ mL^{-1} (Amicon® Ultra-15, MW: 10 kDa, Merck, Darmstadt, Germany).

3.3 Carbohydrate Methods

3.3.1 Monosaccharide Quantification by the Phenol-Sulfuric Acid Method

A *P. stewartii* biofilm, resuspended in 2 mL H_2O, was centrifuged for 1 h at 17,000 xg and the supernatant was analyzed by the phenol-sulfuric acid method described by Masuko *et al.*, 2005 to determine the overall stewartan concentration. Here, different dilutions of 50 µL sample were mixed with 150 µL concentrated sulfuric acid and 30 µL of 5 % (v/v) phenol. The reaction was incubated at 90°C for 5 min. 100 µL of the mixtures were pipetted in 96 well plate and the absorbance at 490 nm read with a microplate reader (Epoch, BioTek, Winooski, USA). Stewartan concentrations were obtained using a stewartan calibration curve (0 - 1 mg $\cdot$ mL^{-1}) (Figure S3). Additionally, the linearity of the phenol-sulfuric acid method was confirmed by glucose and sucrose calibrations (Figure S3).

3.3.2 Capillary Electrophoresis

The analysis of oligosaccharide fragments with capillary electrophoresis was done in the group of Prof. apl. Dr. habil Jörg Fettke (Biopolymer Analytics, University of Potsdam) with the support of Shadha Abduljaleel Al-Rawi. At different time points during a stewartan hydrolysis reaction 50 µL samples were taken and stopped with the addition of 200 µL absolute ethanol. This reaction mixture was then centrifuged (14,000 xg, 10 min), the supernatant dried in a rotation vacuum concentrator (RVC 2-18, Martin Christ Gefriertrocknungsanlagen GmbH, Osterode am Harz, Germany) for 1 h at 50°C and resuspended in 1.5 µL of a 200 mM APTS solution in 15 % (v/v) acetic acid. Finally, 1.5 µL $NaBH_3CN$ in 1 M THF was added and the whole mixture incubated over night at 37 °C. Afterwards, the samples were diluted to 100 µL with H_2O and subjected to capillary electrophoresis (N-CHO coated capillary) with CE buffer as eluent on a PA-800 (Beckman Coulter, Brea, USA) equipped with a laser-induced fluorescence detector as described in (Malinova *et al.*, 2014).

3.3.3 Size-Exclusion Chromatography of Glycan Samples

Size-exclusion chromatography has been used to evaluate the purity of stewartan preparations or to resolve stewartan oligosaccharides which were produced in a stewartan hydrolysis reaction. In each case the glycan species was loaded on a Superdex^{TM} peptide 10/300 with 100 mM acetic acid and the changes in refractive indices were recorded (HPLC system with RID-10A refractive index and SPD-10A absorption detector, Shimadzu, Tokyo, Japan). Oligosaccharide fragments from a 4 mL stewartan hydrolysis reaction (0.14 µM ΦEa1h TSP and 12.5 mg · mL^{-1} stewartan in 50 mM acetic acid) were loaded on a Superdex^{TM} 30 26/60. One RU and two RU fragments were pooled, lyophilized and used as standards in capillary electrophoresis.

3.3.4 MALDI-TOF Analysis of Glycan Samples

The mass spectrometric analysis of oligosaccharide fragments was done in the group and with the support of Prof. apl. Dr. habil Jörg Fettke (Biopolymer Analytics, University of Potsdam). 2 µL of oligosaccharide samples, supplemented with calibration substances (0.4 mg · mL^{-1} mannohexaose, 0.46 mg · mL^{-1} hexaacetyl-chitohexaose and 23 µM ACTH Fragment 18-39), where mixed with 0.2 µL 50 mg · mL^{-1} dihydroxybenzoic acid in 1:1:0.1 (v/v/v) H_2O/acetonitrile/TFA (Ropartz *et al.*, 2011) on a matrix-assisted laser desorption/ ionization (MALDI) target plate and allowed to crystallize. MALDI time-of-flight (TOF) mass spectra were acquired in the positive ion mode on a Microflex^{TM} (Bruker, Billerica, USA) and analyzed with the mMass software (Strohalm *et al.*, 2010).

3.3.5 Stewartan Bulk Viscometric Analysis

The bulk viscosity measurements were done by Valentin Dunsing (Physical Cellular Biochemistry, University of Potsdam) in the group of Dr. Ryan Guterman (Ionic Liquids as Reagents and Polymers Laboratory, Max-Planck-Institute for Colloids and Interfaces) with the help of Antje Völkel. Bulk viscosimetric analysis of differently concentrated stewartan was performed on a falling ball viscosimeter (AMVn Automated Micro Viscometer, Anton Paar, Graz, Austria) with a 70° angle. The specific viscosity η_{spec} was determined from six replicates with:

$$\eta_{spec} = \frac{\eta - \eta_{buffer}}{\eta_{buffer}} \tag{8}$$

where η is the bulk viscosity determined for the stewartan solution and η_{buffer} the viscosity of the buffer.

3.4 Biophysical Methods

3.4.1 Crystallization of WceF

The crystallization of WceF was performed by Dr. Yvette Roske (Crystallography group, Max-Delbrück Center for Molecular Medicine, Berlin). Conditions for the crystallization of WceF were found using the JCSG crystallization screening matrix (Jena Bioscience, Jena, Germany). 200 nL of selenomethionine (SeMet)-substituted WceF or native WceF were mixed in a 1:1 ratio with the reservoir solution containing 18% PEG 2000 MME, 100 mM ammonium sulfate, 100 mM Na-acetate buffer (pH 4.6) or 20 % PEG3350, 200 mM di-ammonium-hydrogen citrate (pH 5.0), respectively, using a Gryphon pipetting robot (Art Robbins Instruments, Sunnyvale, USA). Protein crystals were grown in sitting drops at 20 °C and images were taken with the Rock Imager storage system (Formulatrix®, Bedford, USA). Crystals appeared within one week and were flash-cooled in liquid nitrogen, prior the transfer of the protein crystals in cryo-solution which contained the reservoir solution supplemented with 20 % ethylene glycol.

3.4.2 Diffraction Data Collection and Structure Refinement

Data collection and structure refinement of WceF was done by Dr. Yvette Roske (Crystallography group, Max-Delbrück Center for Molecular Medicine, Berlin). The refraction datasets were collected at BL14.1 and 2 at BESSY II, Berlin, Germany at a wavelength of 0.9798 Å and 0.9184 Å for the SeMet-substituted and native WceF, respectively. Both data sets were recorded at a temperature of 100 K from a single crystal, processed and scaled using the XDS program suite (Sparta *et al.*, 2016). Three molecules in the asymmetric unit were identified with 18 out of 24 Se sites with a 54 % solvent content, as detected by Autosol/PHENIX (Terwilliger *et al.*, 2009). The peptide backbone was identified from the electron density providing a partially continuous trace. Positions of the selenomethionine side chains were seen from clear anomalous signals. The manual model building was performed in COOT (Emsley and Cowtan, 2004) and iteratively refined with Refmac including non-crystallographic symmetries (Murshudov *et al.*, 2011). Phases of the improved model were obtained by molecular replacement with Phaser (McCoy *et al.*, 2007) from the native 2.55 Å dataset with a final R_{work} and R_{free} of 22.42 % and 26.93 %, respectively. Several ethylene glycol molecules are built into remaining difference density at the end of the refinement. After refinement, the structure quality was assessed using MolProbity (Chen *et al.*, 2010). 1,916 residues out of 2,041 refined residues (94%) are in the most favoured regions of the Ramachandran plot and 3 residues were in the disallowed regions (0.15%).

3.4.3 Denaturation Studies with Guanidine Hydrochloride

WceF was dialyzed in 50 mM sodium phosphate buffer, pH 7, over night at 4°C. The denaturation experiments were conducted by mixing WceF with different amounts of denaturation buffer. For the renaturation experiments 500 $\mu g \cdot mL^{-1}$ WceF was fully denatured at 6 M Gdm-HCl and afterwards diluted in 50 mM sodium phosphate buffer, pH 7, to different Gdm-HCl concentrations. Finally, two sets of solutions with WceF mixed with increasing Gdm-HCl concentration were obtained with a final WceF concentration of 10 $\mu g \cdot mL^{-1}$. The samples were always excited after 24 h of preparation at 280 nm and fluorescence recorded at 328 nm using the Fluorolog®-3 spectrofluorimeter (HORIBA Jobin Yvon, Bensheim, Germany).

3.4.4 Confocal Laser Scanning Microscopy

All fluorescent microscopy studies were performed by Valentin Dunsing (Physical Cellular Biochemistry, University of Potsdam) on a Zeiss LSM780 system (Carl Zeiss, Oberkochen, Germany) using a 40x, 1.2NA water immersion objective. Samples were excited with a 488 nm Argon laser which was reflected by a 488 nm dichroic mirror. Fluorescence was detected at a sample depth of 10 µm between 500 and 600 nm and filtered by the pinhole (set on one Airy Unit). The GaAsP detector was set in photon counting mode. The laser power was kept at a count rate below 2 MHz which avoided photobleaching of the sample and detector saturation. The confocal volume was determined by calibration with Alexa Fluor® 488 (Petrásek and Schwille, 2008). In addition the collar ring was adjusted before every measurement to maximize the signal of Alexa Fluor® 488.

3.4.4.1 Fluorescence Correlations Spectroscopy

Fluorescence Correlation Spectroscopy (FCS) studies were conducted with using AlexaFlour® 488, polystyrene (PS) microspheres and fluorescently labeled WceF and ΦEa1h TSP to determine the particle diffusion dynamics. The acquisition of the dynamic confocal fluctuations and data processing is described by Dunsing *et al.*, 2019. Briefly, the autocorrelation function was calculated based on the fluctuations $\delta F(t)$ of the fluorescence signal $F(t)$ around the mean $\langle F(t) \rangle$:

$$G(\tau) = \frac{\langle \delta F(t) \delta F(t+\tau) \rangle_t}{\langle F(t) \rangle_t^2} \tag{9}$$

with τ the lag time. A model describing anomalous diffusion and a Gaussian focal volume geometry was then fitted to the autocorrelation curves (Weiss *et al.*, 2004):

$$G(\tau) = \frac{1}{N}\left(1 + \frac{T}{1-T} \cdot e^{-\frac{\tau}{\tau_b}}\right) \cdot \left(1 + \left(\frac{\tau}{\tau_d}\right)^{\alpha}\right)^{-1} \cdot \left(1 + \frac{1}{S^2} \cdot \left(\frac{\tau}{\tau_d}\right)^{\alpha}\right)^{-1/2} \tag{10}$$

Here, the number of particles N, the structure parameter S and the exponential term, which accounts for photophysical transitions, is given. The anomalous exponent α describes the power law scaling of the diffusion process (Saxton and Jacobson, 1997; Metzler *et al.*, 2014). In case for $\alpha<1$ the process is referred as subdiffusion whereas diffusion in normal fluids is characterized by $\alpha=1$. The diffusion time τ_D was used to obtain the diffusion coefficient:

$$D = \frac{\omega_0^2}{4 \cdot \tau_d} \tag{11}$$

where ω_0 is the lateral extension of the confocal volume. Equation 3 is strictly valid only for normal Brownian diffusion. In cases where $\alpha<1$ the apparent diffusion coefficient D_{app} is calculated as an approximation of D.

Furthermore, to characterize the experienced confinement to the diffusion of particles, the hindrance factor τ_{hind} is introduced with:

$$\tau_{hind} = \frac{\tau_d}{\tau_{d,\ buffer}} \tag{12}$$

where $\tau_{d,\ buffer}$ denotes the diffusion time in buffer.

In analogy to equation 1, the specific hindrance $\tau_{d,spec}$ is expressed by:

$$\tau_{d,spec} = \frac{\tau_d - \tau_{d,buffer}}{\tau_{d,\ buffer}} \tag{13}$$

3.4.4.2 Single-Particle Tracking

Single-Particle Tracking (SPT) was done as described in (Dunsing *et al.*, 2019). Briefly, typically 1000-2000 images of an area of 180 μm^2 were recorded. The SPT data was analyzed using the TrackMate v3.8.0 plugin (Tinevez *et al.*, 2017) for Fiji (Schindelin *et al.*, 2012). Every individual time-averaged mean square displacements (taMSD) was calculated with:

$$\mathrm{taMSD} = \langle r^2(\tau)\rangle_t = \frac{1}{N\text{-}k} \cdot \sum_{i=1}^{N\text{-}k}\left\{\mathbf{r}\big((i+k)\cdot\Delta t\big) - \mathbf{r}\cdot(i\cdot\Delta t)\right\}^2 \tag{14}$$

where N is the number of particle positions in the track, Δt the frame time and $\tau = k \cdot \Delta t$ the lag time between the positions in frames i and i + k. The two-dimensional vector **r**(t) describes the position of a particle at time point t, **r**(t) = (x(t),y(t)). Ensemble averaged taMSDs were obtained by averaging the individual trajectories and D_{app} was determined from the first 10 points by fitting (Metzler *et al.*, 2014):

$$\mathrm{taMSD}(\tau) = 4 \cdot D_{app} \cdot \tau + c \tag{15}$$

with c as a free fit parameter which accounted for static and dynamic errors. The anomaly exponent α was determined from

$$\mathrm{taMSD}(\tau) = 4 \cdot D_{\alpha} \cdot \tau^{\alpha} + d \tag{16}$$

in which d is a free fit parameter to compensate for localization errors. The anomalous transport coefficient is denoted with D_α.

Additionally the angle θ was defined as:

$$\theta = \cos^{-1}\left(\frac{[r\cdot(t+\delta t) - r(t)]^{*}[r\cdot(t+\delta t+\tau) - r\cdot(t+\tau)]}{|r(t+\delta t) - r(t)|\cdot|r(t+\delta t+\tau) - r(t+\tau)|}\right) \tag{17}$$

which is the angle between successive steps of the particle in an interval δt and separated by a lag time τ. To note, * denotes the dot product of the vectors.

3.4.5 Dynamic Light Scattering and Zeta Potential Analysis

The diameter and Zeta potential of polystyrene microspheres was analyzed by dynamic light scattering and laser Doppler micro-electrophoresis using a Zetasizer Nano ZS (Malvern Pananalytical Ltd, Malvern, UK).

3.5 Computational Methods

3.5.1 Atomistic Molecular Dynamics Simulations

Four stewartan systems with all-atom resolution were simulated:

1. 27 chains of stewartan with a length of 3 RU for developing the coarse-grain model (reference system),
2. 40 chains of 20 RU lengths to investigate the structural properties of the coarse-grained ExoPS network,
3. One chain of 3 RU stewartan and
4. One chain of 20 RU stewartan

System 1 was used as a reference system to develop the coarse-grain (CG) model which was transferred to system 2. The purpose of system 3 and 4 was to compare the end-to-end distances with system 1 and 2, respectively. Initial stewartan structures were constructed with the Carbohydrate Builder from the GLYCAM-Web (http://glycam.org) and the topology and coordinate files converted using the glycam2gmx script (Sorin and Pande, 2005; Wehle *et al.*, 2012). Solvation of the structures was carried out with 25 TIP5P water molecules per monosaccharide. One sodium ion per stewartan RU was added to neutralize the negative charge of the β-D-GlcA^{IV} residue. The atomistic Molecular Dynamics (MD) Simulations were performed using the GROMACS 5.1.6 package (van der Spoel *et al.*, 2005) and periodic boundary conditions. The $\mathrm{Glycam}_{\mathrm{OSMOr14}}^{\mathrm{TIP5P}}$ force field (Kirschner *et al.*, 2008; Sauter and Grafmüller, 2016) was used throughout the simulations and interactions parameters for the sodium ions were taken from (Cordomí *et al.*, 2009). A cut-off of 1.4 nm was used for Lennard-Jones and electrostatic interactions and long-range electrostatics were evaluated with the Particle Mesh Ewald method (Darden *et al.*, 1993). Constraints have been introduced for bonds containing hydrogen atoms with the LINCS algorithm (Hess *et al.*, 1997), and water molecules were kept rigid with Settle (Miyamoto and Kollman, 1992). The Leap-Frog integrator was used throughout all atomistic simulations (Birdsall and Langdon, 2005). The configurations were stored every 100 ps. System 1 and 2 were equilibrated with an initial energy-minimization with steepest decent (Hess *et al.*, 2008), a short 1 ns simulation run in the NVT ensemble (Noseé-Hoover thermostat (Nosé and Klein, 1983; Hoover, 1985), reference temperature 300 K) and a 50 ns run in the NPT ensemble (Parinello-Rahmann barostat (Parrinello and Rahman, 1981; Nosé and Klein, 1983), reference pressure 0.1 MPa). Additionally, the system with short stewartan chains (system 1) was further equilibrated for 400 ns in the NVT ensemble using the optimal box size obtained from the previous NPT run followed by a final 100 ns productive MD run (Figure S5). The trajectory of system 2 was used to obtain the optimal box size for the large polymer chains and to derive initial conformations for 20 RU stewartan CG model. System 3 and 4 were simulated to compare the end-to-end distances with system 1 and 2, respectively.

3.5.2 Coarse-Grain Mapping and Assignment of Bonded Potentials

The CG stewartan monosaccharides were mapped onto the three CG beads A, B and C (Figure 9). In case of the charged β-D-GlcA^{IV} the CG C bead, comprising the negative charge, was replaced with an additional CG bead type D. The interaction potentials between the CG sites were generated following the procedure as described by Sauter and Grafmüller, 2017, using VOTCA 1.4.1 (Rühle *et al.*, 2009; Mashayak *et al.*, 2015). Briefly, non-bonded interactions between the CG beads were obtained from the Force Matching method using a cutoff of 1.8 nm. Specific bonded interactions were derived using Boltzmann inversion. Here, a CG monosaccharide was defined by three bonds. An additionally bond described the connections between two CG monosaccharides. In case of 1-3 and 1-4 linkages the angles C_i-B_i-A_{i+1} and B_i-A_{i+1}-C_{i+1} and dihedrals A_i-C_i-B_i-A_{i+1}, B_i-A_{i+1}-C_{i+1}-B_{i+1} and C_i-B_i-A_{i+1}-C_{i+1} were used. For 1-6 linkages the angles B_i-C_i-A_{i+1} and C_i-A_{i+1}-B_{i+1} and dihedrals A_i-B_i-C_i-A_{i+1}, C_i-A_{i+1}-B_{i+1}-C_{i+1} and B_i-C_i-A_{i+1}-B_{i+1} were chosen. The angular A5-B3-A1 and dihedral potential A5-B3-A1-B1 (Figure 9) were additionally added to prevent collapsing of CG A beads and to correct the dihedral distribution function which otherwise would not resemble the atomistic behavior (Figure 13). A final set of explicit short range intramolecular 1-3 and 1-4 interactions (virtual bonds) was implemented which improved the overall reproduction of the atomistic configuration. These were: A1-A2, A2-A3, A3-A4, A3-A5, A5-A6, A6-A7, A3-A1, C2-C3 and D-C6 (Figure 9). CG systems were simulated with the solute-solute interactions obtained from the MD trajectory which were beforehand separated from solute-solvent and solvent-solvent potentials with the Reaction Field method using the rerun option (Tironi *et al.*, 1995). Water molecules are not explicitly represented in the CG simulations.

3.5.3 Solvent-Free Coarse-Grained Molecular Dynamics Simulations

Gromacs 4.6.4 were used in the following coarse-grained (CG) MD simulations. The cut-off for calculating non-bonded interactions was set to 1.8 nm. All CG MD Simulations were done in NVT ensemble using the Leap-Frog integrator. The Noseé-Hoover thermostat was set to T = 300 and bead types were separately coupled. A time step of 1 fs was used and calculations stored every 500 ps. Crashed systems were restarted at the previous time frame. In this way, system 2 was modeled at different RU concentrations of 86, 50, 20 and 10 mM (box edge lengths of 25, 30, 40 and 50 nm, respectively) for 100 ns. In addition, a single CG simulation of system 2 was performed using the Leap-

Frog Stochastic Dynamics Integrator (van Gunsteren and Berendsen, 1988) to correct for the occurrences of stewartan chains with low kinetic temperature (see section 4.1.5). Systems 3 and 4 were simulated for 1 µs.

3.5.4 Coarse-grain model validation and Stewartan Network Analysis

For model validation the radial distribution functions (RDF, calculated with the VMD programme) and distribution functions (obtained from VOTCA) were compared to the atomistic and CG simulations. For the comparison of RDFs of stewartan systems with 3 RU and 20 RU length the RDFs were area normalized.

Pore size distributions were calculated as described by Bhattacharya and Gubbins, 2006. Here, the pore size distribution is defined from the largest sphere which can be fitted at random positions in a pore cavity.

Diffusion coefficients were determined from linear least squares fitting of the MSD over a simulation time of the first 40 ns using:

$$\mathrm{MSD}(t) = 4 \cdot D \cdot t + c \qquad (18)$$

4. Results

4.1 Short Chain-Length Stewartan Forms a Hydrogel with Transient Contacts

Exopolysaccharides (ExoPSs) serve as structural scaffolds forming tight supramolecular structures thus being highly implicated in the stability of the biofilm architecture. In addition, ExoPSs account for viscoelastic gel-like solutions (Maalej *et al.*, 2016; Rederstorff *et al.*, 2017). To analyze the structure of a pure polymeric stewartan network at the micrometer to nanometer scale, Molecular Dynamics (MD) simulations of short stewartan chains and different water content were carried out. Equilibration of long polysaccharide chains takes place on time and length scales that are highly challenging for all-atom MD simulations. Therefore a coarse-grained (CG) model of stewartan was derived, which enables the simulation of large stewartan polysaccharide networks with reasonable computational effort.

4.1.1 All-Atomistic Simulation of Stewartan

The CG stewartan model needs to be able to reproduce the atomistic properties of the ExoPS. Here, system 1 was used for coarse-graining the ExoPS. It comprises stewartan with 3 RU length which is a highly feasible chain length for developing a CG model of stewartan. In addition, this system served as the reference structure from which a CG model can be derived and transferred to different stewartan lengths and concentrations (see section 4.1.2 and 4.1.4). The stewartan chains were solvated with 25 TIP5P water molecules per monosaccharide and simulated in atomistic resolution. System 1 was equilibrated in isothermal–isobaric (NPT) and canonical (NVT) ensembles to acquire a constant pressure and minimized potential energy (Figure S5).

Bacterial polysaccharides display a high conformational diversity (Pol-Fachin *et al.*, 2010; Kang *et al.*, 2014; Tsereteli and Grafmüller, 2017). Indeed, in case of stewartan, this is emphasized by multiple combinations of the stereochemical configurations and linkage patterns of the glycosidic bonds. Consequently, in the atomistic stewartan simulations, the conformational preferences of the dihedrals psi and phi are dependent on the glycosidic linkage types (Figure 8). Over a simulation time of 100 ns, one main maximum was sampled for β 1-3 linkages in the ψ and ϕ heatmap. In addition, stewartan exhibits 1-4 linkages with either α or β configuration. Here, the location of the maximum in the ψ and ϕ distribution, was depend on the stereochemistry, with opposite values for the ψ torsion angle. The ψ and ϕ map of 1-6 linkages displayed a different topology with one main maximum and a less populated state of ψ and ϕ. In addition, the dihedral omega ω also contributed significantly to the flexibility of 1-6 glycosidic linkages (Figure S6). Hence, the flexibility of stewartan has to be considered in the derivation of the CG stewartan model.

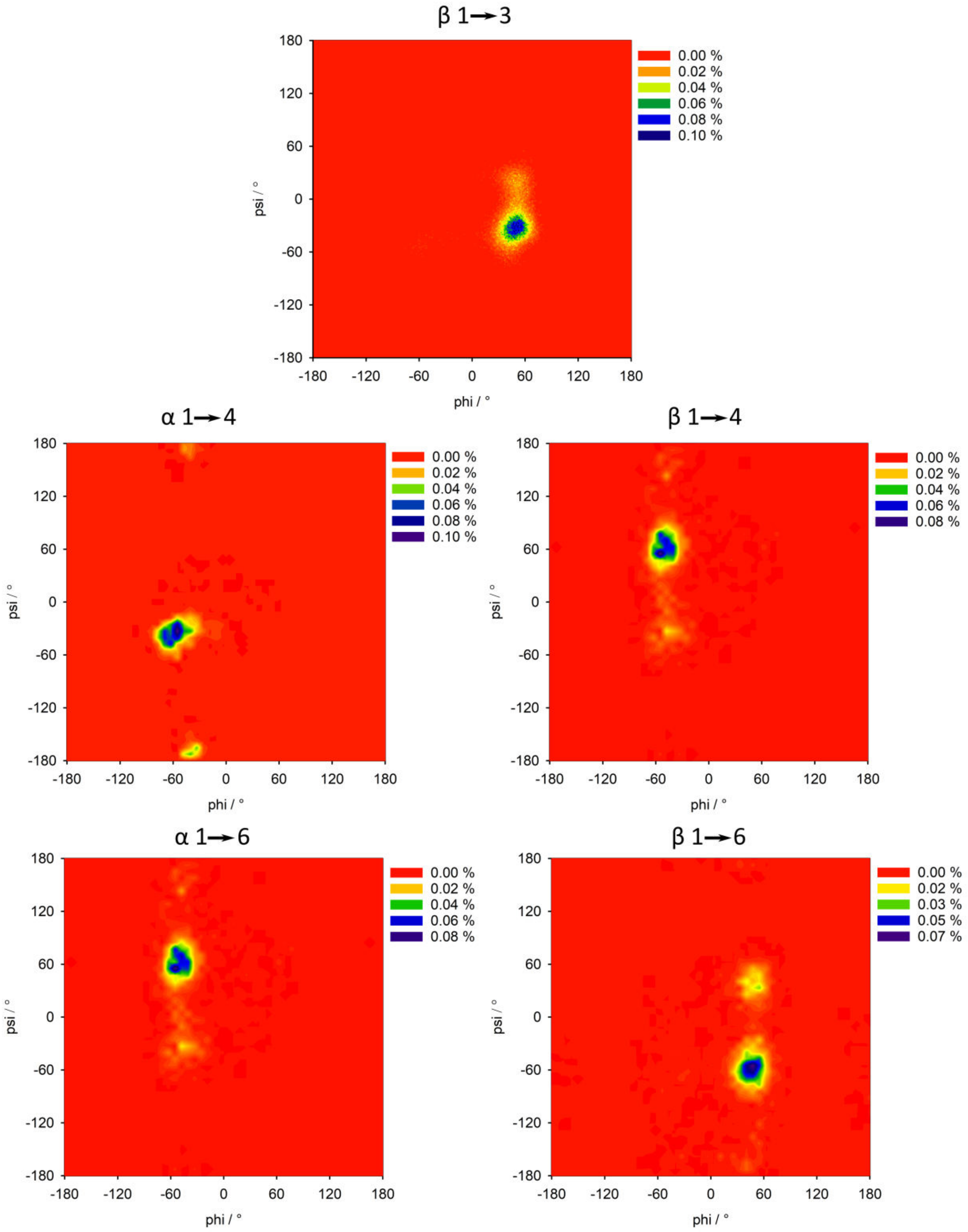

Figure 8: Heat maps of the glycosidic torsion angles psi ψ and phi ϕ for the different linkage types of 3 RU stewartan
Conformations of the stewartan glycosidic bonds were taken from the 100 ns MD run of the atomistic stewartan reference system.

4.1.2 Development of a Coarse-Grained Stewartan Model

The stewartan chains were mapped on the four different CG bead types A, B, C and D (Figure 9), as described in section 3.5.2.

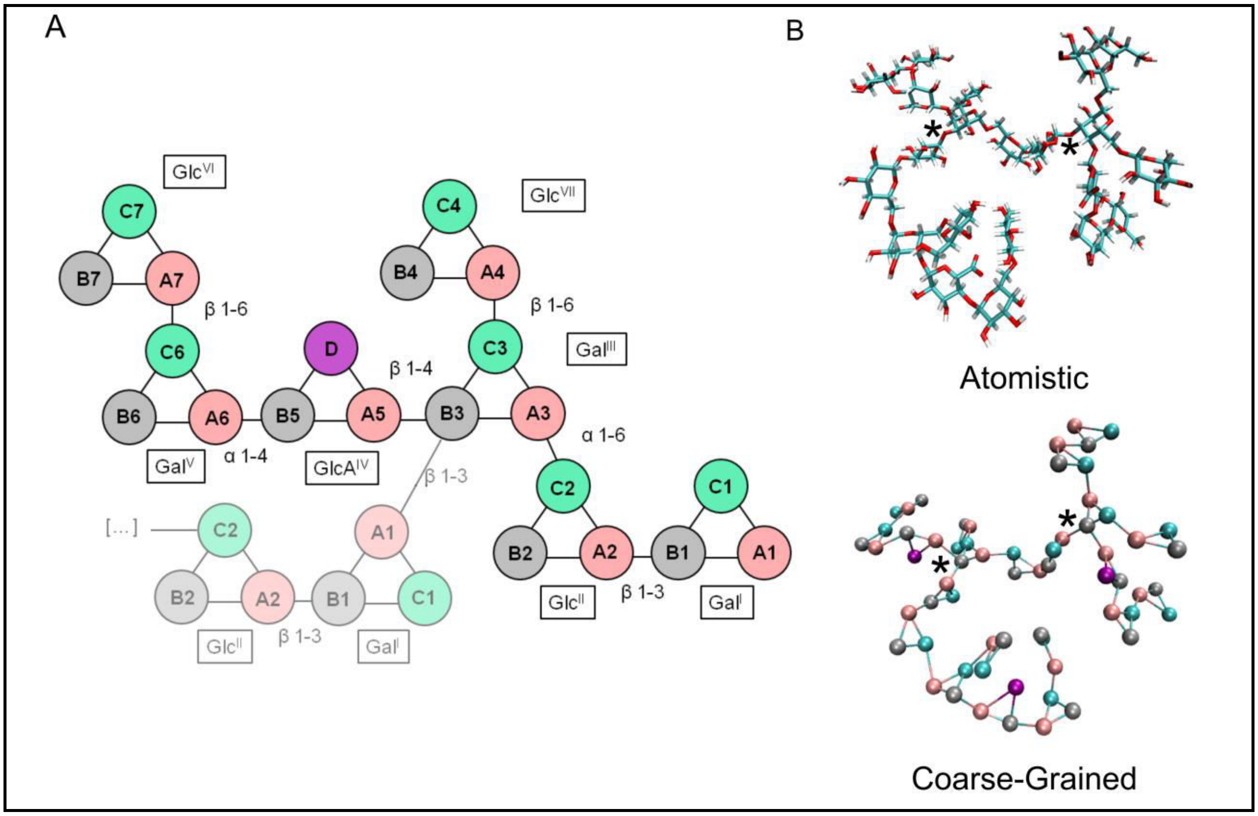

Figure 9: Coarse-Grain mapping scheme of stewartan

The atomistic stewartan was coarse-grained using the four bead types A, B, C and D. (A) The coarse-grain mapping scheme is shown for one RU with labels describing the monosaccharide unit and linkage type. The beginning of the next RU is suggested by a shaded structure. (B) The structure of 3 RU stewartan is shown in atomistic and coarse-grain representation. The atomistic carbons, oxygens and hydrogens are displayed in bond representation in cyan, red and white, respectively. coarse-grained beads A, B, C and D are shown in CPK depiction in light red, grey, cyan and purple, respectively. The glycosidic bonds which connect the RUs are marked with an asterisk.

The interaction potentials between the CG beads were obtained from the atomistic reference system (System 1). The non-covalent interactions were calculated using the force matching method. The resulting potentials are therefore not predefined analytical functions. Nonetheless, the nonbonded interactions between the CG beads resembled Lennard-Jones potentials and are characterized by strong short range repulsion (Figure 10 and Figure S7). The CG interactions exhibited one (A-A) or two attractive wells (B-D) at distances around 0.5 nm. The interaction between CG D atoms appeared purely repulsive as a consequence of their net charges.

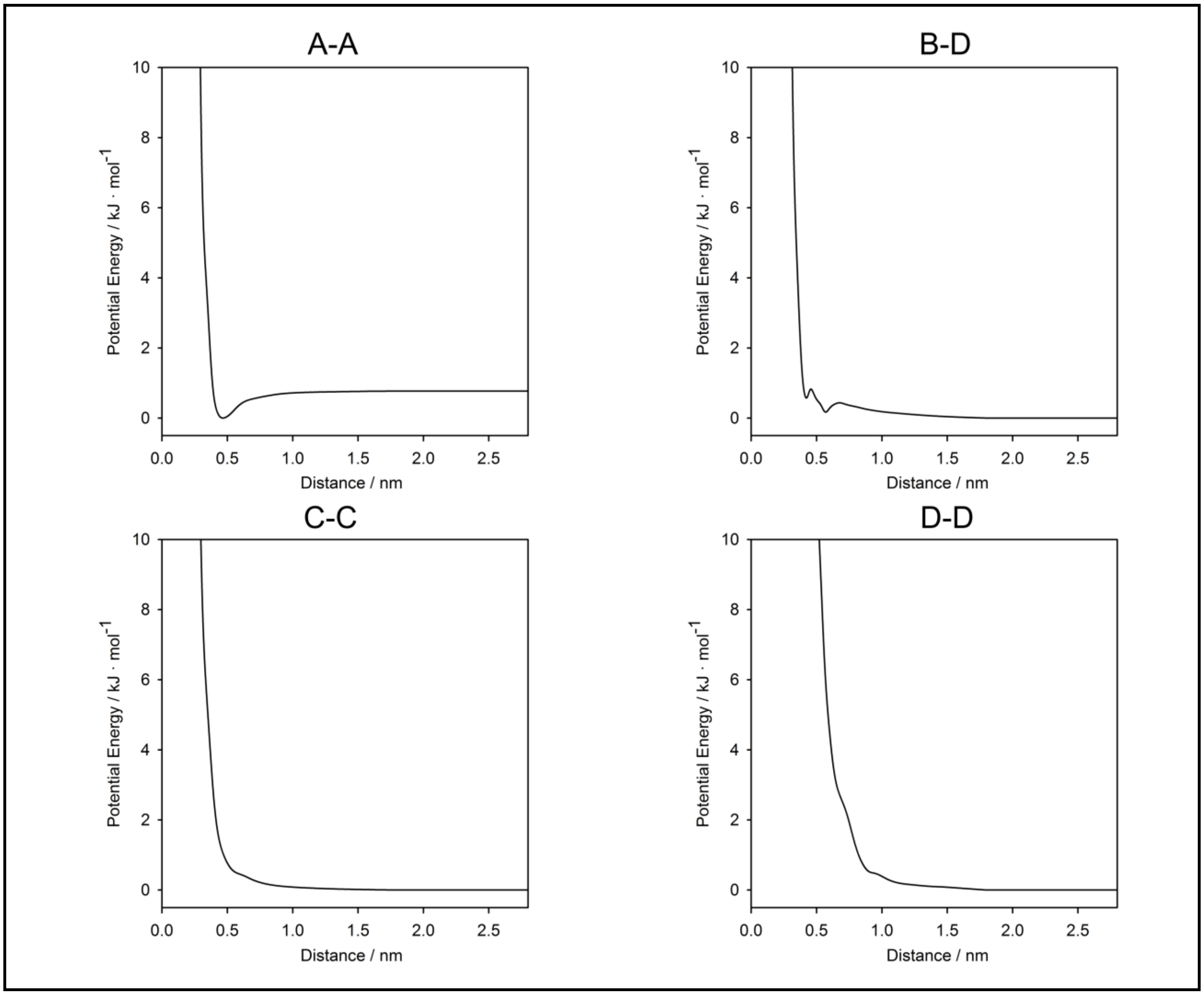

Figure 10: Representative examples of nonbonded potentials used in the coarse-grained simulation of stewartan
The nonbonded potentials between the coarse-grained beads of the stewartan model were obtained from the atomistic reference structure using the force matching method. The coarse-grained mapping of the stewartan structure is shown in Figure 9.

Specific covalent interactions (including potentials for bonds, angles and dihedrals) were derived from the atomistic simulation using Boltzmann Inversion. The bonds within all monosaccharides were described by the same bonded potentials A-B*, A-C* and B-C*. In case of the GlcA^{IV} monomer the A-D* and B-D*potential was used instead of A-C* and B-C, respectively. However, as the position of the CG beads are highly dependent on the stereochemistry of the glycosidic linkage type, different potentials were used to describe each glycosidic link in the 3 RU stewartan molecules. Afterwards, the performance of the CG model with its ability to reproduce the atomistic stewartan behaviour was analyzed. For this purpose, first the distribution functions of the bonded potentials were compared (Figure 11 and Figure S8-S9). For example the atomistic bond distributions of A-C*, B-D* and B3-A8, which connects Gal^{III} and the Gal^{I} subunit from the next RU, are very well captured in the CG simulation. For some inter-monomer bonds, as for example the C2-A3 bond between Glu^{II} and Gal^{III}, the distance distribution, sampled in the all-atomistic system, displayed two maxima. However, throughout the bonded distributions from the CG simulations a slight overestimation of the main maximum was observed in the CG simulations whereas the second peak is usually underrepresented. This behavior has been similarly observed in other studies and is typically associated with Inverse Boltzmann (see section 5) (Hynninen *et al.*, 2011; Sauter and Grafmüller, 2017).

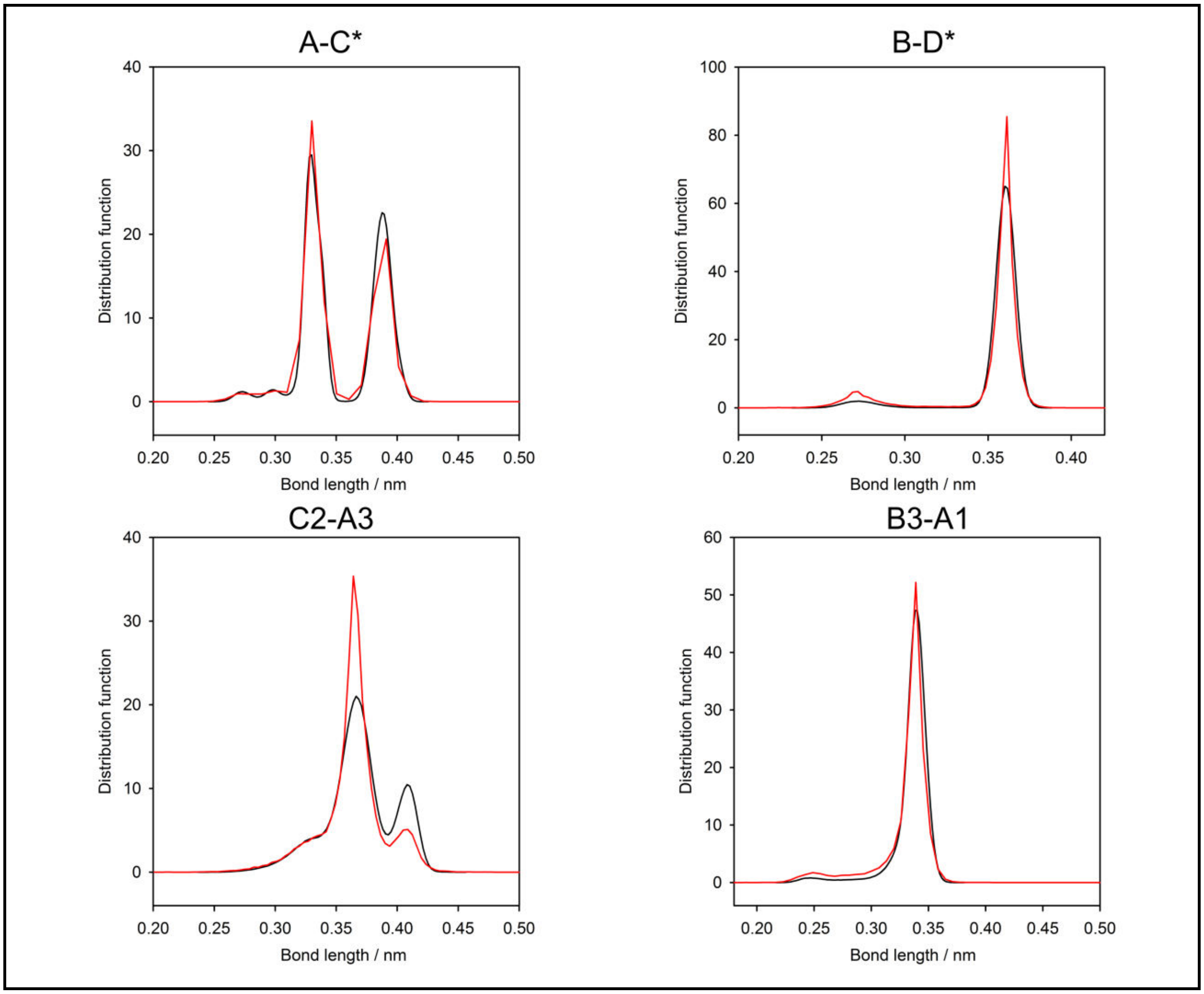

Figure 11: Representative examples of bonded distribution functions of the atomistic and coarse-grained stewartan simulations

The reproduction of the atomistic configurations by the coarse-grained model was analyzed by comparing the bond distribution functions of the atomistic (black) and coarse-grained simulations (red). Bonded potentials were derived from the atomistic reference structure using Boltzmann inversion. Here, the bonds within all monosaccharides are described by the same bonded potentials A-B*, A-C*, B-C* and B-D* (the latter potential in case of the GlcA^{IV} monomer). Different potentials, as shown in Figure 9, were used to describe the linkages between the monosaccharide subunits.

Similarly, angular and dihedral potentials are well captured by the CG model (Figure 12 and Figure S10-S13). Typically, the number of peaks as well as their locations is very well reproduced. Often, dihedrals which account for rotations around bonds within a monosaccharide, e.g. the dihedral B3-A8-C8-B8, showed maxima in the range of 150 to 180° or -150 to -180°. Hence, the glycosidic bonds (in the latter case: B3-A8) lie approximately in the plane of the monomer. In contrast, rotations around bonds which connect the monomers, are much more flexible and posse several local maxima. For example, the B6-C6-A7-B7 dihedral has a main maximum of around 100° and several local maxima at -150°, -80° and 25°. Hence, folding of the stewartan polysaccharide depends on these intermonosaccharide bond rotations and thus typically reflects the behaviour of polysaccharide chains at the atomistic scale. However, similar to the bonded distributions, the main maxima of the angular and dihedral distribution functions are sometimes slightly overrepresented, while other parts of the distribution are somewhat or underrepresented.

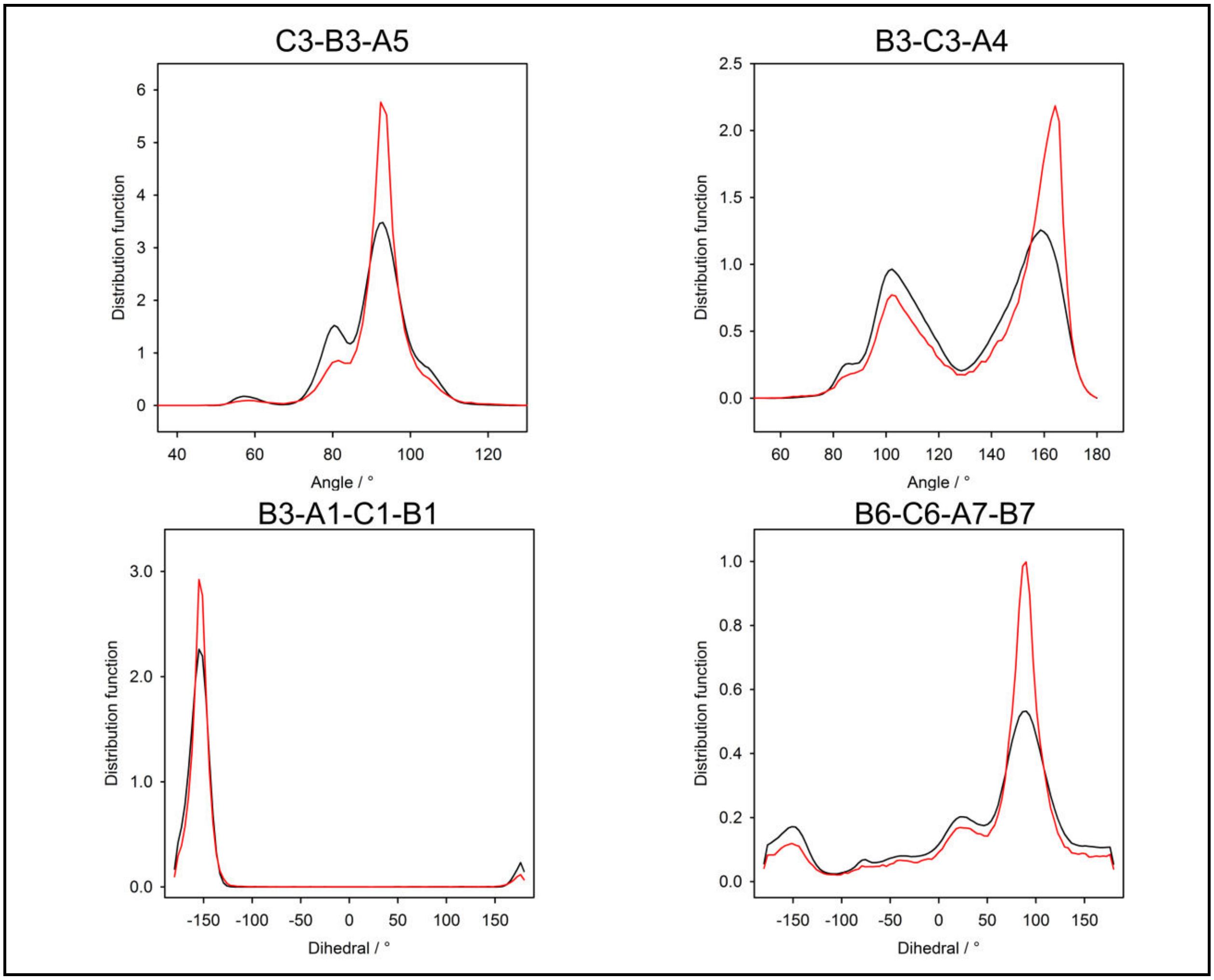

Figure 12: Representative examples of angular and dihedral distribution functions of the atomistic and coarse-grained stewartan simulations

The reproduction of the atomistic configurations by the coarse-grained stewartan model was analyzed by comparing the angular and dihedral distribution functions of the atomistic (black) and coarse-grained simulations (red). Bonded potentials were derived from the atomistic reference structure using Boltzmann inversion. The coarse-grained mapping of the stewartan structure is shown in Figure 9.

The set of bonded potentials used in this work was previously defined from CG cellulose (see section 3.5.2) (Sauter and Grafmüller, 2017). In contrast, stewartan exhibit a more branched structure. This set of specific bonded interactions did not sufficiently reproduced the atomistic configurations in the branched region around the CG Gal^{III} residue which result in unphysical conformations. Therefore, to adapt the CG model to the branched geometry, an additional angular potential (A5-B3-A1) was implemented to prevent collapsing of CG A beads onto each other (Figure 13, A). Moreover, an extra dihedral potential (A5-B3-A1-B1) in the same region was needed to properly describe the rotation of the stewartan branches (Figure 13, B). In the latter case, the CG beads A5, B3, A1 and B1 form a dihedral with a minimum centered at around 80° in the atomistic simulation.

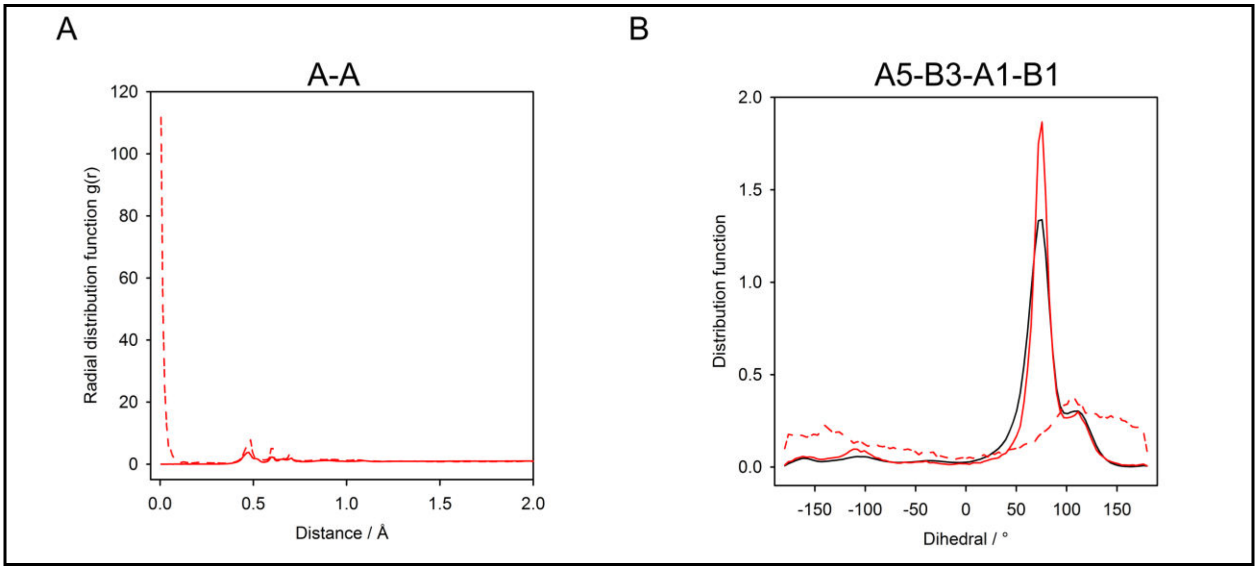

Figure 13: Examples of improvements of the coarse-grained stewartan model

A model for the coarse-graining of atomistic (black) 3 RU stewartan was developed. The initial coarse-grained model (without the addition of the A5-B3-A1 angular and A5-B3-A8-B8 dihedral potential, red, dashed) was further modified (with addition of these two potentials, red, line) to improve (A) the coarse-grained A-A radial distribution function and (B) the rotation of the A5-B3-A8-B8 dihedral, respectively. The coarse-grained mapping of the stewartan structure is shown in Figure 9.

Finally, potentials accounting for explicit short range intra-molecular 1-3 and 1-4 interactions (virtual bonds) were added to improve the reproduction of the atomistic structure.

The local structure and aggregation behaviour of the final CG model of stewartan revealed good agreement with the atomistic system as judged by comparing the radial distribution functions (RDFs) of the respective CG and atomistic systems (Figure 14 and Figure S14). The short range structure seen in the RDFS often display many peaks which originate from the different monosaccharide types in stewartan. Here, for example the short range structural features in the A-A and A-B RDF are excellently captured by the CG simulation. Throughout all RDFs shown the behaviour in the range of 0.5-1.5 nm is very well reproduced. Positions of the peaks in the CG B-B, C-C and C-D RDFs agree with their atomistic counterpart but showed in some cases a slight over- (e.g. in C-D at 0.3 nm) or underrepresentation (e.g. in B-B and C-C from 0.5-1.2 nm). One general exception for which the location of short range peaks are not captured as well are the interactions between the CG D atoms. Here, in the CG simulation the D-D RDF shifted considerable by around 0.5 nm in comparison to the analogues atomistic RDF.

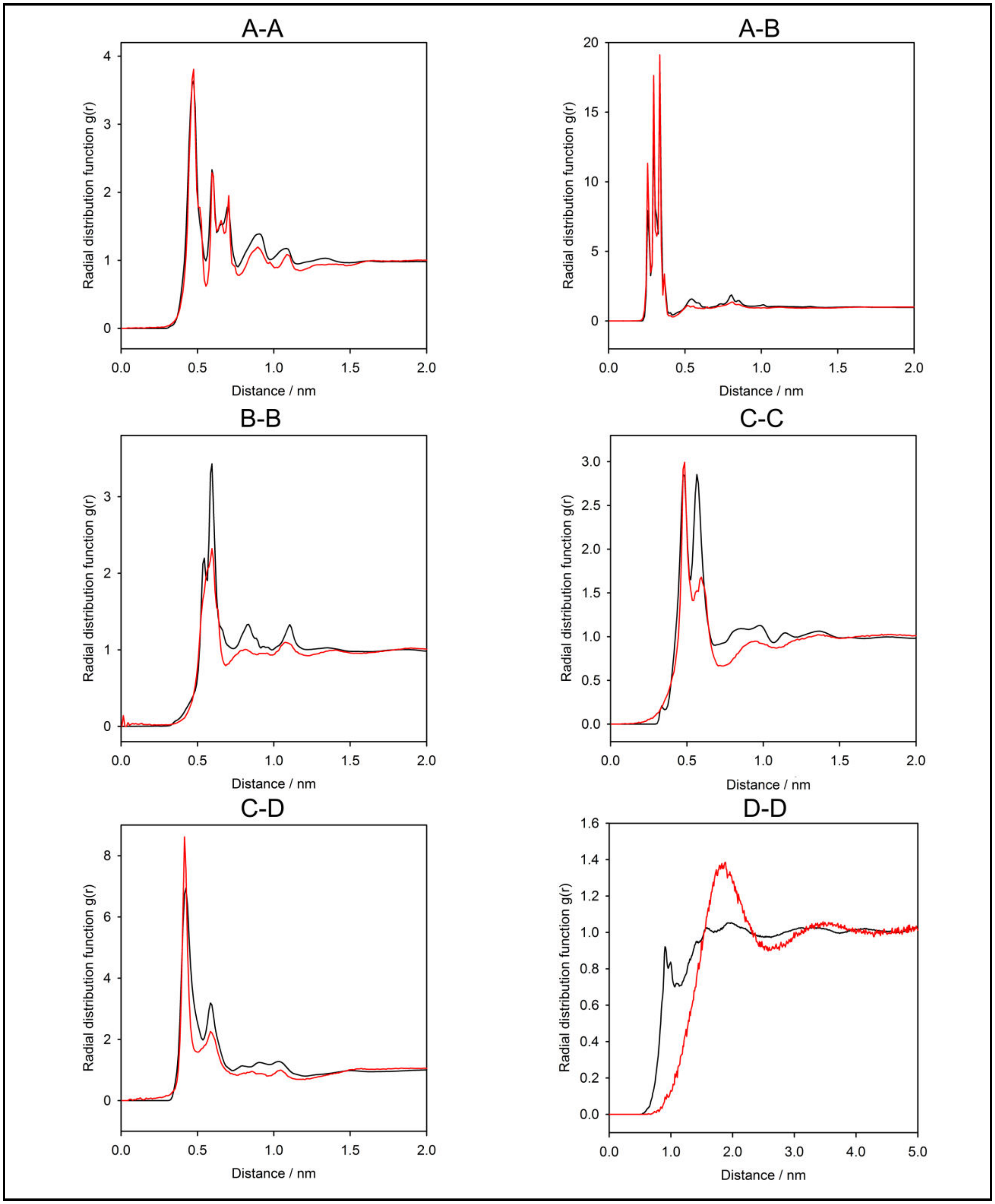

Figure 14: Representative examples of radial distribution functions of the simulation of atomistic and coarse-grained 3 RU stewartan

The reproduction of the atomistic configurations by the coarse-grained model was analyzed by comparing the radial distribution functions of the atomistic simulation (black) and coarse-grained simulations (red). The coarse-grained mapping of the stewartan structure is shown in Figure 9.

However, in preliminary experiments, in which the CG stewartan structure was mapped on eight different bead types (Figure S15), the short-range interaction of the D-D interactions improved and the D-D RDF exhibited no shift in comparison to the atomistic simulation (Figure 15). Hence, the latter mapping scheme provided a better description of the D-D interactions.

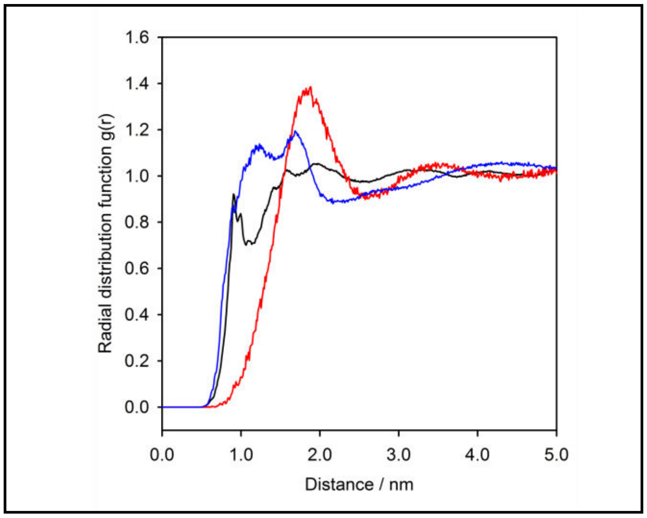

Figure 15: Radial distribution function of the D-D interaction for the atomistic and differently-mapped coarse-grained 3 RU stewartan simulations.
The D-D radial distribution function is shown for the atomistic stewartan simulation (black) and for coarse-grained stewartan systems with a four (red) or eight (blue) bead type mapping scheme. Each simulation was carried out for 100 ns.

To note, the CG simulation of stewartan showed a high tendency to crash (around every nanosecond). Here, CG beads typically moved to close to each other and consequently gained a high potential energy. As a result in the next step the bonded interaction between the both CG atoms increased in a unphysical manner above 1.8 nm where no tabulated potentials were available. Nevertheless, simulations were continued from previous frames and complete 100 ns simulations were obtained. It is here assumed, that the stewartan simulation crashed due to an imbalance in the CG force field. Hence, a more careful evaluation of the choice of explicit non- and bonded potentials has to be undertaken to check if certain potentials are in conflict with each other.

4.1.3 Conformation of 3 RU Coarse-Grained Stewartan Chains

A CG model of 3RU stewartan was developed in the previous section in which each monosaccharide was mapped on three different beady types. Here, an overrepresentation of the bonded potentials was seen. This overdetermination is likely to impose a higher rigidity to the stewartan chains, especially in case of those bonded potential which determine the conformations of the glycosidic links, and the overall structure of 3 RU stewartan can be affected. Hence, to evaluate how strongly the overall polymer conformations are influenced, a single CG stewartan was simulated for 1 µs and revealed an end-to-end distances distribution with a maximum at 4 nm (Figure 16, A and C). The CG end-to-end distance distributions highly overlap with the atomistic one with a maximum at 3 nm. However, the lower end of the end-to-end distance distribution is not captured by the CG simulation which reflects more restricted angular conformations in the CG stewartan model. The conformational space of the stewartan chains in both, the atomistic and CG simulations, are highly confined when an ensemble of chains (27 chains of the same length) are simulated for 100 ns (Figure 16, B and D). Here, the end-to-end distance distributions are narrowed to widths of 0.7 nm. Again, the CG distribution shows slightly more extended chains with a maximum around 3.6 nm whereas in comparison the maximal end-to-end distance from the atomistic counterpart were found to be 3.2 nm. Overall, the CG stewartan polymers highly resemble the atomistic chain conformations in despite the slight overrepresentation of bonded potentials.

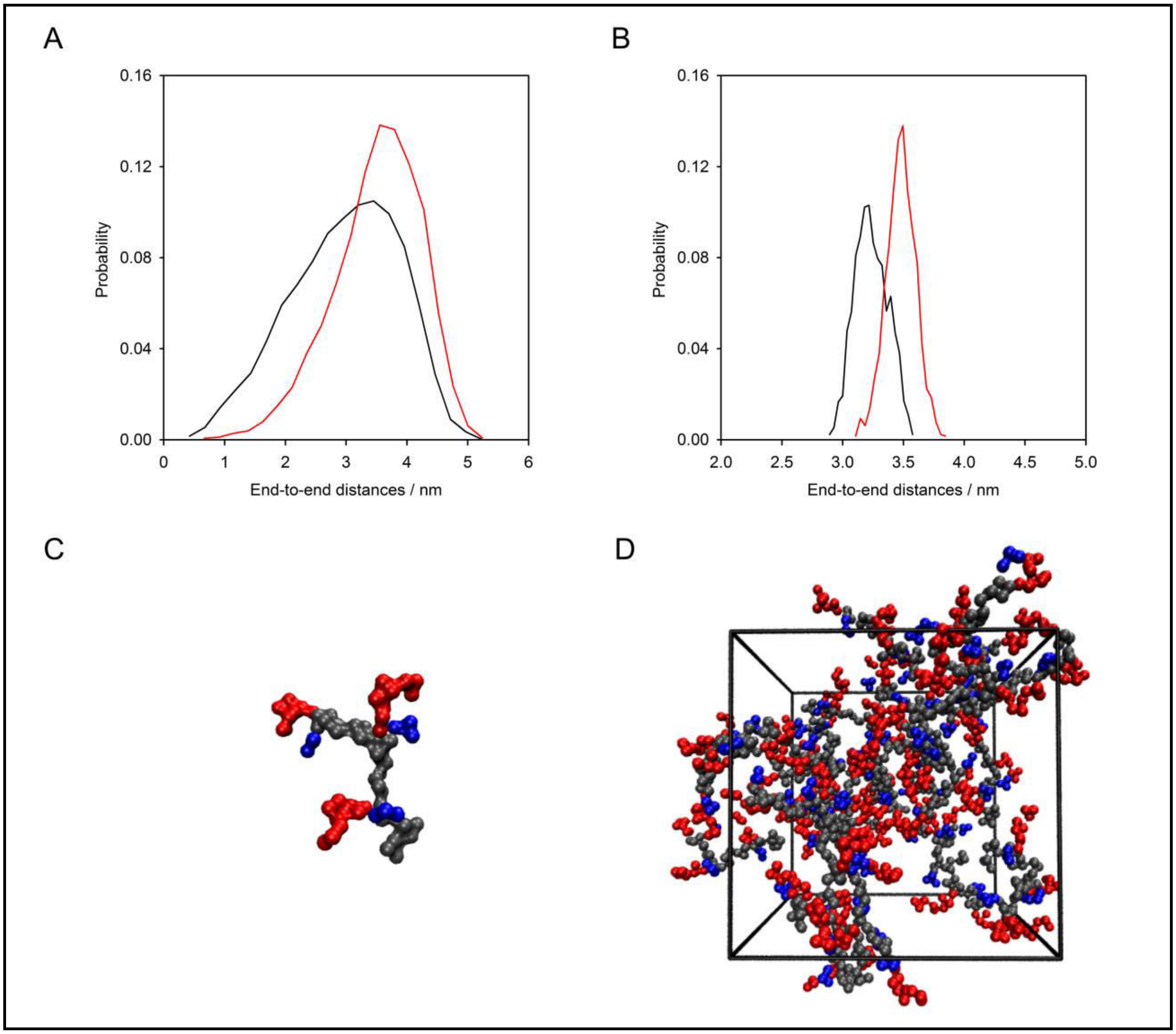

Figure 16: End-to-end distance distributions of atomistic and coarse-grained 3 RU stewartan

The 3 RU stewartan system was used for the development of a coarse-grained model. (A), (B) To verify that the coarse-grained stewartan chains exhibit similar conformations, the end-to-end distances of the atomistic reference (black) were compared to the coarse-grained simulations (red). Here, the distributions are shown for (A) a single stewartan chain and for (B) an ensemble of 27 chains. (C), (D) Simulation snapshots are shown for (C) a single coarse-grained stewartan chain with an end-to-end distance of 3 nm and for (D) the simulation of 27 coarse-grained stewartan chains. The ExoPS polymers are shown in surface depiction with the backbone coarse-grained atoms in grey and the coarse-grained representations of the [(4→1)-β-D-GlcA$^{\mathrm{IV}}$(4→1)-α-D-Gal$^{\mathrm{V}}$(6→1)-β-D-Glc$^{\mathrm{VI}}$ and (6→1)-β-D-Glc$^{\mathrm{VII}}$ branch residues in red and blue, respectively.

4.1.4 Coarse-Grained Simulation of 20 RU Stewartan

CG simulations of 3 RU stewartan revealed that the CG model highly agrees with the atomistic properties as verified by comparing the RDFs and bonded distribution functions. However, stewartan chains with a higher degree of polymerization are required to elucidate a potential stewartan network assembly. In previous studies it was shown, that the potentials from a reference system are transferable to longer chains and other concentrations (Hynninen *et al.*, 2011; Sauter and Grafmüller, 2017; Schneible *et al.*, 2019). Therefore, the 3 RU stewartan CG model, with a concentration of 313 mM, was transferred to a stewartan system with a length of 20 RUs. In the following, the RDFs for the stewartan system with a RU concentration of 86 mM is exemplary analyzed (Figure 17 and Figure S16). Overall, the neighbours in the RDFs highly agree with those for the reference CG and atomistic simulation. In almost all cases, short range structures of 0.2 to 1.2 nm were captured with an excellent agreement. However, the magnitude of the peaks for the longer polymers is higher, as the absolute amount of nearest neighbours is higher in the 20 RU stewartan system. To note, because of the high number of atoms, the simulation of an atomistic stewartan system with the same concentration and polymer length of the CG 20 RU stewartan was not simulated. Therefore, it was not possible to compare the RDFs of CG 20 RU stewartan system to an atomistic reference system.

The RDF of the D-D interaction revealed a peak around 2.0 nm which is in agreement with the RDF from the reference system. Although, close range interactions between 0.8 to 1.5 nm are further reduced in the 20 RU stewartan system. Furthermore, the D-D RDF of the 20 RU stewartan simulation is noisy and consequently reflects the poor sampling of D-D interactions as the number of D beads is lower compared to other CG bead types. Prolonged simulations are proposed to increase the sampling of D-D interactions.

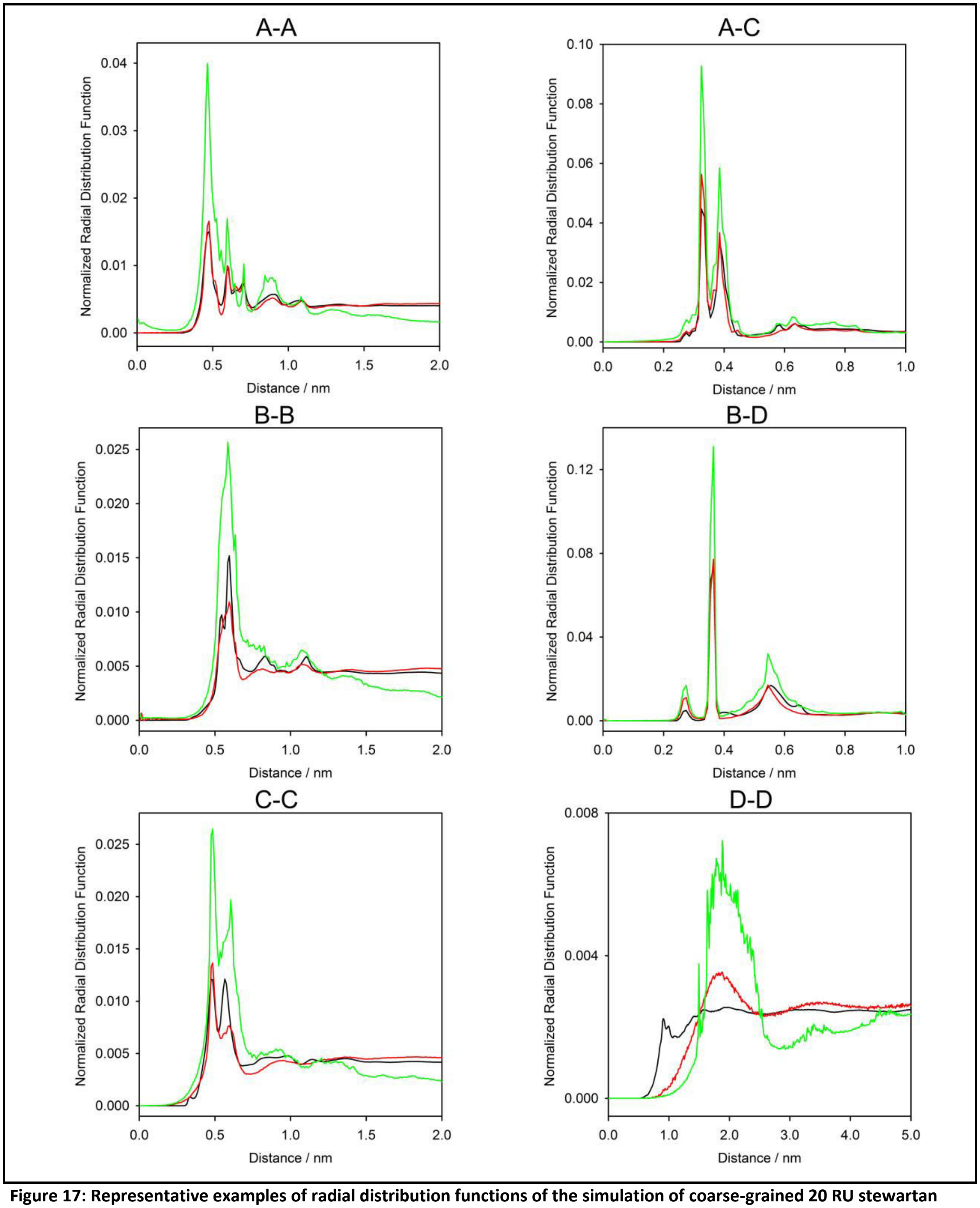

Figure 17: Representative examples of radial distribution functions of the simulation of coarse-grained 20 RU stewartan
The radial distribution functions of coarse-grained 20 RU stewartan system (green) were compared to the 3 RU stewartan systems (atomistic - black, coarse-grained - red). The coarse-grained mapping of the stewartan structure is shown in Figure 9.

4.1.5 The Structure of the Coarse-Grained 20 RU Stewartan Network

Four different concentrations of 20 RU stewartan (with RU concentrations of 86, 50, 20 and 10 mM) were simulated by increasing the box size and keeping the number of molecules constant. Snapshots of the simulation box already reveal a dense arrangement with evenly distributed 20 RU stewartan chains at the highest RU concentrations (86 and 50 mM) (Figure 18). In contrast, gaps between the stewartan chains increase with the dilution of the system (RU concentration of 20 and 10 mM).

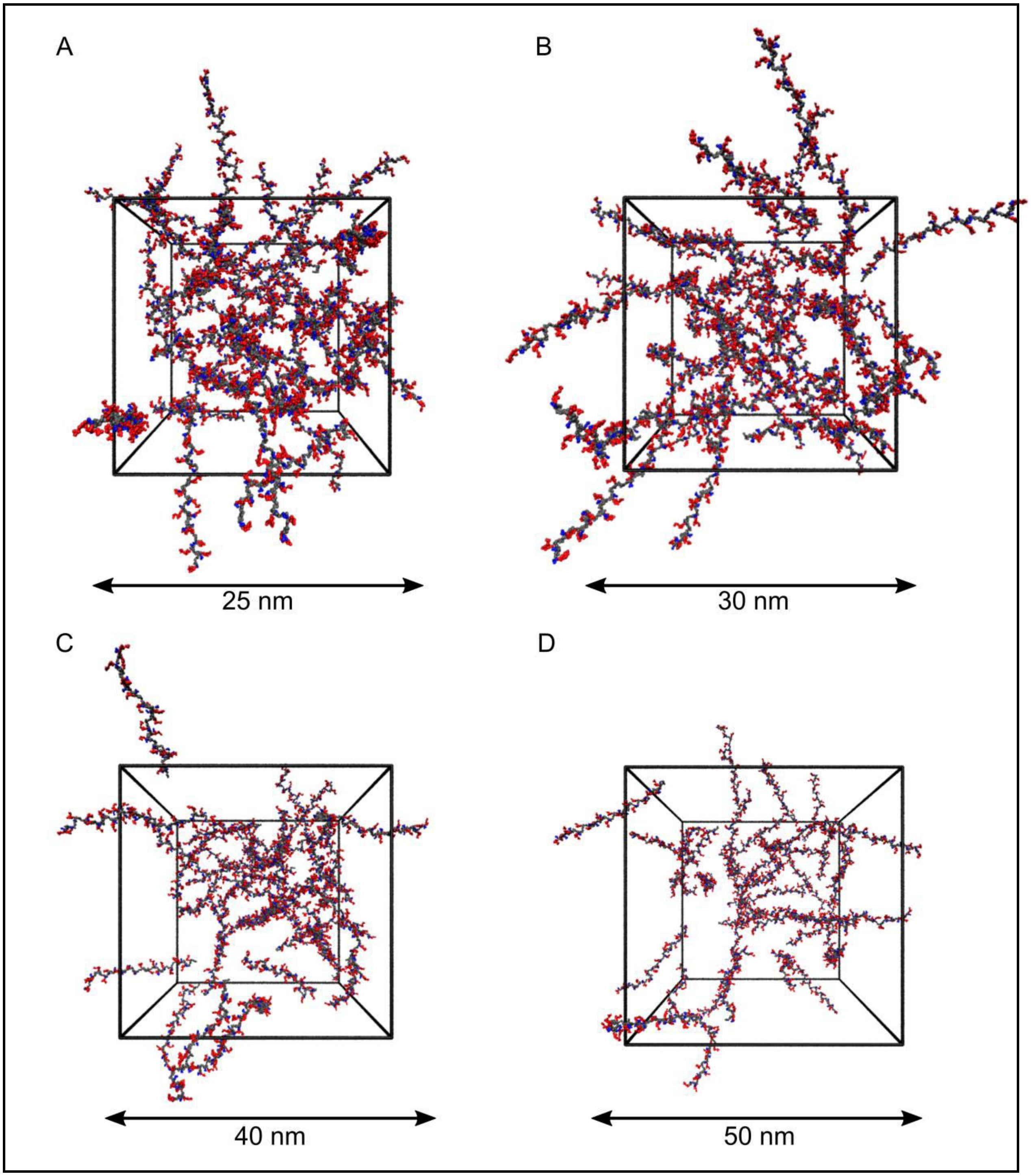

Figure 18: Snapshots of different concentrated coarse-grained 20 RU stewartan systems
Coarse-grained stewartan system with RU concentrations of (A) 86, (B) 50, (C) 20 and (D) 10 mM were obtained by increasing the box size to 15,625, 27,000, 64,000 and 125,000 nm^3, respectively, and keeping the number of stewartan molecules constant. The edge length of the box is shown below each depiction. Snapshots were taken at the end of the 100 ns simulations. The ExoPS polymers are shown in surface depiction with the backbone coarse-grained atoms in grey and the coarse-grained representations of the [(4→1)-β-D-GlcA^{IV}(4→1)-α-D-Gal^{V}(6→1)-β-D-Glc^{VI} and (6→1)-β-D-Glc^{VII} branch residues in red and blue, respectively.

The end-to-end distances of the 20 RU stewartan chains reached a constant value of approximately 19.5 nm in the first 20 ns of the simulation independent of the RU concentrations (Figure 19, A). In a typical conformation, the backbone of the stewartan polymer had a snake-like form with the branches pointing away with nearly 90° angles as seen in Figure 19, B.

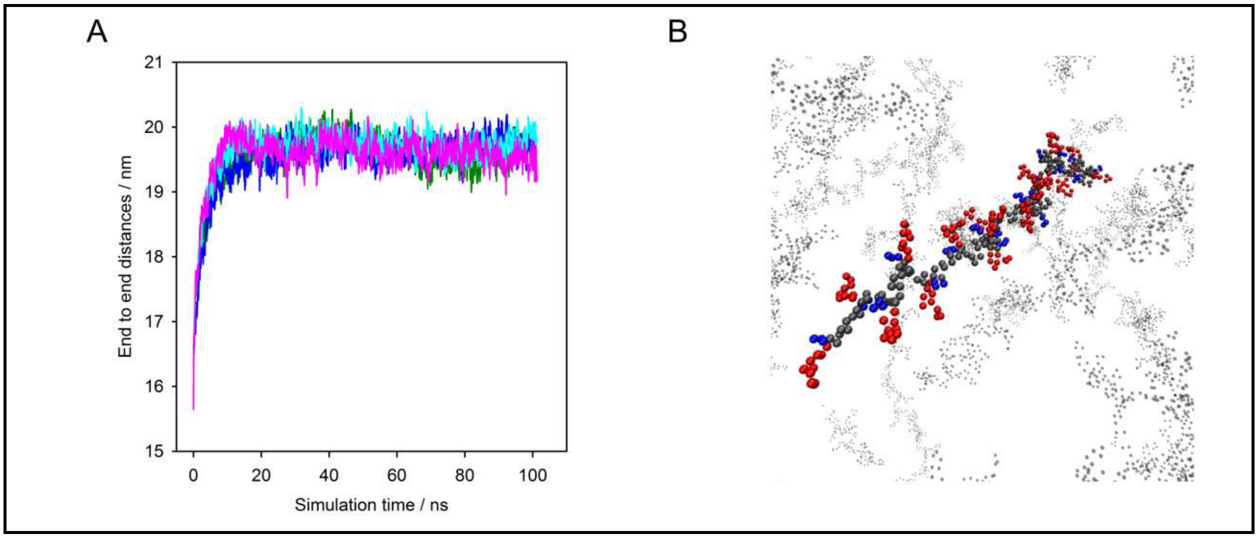

Figure 19: Conformation of the coarse-grained 20 RU stewartan chains

(A) The end-to-end distances over the 100 ns of the coarse-grained simulation of 20 RU stewartan is shown. Stewartan systems with a RU concentration of 86, 50, 20 and 10 mM are depicted in green, blue, cyan and purple. (B) Additionally a snapshot of a single stewartan chain from the 86 mM RU system is provided. The ExoPS polymer is shown in CPK depiction with the backbone coarse-grained atoms in grey and the coarse-grained representations of the [(4→1)-β-D-GlcA^{IV}(4→1)-α-D-Gal^{V}(6→1)-β-D-Glc^{VI} and (6→1)-β-D-Glc^{VII} branch residues in red and blue, respectively. The other stewartan chains are found in the background of the snapshot and are indicated in grey.

To quantitatively analyze the morphology of the stewartan network at different concentrations the number of interchain contacts and pore size distribution in the network were calculated (Table 3). At high RU concentrations (86 and 50 mM) the number of contacts per stewartan molecule within 1 nm remained in the same range. Four to ten-fold less contacts were determined at RU concentrations of 20 and 10 mM. For example 389 ± 86 average contacts per residue were formed during the CG simulation of 86 mM RU whereas the number of contacts decreased to 38 ± 25 in the most diluted system with a RU concentration of 10 mM.

Table 3: Average number of contacts between 20 RU coarse-grained stewartan chains
The number of contacts per stewartan chain was averaged over the 100 ns of the 20 RU stewartan simulation.

RU concentration / mM	Average number of contacts per chain	Error*
86	389.1	± 85.7
50	411.7	± 80.3
20	114.6	± 42.1
10	38.2	± 24.5

* the standard deviation is shown as errors

A similar picture emerges from the analysis of the distribution of pore sizes within the stewartan networks (Figure 20). The pore diameters are of the same size for the two higher concentrations of 86 and 50 mM RU (around 3 nm) and increase at lower RU concentration to 7 and 11 nm for 20 and 10 mM RUs, respectively. Hence, the swelling of the polymer solution with increasing water content is reflected.

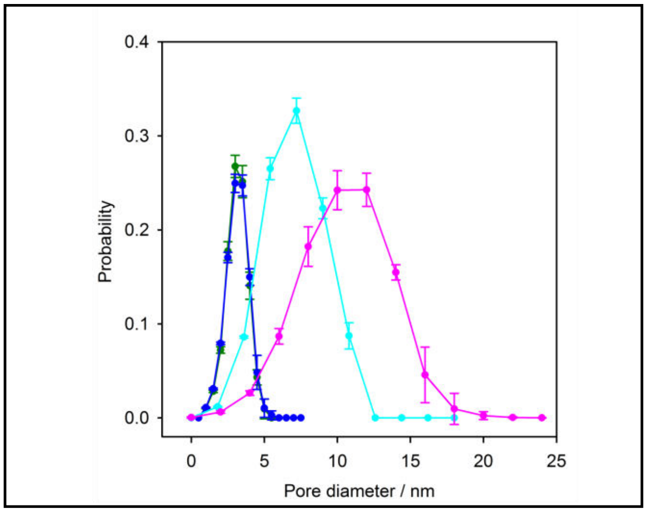

Figure 20: Pore diameter distribution of the coarse-grained 20 RU stewartan systems
20 RU stewartan was simulated at different RU concentrations: 86 (green), 50 (blue), 20 (cyan) and 10 mM (purple) for 100 ns and the pore diameter distribution of the stewartan networks were calculated as described by Bhattacharya and Gubbins, 2006. The errors shown represent the standard deviation of the pore diameter calculation at 90, 95 and 100 ns.

Next, it was examined whether the stewartan solutions formed rigid polysaccharide networks in which the interchain contacts influence the diffusion dynamics of the stewartan molecules. On one hand, independent of the dilution of the 20 RU stewartan systems, the number of contacts between the stewartan molecules varied throughout the simulation time (Figure 21, A). Hence, interchain contacts were only transiently formed. On the other hand, although more contacts are formed in high concentrated stewartan systems (RU concentrations of 86 and 50 mM), their mean square displacements (MSDs) overlay with that from the more diluted systems (Figure 21, B). This is emphasized by the ExoPS diffusion coefficients determined from the MSD plots which are almost similar for all investigated systems (31, 28, 29 and 33 · 10^{-6} cm^2 · s^{-1} for RU concentration of 86, 50, 20 and 10 mM, respectively). Hence, the contacts between stewartan chains did not account for a strong long-term association of ExoPSs molecules.

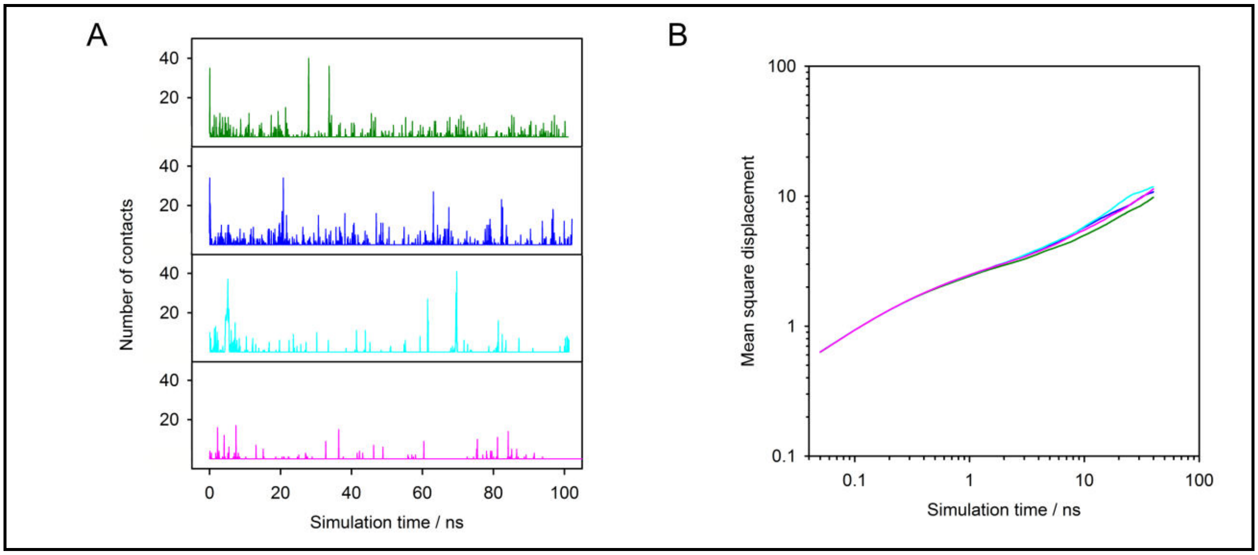

Figure 21: Network dynamics of the coarse-grained 20 RU stewartan system

Coarse-grained 20 RU stewartan was simulated at different RU concentrations: 86 (green), 50 (blue), 20 (cyan) and 10 mM (purple) for 100 ns. (A) The number of interchain contacts of an example stewartan molecule within 1 nm and (B) the average mean square displacement of the stewartan chains were analyzed over the first 60 ns trajectory.

Lastly, inspection of the CG simulation of 20 RU stewartan revealed a portion of stewartan chains which stopped fluctuating and effectively freezed during the 100 ns simulation time (Figure S17). This phenomenon occurred with around 15-18 % (6-7 molecules) of the chains at different time points during the simulations for all analyzed concentrations. This was confirmed by the root mean square deviation (RMSD) of an example chain which showed a fluctuation around its mean position until 60 ns at which the kinetic temperature suddenly dropped (to around 0.8 K). Freezing of individual stewartan chains was not detected in the reference stewartan simulation. Stewartan chains did not freeze when the leap-frog stochastic dynamics integrator was used. At the moment the latter integrator has only been applied for the CG 20 RU stewartan system with a RU concentration of 86 mM and the average properties of the stewartan solution were found to be similar regarding the analysis of the MSDs, interchain contacts and pore size distributions. It is therefore proposed that the freezing of chains result as an artefact of the thermostat parameters used in the CG simulations of stewartan. Still, the first chains were found to freeze after a simulation time around 30 ns. In this regime, the stewartan network was already formed and hence the results here shown are still representative for the physicochemical properties of the stewartan solution.

4.2 Reconstituted Stewartan Forms a Diffusion-Limited Network

The biofilm is a thick multilayered bacterial assembly in which biochemical properties and its composition vary in time and space. These properties govern a tight control of the diffusion of biomolecules and prevent access of toxins and antibiotics. As shown in section 4.1.5, stewartan chains with a length of 20 RU formed hydrogels with transient interchain contacts. Next, the influence of the stewartan matrix on the mobility of fluorescent particles was investigated. Therefore stewartan ExoPSs were isolated from *Pantoea stewartii* (*P. stewartii)* biofilms.

4.2.1 Purification of the Exopolysaccharide Stewartan

P. stewartii colonies were grown at 30°C where the highest proliferation rate can be expected. Biofilm formation was initiated by the addition of glucose to the growth medium. After 24 h slimy, yellowish colonies were visible which enlarged after additional 48 h incubation (Figure 22). *P. stewartii* biofilms showed a mucoid and ropy character as found for other biofilm-forming bacteria (Ruas-Madiedo and de los Reyes-Gavilán, 2005). Likewise colonies exhibited a high viscosity when pipetted up and down.

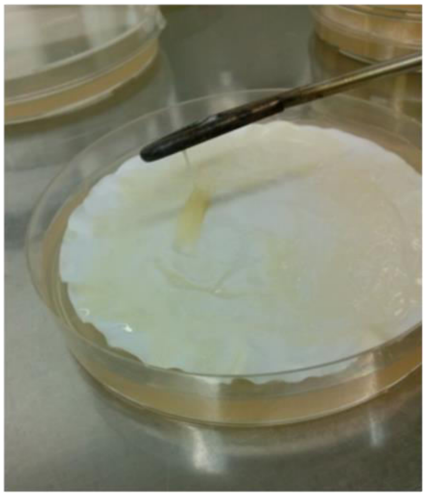

Figure 22: *Pantoea stewartii* colonies
Pantoea stewartii cells were plated on membrane filters on top of the casamino acid-peptone-glucose agar medium. After 72 h incubation at 30°C an image of the colonies was taken.

Afterwards the biofilm was centrifuged to remove bacterial cells/ debris and the ExoPS was precipitated with 80 % (v/v) ethanol. This crude stewartan preparation showed contaminations in the absorbance around 260 nm (Figure 23, A). Biofilms usually contain a high amount of extracellular DNA which originates from dead bacterial cells (Okshevsky *et al.*, 2015; Okshevsky and Meyer, 2015). Therefore, DNA contaminations from the stewartan preparation were removed by treatment with

Benzonase® Nuclease and subsequent dialysis against water. Afterwards the stewartan preparation showed reduced nucleic acid contaminations. Additionally, homogeneity was also judged from size-exclusion chromatography (Superdex^{TM} peptide 10/300) in which other contaminations eluted around a retention volume of 15 mL (Figure 23, B). These contaminations did not arise from nucleic acids as they remained in the stewartan preparation even after Benzonase® Nuclease digestion. Nevertheless, contaminations were removed by dialyzing stewartan twice against 100 mM and 50 mM acetic acid, respectively. Presumably, positively charged contaminations bound to the negative charges of the stewartan polymer but were competitively removed by the high concentration of H^+ ions at low pH. Consequently both purification steps were combined (Benzonase® Nuclease treatment with subsequent dialysis in acetic acid) to purify homogenous stewartan ExoPSs from *P. stewartii* biofilms.

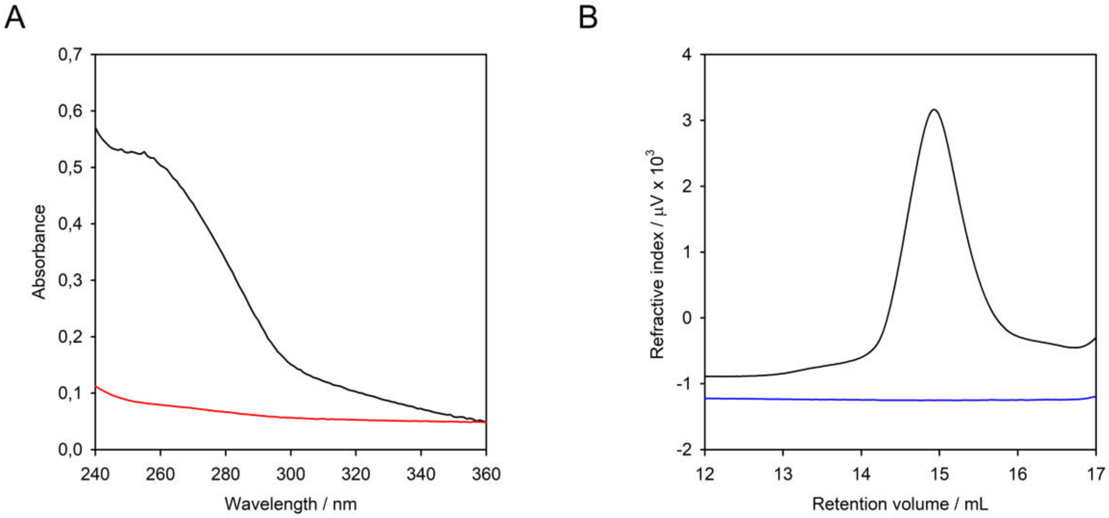

Figure 23: Purification of stewartan exopolysaccharide

Stewartan was purified from *Pantoea stewartii* colonies. The homogeneity of the stewartan preparation was judged from (A) absorbance spectra and from (B) size-exclusion chromatography runs (Superdex^{TM} peptide 10/300). The crude stewartan preparation (black) was either treated with Benzonase® Nuclease (red) or dialyzed against acetic acid (blue).

To estimate the concentration of stewartan in a *P. stewartii* biofilm, the ExoPS concentration was determined using the phenol sulfuric acid method (Table 4). The amount of secreted stewartan increased with the age of biofilm from 13.5 mg · mL^{-1} to 15.3 mg · mL^{-1} for 24 h and 72 h old biofilms, respectively. Nevertheless, as the biofilm grows more bacterial cells proliferate and the amount of ExoPS produced by each cell remained the same.

Table 4: Stewartan concentration in *Pantoea stewartii* biofilms
Pantoea stewartii biofilms were grown on CPG medium for 20.5 or 65 h. The overall stewartan concentration was determined with the phenol sulfuric acid method.

Biofilm Age / h	20.5	65
Stewartan Concentration / g · L^{-1}	13.5	15.3
OD600	0.93	1.04
Stewartan Secreted Per Cell* / g · L^{-1}	14.5	14.6

* determined as the ratio of the concentration of stewartan and the OD_{600}

4.2.2 Diffusion Studies of Nanoparticles in the Stewartan Network

The size of the analyzed fluorescent particles ranged from a Stokes diameter of 1.1 nm to 190 nm to cover a broad size distribution. Polystyrene microspheres (PS) with 42 and 190 nm diameter were bought from Polysciences, Inc. (Hirschberg an der Bergstrasse, Germany). They were chosen as they didn't contain reactive chemical groups on their surface which presumably reflects chemical inertness. However, their size was checked in light scattering studies (Table 5). It was found that 42 nm microsphere actually differed in their size and showed a larger diameter of around 64 nm. Similarly, 190 nm beads were found to be slightly larger (193 nm diameter). Consequently, throughout this work they will be referred to as 64 and 193 nm PS microspheres. In addition, PS microspheres were found to have a negative zeta potential in the analyzed buffers (Table 5).

Table 5: Overview of fluorescent tracer molecules used in this study and their characterization by light-scattering experiments

Fluorescent tracer molecule	Buffer	Zeta potential	Error	Diameter / nm	Error
Alexa Fluor® 488	water	n.d.*	/	1.1**	/
42 nm PS Microsphere	MES, pH 5	-19,9	± 0.5	64.1	± 0.5
	Tris, pH 8	-33.4	± 1.1	64.1	± 0.1
190 nm PS Microsphere	MES, pH 5	-12.1	± 2.2	192.7	± 2.6
	Tris, pH 8	-25.3	± 2.7	193.1	±1.3
P22 bacteriophages	MES, pH 5	-7.5	± 0.3	70.9	±1.0
	Tris, pH 8	-13.6	± 1.8	72.9	± 0.7

*n.d.: not determined
**the diameter of Alexa Fluor® 488 was determined from fluorescence correlation spectroscopy measurements (Petrášek and Schwille, 2008)

The diffusion of fluorescent particles was analyzed using fluorescence correlation spectroscopy. In polymer solutions, the diffusivity of nanoparticles with a size smaller or similar than that of the polymer is often insufficiently described by the Stokes-Einstein law (Cai *et al.*, 2011; Nath *et al.*, 2018).

Hence, to characterize the particle's mobility, the diffusion time in stewartan τ_d is normalized with the diffusion time of the same particle in buffer τ_{buffer}. This hindrance factor $\tau_{hind} = \frac{\tau_d}{\tau_{d,buffer}}$ enables the determination of the relative diffusion times and magnitude of confinement instead using the viscosity term from the Stokes-Einstein relation.

Indeed, the fluorescent particles are hindered in their mobility as they diffuse through a 10 mg · mL^{-1} stewartan solution (Table 6). The hindrance for the smallest particle analyzed, Alexa Fluor®488, was characterized by a hindrance factor of 1.1, but the confinement increased for 64 and 193 nm PS microspheres (hindrance factor of 11.9 and 23.3, respectively). Apparently, the nano- and microviscosity experienced by these particles differed with particle size and consequently rose from the diffusion of Alexa Fluor®488 to 193 nm PS beads. As a result Alexa Fluor®488 was almost not confined by the stewartan matrix whereas 64 and 193 nm PS microspheres experienced the most hindrance.

In comparison, diffusion in 40 % (w/v) sucrose revealed similar values for the diffusion hindrance of the same set of tracer molecules (hindrance factors ranged from 5.0 to 6.1s). Consequently, in 40 % (w/v) sucrose the diffusion of all particles was almost evenly confined. Sucrose was chosen as a non-polymer model system, which still produces viscous solutions. In conclusion, a size dependent hindrance on the diffusion of molecules is an inherent feature of the polymeric stewartan matrix.

Table 6: Hindrance factors determined from the diffusion of different-sized fluorescent tracer particles

The hindrance factor was used as a description of the experienced confinement to the diffusion of fluorescent tracer molecules in 10 mg · mL^{-1} stewartan. The diffusion time τ in stewartan or buffer was determined from fluorescence correlation spectroscopy experiments.

Fluorescent tracer molecule	Hindrance factor τ_{hind}	
	10 mg · mL^{-1} stewartan	40 % (w/v) sucrose
Alexa Fluor® 488	1.1	6.1
64 nm bead	11.9	5.0
193 nm bead	23.3	5.2

The confinement of the diffusion of fluorescent particle became more apparent with increasing stewartan concentrations (Figure 24, A). Hence, 193 nm PS beads were not confined in a 1 mg · mL^{-1} stewartan solution (hindrance factor of 1) whereas the mobility was greatly slowed down in 10 mg · mL^{-1} stewartan by a factor of 20. Similarly, 64 nm microspheres decrease in their mobility up to a hindrance factor of 40 in 1 and 20 mg · mL^{-1} stewartan. This diffusion behavior is reflected by the anomaly exponents that characterizes the anomalous diffusion behavior (Figure 24, C). Here, the PS microspheres showed free and unhindered Brownian diffusion in buffer (0 mg · mL^{-1} stewartan, α = 1), but their mobility decreased with increasing stewartan concentrations (up to an anomaly factor of 0.6 in 20 mg · mL^{-1} stewartan). In contrast, Alexa Fluor®488 was only slightly confined by highly concentrated stewartan solutions (a hindrance factor of around 1.5 in 20 mg · mL^{-1} stewartan) with only a minor increase of α (Figure 24, B and D).

To investigate, if size is the only variable which affects the mobility, diffusion studies were extended to a pH of 8. Indeed, the diffusion of 64 nm PS beads at a pH of 8 was less subdiffusive as shown by lower hindrance factors and higher anomaly exponents as compared to the diffusion at pH 5 (Figure 24, A and C). Minor differences were seen for the mobility of 193 nm PS particles at these two pH values over all investigated stewartan concentrations. The diffusion of Alexa Fluor®488 was unaffected by the change in pH (Figure 24, B and D).

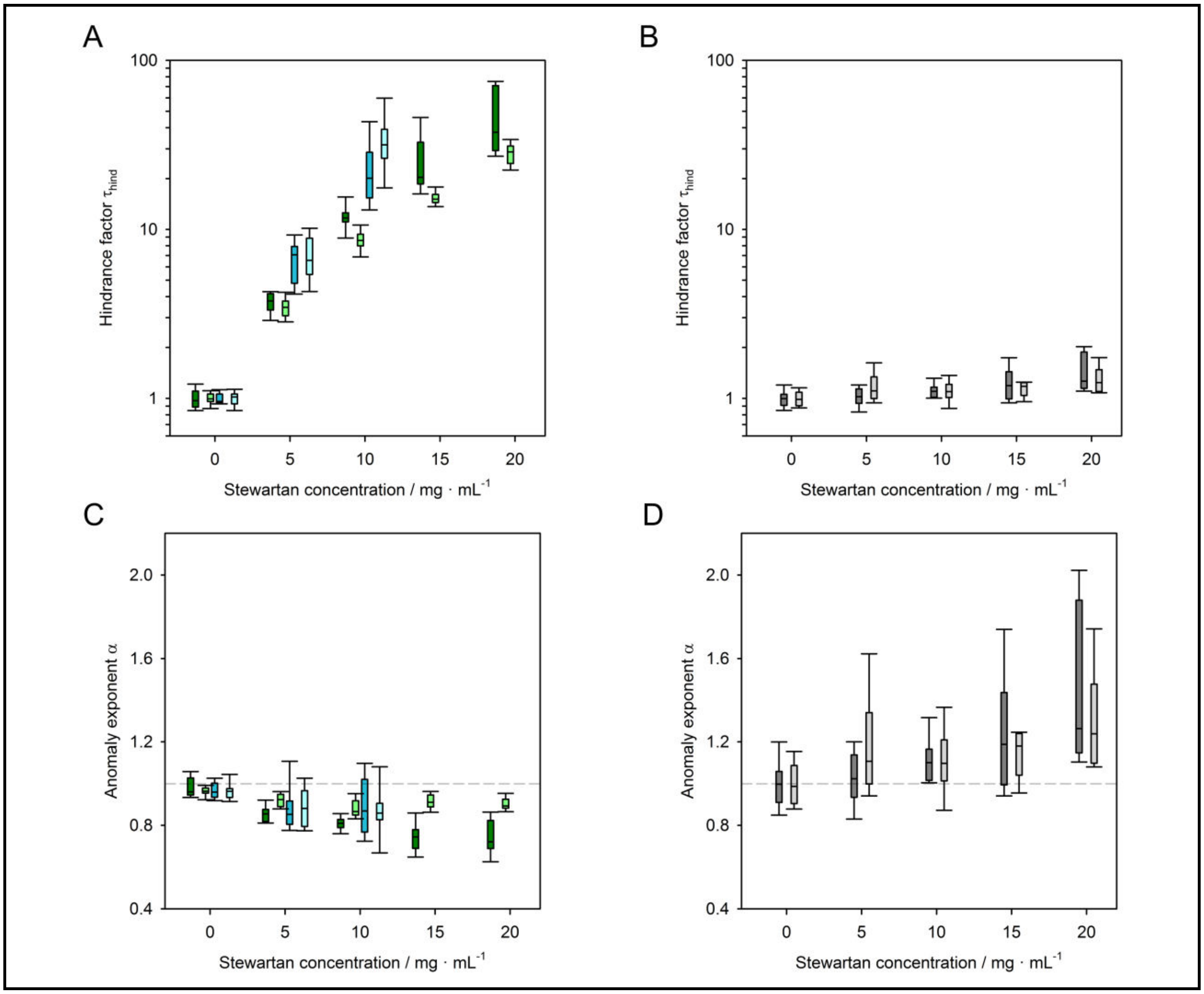

Figure 24: Diffusion of fluorescent particles at different concentrations of stewartan

The diffusion of Alexa Fluor®488 (grey) and PS beads (64 nm, green, and 193 nm, blue) was conducted at pH 5 (dark color) or pH 8 (light color). Diffusion of these particles in different stewartan concentrations was analyzed with (A), (B) the hindrance factor and (C), (D) the anomaly exponent α.

Analysis of the specific viscosities has been used to elucidate the polymeric properties of polysaccharides (Krause *et al.*, 2001; Ganesan *et al.*, 2016). In analogy, the specific hindrance factor, determined from the diffusion times, as a measure for the confinement experienced by the fluorescent PS beads in a stewartan solution was plotted against the stewartan concentration (Figure 25). For every PS microsphere type, this analysis revealed two distinct diffusion regimes in which the data points scale with different exponents. Consequently, a transition point c_t was determined as the intersection of two power-law fits (6.9 and 6.9 mg · ml^{-1} for 64 and 193 nm beads). A similar behavior was seen for the specific viscosity of stewartan which were obtained from the falling ball viscosimeter measurements (c_t = 7.1 mg · ml^{-1}). The first regimes are characterized by an almost linear dependence with exponents of 1.0, 0.9 and 1.0 for the dynamic viscosity, 64 nm and 193 nm PS beads, respectively. Accordingly, the high concentration regimes scaled with $c^{3.6}$, $c^{2.0}$ and $c^{3.7}$.

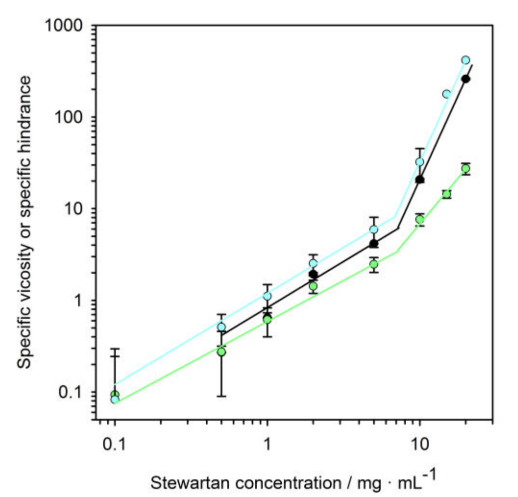

Figure 25: Power-law scaling of the specific viscosity/ specific hindrance in dependence to the stewartan concentration

The specific viscosities of stewartan were determined from the diffusion of 64 (green), 193 nm polystyrene microspheres (blue) and from the falling ball viscosimetric measurements. The different regimes were separately fitted by a power-law function and the transition point c_t was obtained at the intersection.

To gain a deeper understanding into the slow diffusion dynamics of 193 nm PS microspheres above 10 mg · mL^{-1} stewartan, the time-averaged mean square displacements (taMSD) of 193 nm PS particles were analyzed (Figure 26, A). Here, the values for the taMSD decreased with increasing stewartan concentrations. The anomaly exponent α ranged from 0.8 to 0.6 for 5 to 20 mg · mL^{-1} stewartan, respectively (Figure 26, B). Apparently, the diffusion of 193 nm PS beads is marked by a subdiffusive behavior which increased with the stewartan concentration. The diffusion of 193 nm PS beads in 40 % (w/v) sucrose showed no subdiffusion with α around 1. In comparison the diffusion in simple fluids is also described with α=1 but showed higher taMSD values than compared to the diffusion in

40 % (w/v) sucrose. To note, the taMSD for the diffusion in sucrose deviates from a linear slope (above 0.5 s) which presumably originates from poor statistics at large lag times.

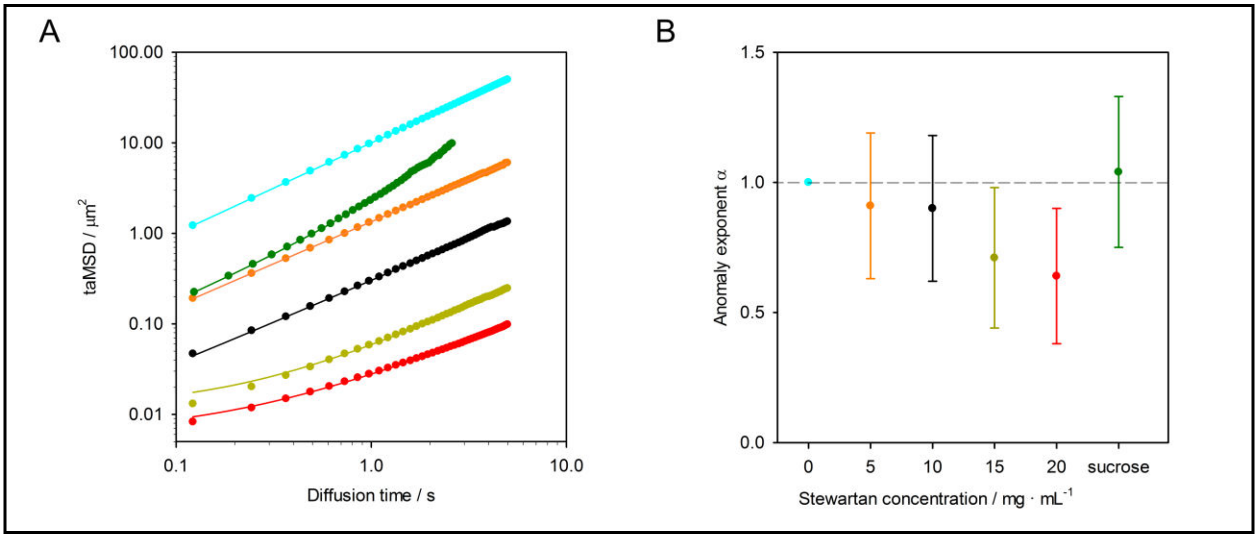

Figure 26: Single-particle tracking of 193 nm polystyrene microspheres at different stewartan concentrations
The diffusion of 193 nm beads in 40 % (w/v) sucrose (green), 5 (orange), 10 (black), 15 (dark yellow) and 20 mg · mL^{-1} stewartan (red) was analyzed in (A) time-averaged mean square displacement plots and (B) by determination of the anomaly exponent α of fits from the individual time-averaged mean square displacement curves. As comparison a simulation of a diffusion in a simple fluid (0 mg · mL^{-1} stewartan, D_{app}=2.5 µm^2 · s^{-1}, α=1) is shown in cyan.

4.2.3 Characterization of the Bacteriophage Particle Diffusivity in the Stewartan Matrix

The investigations of the diffusion dynamics of small-sized particles in the stewartan network were extended on bacteriophages as they are of high clinical relevance used as antibiotic alternatives (Harper *et al.*, 2014). P22 bacteriophages were chosen as a model system. These phages are not infective for *P. stewartii* and lack an enzymatic activity towards stewartan (Andres *et al.*, 2012; Andres *et al.*, 2013). P22 bacteriophages showed a negative zeta potential with a diameter of 71 to 73 nm and are therefore of comparable size to the 64 nm PS microspheres (Table 5). Similar to the 64 nm PS beads, P22 bacteriophages are confined by the stewartan matrix in dependence of the concentration of the ExoPS (Figure 27, A). Diffusion in 10 and 20 mg · mL^{-1} stewartan solutions was characterized by hindrance factors of around 3 and 20, respectively. The anomaly exponent indicated subdiffusion with 0.9 and 0.8 (Figure 27, B). Consequently, the mobility of P22 phages was higher and less confined compared to the diffusion of 64 nm PS beads. In contrast, diffusion of bacteriophages in 40 % (w/v) sucrose showed no subdiffusion (α ~ 1) and a confinement around 4.

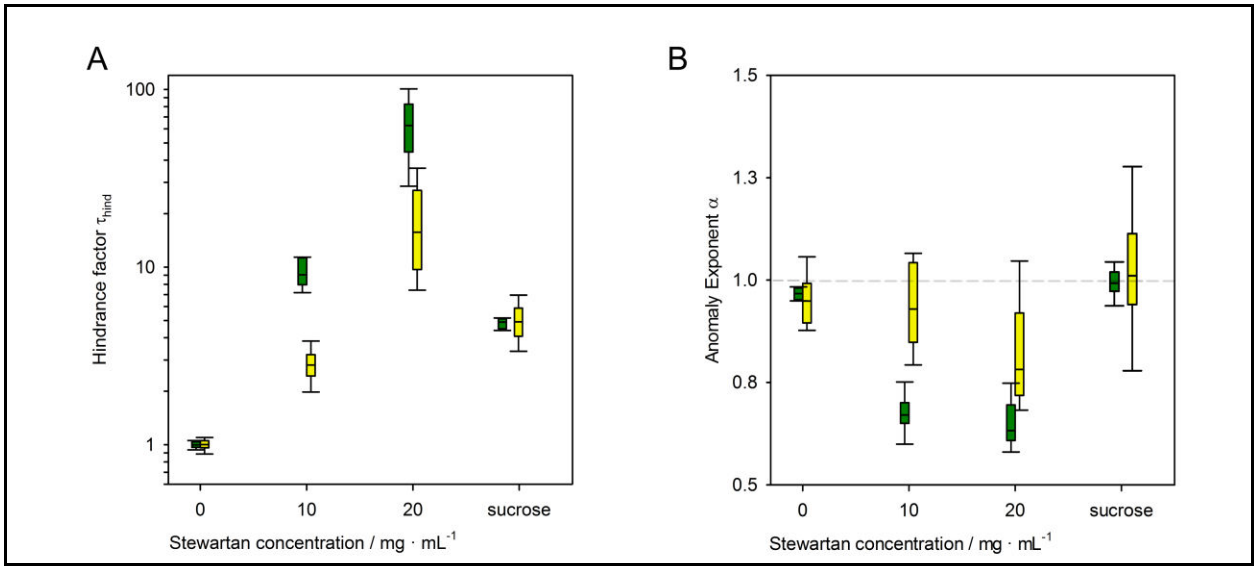

Figure 27: Diffusion of P22 bacteriophage particles at different stewartan concentrations and 40 % (w/v) sucrose
Diffusion of P22 bacteriophages (yellow) was compared to the mobility of 64 nm beads (green). Diffusion was characterized by (A) the hindrance experienced and (B) the anomaly exponent α.

Single-particle tracking (SPT) experiments with bacteriophages revealed two populations of P22 particles which differed in their mobility (Figure 28, A and B). One population randomly diffuses through a 20 mg · mL^{-1} stewartan matrix with diffusion coefficients around 1 µm^{2} · s^{-1} whereas the mobility of a second population was found to be confined to a small area (D_{app} = 0.001 to 0.01 µm^{2} · s^{-1}). The latter was not present in 10 mg · mL^{-1} stewartan or in 40 % (v/v) sucrose. Again the diffusion of P22 bacteriophages was moderate subdiffusive with α values of 0.8 in 10 and 20 mg · mL^{-1} stewartan whereas the confined population showed highly subdiffusive diffusion dynamics with an anomaly exponent of 0.3 (Figure 28, C and D). Free Brownian motion was seen for the mobility of the phage particles in 40 % (w/v) sucrose.

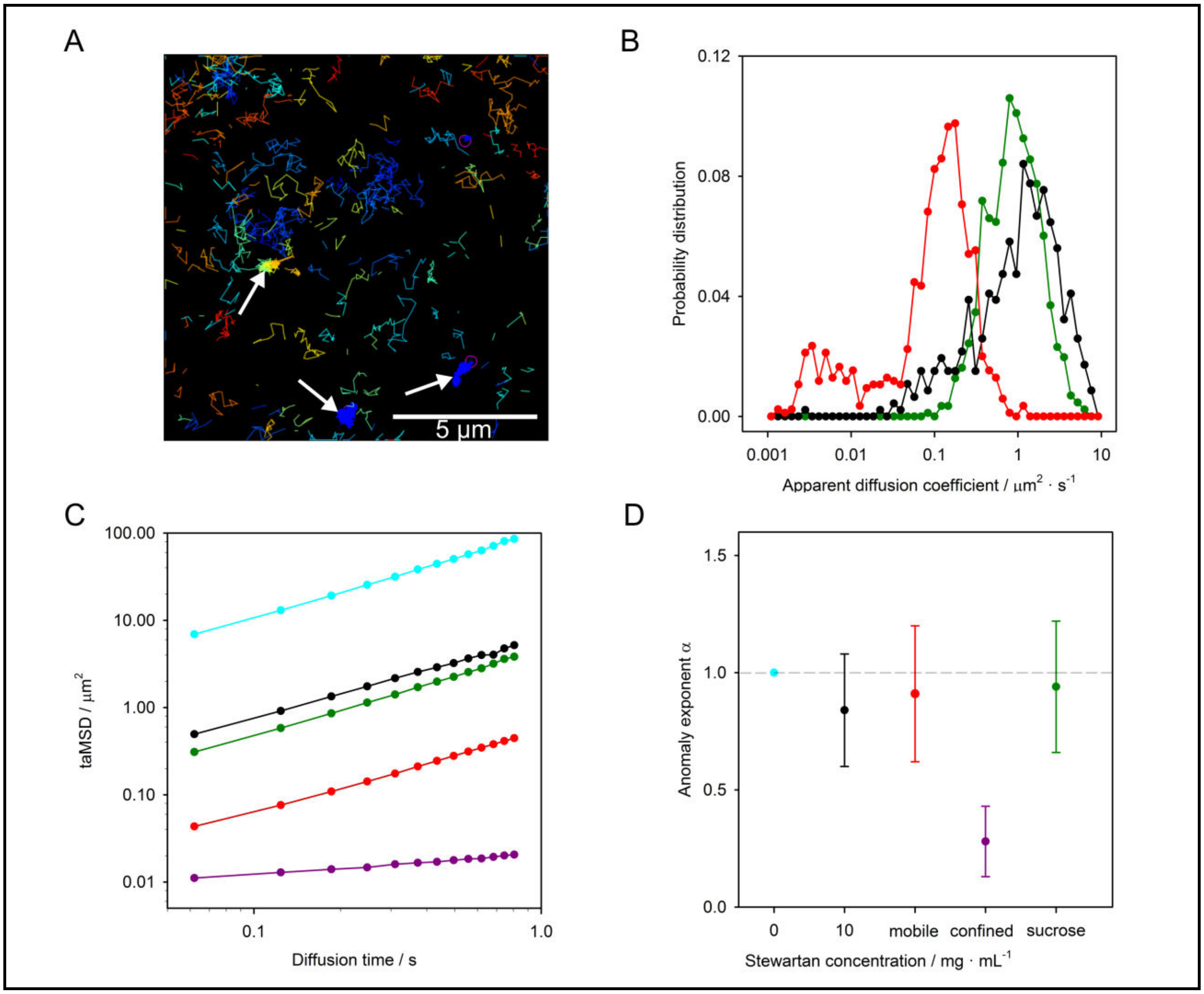

Figure 28: Single-particle tracking of P22 bacteriophages at different stewartan concentrations and 40 % (w/v) sucrose
(A) Snapshot of P22 bacteriophage trajectories in 20 mg · mL^{-1} stewartan. The mobility of a population of P22 particles was confined to a small area and examples are indicated with arrows. (B), (C) and (D) The diffusion of P22 phages was analyzed in 40 % (w/v) sucrose (green), 10 (black) and 20 mg · mL^{-1} stewartan (mobile population, red, confined population, purple). (B) The distribution of the apparent diffusion coefficients are shown. (C) Mean square displacement plots for the mobility of P22 bacteriophages were plotted and (D) the anomaly exponent α derived. (C), (D) As comparison a simulated diffusion in a simple fluid (0 mg · mL^{-1} stewartan, D_{app}=1.1 µm^2 · s^{-1}, α=1) is shown in cyan.

The analysis of the distribution of the angle θ between successive steps calculated from the P22 phage SPT trajectories was used to further characterize the diffusion behavior of P22 particles (Figure 29). Here the motion of the phages in 40 % (v/v) sucrose and 10 mg · mL^{-1} stewartan can be described by a stochastically random distribution of θ from 0 to 180°. However, in 20 mg · mL^{-1} stewartan the distribution is shifted towards large angles with a maximum at 180°. Apparently, the diffusion of the bacteriophages in the latter stewartan solution is more prone to be described by a complete turnaround of the direction between two successive steps. This maximum is even more pronounced for the confined population of P22 particles.

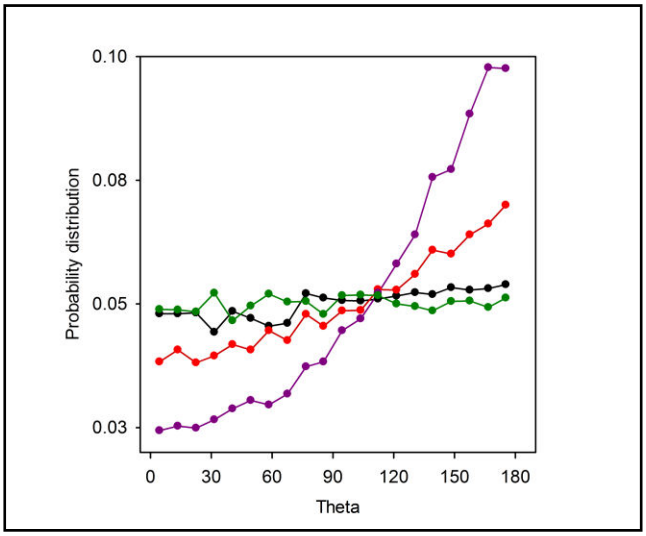

Figure 29: Probability distribution of the angle theta in single-particle tracks of P22 bacteriophages
The probability distribution for the diffusion of P22 particles was analyzed in 40 % (v/v) sucrose (green), 10 (black) and 20 mg · mL^{-1} stewartan (mobile population, red, confined population, purple).

4.3 Biophysical Characterization of Biofilm Remodeling Enzymes

Stewartan polymers formed a diffusion-limited network. The structural features of the ExoPS three dimensional structure are intrinsically coded in the monosaccharide sequence of stewartan (Bernhard, 1996; Carlier *et al.*, 2009). Mutations in the *P. stewartii wce I-III* gene cluster resulted in alterations of the final stewartan monosaccharide composition (Langlotz *et al.*, 2011; Wang *et al.*, 2012). Likewise, any modifications of the stewartan chains will influence the three-dimensional arrangement and the associated physicochemical properties. In the following, protein candidates were found which enzymatically modify the stewartan chains and the structural impact on the ExoPS matrix was analyzed.

4.3.1 Structural Analysis of WceF – A Bacterial Tailspike-Like Protein

The structure and function of the gene product of *wceF* from the *wceI* gene cluster in *P. stewartii* has yet not been elucidated. *P. stewartii* mutants, in which *wceF* was deleted, produced stewartan chains of higher size compared to the wildtype (Schollmeyer *et al.*, 2012). Consequently, the gene product of *wceF* might be involved in the stewartan biosynthesis. WceF is a 80.4 kDa protein (UniProt: H3REJ8). The first 27 amino acids comprise a twin-arginine translocation signal peptide which is commonly found in bacteria in proteins which are translocated across the inner membrane (DeLisa *et al.*, 2003; Palmer and Berks, 2012). To elucidate the function of WceF the latter was first analyzed in a Blast search and homologs were found in more than 20 *P. stewartii* related species such as *Pantoea ananatis, Pantoea agglomerand* or *Erwinia* amylovora (Figure 30). Here, the sequence identity ranged from 96 to 61 %. Additionally, further homologs, which are mainly polygalacturonases and thus implicated in polysaccharide degradation, were found in other species such as the *Yersinia enterocolitica* exopolygalacturonase (38 %), *Thermotoga maritima* exopolygalacturonase (38 %), *Asperigillus flavus* putative rhamnogalacturonase (33 %) and *Prunus persica* polygalacturonase (31 %). The sequences which were covered by the homology analysis rather lie between the amino acids 200-400 of WceF. Other sequence similarities of WceF have been found with the tailspike proteins (TSPs) from the *Salmonella* Phage P22 (26 %) and *Shighella* Phage Sf6 (25 % sequence identity). In the latter homologs, the sequence identities were found at the N-terminus of WceF (between amino acids 1-300). Hence, these results therefore point to a putative polysaccharide degradation function of WceF in *P. stewartii*.

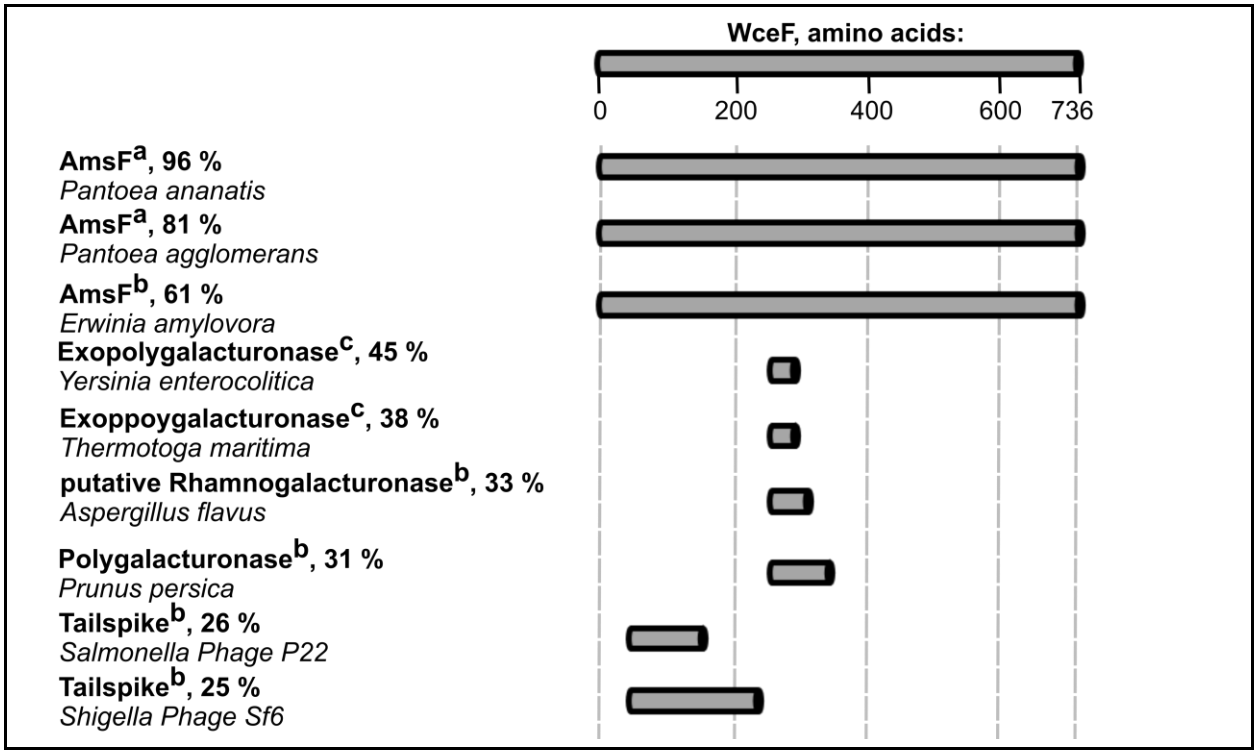

Figure 30: Overview of representative examples of WceF homologs

Homologs and the respective sequence identities to full-length WceF (UniProt: H3REJ8) were found with BlastP in a) a non-redundant sequence database, b) UniProtKN/Swiss-Prot and c) Protein Data Bank. Proteins are depicted in bold and hosts in italic. The sequence identities of the homologs to WceF are given.

To further elucidate the structural and functional context of the protein, WceF was purified and crystallized. For this purpose, a WceF variant was used in which the N-terminal twin-arginine signal peptide was deleted to ensure a feasible recombinant expression in *E. coli*. A crystal structure of WceF was then refined of 2.9 Å resolution. As confirmed by size exclusion chromatography WceF crystallized as a trimer in the asymmetric unit (Figure 31 and Figure S19).

The overall structure of the trimer revealed an elongated molecule with an overall length of 165 Å (Figure 31, A). The subunits arranged themselves around a threefold axis with intertwined monomers. Especially at the C-terminus the molecule was more tightly packed resulting in a funnel-like structure which narrowed from top (funnel diameter ca. 74 Å) to bottom (ca. 38 Å) (Figure 31, B and C). The interior space of the funnel was mainly dominated by hydrophilic interactions solvated with 42 crystal water molecules. Two adjacent monomeric subunits buried an 5086 Å^2 interface including 75 hydrogen bonds and 22 salt bridges.

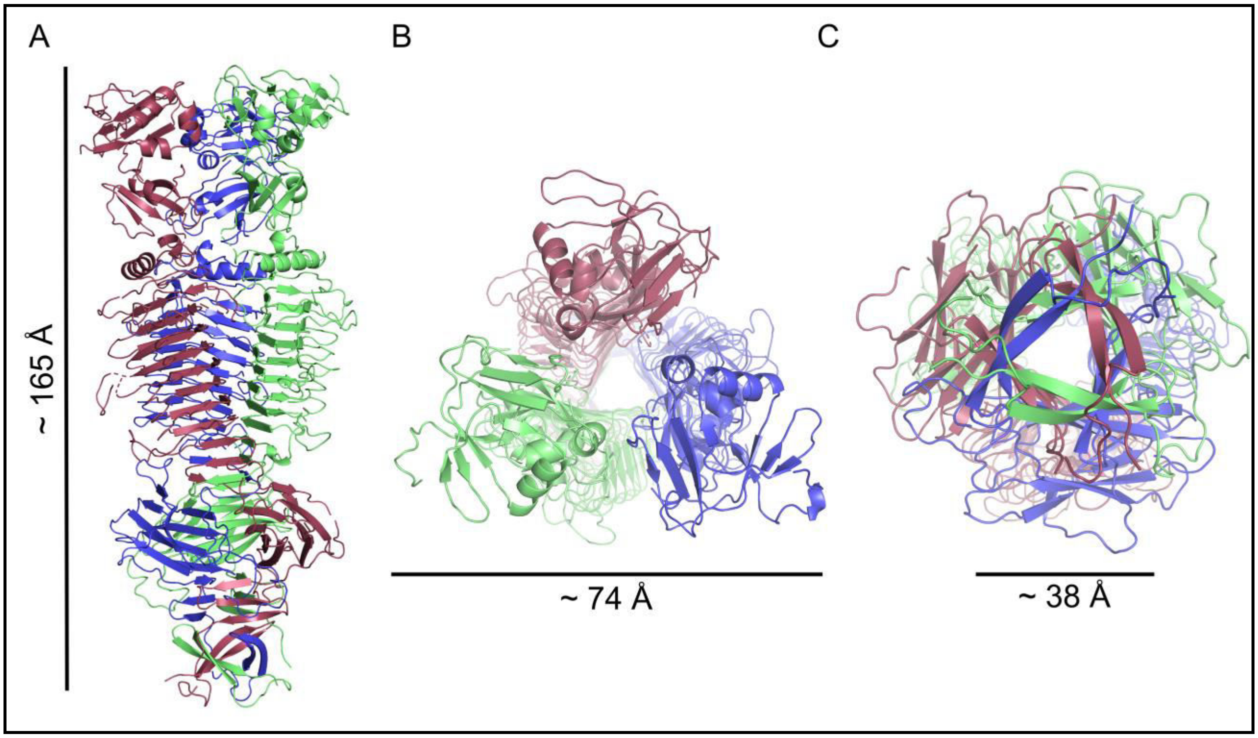

Figure 31: Overall structure of trimeric WceF

WceF crystallized as a trimer and the monomeric subunits (depicted in red, blue and green in cartoon representation) are arranged around a threefold axis with view (A) from the side (B) from top and (C) from bottom.

The monomeric structure of WceF comprised separate distinguishable motifs which are partitioned by loop regions (Figure 32, A and B). The N-terminal domain of WceF (amino acids: 38-147) consisted of two β-strands connected by three α-helices and a three stranded antiparallel β-sheet. This domain is succeeded by a four stranded Greek key motif formed by the amino acids 148-234. The most central part of the monomer folded into a right handed parallel β-helix (amino acids: 269-527). It rises up to

49 Å with nine coils in total. Every coil was composed of the β-strands B1, B2 and B3 connected by the loops L1, L2 and L3. The cross-sections showed L-shaped coils (Figure 32, C). An α-helix lied orthogonal on top of the β-helical motif and capped the hydrophobic interior. The latter is dominated by stacking interactions of cysteins, isoleucins, leucins, phenylalanins, valins and mixed amino acids residues (Figure 32, D and Table S1). Apparently, water molecules are excluded from that area.

Finally, the proceeding polypeptide chain adopted a concave shape with a four stranded antiparallel jelly roll (amino acids: 528-674) and ended with two additional antiparallel β-sheets (amino acids: 675-699 and 700-736). The latter domain, being the most intertwined segment in the trimeric structure and thus were tightly packed, resulted in the final trimeric orientation in which each monomer is tilted away from the common axis in a funnel-like manner.

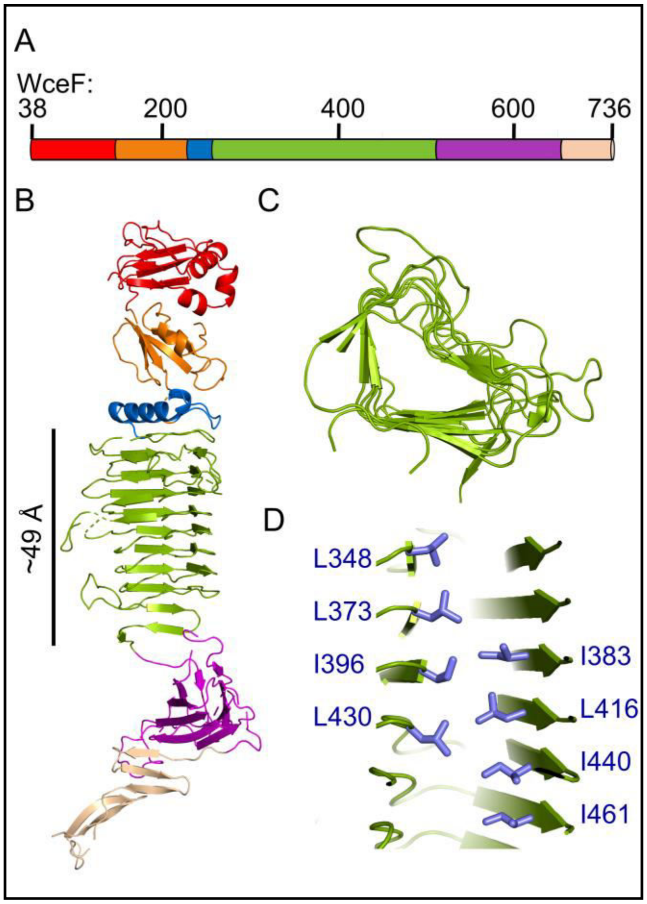

Figure 32: Structure of monomeric WceF
(A) A WceF monomer consists of an N-terminal domain (red, amino acids: 38-147), a Greek key motif (orange, amino acids: 148-234), a capping α-helix (blue, amino acids 235-268), a β-helix (green, amino acids 269-527), a jelly roll (purple, amino acids 528-674) and additional β-sheets (wheat, amino acids 675-736) at the end of the polypeptide chain. (B) The WceF monomeric structure is shown in cartoon representation with (C) a cross-section of the central β-helix and (D) the hydrophobic interior of the β-helix which is dominated by hydrophobic stacking amino acids, here displayed with a selection of residues.

The β-solenoid architecture of WceF is highly characteristic for many bacterial proteins implicated in degradation and modification of polysaccharides (Larsson *et al.*, 2003; Jenkins *et al.*, 2004; Czerwinski *et al.*, 2005). Especially triple-stranded β-helices has been shown for the bacteriophage P22 and Sf6 TSPs (Steinbacher *et al.*, 1994; Müller *et al.*, 2008; Seul *et al.*, 2014) with the latter proteins already shown to share a homologous N-terminal domain with WceF. The N-terminal domains of P22 TSP and WceF superimposed with a RMSD of 5.5 Å (Figure 33, B). In P22 TSP this domain is known as the particle-binding domain connecting the TSP to the bacteriophage forming a dome-like structure in the trimer (Steinbacher *et al.*, 1994). In contrast, the β-helices of both proteins were more similar in their structure which superimposed with a RMSD of 1.3 Å in despite of the poor sequence identity in that region (Figure 33, A and Figure 30, respectively). Apparently, the overall fold is highly conserved throughout both protein species. As a distinguishing feature, WceF displayed a shorter β-helix and the β-helical loops lacked integrated α-helical elements.

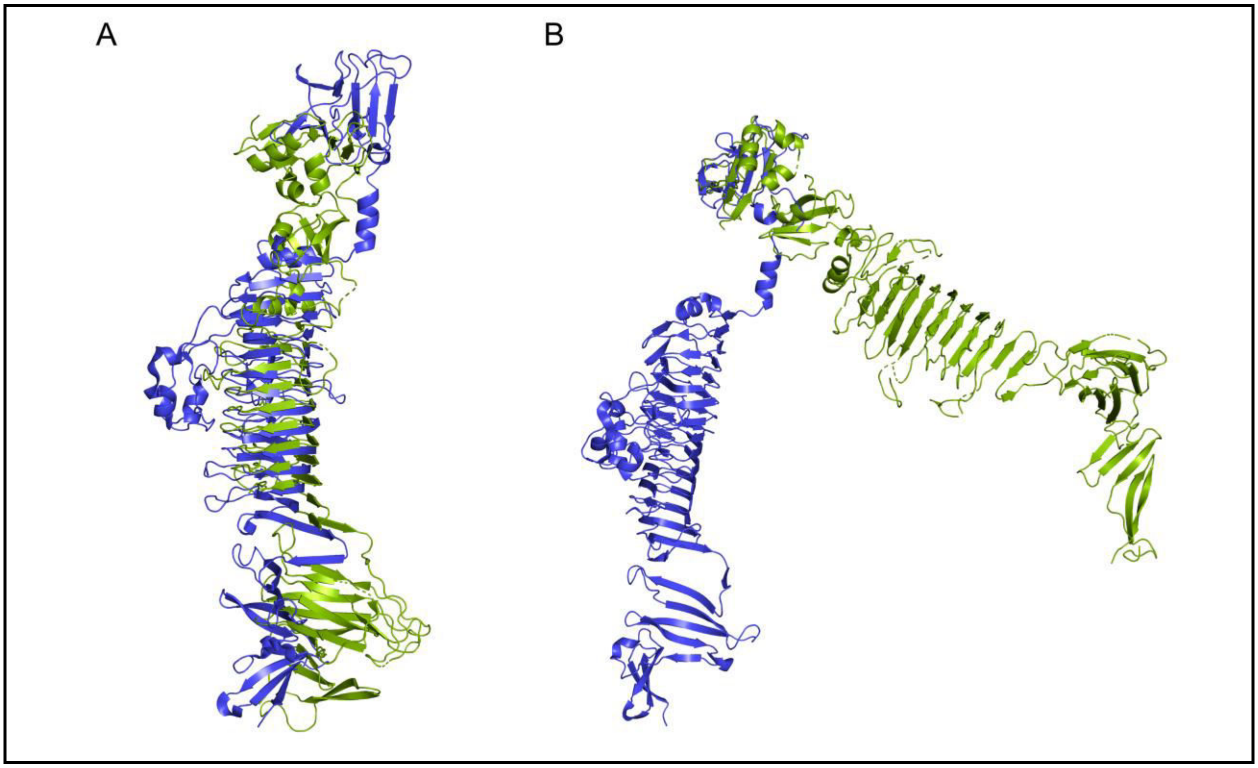

Figure 33: WceF superimposition with P22 TSP (pdb: 2XC1)
The sequences of (A) the β-helices of WceF (green), amino acids 269-527, and P22 TSP (blue), amino acids 141-543, and (B) of the N-terminal domains (WceF amino acids: 38-147, P22 TSP amino acids: 7-124) were superimposed with an root mean square deviation of 1.3 and 5.5 respectively. Protein structures are shown in cartoon representation.

4.3.2 WceF lacks the high Protein Stability

The three dimensional structure of WceF and bacteriophage TSPs showed a high similarity. The latter were found to be thermostable enzymes which ensure the infectivity of the bacteriophage even under extreme extracellular conditions. But TSPs slowly denature in the presence of detergents above temperatures of 70°C (Barbirz *et al.*, 2009). However, in spite of the trimeric β-solenoid structure, WceF denatured when incubated with 2 % (w/v) SDS at room temperature and migrated as a monomer in an SDS-PAGE (Figure 34). In comparison, P22 TSP is SDS resistant under these conditions and the trimer was detected (apparent molecular mass of 190 kDa), in agreement with previous results (Manning and Colón, 2004; Mishra *et al.*, 2007). Eventually, when heated to 100°C in 2 % SDS prior to electrophoresis the P22 TSP denatured to monomers.

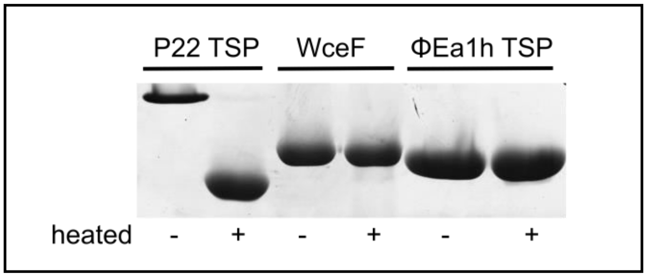

Figure 34: SDS-Resistance test of TSPs and WceF
Prior to the SDS-PAGE protein samples were incubated with SDS-PAGE sample buffer, including 2 % (w/v) SDS, at room temperature (-) or heated for 5 min at 100°C (+).The amount loaded for each protein species, P22 TSP, WceF and ΦEa1h TSP, was 2.3 µg.

Next, the stability of the trimeric interfaces of WceF was analyzed and compared to TSPs, in order to reveal potential structural differences which might explain the sensitivity of WceF towards SDS. Previous studies showed, that the C-terminal fragments of TSPs, constructs which lack the N-terminal phage-binding domain, account for the thermostability, protease and SDS resistance (Miller *et al.*, 1998a, 1998b; Kreisberg *et al.*, 2002; Freiberg *et al.*, 2003). Hence, the interfaces of the C-terminal parts of WceF and TSPs were compared (Table 7). WceF exhibits an interface area of 4998 Å which is higher than the interface area of P22 and ΦAB6 TSP. Similarly, WceF comprises more residues in the interface. Here, the C-terminal trimer is stabilized by 86 hydrogen bonds and 25 salt bridges. In contrast, the P22 TSP and ΦAB6 TSP interfaces exhibit around 65 hydrogen bonds and 11 salt interactions. Finally, the trimer association of WceF is more stable with a ΔG of -42.1 kcal · mol^{-1} than compared to the P22 TSP and ΦAB6 TSP interfaces with -36.2 kcal · mol^{-1} and -40.1 kcal · mol^{-1}, respectively. Hence, the stabilization of the trimeric oligomerization of WceF is similar to those of other TSP and thus do not account for differences in the resistance against SDS.

In addition, the comparison of the full-length proteins showed that the N-terminal domain of WceF and ΦAB6 TSP did not contribute to the stabilization of the trimeric associations (Table S2).

Table 7: Biophysical characterization of the interfaces of WceF and TSPs

The interface between the amino acid sequences of the C-terminal fragment (polypeptide chain from the β-helix to the C-terminus) for P22 (pdb: 2XC1) and ϕAB6 (pdb: 5JS4) were compared to WceF. Here the interface is defined as the area between two adjacent subunits.

	Interface of C-terminal fragments		
	WceF	**P22 TSP**	**ϕAB6 TSP**
amino acids	232-735	126-666	98-565
Chains forming the interface	E-F	A-B	A-C
Interface area / Å	4998	4170	4241
Number of residues in interface	140	115	118
Number of hydrogen bonds	86	65	64
Number of salt bridges	25	11	11
Solvation free energy ΔG	-42.1	-36.2	-40.1

4.3.3 Structure Prediction of the ΦEa1h Bacteriophage Tailspike Protein

The ΦEa1h bacteriophage is used in biocontrol agents against *Erwinia* and *Pantoea* species (Boulé *et al.*, 2011; Müller *et al.*, 2011; Schwarczinger *et al.*, 2017). It expresses a TSP (UniProt: Q9G072) which cleaves stewartan polysaccharide chains and consequently has been used in the elucidation of the stewartan monosaccharide structure (Nimtz *et al.*, 1996). No crystals could be obtained in crystallization attempts of the ΦEa1h TSP. Hence, the native three dimensional structure was predicted using the Phyre^2 server (Figure 35). With the full sequence of the ΦEa1h TSP, twenty structures were modeled based on sequence alignments with proteins from the Protein Data Bank. The results covered the first 339 amino acids of ΦEa1h TSP. The first three models (templates: rhamnogalacturonase from *aspergillus aculeatus (Petersen et al., 1997)*, exopolygalacturonase from *thermotoga maritima* (Pijning *et al.*, 2009) and bacteriophage Φ29 gp 12 (Xiang and Rossmann, 2011) revealed a central parallel three stranded β-helix which differed in the number of coils and consequently in the length of the β-helix. Similar to the previous described structures of WceF and P22 TSP an α-helix lies on top of the β-helical structures to seal the helical interior.

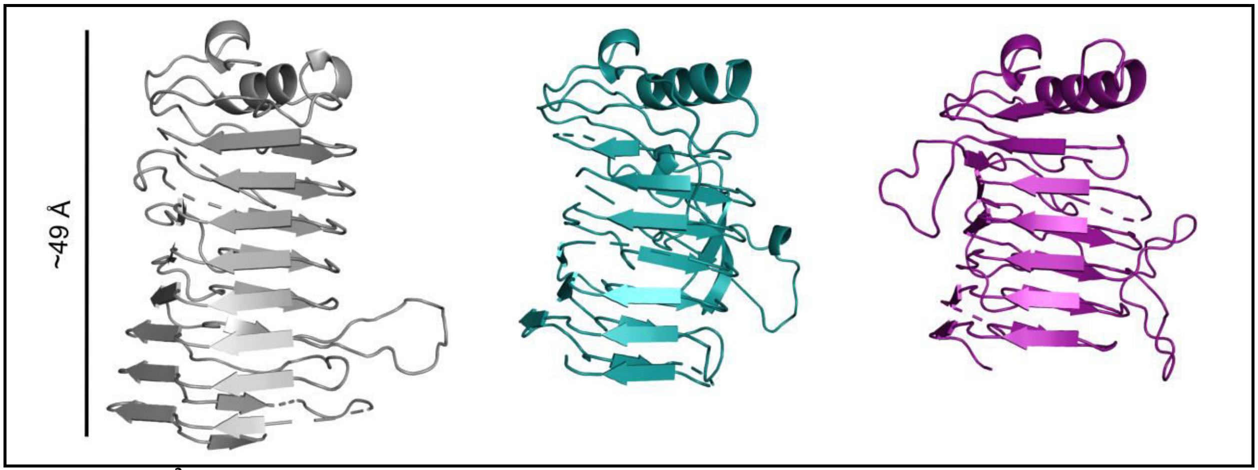

Figure 35: Phyre^2 structure prediction of the ΦEa1h TSP β-helix

Three models predicted a central β-helix for the amino acids 82-323 (grey), 75-316 (cyan) and 83-318 (purple) with confidences of 98.9 %. Predictions are shown in cartoon representation.

At the N-Terminus a four stranded Greek key motif was predicted (confidence 99.3 %) based on the template structure of TSP 2 from bacteriophage cba120 (Plattner *et al.*, 2018). The order of β-strands was found to be highly identical to the Greek key motif of WceF and both structural motifs highly superimposed with a RMSD of 0.62 Å (Figure 36, A and B). Additionally, the β-helical structures of both proteins overlap with a RMSD of 1.80 Å (Figure 36, C). Nevertheless no particle-binding domain was predicted as seen in WceF and other TSP (Seul *et al.*, 2014; Lee *et al.*, 2017).

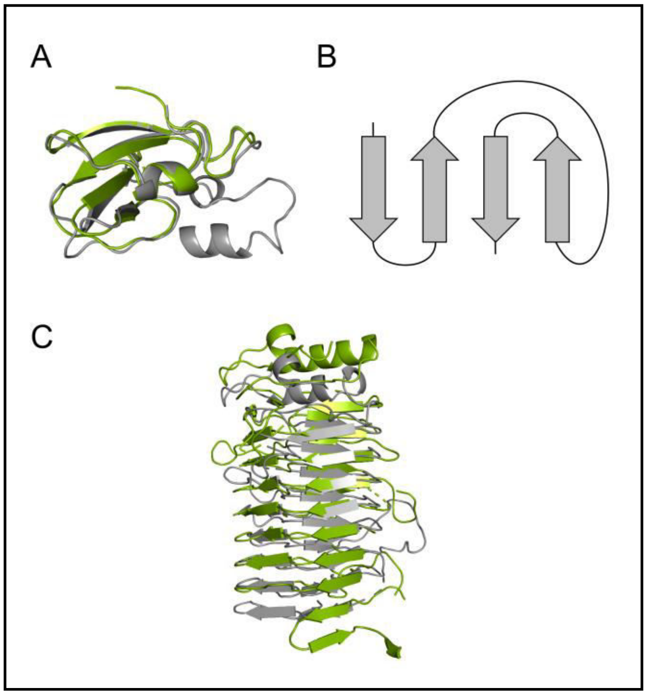

Figure 36: Superimposition of the Phyre^2 predicted structure of ΦEa1h TSP with WceF

The protein structures are shown in cartoon representation of (A) the Greek key motif of WceF (green, amino acids 148-234) and a model of the N-terminus of ΦEa1h TSP (grey, amino acids 14-106, Phyre^2 confidence: 99.3) sharing (B) the same Greek key topology. (C) Superimposition of the β-helices of WceF (green, amino acids: 269-527) and the model of ΦEa1h TSP (grey, amino acids: 82-323, Phyre^2 confidence: 98.9 %) with root mean square deviations of (A) 0.62 Å and (C) 1.80 Å respectively.

Hence, the fold of the ΦEa1h TSP is highly similar to the three dimensional structure of WceF and other TSPs. Additionally, it oligomerized into trimers as confirmed by size exclusion chromatography (Figure S19). Nevertheless, in agreement with WceF the ΦEa1h TSP showed no SDS resistance at room temperature (Figure 34).

4.3.4 WceF and the ΦEa1h TSP are Stewartan-Specific Glycosidases

TSPs have been shown to cleave bacterial surface exposed glycan structures which results in small oligosaccharide fragments as products of the digestion (Barbirz *et al.*, 2008; Schulz *et al.*, 2010; Lee *et al.*, 2017). In case of a biofilm forming bacterial culture this enzymatic activity can be beneficial for the bacteriophage in order to pass the biofilm barrier in fulfillment of the infection process. WceF shares the domain architecture as found for TSPs (see section 4.3.1). Consequently, in analogy to TSPs, WceF was incubated with isolated stewartan, which is the most abundant component in *P. stewartii* biofilms (Roper, 2011), at 10°C (Figure 37). Indeed, WceF accepted the ExoPS as a substrate and furthermore cleavage of stewartan was seen in an increase in reducing ends over time. Here, an initial moderate rise in cleavage of stewartan took place, but after around 225 h the reaction accelerated and a higher number of reducing ends up to 0.4 mM were produced. Reactions without stewartan or WceF showed no increase in reducing ends which therefore ruled out any unspecific cleavage of the stewartan ExoPSs. As supposed, WceF binds and cleaves stewartan over a time period of 300 h (12.5 days). These results were compared to a stewartan digestion by the *Erwinia* Phage ΦEa1h TSP. Here, the ΦEa1h TSP cleaved stewartan at significantly higher velocity than WceF. The number of reducing ends immediately increased with the addition of TSP and rose up to 0.3 mM in 0.5 h, at which the reaction slowly saturated.

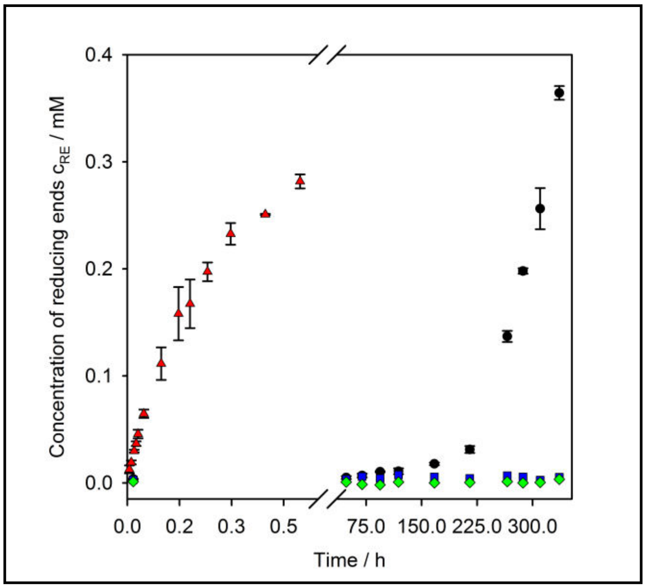

Figure 37: Stewartan digestion by WceF and ΦEa1h TSP
1 mg · mL^{-1} stewartan was incubated with 1.2 µM WceF (black) or 141 nM ΦEa1h TSP (red) at 10°C. Reducing ends were analyzed over the reaction time using the MBTH-test. Reactions without WceF (green) or without stewartan (blue) served as controls.

4.3.5 Enzymatic Stewartan Degradation at Different Temperatures

The hydrolysis of stewartan by WceF at 10°C was shown to be a slow process (Figure 37). The activity of WceF towards stewartan was increased by rising the temperature to 30°C (Figure 38). Here, reducing ends were formed roughly after 75 h. It was further noticed, that the reducing end kinetic followed an exponential increase. No saturation in the formation of reducing ends was seen on this time scale and most likely, an even longer time period need to be investigated to see the completion of the reaction. It became apparent, that at low temperatures the stewartan degradation is sufficiently slowed down to reveal separate kinetic regimes. To derive an estimation about the reaction velocity at different temperatures the slope of these isolated kinetic regimes were analyzed. Consequently, the reducing end formation in the time interval of 225 h to 300 h is characterized with a $k_{cat,app}$ of $0.044\ U \cdot \mu mol^{-1}$. As expected for the stewartan degradation at higher temperatures, the turnover number at 30°C increases to $k_{cat,app} = 0.085\ U \cdot \mu mol^{-1}$.

In addition, the degradation of polymers has also been described by zeroth order kinetics (see section 3.2.6) (Hjerde *et al.*, 1996; Tayal *et al.*, 1999; Tømmeraas and Melander, 2008). A physical explanation has been given as at the beginning of the reaction, sufficient substrate is available to form an enzyme-substrate complex (Tayal *et al.*, 1999; Li *et al.*, 2004). Increasing the number of substrate will not result in an increase of substrate-bound enzyme complexes and thus an increase in the reaction velocity. Supportingly, it is here assumed that stewartan has a weight-average molecular weight of 3 MDa (Schollmeyer *et al.*, 2012). This would yield a polymer of roughly 3000 RUs or hydrolysable bonds. Indeed, a stewartan concentration of $1\ mg \cdot mL^{-1}$ would then equal approximately 3 mM substrate bonds, which is in contrast to 1200 mM WceF. Hence, the initial stewartan hydrolysis kinetic is presumably independent of the substrate concentration and was consequently fitted with a zeroth order kinetic rate law. With this, the apparent rate constants $k_{0,app}$ of $6.15\ mM \cdot h^{-1}$ and $3.18\ mM \cdot h^{-1}$ for the stewartan hydrolysis at 30°C and 10°C, respectively, were obtained. The latter, when normalized to the enzyme concentration and expressed in Units, are similar to the turnover numbers $k_{cat,app}$ obtained by the classical Michaelis-Menten kinetic analysis.

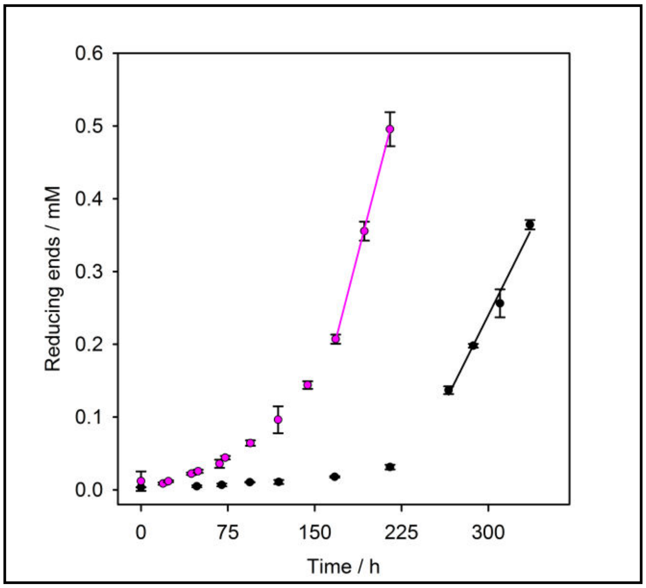

Figure 38: Stewartan digestion by WceF at different temperatures

1 mg · mL^{-1} stewartan was digested by WceF at 10°C (black) or 30°C (purple). Reducing ends were analyzed over the reaction time using the MBTH-test. The apparent turnover number or rate constants were determined from the slopes of separate kinetic regimes.

In contrast to the hydrolysis kinetics of WceF, the ΦEa1h TSP is a very efficient stewartan depolymerase at 10°C (Figure 39, A). The apparent turnover number $k_{cat,app}$, as determined from the slope of the plot of reducing end concentration against the time, was 149 U · µmol^{-1}. The same analysis was applied to the stewartan degradation by the ΦEa1h TSP at 30°C (Figure 39, B) and $k_{cat,app}$ with a value of 307 U · µmol^{-1} was determined. Hence, the stewartan hydrolysis of the ΦEa1h TSP is approximately 3300 to 3600-fold faster at 10°C and 30°C, respectively, than compared to WceF.

In addition, the stewartan hydrolysis by the ΦEa1h TSP at 30°C saturated approximately after 0.5 h (Figure 39, B). However, after the reaction resided for about 50 h in saturation, an additional increase in the enzymatic activity was seen. This additional increase is characterized with an apparent turnover of 0.27 U · µmol^{-1}. Consequently, the cleavage of stewartan by the ΦEa1h TSP at 30° is marked by a first fast hydrolysis of the ExoPS which precedes a second slower stewartan degradation.

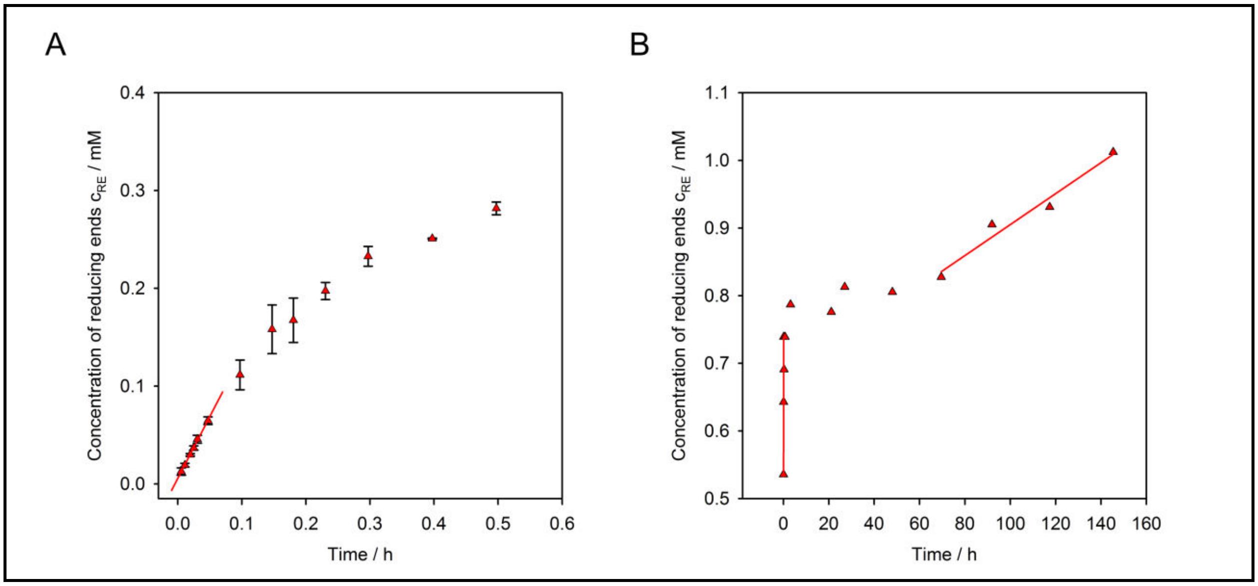

Figure 39: Kinetic analysis of the stewartan digestion by the ΦEa1h TSP
1 mg · mL^{-1} stewartan was digested by ΦEa1h TSP at (A) 10°C and (B) 30°C. Reducing ends were analyzed over the reaction time using the MBTH-test. The apparent turnover number or rate constants were determined from the slopes of the increase in reducing ends.

4.3.6 WceF and ΦEa1h TSP Produce Similar Oligosaccharide Fragments

Cleavage of glycan structures by TSPs produced oligosaccharide fragments which were analyzed by means of SDS-PAGE, size-exclusion chromatography or capillary electrophoresis (Andres *et al.*, 2013; Broeker *et al.*, 2018; Kunstmann *et al.*, 2018b). In agreement, the reaction products of the stewartan degradation at 30°C were analyzed using size-exclusion chromatography (Figure 40). In case of the degradation reaction of WceF an increase in reducing ends was already visible from 30 h (up to 80 h). At specific time points, samples of the reaction were stopped by 0.5 M NaOH and applied to size-exclusion chromatography. The large excess of NaOH caused large changes of the refractive index at the migration front (around 18-20 mL) (Figure S21). In rare cases, the NaOH also accounted for signals around an elution time of 17 mL. However, the signals which originated from the stewartan oligofragments were detected at retention volumina of 10 - 16 mL and were not disturbed by the NaOH signal (Figure 40). Throughout the reaction single RUs (as verified by mass spectrometry, Figure S23), which eluted at 15 mL in size-exclusion chromatography, as well as oligosaccharide fragments of larger size (around 10 mL) were produced. The actual amount of each species increased during the reaction time. Reactions without WceF showed no products formed during the incubation (Figure S21). Stewartan digestion by the ΦEa1h TSP at 30°C over a time of 150 h was found to be biphasic (Figure 39, B). In the first 30 min the production of reducing ends saturated and in agreement, as confirmed with mass spectrometry (Figure S20), one and two RUs with a retention volume of 15 and 14 mL, respectively, were produced in this time period (Figure 40, B). Larger fragments were also seen at retention volumina of 10-12 mL. The respective signals of the latter consisted of different oligosaccharide species which were not completely baseline separated in these experiments. These signals disappeared before the hydrolysis reaction completely saturated and thus more one and two RUs were produced. As soon as after 50 h the additional increase in reducing ends took place, more one and two RU species were formed (Figure 40, B). Hence in this time period, long stewartan chains, which were not resolved by size-exclusion chromatography, were digested to the latter two species.

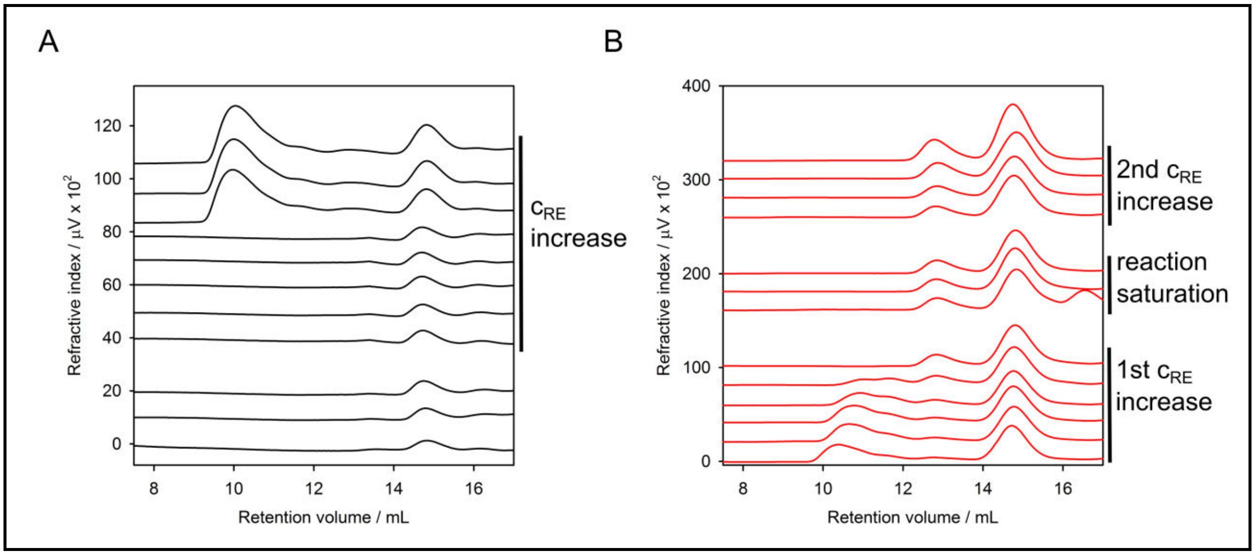

Figure 40: Size-Exclusion Chromatography analysis of stewartan degradation by WceF and ΦEa1h TSP

1 mg · mL^{-1} stewartan was digested at 30°C by (A) WceF or (B) the ΦEa1h TSP. The curves for the reducing end formation over time are shown in Figure 38 and Figure 39. Samples from the hydrolysis reaction were stopped at different time points with NaOH. Afterwards, the inactivated samples were loaded on a Superdex^{TM} peptide 10/300 and the stewartan oligosaccharide products formed during the reaction analyzed. Time points in the stewartan degradation by WceF were 24 h, 44 h and 49 h, 68 h, 73 h, 94 h, 118, 144, 168, 193 h, 215 h (Figure 38). In case of the stewartan cleavage by the ΦEa1h TSP the time points 0.04 h, 0.08 h, 0.1 h, 0.3 h, 0.7 h, 3.1 h and 21 h, 27 h, 48 h and 70 h, 92 h, 117 h, 145 h were chosen (Figure 39). Each reaction is marked by different phases in the reducing end (c_{RE}) formation which are indicated.

During the stewartan digestion, WceF as well as ΦEa1h TSP produced different lengths of RU oligosaccharides. These fragments were further analyzed by capillary electrophoresis to provide a better resolution (Figure 41). Due to the different cleaving velocities of WceF and ΦEa1h TSP the oligosaccharide products were compared after different reaction times, 197 h and 6 min for WceF and ΦEa1h TSP, respectively. At 30°C, WceF produced oligosaccharides species at 5.4, 6.0, 6.3, 6.6 and 6.9 mL (Figure 41, A). The first two species were assigned to one and two RU, respectively, using purified standards of each oligosaccharide (Figure S20). The separation of different sized oligosaccharides with identical mass-to-charge ratio in capillary electrophoresis follows a linear dependence of the retention time to the logarithm of the molecular mass (Werner *et al.*, 1993; Guttman *et al.*, 1994). Assuming the other signals originate from three, four and five RU fragments, this dependency is given (Figure 41, B and Figure S22). The same products were found for stewartan digestion by the ΦEa1h TSP already after 6 min, again reflecting the high activity of the TSP against stewartan. Consequently, the capillary electrophoresis profile of stewartan digestion by WceF to the electropherogramm of ΦEa1h TSP-stewartan-cleavage and (one and two) RUs standards were highly similar. Therefore, WceF is likely to by an endogalactosidase and cleaves the β-D-Gal^{III}(1→3)-α-D-Gal^{I} linkage between the stewartan repeating units.

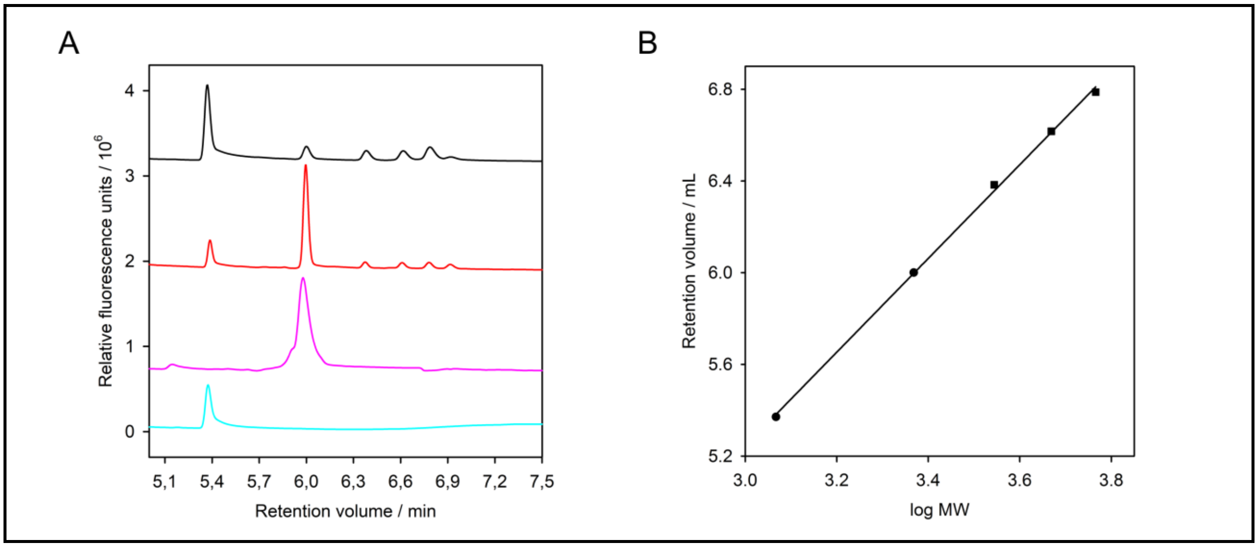

Figure 41: Capillary electrophoresis analysis of the stewartan digestion by WceF or ΦEa1h TSP
(A) 1 mg · mL^{-1} stewartan was digested with WceF for 197 h (black) or ΦEa1h TSP for 0.5 h (red) and oligosaccharide fragments were fluorescently labeled to enable capillary electrophoresis. Purified one RU (cyan) and two RU (purple) were loaded as standards. (B) The retention volumes of each oligosaccharide species was determined and plotted against the logarithm of its molecular weight (one and two RU, circles) or the molecular weight was assumed to be three, four and five RU (squares).

4.3.7 Activity Profiles of WceF and ΦEa1h TSP at Different Conditions

Finally, beside the difference in the hydrolysis velocity (Figure 37), the activity of both enzymes under different conditions was investigated. The stewartan digestion by WceF is highly dependent on the NaCl concentration (Figure 42, B). The highest activity is reached at a moderate concentration of 50 µM NaCl and consequently dropped with increasing NaCl concentrations. Furthermore, WceF showed an activity only at a pH of 5 and did not cleave stewartan at other pH values (Figure 42, A). In contrast, the ΦEa1h TSP showed enzymatic activity throughout a broad range of NaCl concentrations (50-500 µM) and pH values (5 – 9.5) (Figure 42).

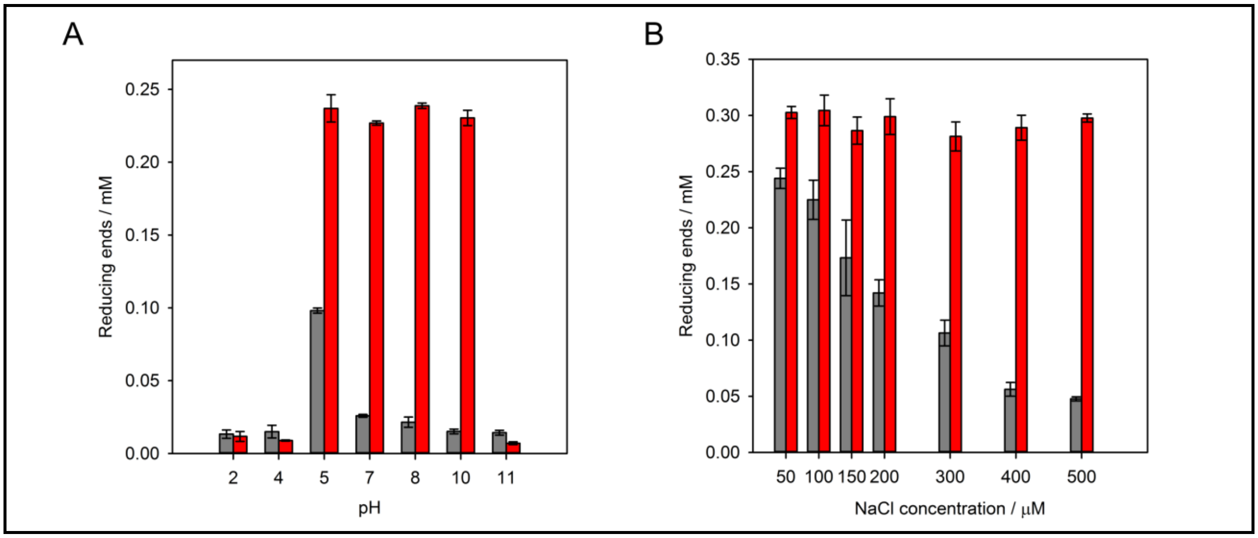

Figure 42: Stewartan degradation under different conditions
1 mg · mL^{-1} stewartan was digested at 30°C by WceF for 120 h (grey) or ΦEa1h TSP for 72 h (red) at different (A) pH and (B) NaCl concentrations. Reducing ends were analyzed over the reaction time using the MBTH-test. Measurements were done in triplicates and errors are shown as standard deviation.

Next, the influence of the confinement of the stewartan matrix on the diffusion of WceF and ΦEa1h TSP was investigated. Again, the stewartan degradation activity of both proteins was analyzed after different incubation times (WceF: 120 h, ΦEa1h TSP: 24 h). WceF produced reducing ends up to 0.3 and 0.4 mM at 1 and 5 mg · mL^{-1} of the ExoPS, respectively, but showed a reduced activity at 10 mg · mL^{-1} stewartan (Figure 43). In contrast, the ΦEa1h TSP already cleaved stewartan to RU concentration of around 0.4 mM when incubated with 1 mg · mL^{-1} stewartan or 10 mg · mL^{-1} stewartan. Still, the ΦEa1h TSP has the highest activity in 5 mg · mL^{-1} stewartan.

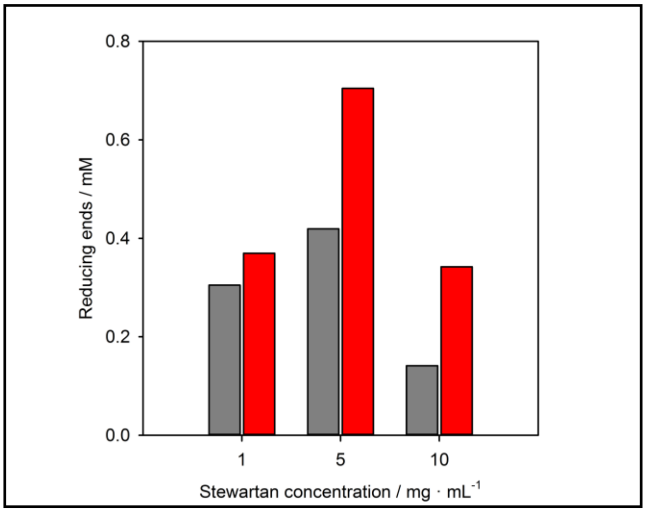

Figure 43: Stewartan degradation at different stewartan concentrations
Stewartan with different concentrations was digested at 30°C by WceF for 120 h (grey) or with the ΦEa1h TSP for 72 h (red). Reducing ends were analyzed over the reaction time using the MBTH-test

4.3.8 Characterization of Enzymatic Remodeling of the Stewartan Matrix

FCS experiments with fluorescently labeled WceF were conducted to clarify if the reduced activity of WceF in highly concentrated stewartan solutions arose from a reduced diffusion. Indeed, in 10 mg · mL^{-1} stewartan, WceF immediately associated into spherical protein aggregates (Figure 44, B). The fluorescently labeled WceF formed clusters or even clumps as seen by intense fluorescent spots. The sizes of these cluster ranged from around 5 µm (low dense clumps) to 1.5 µm (tightly packed aggregates). A similar picture emerges from the analysis of the aggregation behaviour of WceF in 1 mg · mL^{-1} stewartan (Figure 44, A). Here, the number of spots of fluorescent crosslinked WceF populations is lower than compared to the WceF clusters in 10 mg · mL^{-1} stewartan but in contrast they exhibit larger sizes. The latter ranged from approximately 3 µm to 10 µm. Presumably, less stewartan interaction sites for WceF are provided in stewartan solutions with a low ExoPS density which results in a decreased number of clusters. However, to a much lower extent, aggregation of WceF was also seen in pure buffer solutions. Hence, WceF is slightly prone to undergo aggregation under these conditions which is enhanced by the presence of the ExoPS stewartan. It is to note here, that the images of fluorescently labeled WceF were taken with different magnifications.

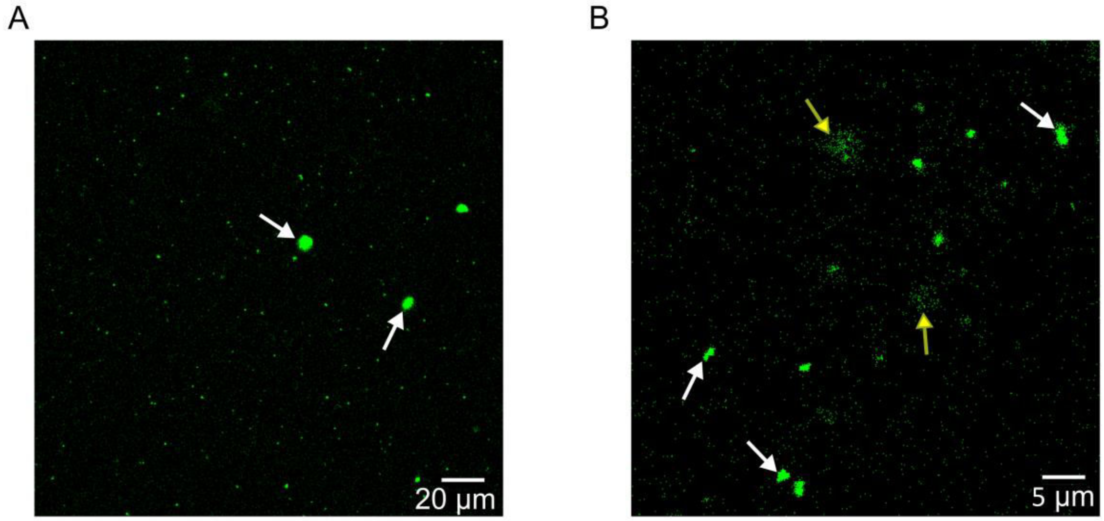

Figure 44: Characterization of the diffusion of WceF molecules in the stewartan network
WceF was fluorescently labeled and incubated with (A) 1 mg · mL^{-1} or (B) 10 mg · mL^{-1} stewartan. Examples of WceF clusters are denoted by yellow (low density clumps) or white (high density aggregates) arrows.

When ΦEa1h TSP was added to stewartan solutions of high concentration (10 mg · mL^{-1}), the stewartan ExoPSs were cleaved in an exponential manner and the reaction saturated after 30 min at around 400 mM RUs (Figure 45, B). The standard deviations, compared to stewartan digestions at lower ExoPS concentrations, were considerably higher. The latter might result from errors due to pipetting with highly viscous stewartan solutions. The apparent rate constant $k_{0,app}$ was determined with 102 U · h^{-1} (Figure 45, B). Hence, the degradation of 10 mg · mL^{-1} stewartan was slightly slower than the hydrolysis of the ExoPS in 1 mg · mL^{-1} stewartan solutions which was caused due to an increased diffusional restriction of the reaction. In contrast to WceF, no aggregates of ΦEa1h TSP proteins were seen (Figure 45, A). Instead, the confinement to the diffusion experienced by the ΦEa1h TSP proteins and 64 nm PS microspheres was already released after 0.1 h (6 min) and 0.8 h (48 min), respectively (Figure 45, C). The anomaly exponent for the diffusion of 64 nm beads increased from sub- to normal Brownian diffusion (α from 0.75 to around 1) (Figure 45, D). Hence, ΦEa1h TSP enzymatically cleaved the stewartan polymers and eliminated the associated ExoPS matrix confinements. To note, the fluorescent label did not influence the enzymatic activity of the ΦEa1h TSP as confirmed by a comparison of a stewartan hydrolysis with the native enzyme (Figure S24).

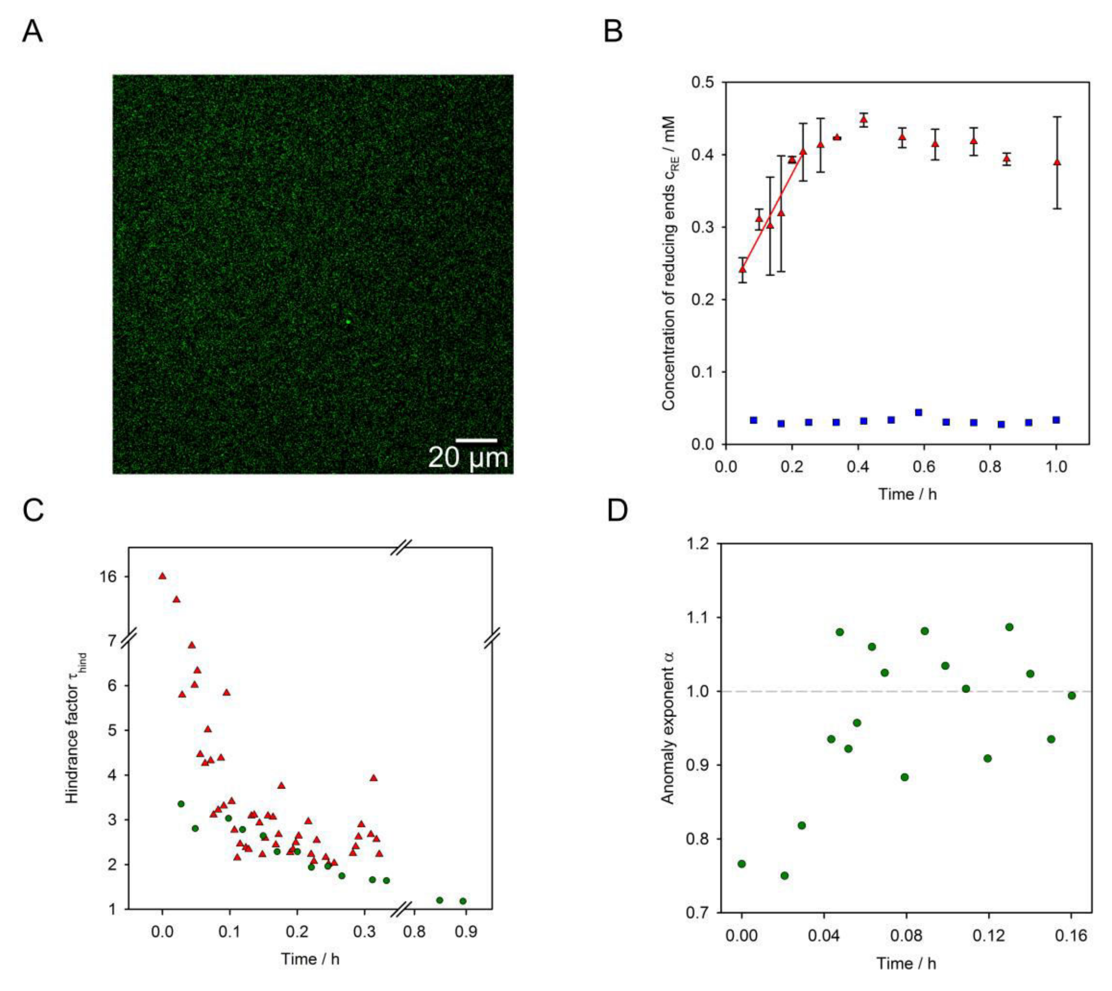

Figure 45: Elimination of the stewartan matrix confinement by the ΦEa1h TSP

10 mg · mL^{-1} stewartan were incubated with the ΦEa1h TSP. (A) Snapshot of the diffusion of fluorescently labeled ΦEa1h TSPs in the stewartan lattice. (B) The production of reducing ends was followed over time using the MBTH-test (red) and a reaction without ΦEa1h TSP (blue) served as control. (C) The hindrance factor and (D) anomaly exponent α were analyzed for the diffusion of ΦEa1h TSP (red) or 64 nm PS microspheres (green).

The loss of the intrinsic confinements of the stewartan matrix due to the ExoPS digestion of ΦEa1h TSP was investigated for 64 and 193 nm PS microspheres over a broad range of stewartan concentrations (Figure 46). As expected, after 1 h incubation with the ΦEa1h TSP the hindrance factor was reduced to almost no hindrance (τ_{hind} ~ 1) (Figure 46, A). In the same way, the anomaly exponent increased to unity (Figure 46, B). Consequently, the ΦEa1h TSP effectively reduces diffusion hindrances independent of the density of the stewartan hydrogel network.

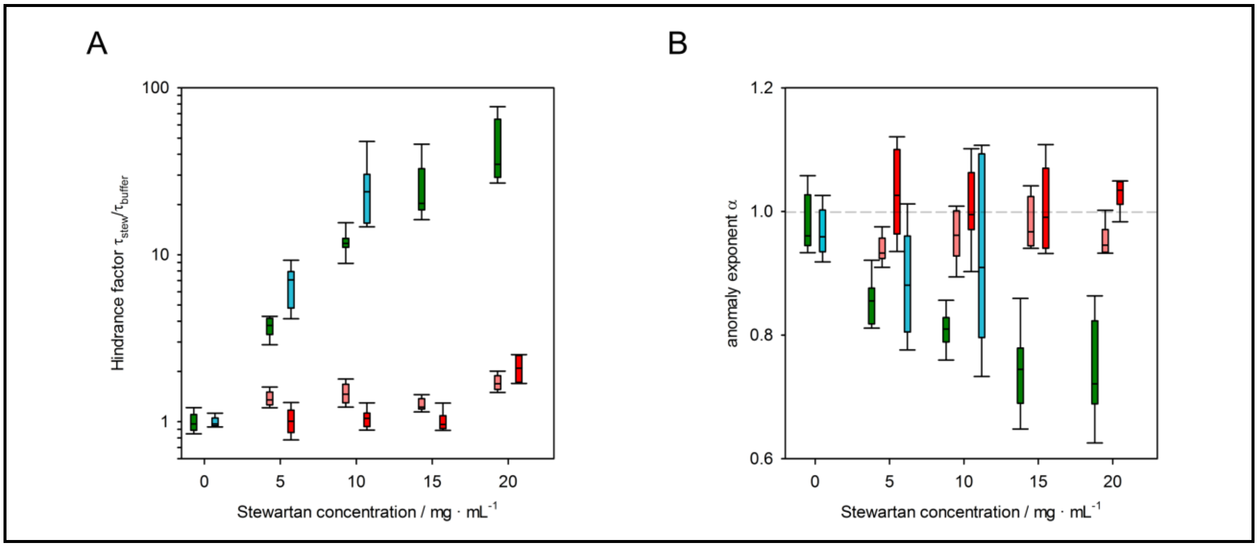

Figure 46: Diffusion of fluorescent particles at different stewartan concentrations after the addition of ΦEa1h TSP

The diffusion of PS beads was analyzed with (A) the hindrance factor and (B) the anomaly exponent α before (PS beads: 64 nm, green, and 193 nm, blue) or after 1 h (PS beads: 64 nm, light red, and 193 nm, red) incubation with the ΦEa1h TSP.

5. Discussion

5.1 Physicochemical Characterization of the Stewartan Network

Bacterial ExoPSs are highly soluble polymeric entities (Sutherland, 2001a; Miao *et al.*, 2015; Insulkar *et al.*, 2018; Yang *et al.*, 2018), which can form large networks (Ganesan *et al.*, 2013; Chalykh *et al.*, 2017; Schneible *et al.*, 2019) or even crystalline supracellular structures (Fang and Catchmark, 2015; Giese *et al.*, 2015). In this work, stewartan was purified from *P. stewartii* biofilms and the ExoPS formed networks which impeded the diffusion of fluorescent particles up to a factor of 60 (compared to free diffusion in buffer). This impaired diffusion was shown to be dependent on the size of the tracer molecule and pH of the buffer solution. A detailed discussion on the diffusion behaviour can be read below (see section 5.4). In this work, the flow behaviour of purified long-chained stewartan was investigated. Two separate regimes were found in a plot of the specific viscosity/ specific hindrance against the stewartan concentrations. These crossovers in the flow behaviour of polysaccharides were used as a mechanical description of the association of the polymers (Arvidson *et al.*, 2006; Poinot *et al.*, 2014; Ganesan *et al.*, 2016). A transition point c_t was determined at a concentration of 7 mg · mL stewartan. As found for other ExoPSs the commonly observed transition from c^1 to $c^{2\text{-}3.7}$ scaling regimes is indicative for a crossover from semidilute nonentangled to semidilute entangled solutions ($c_t = c_e$ with c_e = critical entanglement concentration) (Heo and Larson, 2005; Mitsumata *et al.*, 2013; Ganesan *et al.*, 2016). ExoPSs, which exhibit charged or hydrophobic modifications, undergo a transition of flow behaviour at similar c_t's due to increased interchain associations (Akiyama *et al.*, 2007; Nyström *et al.*, 2009; Ganesan *et al.*, 2013). Additionally, rheological investigations of ExoPSs described a critical coil overlap concentrations c* (the point of interpenetration of polymers) which is usually found roughly at the point where the viscosity is half till twice the solvent viscosity (Krause *et al.*, 2001; Desbrieres, 2002; Wyatt and Liberatore, 2009). However, due to a small resolution of data points in the range of 0 to 0.5 mg · mL^{-1} stewartan, the c* for polymeric stewartan solutions was not determined in this work.

The here reported magnitude of the scaling regimes and position of the transition points imply rather disordered and flexible stewartan solutions (Arvidson *et al.*, 2006) which is supported by multiple combinations of stereochemical configurations and linkage patterns in stewartan. In contrast the solution regimes of highly stabilized supramolecular structures or dense hydrogels of polysaccharides showed early overlap transitions and semidilute regimes with steep slopes (up to exponents of c^9) (Desbrieres, 2002; Arvidson *et al.*, 2006). Typically, these types of polysaccharides lack a highly branched molecular structure (e.g. chitosan, levan). Here, oligosaccharide side-chains were generally shown to promote conformational flexibility and negatively influence the tight packing of polysaccharide chains into higher three dimensional assemblies (Tako and Nakamura, 1985, 1986; Christensen *et al.*, 1995; Tuinier *et al.*, 2001; Schuster *et al.*, 2012). In addition, the negative repulsion from the carboxyl groups as found for stewartan need to be overcome in order to tightly associate. These negative charges are prone to be bridged by polyvalent ions or display nonspecific binding sites for proteins which may lead to crosslinked polysaccharide gels with increased mechanical stability (Seviour *et al.*, 2012; Tielen *et al.*, 2013; Azeredo and Waldron, 2016; Chalykh *et al.*, 2017; Nakauma *et al.*, 2017). Hence, the intrinsic stewartan monosaccharide sequence governs the physical parameter of its own solutions and due to the branched flexible structure prevents the formation of tightly packed networks. This might display an advantageous characteristic in the early steps of the *P. stewartii* biofilm formation. Herrera *et al* showed that the surface motility of *P. stewartii* cells is critical for microcolony formation and pathogenicity (Herrera *et al.*, 2008). Consequently, a strong confining ExoPS network and thus a highly viscous extracellular medium would therefore probably impede with the intercolony migration which is linked to biofilm-specific cell aggregation.

Stewartan from *P. stewartii* was shown to consist of chains with a high degree of polymerization with a molecular weight around 1-4 MDa (~ 1000-4000 RUs) (Schollmeyer *et al.*, 2012). Additionally, 20 RU stewartan was simulated in CG MD simulations for 100 ns. The final three dimensional structure contained stewartan chains which transiently formed weak interchain contacts. Hence, this system represents a stewartan solution in the dilute regime. Likewise, the stewartan hydrogel swelled with increasing water content, resulting in a more diluted polymer solution. However, the chain length of polysaccharides is an important factor which governs the properties of an exopolysaccharide network (Arvidson *et al.*, 2006; Galván *et al.*, 2013; Ganesan *et al.*, 2013). Hence, differences in the physiochemical characteristics between 20 RU (CG MD simulation) and 4000 RU stewartan solutions are expected. In addition, the likelihood of entanglements increases with the chain length (Heo and Larson, 2005; Ganesan *et al.*, 2016) and thus is unlikely to be seen in CG 20 RU stewartan simulations.

5.2 The Stewartan Network in *Pantoea stewartii* Biofilms

The physicochemical analysis of stewartan solutions was done with the isolated stewartan from *P. stewartii* biofilms. However, the extracellular matrix contains several other biomolecules, which will additionally influence the mechanical response of the surrounding medium. For example, the protein and polysaccharide components of the extracellular matrix of *E. coli* AR3110 form a dense composite material (Serra *et al.*, 2013a; Serra *et al.*, 2015). Here, cellulose provided filamentous connections between the cells, whereas curli protein fibers formed cell surrounding "baskets" (Serra *et al.*, 2013a). Consequently, brittle biofilm cryosection were obtained from bacterial mutants, which were deficient in the cellulose production. Hence, the here presented results have to be considered as an estimate of the whole biofilm properties, but as a very close approximation, as stewartan is the most abundant component and major virulence factor in *P. stewartii* biofilms (Nimtz *et al.*, 1996; Herrera *et al.*, 2008; Roper, 2011). Additionally, it is to note here, that the diffusion experiments in this work were not conducted at conditions similar to those provided by the lumen of the xylem, which is a rich pool of different salts (van Ieperen, 2007; Nardini *et al.*, 2011). For example, the ionic strength was found to be important in modulating the physicochemical properties (e.g. viscosity) of the ExoPS solution (Orgad *et al.*, 2011; Morrow *et al.*, 2015; Torres *et al.*, 2015; Yu *et al.*, 2017). Consequently, more work has to be done in characterizing the influence of ions on the viscoelastic properties of stewartan.

The average stewartan concentration of around 15 $mg \cdot mL^{-1}$ was calculated in this work for 65 h old biofilms, a concentration which is above the critical entanglement concentration. Nevertheless, in these experiments, the ExoPS concentration is averaged over the entire biofilm and did not consider biofilms as rather heterogeneous structures with respect to the density of the extracellular matrix (Lawrence *et al.*, 2007; Xiao and Koo, 2010; Chew *et al.*, 2014; Mosquera-Fernández *et al.*, 2016). The lowest concentration of the extracellular material is usually found at the periphery of the biofilm assembly (Abedon, 2016; Vidakovic *et al.*, 2018). Therefore, *P. stewartii* biofilms may exhibit regions of high stewartan concentrations (close to the bacterial cells) which are characterized by a non-Newtonian fluid with entangled polysaccharide polymers whereas other areas might display a rather dilute flow behaviour of stewartan below the transition concentration of 7 $mg \cdot mL^{-1}$.

5.3 Limitations and improvements of the coarse-grained stewartan model

In this work, a stewartan CG model was derived from an all-atomistic MD simulation in a hybrid approach by obtaining bonded and nonbonded potentials using the force matching method and Boltzmann inversion, respectively. This strategy was shown to successfully reproduce the atomistic configurations in cellulose and chitosan systems (Sauter and Grafmüller, 2017; Schneible *et al.*, 2019). In agreement, the RDFs of the CG stewartan system highly overlay with those of the atomistic reference system. However, the simulations of CG stewartan often crashed which might be a result of an overdetermination of the interactions in the CG stewartan model. Hence, too many bonded potentials were used to coarse-grain stewartan which most likely overconstrained the flexible nature of the ExoPS. For that reason, it is proposed here, to adopt the choice of bonded potentials to the stereochemistry of each specific glycosidic linkage types. The overdetermination of bonded potentials was also seen, when the distribution functions of the CG model were compared to the atomistic analogue. Here, the calculation of bonded potentials by Boltzmann inversion sometimes overestimated the main maximum in the angular or dihedral distributions whereas secondary maxima were poorly represented. This behaviour was also recognized in other studies when using Boltzmann inversion (Hynninen *et al.*, 2011; Sauter and Grafmüller, 2017). However, it is important to mention, that the distribution functions of the atomistic and CG stewartan systems in this work are generally in excellent agreement. Particular distributions could be improved by an iterative refinement of the Boltzmann inversion derived potentials (iterative Boltzmann inversion) (Moore *et al.*, 2014; Choudhury *et al.*, 2016; Li *et al.*, 2016) where the limitations of Boltzmann inversion, such as the sensitivity to environmental parameters (density, temperature or neighbour CG sites), are overcome (Markutsya *et al.*, 2013; Moore *et al.*, 2014; Fan and Maranas, 2015).

Furthermore, the charged interactions between the CG glucoronic acid residues were less well sampled in CG stewartan in agreement with the all-atomistic model. The extension of the CG model to an eight bead mapping scheme further improved the charged interactions. Although, other suggestions might additionally refine the force matching of the charged potentials. First, the mapping of the CG sites on the center of charge (instead of center of mass) of the underlying group of atoms resulted in a better description of the coulomb interactions (Cao and Voth, 2015; Dannenhoffer-Lafage *et al.*, 2019; Jin *et al.*, 2019). Secondly, the potential of mean force provides a description of the atomistic model and in CG simulations intra- and intermolecular potentials are added pairwise to give an approximation of the potential of mean force (Das and Andersen, 2009; Dunn *et al.*, 2016). The calculation of separate CG potentials derived from the atomistic Lennard-Jones or Coulomb interaction, which can be further modified, might also contribute to an additional improvement of the charged interactions (Dannenhoffer-Lafage *et al.*, 2019). Thirdly, electrostatic interactions are screened by the surrounding solvent and ions (Wu *et al.*, 2010; Ingólfsson *et al.*, 2014; Lafond and Izvekov, 2018). Therefore, many-body CG interactions have been introduced which recover the potential of mean force with increased accuracy (Das and Andersen, 2012; John and Csányi, 2017).

5.4 Stewartan Chain Dynamics and Consequences for the Diffusion of Biomolecules

Many studies focused on the description of the diffusion dynamics of particles in polymer solvents (Holyst *et al.*, 2009; Guo *et al.*, 2012; Grabowski and Mukhopadhyay, 2014; Kort *et al.*, 2015; Banks *et al.*, 2016). The mobility of particles depend on separate time and length scales and within these certain regimes the Stokes-Einstein relation does not apply (Cai *et al.*, 2011; Nath *et al.*, 2018).

In this work, one important parameter which determined the particles diffusivity was the probe's diameter. As shown, the hindrance experienced by the fluorescent tracer molecules increased with particle size. Depending on the stewartan concentration, the diffusion of large PS microspheres (193 nm) scaled in the same order than the macroviscosity determined with the falling ball viscosimeter. It appears that these large PS beads experience the full macroviscosity of the stewartan solution beyond the continuum limit which makes the description with the Stokes-Einstein relation valid. Higher diffusion dynamics were obtained as the size of the PS microspheres decreased, thus the local viscosity was probed (Holyst *et al.*, 2009; Kohli and Mukhopadhyay, 2012). The latter varies with the particle diameter in relation to the correlation length (average mesh size ξ) and radius of gyration of the polysaccharide polymers (Cai *et al.*, 2011; Nath *et al.*, 2018). Lastly, a third regime was described in which the particle diameter is much smaller than ξ and the probe will exhibit diffusion coefficients very close to the ones in pure solvent (Cai *et al.*, 2011; Nath *et al.*, 2018). This is in agreement with the diffusion dynamics of Alexa Fluor® 488 which yielded diffusion times similar to those in buffer alone (hindrance factor close to unity). Hence, the pore diameter of the stewartan network must be small enough (below 193 nm) to prevent the penetration of the interstitial space by the largest PS beads (Cai *et al.*, 2015), but in the range of 64 nm to partially hinder the diffusion of 64 nm PS microspheres. In agreement, pore formation between the stewartan chains were seen in CG MD Simulations. The pore diameter varied with the stewartan concentration from 3 to 11 nm for the RU concentrations of 86 and 10 mM, respectively. However, simulations with increased stewartan chain lengths might be able to reproduce the pore dimensions as seen in the diffusion experiments.

In addition, differences in the hindrance experienced by the florescent tracer molecules in stewartan were also observed in dependence to the pH. This suggests that the mobility is additionally affected by electrostatic interactions of the probes with the stewartan polymer. As one obvious explanation, the stewartan carboxylic groups (pKa ~ 3, Wang *et al.*, 1991) are more negatively charged at pH 8 which will influence the interaction with PS beads, which exhibit negative zeta potentials, by electrostatic repulsion. Indeed, interactions of biomolecules or nano-sized objects with the extracellular matrix of the biofilm have been reported (Dengler *et al.*, 2015; Ikuma *et al.*, 2015; Harper *et al.*, 2019). Furthermore, the biofilm permeability of antibiotics depends on the overall charge and may render them ineffective in cases where they adsorb to biofilm components (Stewart *et al.*, 2009; Tseng *et al.*, 2013; Singh *et al.*, 2016). In addition, the negative charges of the glucuoronic acids subunits account for a strong water association thus increasing the particle's local viscous drag (Nockemann *et al.*, 2008; Yang *et al.*, 2009; Besbes *et al.*, 2011). Further evidence from this work, that interactions with the stewartan matrix resulted in a reduced mobility, comes from diffusion experiments with P22 bacteriophage particles. Here, the mobility of the phages was found to be three to four times faster than the diffusion of 64 nm PS beads. As the phage particle diameter is larger (71-73 nm) than that of these microspheres, the individual experienced confinement cannot sufficiently be explained with the differences in size of the particles. Indeed, the P22 phages exhibited lower negative Zeta potentials than the PS microspheres and likely are therefore less repelled from the stewartan polymer material. Other types of interactions, such as hydrophobic interactions, are also expected to influence the diffusion behaviour of PS beads and P22 phages in stewartan solutions due to differences in their surface properties (Asensio *et al.*, 2013; Janczarek *et al.*, 2015; Kuttel *et al.*, 2015; Chin *et al.*, 2017). These results suggest that the stewartan polymers are prone to form a three dimensional network which is sufficient to display characteristics from intact biofilms, such as the selective transport of particles. Here, biofilms were described as molecular sieves (Flemming and Wingender, 2010).

5.5 Phage Particle Diffusion in Biofilm

During the stewartan diffusion experiments one population of phages was highly confined by the ExoPS matrix with diffusion coefficients 100 to 1000 fold lower than freely diffusing P22 bacteriophages (at a stewartan concentration of $10\,\mathrm{mg \cdot mL^{-1}}$). This might prove an effective entanglement of stewartan polysaccharides in which the meshes of the entangled stewartan network are transiently formed in dependence to the entanglement length (Cai *et al.*, 2011; Nath *et al.*, 2018). These length scales account for heterogeneities in the stewartan mesh-like network and eventually phages became trapped in pores. In support of this finding, a population of 64 nm PS microspheres were also found to be trapped in pores in preliminary experiments, resulting in low diffusion coefficients. Indeed, in contrast to the freely diffusing agents, the diffusion behaviour of trapped bacteriophage particles deviate from a classical random walk and showed a biased towards successive steps in opposite direction ($\theta = 180°$). Here, it is proposed that bacteriophages reside within the interstitial space where they often collide with the stewartan material. In agreement, trapping of phages in biofilms was seen even for bacteriophages which exhibited a respective enzymatic activity toward the ExoPS (Hu *et al.*, 2012; Vidakovic *et al.*, 2018). As a result phages accumulated at the low-dense periphery of the biofilm and the infection rate decreased with the deepness of biofilm penetration. Additionally, bacteria associate into mixed-biofilm species which further impair with the bacteriophages infectivity (Kay *et al.*, 2011; Chew *et al.*, 2014). Consequently, there is a big demand for engineered phages with flexible host specificity and additional hydrolytic functions to overcome dense biofilm architectures with different compositions of the extracellular matrix (Lu and Collins, 2007; Alcaine *et al.*, 2016; Cao *et al.*, 2016; Lin *et al.*, 2017).

5.6 Interactions of WceF and ΦEa1h TSP with the Stewartan Matrix

The TSP from the ΦEa1h bacteriophage is a very fast and efficient stewartan hydrolase compared to WceF. Incubations of the TSP with 10 mg · mL^{-1} stewartan results in an almost complete loss of the diffusion-limiting properties of the ExoPS network within 45 min at room temperature. The mobility of 64 nm PS microspheres underwent a transition from anomalous subdiffusion to normal Brownian diffusion (anomaly exponent $\alpha \sim 1$). This findings are in agreement with TSPs being highly efficient polysaccharide depolymerases (Schwarzer *et al.*, 2009; Cornelissen *et al.*, 2012; Gutiérrez *et al.*, 2015; Kunstmann *et al.*, 2018a). Additionally, TSPs comprise highly stable three dimensional folds which ensure enzymatic activities at different environmental conditions (Barbirz *et al.*, 2009). Consequently, the ΦEa1h TSP is active over a broad range of pH values and NaCl concentrations.

Here, it was shown that the ΦEa1h TSP cleaves stewartan to oligosaccharides of different sizes. During the stewartan hydrolysis a distribution of stewartan oligosaccharides was produced which presumably spans the whole length from one RU to uncleaved stewartan polysaccharide. Analysis of the hydrolysis products by capillary electrophoresis resolved oligosaccharide fragments up to 5 RU lengths. The depolymerisation of stewartan by the ΦEa1h TSP at 30°C was shown to be biphasic. Reducing ends were immediately produced in the beginning of the reaction. Here, large oligosaccharide fragments were detected in size-exclusion chromatography which were further digested to one and two RUs. After a saturation of the hydrolysis activity of 30 h and additional second increase in reducing ends was detected and more 1 and 2 RUs were produced. Several studies revealed, that ExoPS solutions contained a mixture of ordered and unordered polysaccharide regions (Christensen *et al.*, 1993; Christensen *et al.*, 1996). Indeed, the depolymerisation of these ExoPS solutions by acid hydrolysis was dependent on the conformational state of the polysaccharide (Hjerde *et al.*, 1996). Comparable enzymatic degradation studies showed that the cleavage of polysaccharides is characterized by distinct kinetic regimes (Tayal *et al.*, 1999; Li *et al.*, 2004), in agreement with the biphasic stewartan hydrolysis of the ΦEa1h TSP. Hence, the fast stewartan hydrolysis kinetic at the beginning of the reaction could be explained by the degradation of more accessible stewartan populations whereas less accessible polymers are cleaved in a slower second degradation step. In addition, in this second kinetic regime long stewartan precursor molecules, which were not resolved by size-exclusion chromatography, are further digested to small-sized RUs oligomers instead of the hydrolysis of two RUs to one RUs. This emphasize that the ΦEa1h TSP might favour polysaccharide chains with a high degree of polymerization. In support of this hypothesis, enzymes, which degrade high molecular weight polysaccharides, usually bind the large polymer chains in a set of binding subsites

(Highsmith *et al.*, 1975; Michel *et al.*, 2003; Nielsen *et al.*, 2009; Kang *et al.*, 2016). Here, a critical number of binding sites must be occupied to position the polysaccharide chain in a more favourable conformation for the succeeding hydrolysis step (Highsmith *et al.*, 1975; Cramer *et al.*, 1994; Nielsen *et al.*, 2009). Consequently, lower K_M value are obtained for the binding of long polysaccharide chains and thus the enzymatic efficiency increases (Cramer *et al.*, 1994). Hence, the biphasic stewartan degradation by the ΦEa1h TSP might also be a result of the early cleavage of long stewartan chains and a delayed hydrolysis of shorter ExoPS. However, these two kinetic regimes were separated by a 50 h long saturation of long chained stewartan degradation. It is here proposed, that the cleaved fragments still reside in the active site by nonproductive binding (Varrot *et al.*, 2003; Yamasaki *et al.*, 2005). As soon, as the oligosaccharide products are displaced from the active site, new substrate can be bound.

Nevertheless, studies which concentrated on the interactions of TSPs with high-molecular weight polysaccharide fragments (above several RU) are rare but are highly needed to understand the influence of chain length and polysaccharide network formation on the enzymes hydrolysis activity (Cramer *et al.*, 1994; Fennouri *et al.*, 2012; Fennouri *et al.*, 2013; Kang *et al.*, 2016). The active site of TSPs are composed of elongated shallow binding grooves on the surface of the β-helix (Barbirz *et al.*, 2008; Andres *et al.*, 2013; Schwarzer *et al.*, 2015; Lee *et al.*, 2017). The interaction with their ligands is mainly mediated by electrostatic interactions, such as hydrogen bonds, with a strong negative enthalpic contribution (Baxa *et al.*, 2001; Andres *et al.*, 2013; Kang *et al.*, 2016; Kunstmann *et al.*, 2018a). Binding of P22 TSP to a Shigella flexneri O-antigen dodecasaccharide requires a flexible polysaccharide chain and partially unconstrained protein backbone to avoid steric clashes (Kang *et al.*, 2016). In agreement with the stewartan digestion by the ΦEa1h TSP, enzymatic degradation of high molecular weight hyaluronan resulted in an oligosaccharide size distribution which shifted towards smaller fragments depending on to the incubation time (Fennouri *et al.*, 2012; Fennouri *et al.*, 2013).

The fast stewartan hydrolysis kinetic of the ΦEa1h TSP is in contrast to the ExoPS degradation by WceF which is much more slower process. Here, the increase in reducing ends is characterized by a pronounced lag phase. To best of knowledge, this is the first description of a bacterial tailspike-like protein. It was noticed that WceF formed aggregates with stewartan. The size of these highly dense protein clusters correspond to roughly 500 to 1000 WceF molecules in 10 and 1 mg · mL^{-1} stewartan, respectively, as deduced from the analysis of the hydrodynamic radius from WceF size-exclusion chromatography experiments. In the previous chapter (section 5.4) the model of a molecular sieve was derived, describing the influence of non covalent interactions on the diffusion of difference sized probes in the polymeric stewartan network. As a consequence, it is here assumed that WceF clusters are formed in association with the ExoPS which provide interfaces for electrostatic and hydrophobic interactions (Tielen *et al.*, 2013). A similar behaviour has been found for lectins which are multivalent carbohydrate binding proteins (Sharon, 2007; Kumar *et al.*, 2012). They provide several glycan epitopes which give rise to the cross-linking activities of lectins (Dam and Brewer, 2010). For example, the lectin Con A formed aggregates with mannose-modified polymers of 300 to 500 nm (Kim *et al.*, 2005). Hence, it is here proposed that the trimeric WceF provide three independent stewartan binding sites which results in a lectin-like cluster formation. These protein-ExoPS interactions might then account for a hindered diffusion of WceF and consequently result in the observed lag phase in the production of reducing ends.

Furthermore the long-lasting attachment of WceF with its substrate might be indicative for a processive mode of stewartan hydrolysis. Here, the processivity of enzymes is defined as the strong attachment of the protein to the substrate where it performs a series of catalytic events before it dissociates (Breyer and Matthews, 2001; Horn *et al.*, 2006). Indeed, mainly one RU fragments were produced in incubations of WceF with stewartan. In agreement, the processivity of the chitinase B hydrolysis of chitosan was roughly measured by studying the ratio between the production of oligosaccharide dimers and monomers (Sørbotten *et al.*, 2005; Horn *et al.*, 2006). Hence, WceF might remain bound to the stewartan polymer and moves along the chain while enzymatically releasing single RUs. As a result, the long chains of stewartan would be degraded in a stepwise fashion. In agreement with what was observed in this work, as soon as the stewartan substrate polymers are small enough, they would be detected a later time points in the hydrolysis kinetic in the size-exclusion chromatography experiments. Still, although to a lesser extent, fragments with other sizes were produced, which proves that WceF is an endo-acting stewartan-specific depolymerase. Furthermore, a high processivity usually comes with a trade-off between a high affinity of the enzyme towards the substrate and a low hydrolysis velocity (Cramer *et al.*, 1994; Breyer and Matthews, 2001; Nakamura *et al.*, 2014) which is in agreement with the low hydrolytic activity seen for WceF. In contrast, the ΦEa1h TSP hydrolysis of stewartan is marked by less processivity and a more even distribution of produced oligosaccharide lengths. Indeed, large oligosaccharides were immediately seen in the size-exclusion chromatography experiments. Hence, the ΦEa1h bacteriophage cleaves stewartan and more deeply penetrates the biofilm in order to reach the bacterial cell due to a fast dissociation of the TSP from the initial ExoPS substrates. In contrast, other TSPs were shown to cleave the capsular polysaccharide in a highly processive manner which helps in guiding the bacteriophage along the covalently attached polysaccharide towards the bacterium (Schwarzer *et al.*, 2009).

5.7 Putative Function of WceF in *Pantoea stewartii* biofilms

The wildtype WceF exhibits an N-terminal twin-arginine translocation signal peptide thus in *P. stewartii* WceF is translocated across the inner membrane (DeLisa *et al.*, 2003; Palmer and Berks, 2012). In this work, it was not investigated, if WceF is secreted to the periplasm or the extracellular medium but this information would be highly relevant in the discussion of the putative function of WceF in *P. stewartii* biofilms. For this reason, antibodies against WceF were raised in the group of Prof. Dr. Katja Hanack (Immunotechnology, University Potsdam) which are currently tested for their sensitivity and cross-reactivity. These antibodies would allow the detection of WceF in subcellular fractionations of *P. stewartii* by enzyme-linked immunosorbent assay or western blots (Mansell *et al.*, 2010; Blair *et al.*, 2018). The latter could be complemented with real-time polymerase chain reaction to detect the WceF mRNA which might be linked to stage-specific biofilm phenotypes.

Hence, in the following, the putative function of WceF is discussed for both cases in which the enzyme is secreted to either the extracellular medium or the periplasm.

In the diffusion experiment it was seen that WceF formed aggregates with the stewartan matrix. Such clustering of colloidal particles with components of the extracellular matrix is a common feature which has been recognized in many other bacterial biofilms (Duran-Pinedo *et al.*, 2011; Stewart *et al.*, 2013; Vidakovic *et al.*, 2018). Likewise, clumping of bacterial cells co-localizes with dense regions in the extracellular matrix of S. epidermidis (Stewart *et al.*, 2013). Furthermore, when fluorescent beads are incubated with purified protein curli fibers, one component of the extracellular matrix of E. coli, they spontaneously formed clusters (Vidakovic *et al.*, 2018). All the here mentioned clusters of cells or beads had a size (1 to 5 µm) similar to the WceF clusters seen in this work. Although, the physicochemical properties of stewartan, S. epidermidis extracellular matrix and curli fibers differ, this points to an important function of the extracellular matrix to specifically accumulate proteins with beneficial functions (Tielen *et al.*, 2013). Indeed, as a proof of principle, Tielen *et al* showed that proteins can interact with the extracellular matrix components thereby preventing their degradation by extracellular proteases (Tielen *et al.*, 2013). Flemming *et al* introduced the concept of the extracellular matrix as an external digestion system (Flemming *et al.*, 2016). As a consequence proteins can reside in the extracellular matrix and provide the enzymatic degradation activity of the extracellular material as nutrient source (Flemming, 2016). For these reasons a slow digestion of stewartan, as seen by WceF, might be useful in times of starvation to provide a long-lasting energy source. In agreement, other endoglycanases have been described in the extracellular medium which trim the chain length of already secreted ExoPSs (York and Walker, 1997; Jones *et al.*, 2007).

As WceF is part of the wce gene cluster WceF might also be involved in the biosynthesis of stewartan in the periplasm. Here, stewartan is synthesized by the Wzx/Wzy-dependent pathway. This route of polysaccharide biosynthesis is highly conserved throughout bacterial species and ExoPSs (Whitfield, 2006; Islam and Lam, 2014; Schmid *et al.*, 2015). Likewise, the Wzx/Wzy-dependent pathway comprises glycosyltransferase and enzymes for the modification of oligosaccharides. Biosynthesis is commonly initiated with the transfer of the first monosaccharide onto a phosphorylated lipid linker which serves as an anchor for stepwise ExoPS synthesis. Polysaccharides are secreted by wzx and outer membrane polysaccharide export (OPX) proteins. Polymerization of the single building blocks is accomplished by the wzy protein. Additionally, the respective operons contain polysaccharide co-polymerases (POP). POP and OPX proteins form an contiguous scaffold which spans the cell envelope (Collins *et al.*, 2007). These complexes are believed to be involved in periplasmic chain length control of the final polymer (Marolda *et al.*, 2006; Galván *et al.*, 2013; Bianco *et al.*, 2014). In the ExoPS synthesis pathway of Rhizobium leguminosarum bv. trifolii disruption of the PCP gene results in the production of ExoPS chains with a higher molecular weight than compared to the wildtype (Marczak *et al.*, 2014). In contrast, another study showed that loss of the function of PCP proteins reduced the chain length distributions of the ExoPSs (Galván *et al.*, 2013). This raised the concept of PCP proteins which adjust the balance between chain extension and termination (Cuthbertson *et al.*, 2009). In contrast, no PCP proteins are expressed from the wce gene cluster in *P. stewartii*. However, Schollmeyer at al observed a connection between the wceF deletion on the *P. stewartii* genome and an increase of the ExoPS size distribution profile by a factor of around four (Schollmeyer *et al.*, 2012). Presumably, this shift in the size distribution of stewartan will dramatically influence the viscous properties of the biofilm. Hence, WceF therefore might still be involved in stewartan chain length determination in the periplasm and compensates for the non-existing PCP homolog. Indeed, this hypothesis is supported by a case where the glycoside hydrolase Sph3 has been reported to be encoded in the glucosamingalactan biosynthesis cluster (Bamford *et al.*, 2015). Similar to WceF, Sph3 showed no homology to known glycoside hydrolase families. Targeting of polysaccharide chains in the periplasm is a common feature to regulate the ExoPS chain length (Galván *et al.*, 2013; Marczak *et al.*, 2014) or to degrade ExoPS which failed to become exported (Bakkevig *et al.*, 2005). Within these types of enzymes is the periplasmic lyase VexL from *Salmonella* enterica serovar typhi which showed a narrow maximum of K-antigen cleavage at pH 5.5 (Liston *et al.*, 2018). It was proposed that the protein has evolved structural and catalytic advantages which facilitated the cleavage of the Vi-antigen at a low periplasmic pH. Indeed, a similar sharp activity profile was seen for the stewartan hydrolysis of WceF at different pH and NaCl concentrations.

5.8 Structural Analysis of WceF and ΦEa1h TSP

The three dimensional structure of WceF displayed a β-solenoidal fold which resembled the domain architecture of bacteriophage TSPs. This is emphasized by a central compact β-helix and an N-terminal domain which superimposed with the phage particle-binding domain of P22 TSP. The C-terminus showed a rich composition of β-sheet elements in agreement with other TSPs (Barbirz *et al.*, 2008; Müller *et al.*, 2008; Lee *et al.*, 2017). The central β-helix was also predicted for the ΦEa1h TSP. In contrast, the N-terminus of ϕEa1h TSP lacked a comparable particle-binding domain. In these cases, adapter proteins are encoded on the genome of the phage which attach the TSP to the bacteriophage particle (Stummeyer *et al.*, 2006; Leiman *et al.*, 2007; Tu *et al.*, 2017). Additionally, a Greek key motif was predicted for the ΦEa1h TSP N-terminus. The latter was also found on WceF and shares the same topology of β-sheets. Due to the high structural similarity of the Greek key motif between both proteins, it is tempting to speculate, that both proteins originate from a same ancestor template. Indeed, a similar conclusion was made, when the structure of three bacterial pectate lyases were compared to the P22 TSP (Jenkins *et al.*, 1998). In support of this hypothesis, the integration of phage genes into the bacterial genome by horizontal gene transfer is a frequently observed process which enhances the bacterial fitness (Obeng *et al.*, 2016; Touchon *et al.*, 2017).

It has been observed in this work, that neither WceF nor the ΦEa1h TSP showed a SDS-resistance at ambient temperatures as typically seen for TSPs (Barbirz *et al.*, 2009; Lee *et al.*, 2017). No difference in the stability of the trimeric interface of WceF was observed when compared to other TSPs. However, in thermal unfolding experiments of TSPs it was shown, that the slow trimeric dissociation is rate-limiting and is followed by a more rapid unfolding of the less stable subunits (Chen and King, 1991; Miller *et al.*, 1998b). Barbirz *et al* proposed that hydrogen bonds of the β-helix extend into connecting arches and turns which thus account for the high stability of the TSP structures (Manning and Colón, 2004; Barbirz *et al.*, 2009). To overcome the high activation enthalpy, these interactions need to be broken in a cooperative process (Truhlar *et al.*, 2004; Barbirz *et al.*, 2009). The latter results in a kinetic stabilization of the TSPs which is emphasized by long equilibration times and hysteresis between the denaturation and renaturation states (Fuchs *et al.*, 1991; Lai *et al.*, 1997; Barbirz *et al.*, 2009). In preliminary guanidine hydrochloride fluorescence titration experiments of WceF no significant hysteresis was seen between the unfolding and refolding of WceF thus ruling out a high kinetic barrier. It is therefore proposed, that although the β-helix overall architecture does not differ from that of the TSPs, it does not result in a similar kinetically stabilized hydrogen bond network. This might be due to the overall funnel structure of WceF, in which the C-terminus of the trimer is the most intertwined region and the preceding trimeric fold rather opens up instead of forming a tightly packed assembly. In agreement with further studies on TSPs, the design and biophysical characterization of truncated WceF constructs would further contribute to the understanding of WceF trimer folding and stabilization processes (Schuler *et al.*, 2000; Freiberg *et al.*, 2003; Reich *et al.*, 2009).

6. Summary and Outlook

Biofilms are dense and complex arrangements of bacterial cells and extracellular polymeric substances. In this work a bottom up approach was chosen to effectively describe the structural properties of the extracellular stewartan matrix which is ultimately linked to the infectivity of glycan-based biofilms such as the one from *P. stewartii*. Here, the physicochemical characteristics of stewartan solutions were analyzed in an interdisciplinary work which relates the structural aspects of stewartan polymers to the functional implications in biofilms.

This work provided a detailed description of the physicochemical properties of the ExoPS species stewartan from *P. stewartii*. It was found that purified stewartan polymers alone are sufficient to form three dimensional networks which resemble characteristics of whole biofilms, such as the viscoelasticity and diffusion-limiting properties. Analysis of the diffusion dynamics of fluorescent tracer molecules in reconstituted stewartan solutions showed that the mobility of these particles depend on the size of the nanoparticle and charge of the stewartan polymer. Furthermore, the diffusion of fluorescent molecules became more anomalous as a result of an increased density of stewartan polymers and the appearance of stewartan chain entanglements. The pores between the stewartan chains were heterogeneous regarding their size and a fraction of bacteriophage particles was trapped within small-sized network meshes.

In agreement with other biological hydrogels, stewartan acts as a molecular sieve and selectively controls the transport of molecules within the stewartan network (Witten and Ribbeck, 2017). From these findings, this work gave a description of the material properties of glycan-based biofilms such as *P. stewartii*. Furthermore, the structure of the exopolysaccharide, including branches, monosaccharide composition and modifications, ultimately determines the arrangement of polysaccharide chains in the respective network. This work therefore proposes, that this approach might be generalized for other ExoPSs from biofilms of different bacterial species. The increased knowledge about the fine-tuning of the strength of polysaccharide network assemblies is highly important towards the design of polysaccharide-based drug delivery agents (Di Meo *et al.*, 2007; Hu *et al.*, 2013; García-González *et al.*, 2015; Nayak *et al.*, 2016; Schneible *et al.*, 2019) or for bioremediation approaches in which heavy metal contaminations are removed from the environment (Prado Acosta *et al.*, 2005; Mota *et al.*, 2016; Sajayan *et al.*, 2017).

Further diffusion and bulk rheology studies should extend the reduced systems from this work by adding additional components from the extracellular matrix until a whole biofilm-like setup has been generated. The thorough analysis of these systems would then lead to a comprehensive understanding of the contribution of each extracellular species to the overall biofilm architecture. These whole systems can thus be exploited to design drugs with superior physicochemical properties which permit the facilitated penetration of the biofilm and effective killing of bacterial cells.

In this work a coarse-grained computational stewartan model was developed with stewartan polymers which exhibited a degree of polymerization of 20 RU. This system constitutes a first initial CG description of stewartan and further modifications on the CG model development have been suggested to enable MD Simulations with microsecond time scales. Additionally, increasing the size of the CG stewartan polymers could elucidate the influence of chain length and entanglements on stewartan network properties accessible from experiments like its microviscosity. Furthermore, in equilibrated ExoPS networks, simulations could mimic the diffusion of probes with different properties (size, charge, hydrophobic interactions) and thus allow a more detailed study of the interaction of nano-sized objects with the network (Schneible *et al.*, 2019).

Currently, there is just a scarce body of literature available that might describe how mechanical properties of biofilms relate to biochemical control and dynamic changes within a bacterial community. Especially, enzymatic remodeling processes take place which might be the driving forces that control pathogenicity. In this work, the hydrolisis of stewartan polymers by the enzymes WceF and ΦE1h TSP was analyzed. Surprisingly, WceF, which is expressed from the *P. stewartii* stewartan biosynthesis gene cluster, exhibited a highly similar three dimensional structure to TSPs. Hence, a common ancestor of WceF and the ΦEa1h TSP was proposed. Still, despite the structural similarity, WceF lacked the high stability seen in many other TSP. Additionally, the hydrolysis of stewartan polymers by the ΦEa1h TSP is a highly fast process which reflects the ability of the bacteriophage to efficiently pass the biofilm barrier in order to infect the bacterial cells. Cleavage of stewartan by the ΦE1h TSP resulted in a complete loss of the intrinsic diffusion-limiting properties of the stewartan network and hence the mobility of bacteriophages would therefore not be confined anymore. Finally, WceF formed tight interactions with the stewartan network and micrometer clusters were formed which are might be the reason for the slow stewartan hydrolysis kinetic. Furthermore, stewartan is degraded by WceF in a processive manner, in contrast to the ΦEa1h TSP.

Differences in the stewartan degradation activities of ΦEa1h TSP and WceF might be encoded in the structural properties of the active sites. Binding of oligosaccharide fragments to the TSP have been analyzed by soaking experiments or MD simulations (Barbirz *et al.*, 2008; Müller *et al.*, 2008; Schulz *et al.*, 2010; Kang *et al.*, 2016; Lee *et al.*, 2017). The association of oligosaccharides was further characterized in surface plasmon resonance, isothermal titration calorimetry or fluorescence titration (Singh *et al.*, 2010; Andres *et al.*, 2013; Broeker *et al.*, 2013; Kunstmann *et al.*, 2018a). Consequently all the latter methods might be used to further investigate the difference in stewartan binding sites between ΦEa1h TSP and WceF. It is of crucial interest to understand the driving forces of protein interactions with the components of the extracellular matrix to pave the way for treatments of biofilm infections which involve the hydrolase-mediated biofilm degradation (Fleming *et al.*, 2017; Olsen *et al.*, 2018b; Patel *et al.*, 2019).

7. References

Abedon ST 2016. Bacteriophage exploitation of bacterial biofilms. Phage preference for less mature targets? FEMS microbiology letters 363. doi:10.1093/femsle/fnv246.

Ackermann H-W 2003. Bacteriophage observations and evolution. Research in Microbiology 154, 245–251. doi:10.1016/S0923-2508(03)00067-6.

Akiyama E, Morimoto N, Kujawa P, Ozawa Y, Winnik FM and Akiyoshi K 2007. Self-assembled nanogels of cholesteryl-modified polysaccharides: effect of the polysaccharide structure on their association characteristics in the dilute and semidilute regimes. Biomacromolecules 8, 2366–2373. doi:10.1021/bm070136q.

Alcaine SD, Law K, Ho S, Kinchla AJ, Sela DA and Nugen SR 2016. Bioengineering bacteriophages to enhance the sensitivity of phage amplification-based paper fluidic detection of bacteria. Biosensors & bioelectronics 82, 14–19. doi:10.1016/j.bios.2016.03.047.

Alibolandi M, Mohammadi M, Taghdisi SM, Abnous K and Ramezani M 2017. Synthesis and preparation of biodegradable hybrid dextran hydrogel incorporated with biodegradable curcumin nanomicelles for full thickness wound healing. International journal of pharmaceutics 532, 466–477. doi:10.1016/j.ijpharm.2017.09.042.

Andres D, Baxa U, Hanke C, Seckler R and Barbirz S 2010a. Carbohydrate binding of Salmonella phage P22 tailspike protein and its role during host cell infection. Biochemical Society transactions 38, 1386–1389. doi:10.1042/BST0381386.

Andres D, Gohlke U, Broeker NK, Schulze S, Rabsch W, Heinemann U, Barbirz S and Seckler R 2013. An essential serotype recognition pocket on phage P22 tailspike protein forces Salmonella enterica serovar Paratyphi A O-antigen fragments to bind as nonsolution conformers. Glycobiology 23, 486–494. doi:10.1093/glycob/cws224.

Andres D, Hanke C, Baxa U, Seul A, Barbirz S and Seckler R 2010b. Tailspike interactions with lipopolysaccharide effect DNA ejection from phage P22 particles in vitro. The Journal of biological chemistry 285, 36768–36775. doi:10.1074/jbc.M110.169003.

Andres D, Roske Y, Doering C, Heinemann U, Seckler R and Barbirz S 2012. Tail morphology controls DNA release in two Salmonella phages with one lipopolysaccharide receptor recognition system. Molecular microbiology 83, 1244–1253. doi:10.1111/j.1365-2958.2012.08006.x.

Anthon GE and Barrett DM 2002. Determination of reducing sugars with 3-methyl-2-benzothiazolinonehydrazone. Analytical Biochemistry 305, 287–289. doi:10.1006/abio.2002.5644.

Arias-Andres M, Klümper U, Rojas-Jimenez K and Grossart H-P 2018. Microplastic pollution increases gene exchange in aquatic ecosystems. Environmental pollution (Barking, Essex : 1987) 237, 253–261. doi:10.1016/j.envpol.2018.02.058.

Arvidson SA, Rinehart BT and Gadala-Maria F 2006. Concentration regimes of solutions of levan polysaccharide from Bacillus sp. Carbohydrate Polymers 65, 144–149. doi:10.1016/j.carbpol.2005.12.039.

Asensio JL, Ardá A, Cañada FJ and Jiménez-Barbero J 2013. Carbohydrate-aromatic interactions. Accounts of chemical research 46, 946–954. doi:10.1021/ar300024d.

Azeredo HMC and Waldron KW 2016. Crosslinking in polysaccharide and protein films and coatings for food contact – A review. Trends in Food Science & Technology 52, 109–122. doi:10.1016/j.tifs.2016.04.008.

Baere T de, Verhelst R, Labit C, Verschraegen G, Wauters G, Claeys G and Vaneechoutte M 2004. Bacteremic infection with Pantoea ananatis. Journal of clinical microbiology 42, 4393–4395. doi:10.1128/JCM.42.9.4393–4395.2004.

Bakkevig K, Sletta H, Gimmestad M, Aune R, Ertesvåg H, Degnes K, Christensen BE, Ellingsen TE and Valla S 2005. Role of the Pseudomonas fluorescens alginate lyase (AlgL) in clearing the periplasm of alginates not exported to the extracellular environment. Journal of Bacteriology 187, 8375–8384. doi:10.1128/JB.187.24.8375–8384.2005.

Bamford NC, Snarr BD, Gravelat FN, Little DJ, Lee MJ, Zacharias CA, Chabot JC, Geller AM, Baptista SD, Baker P, Robinson H, Howell PL and Sheppard DC 2015. Sph3 Is a Glycoside Hydrolase Required for the Biosynthesis of Galactosaminogalactan in Aspergillus fumigatus. The Journal of biological chemistry 290, 27438–27450. doi:10.1074/jbc.M115.679050.

Banks DS, Tressler C, Peters RD, Höfling F and Fradin C 2016. Characterizing anomalous diffusion in crowded polymer solutions and gels over five decades in time with variable-lengthscale fluorescence correlation spectroscopy. Soft Matter 12, 4190–4203. doi:10.1039/c5sm01213a.

Barbirz S, Becker M, Freiberg A and Seckler R 2009. Phage tailspike proteins with beta-solenoid fold as thermostable carbohydrate binding materials. Macromolecular bioscience 9, 169–173. doi:10.1002/mabi.200800278.

Barbirz S, Müller JJ, Uetrecht C, Clark AJ, Heinemann U and Seckler R 2008. Crystal structure of Escherichia coli phage HK620 tailspike. Podoviral tailspike endoglycosidase modules are evolutionarily related. Molecular microbiology 69, 303–316. doi:10.1111/j.1365-2958.2008.06311.x.

Baruah R, Maina NH, Katina K, Juvonen R and Goyal A 2017. Functional food applications of dextran from Weissella cibaria RBA12 from pummelo (Citrus maxima). International journal of food microbiology 242, 124–131. doi:10.1016/j.ijfoodmicro.2016.11.012.

Baxa U, Cooper A, Weintraub A, Pfeil W and Seckler R 2001. Enthalpic Barriers to the Hydrophobic Binding of Oligosaccharides to Phage P22 Tailspike Protein †. Biochemistry 40, 5144–5150. doi:10.1021/bi0020426.

Belas R and Suvanasuthi R 2005. The ability of Proteus mirabilis to sense surfaces and regulate virulence gene expression involves FliL, a flagellar basal body protein. Journal of Bacteriology 187, 6789–6803. doi:10.1128/JB.187.19.6789-6803.2005.

Bellemann P, Bereswill S, Berger S and Geider K 1994. Visualization of capsule formation by Erwinia amylovora and assays to determine amylovoran synthesis. International Journal of Biological Macromolecules 16, 290–296.

Bernhard F 1996. Genetic transfer of amylovoran and stewartan between Erwinia amylovora and Erwinia stewartii. Microbiology 142, 1087–1096.

Besbes I, Alila S and Boufi S 2011. Nanofibrillated cellulose from TEMPO-oxidized eucalyptus fibres: Effect of the carboxyl content. Carbohydrate Polymers 84, 975–983. doi:10.1016/j.carbpol.2010.12.052.

Bhattacharya S and Gubbins KE 2006. Fast method for computing pore size distributions of model materials. Langmuir : the ACS journal of surfaces and colloids 22, 7726–7731. doi:10.1021/la052651k.

Bianco MI, Jacobs M, Salinas SR, Salvay AG, Ielmini MV and Ielpi L 2014. Biophysical characterization of the outer membrane polysaccharide export protein and the polysaccharide co-polymerase protein from Xanthomonas campestris. Protein expression and purification 101, 42–53. doi:10.1016/j.pep.2014.06.002.

Bicudo EL, Macedo VO, Carrara MA, Castro FFS and Rage RI 2007. Nosocomial outbreak of Pantoea agglomerans in a pediatric urgent care center. The Brazilian journal of infectious diseases : an official publication of the Brazilian Society of Infectious Diseases 11, 281–284. doi:10.1590/s1413-86702007000200023.

Birdsall CK and Langdon AB 2005. Plasma physics via computer simulation, New York Taylor & Francis.

Birjiniuk A, Billings N, Nance E, Hanes J, Ribbeck K and Doyle PS 2014. Single particle tracking reveals spatial and dynamic organization of the E. coli biofilm matrix. New journal of physics 16, 85014. doi:10.1088/1367-2630/16/8/085014.

Blair KM, Mears KS, Taylor JA, Fero J, Jones LA, Gafken PR, Whitney JC and Salama NR 2018. The Helicobacter pylori cell shape promoting protein Csd5 interacts with the cell wall, MurF, and the bacterial cytoskeleton. Molecular microbiology 110, 114–127. doi:10.1111/mmi.14087.

Block CC, Hill JH and McGee DC 1998. Seed Transmission of Pantoea stewartii in Field and Sweet Corn. Plant Disease 82, 775–780. doi:10.1094/PDIS.1998.82.7.775.

Bogino PC, Oliva MdlM, Sorroche FG and Giordano W 2013. The role of bacterial biofilms and surface components in plant-bacterial associations. International journal of molecular sciences 14, 15838–15859. doi:10.3390/ijms140815838.

Borgersen Q, Bolick DT, Kolling GL, Aijuka M, Ruiz-Perez F, Guerrant RL, Nataro JP and Santiago AE 2018. Abundant production of exopolysaccharide by EAEC strains enhances the formation of bacterial biofilms in contaminated sprouts. Gut microbes 9, 264–278. doi:10.1080/19490976.2018.1429877.

Boulé J, Sholberg PL, Lehman SM, O'gorman DT and Svircev AM 2011. Isolation and characterization of eight bacteriophages infecting Erwinia amylovora and their potential as biological control agents in British Columbia, Canada. Canadian Journal of Plant Pathology 33, 308–317. doi:10.1080/07060661.2011.588250.

Bragard C, Dehnen-Schmutz K, Di Serio F, Gonthier P, Jacques M-A, Jaques Miret JA, Justesen AF, MacLeod A, Magnusson CS, Milonas P, Navas-Cortes JA, Parnell S, Potting R, Reignault PL, Thulke H-H, Civera AV, Yuen J, Zappalà L, Battilani P, Pautasso M and van der Werf W 2019. Risk assessment of the entry of Pantoea stewartii subsp. stewartii on maize seed imported by the EU from the USA. EFSA Journal 17, 39. doi:10.2903/j.efsa.2019.5851.

Braun EJ 1982. Ultraestructural investigation of resistant and susceptible maize inbred infected with Erwinia stewartii. Phytopathology 72, 159–166.

Bren L 2007. Bacteria-eating virus approved as food additive. FDA consumer 41, 20–22.

Breyer WA and Matthews BW 2001. A structural basis for processivity. Protein science : a publication of the Protein Society 10, 1699–1711.

Bridier A, Dubois-Brissonnet F, Boubetra A, Thomas V and Briandet R 2010. The biofilm architecture of sixty opportunistic pathogens deciphered using a high throughput CLSM method. Journal of microbiological methods 82, 64–70. doi:10.1016/j.mimet.2010.04.006.

Broeker NK, Andres D, Kang Y, Gohlke U, Schmidt A, Kunstmann S, Santer M and Barbirz S 2017. Complex carbohydrate recognition by proteins: Fundamental insights from bacteriophage cell adhesion systems. Perspectives in Science 11, 45–52. doi:10.1016/j.pisc.2016.10.001.

Broeker NK, Gohlke U, Müller JJ, Uetrecht C, Heinemann U, Seckler R and Barbirz S 2013. Single amino acid exchange in bacteriophage HK620 tailspike protein results in thousand-fold increase of its oligosaccharide affinity. Glycobiology 23, 59–68. doi:10.1093/glycob/cws126.

Broeker NK, Kiele F, Casjens SR, Gilcrease EB, Thalhammer A, Koetz J and Barbirz S 2018. In Vitro Studies of Lipopolysaccharide-Mediated DNA Release of Podovirus HK620. Viruses 10. doi:10.3390/v10060289.

Bush K 2010. The coming of age of antibiotics: discovery and therapeutic value. Annals of the New York Academy of Sciences 1213, 1–4. doi:10.1111/j.1749-6632.2010.05872.x.

Cai L-H, Panyukov S and Rubinstein M 2011. Mobility of Nonsticky Nanoparticles in Polymer Liquids. Macromolecules 44, 7853–7863. doi:10.1021/ma201583q.

Cai L-H, Panyukov S and Rubinstein M 2015. Hopping Diffusion of Nanoparticles in Polymer Matrices. Macromolecules 48, 847–862. doi:10.1021/ma501608x.

Cao B, Yang M and Mao C 2016. Phage as a Genetically Modifiable Supramacromolecule in Chemistry, Materials and Medicine. Accounts of chemical research 49, 1111–1120. doi:10.1021/acs.accounts.5b00557.

Cao Z and Voth GA 2015. The multiscale coarse-graining method. XI. Accurate interactions based on the centers of charge of coarse-grained sites. The Journal of Chemical Physics 143, 243116. doi:10.1063/1.4933249.

Carlier A, Burbank L and Bodman SB von 2009. Identification and characterization of three novel EsaI/EsaR quorum-sensing controlled stewartan exopolysaccharide biosynthetic genes in Pantoea stewartii ssp. stewartii. Molecular microbiology 74, 903–913. doi:10.1111/j.1365-2958.2009.06906.x.

Cassini A, Högberg LD, Plachouras D, Quattrocchi A, Hoxha A, Simonsen GS, Colomb-Cotinat M, Kretzschmar ME, Devleesschauwer B, Cecchini M, Ouakrim DA, Oliveira TC, Struelens MJ, Suetens C, Monnet DL, Strauss R, Mertens K, Struyf T, Catry B, Latour K, Ivanov IN, Dobreva EG, Tambic Andraševic A, Soprek S, Budimir A, Paphitou N, Žemlicková H, Schytte Olsen S, Wolff Sönksen U, Märtin P, Ivanova M, Lyytikäinen O, Jalava J, Coignard B, Eckmanns T, Abu Sin M, Haller S, Daikos GL, Gikas A, Tsiodras S, Kontopidou F, Tóth Á, Hajdu Á, Guólaugsson Ó, Kristinsson KG, Murchan S, Burns K, Pezzotti P, Gagliotti C, Dumpis U, Liuimiene A, Perrin M, Borg MA, Greeff SC de, Monen JCM, Koek MBG, Elstrøm P, Zabicka D, Deptula A, Hryniewicz W, Caniça M, Nogueira PJ, Fernandes PA, Manageiro V, Popescu GA, Serban RI, Schréterová E, Litvová S, Štefkovicová M, Kolman J, Klavs I, Korošec A, Aracil B, Asensio A, Pérez-Vázquez M, Billström H, Larsson S, Reilly JS, Johnson A and Hopkins S 2019. Attributable deaths and disability-adjusted life-years caused by infections with antibiotic-resistant bacteria in the EU and the European Economic Area in 2015: a population-level modelling analysis. The Lancet Infectious Diseases 19, 56–66. doi:10.1016/S1473-3099(18)30605-4.

Cavaliere R, Ball JL, Turnbull L and Whitchurch CB 2014. The biofilm matrix destabilizers, EDTA and DNaseI, enhance the susceptibility of nontypeable Hemophilus influenzae biofilms to treatment with ampicillin and ciprofloxacin. MicrobiologyOpen 3, 557–567. doi:10.1002/mbo3.187.

Chalykh AE, Matveev VV, Muravlev DA, Mityuk DY and Philippova OE 2017. Nanostructure of xanthan networks. Nanotechnologies in Russia 12, 1–8. doi:10.1134/S1995078017010037.

Chanmee T, Ontong P and Itano N 2016. Hyaluronan: A modulator of the tumor microenvironment. Cancer letters 375, 20–30. doi:10.1016/j.canlet.2016.02.031.

Charles C, Rout S, Laws A, Jackson B, Boxall S and Humphreys P 2017. The Impact of Biofilms upon Surfaces Relevant to an Intermediate Level Radioactive Waste Geological Disposal Facility under Simulated Near-Field Conditions. Geosciences 7, 57. doi:10.3390/geosciences7030057.

Chaturongakul S and Ounjai P 2014. Phage-host interplay: examples from tailed phages and Gram-negative bacterial pathogens. Frontiers in microbiology 5, 442. doi:10.3389/fmicb.2014.00442.

Chen B and King J 1991. Thermal unfolding pathway for the thermostable P22 tailspike endorhamnosidase. Biochemistry 30, 6260–6269. doi:10.1021/bi00239a026.

Chen F, Zhang Z, Deng Z, Zhang R, Fan G, Ma D and McClements DJ 2018. Controlled-release of antacids from biopolymer microgels under simulated gastric conditions: Impact of bead dimensions, pore size, and alginate/pectin ratio. Food research international (Ottawa, Ont.) 106, 745–751. doi:10.1016/j.foodres.2018.01.038.

Chen VB, Arendall WB, Headd JJ, Keedy DA, Immormino RM, Kapral GJ, Murray LW, Richardson JS and Richardson DC 2010. MolProbity: all-atom structure validation for macromolecular crystallography. Acta crystallographica. Section D, Biological crystallography 66, 12–21. doi:10.1107/S0907444909042073.

Chew SC, Kundukad B, Seviour T, van der Maarel JRC, Yang L, Rice SA, Doyle P and Kjelleberg S 2014. Dynamic remodeling of microbial biofilms by functionally distinct exopolysaccharides. mBio 5, e01536-14. doi:10.1128/mBio.01536-14.

Chin J, Sinha S, Nalaparaju A, Yam J, Qin Z, Ma L, Liang Z-X, Lu L, Bhattacharjya S and Yang L 2017. Pseudomonas aeruginosa Psl Exopolysaccharide Interacts with the Antimicrobial Peptide LG21. Water 9, 681. doi:10.3390/w9090681.

Choudhury CK, Carbone P and Roy S 2016. Scalability of Coarse-Grained Potentials Generated from Iterative Boltzmann Inversion for Polymers: Case Study on Polycarbonates. Macromolecular Theory and Simulations 25, 274–286. doi:10.1002/mats.201500079.

Christensen BE, Smidsrød O and Stokke BT 1996. Metastable, Partially Depolymerized Xanthans and Rearrangements toward Perfectly Matched Duplex Structures. Macromolecules 29, 2939–2944. doi:10.1021/ma951445o.

Christensen BE, Smidsroed O, Elgsaeter A and Stokke BT 1993. Depolymerization of double-stranded xanthan by acid hydrolysis: characterization of partially degraded double strands and single-stranded oligomers released from the ordered structures. Macromolecules 26, 6111–6120. doi:10.1021/ma00074a037.

Christensen BE, Stokke BT and Smidsrød O 1995. Xanthan—The natural water soluble cellulose derivative. In Cellulose and cellulose derivatives. Physico-chemical aspects and industrial applications (eds JF Kennedy, GO Phillips, PA Williams and L Piculell), pp. 265–278. Woodhead, Cambridge.

Collins RF, Beis K, Dong C, Botting CH, McDonnell C, Ford RC, Clarke BR, Whitfield C and Naismith JH 2007. The 3D structure of a periplasm-spanning platform required for assembly of group 1 capsular polysaccharides in Escherichia coli. Proceedings of the National Academy of Sciences of the United States of America 104, 2390–2395. doi:10.1073/pnas.0607763104.

Comeau AM, Hatfull GF, Krisch HM, Lindell D, Mann NH and Prangishvili D 2008. Exploring the prokaryotic virosphere. Research in Microbiology 159, 306–313. doi:10.1016/j.resmic.2008.05.001.

Cook KA, Weinzierl RA, Pataky JK, Esker PD and Nutter FW 2005. Population Densities of Corn Flea Beetle (Coleoptera: Chrysomelidae) and Incidence of Stewart's Wilt in Sweet Corn. Journal of Economic Entomology 98, 673–682. doi:10.1603/0022-0493-98.3.673.

Cordomí A, Edholm O and Perez JJ 2009. Effect of Force Field Parameters on Sodium and Potassium Ion Binding to Dipalmitoyl Phosphatidylcholine Bilayers. Journal of chemical theory and computation 5, 2125–2134. doi:10.1021/ct9000763.

Cornelissen A, Ceyssens P-J, Krylov VN, Noben J-P, Volckaert G and Lavigne R 2012. Identification of EPS-degrading activity within the tail spikes of the novel Pseudomonas putida phage AF. Virology 434, 251–256. doi:10.1016/j.virol.2012.09.030.

Cowen L, Bradley P, Menke M, King J and Berger B 2002. Predicting the beta-helix fold from protein sequence data. Journal of computational biology : a journal of computational molecular cell biology 9, 261–276. doi:10.1089/10665270252935458.

Cramer JA, Bailey LC, Bailey CA and Miller RT 1994. Kinetic and mechanistic studies with bovine testicular hyaluronidase. Biochimica et biophysica acta 1200, 315–321. doi:10.1016/0304-4165(94)90173-2.

Cruz AT, Cazacu AC and Allen CH 2007. Pantoea agglomerans, a plant pathogen causing human disease. Journal of clinical microbiology 45, 1989–1992. doi:10.1128/JCM.00632-07.

Cuthbertson L, Mainprize IL, Naismith JH and Whitfield C 2009. Pivotal roles of the outer membrane polysaccharide export and polysaccharide copolymerase protein families in export of extracellular polysaccharides in gram-negative bacteria. Microbiology and molecular biology reviews : MMBR 73, 155–177. doi:10.1128/MMBR.00024-08.

Czerwinski EW, Midoro-Horiuti T, White MA, Brooks EG and Goldblum RM 2005. Crystal structure of Jun a 1, the major cedar pollen allergen from Juniperus ashei, reveals a parallel beta-helical core. Journal of Biological Chemistry 280, 3740–3746. doi:10.1074/jbc.M409655200.

Dam TK and Brewer CF 2010. Lectins as pattern recognition molecules: the effects of epitope density in innate immunity. Glycobiology 20, 270–279. doi:10.1093/glycob/cwp186.

Danese PN, Pratt LA and Kolter R 2000. Exopolysaccharide production is required for development of Escherichia coli K-12 biofilm architecture. Journal of Bacteriology 182, 3593–3596. doi:10.1128/jb.182.12.3593-3596.2000.

Dannenhoffer-Lafage T, Wagner JW, Durumeric AEP and Voth GA 2019. Compatible observable decompositions for coarse-grained representations of real molecular systems. The Journal of Chemical Physics 151, 134115. doi:10.1063/1.5116027.

Darden T, York D and Pedersen L 1993. Particle mesh Ewald: An N ·log(N) method for Ewald sums in large systems. The Journal of Chemical Physics 98, 10089–10092. doi:10.1063/1.464397.

Das A and Andersen HC 2009. The multiscale coarse-graining method. III. A test of pairwise additivity of the coarse-grained potential and of new basis functions for the variational calculation. The Journal of Chemical Physics 131, 34102. doi:10.1063/1.3173812.

Das A and Andersen HC 2012. The multiscale coarse-graining method. IX. A general method for construction of three body coarse-grained force fields. The Journal of Chemical Physics 136, 194114. doi:10.1063/1.4705417.

DeLisa MP, Tullman D and Georgiou G 2003. Folding quality control in the export of proteins by the bacterial twin-arginine translocation pathway. Proceedings of the National Academy of Sciences of the United States of America 100, 6115–6120. doi:10.1073/pnas.0937838100.

Dengler V, Foulston L, DeFrancesco AS and Losick R 2015. An Electrostatic Net Model for the Role of Extracellular DNA in Biofilm Formation by Staphylococcus aureus. Journal of Bacteriology 197, 3779–3787. doi:10.1128/JB.00726-15.

Desbrieres J 2002. Viscosity of semiflexible chitosan solutions: influence of concentration, temperature, and role of intermolecular interactions. Biomacromolecules 3, 342–349. doi:10.1021/bm010151+.

Di Lorenzo A, Varcamonti M, Parascandola P, Vignola R, Bernardi A, Sacceddu P, Sisto R and Alteriis E de 2005. Characterization and performance of a toluene-degrading biofilm developed on pumice stones. Microbial cell factories 4, 4. doi:10.1186/1475-2859-4-4.

Di Luca, M., Tkhilaishvili, T., Trampuz, A. 2018. SPECIFIC ANTIBIOFILM PROPERTIES OF BACTERIOPHAGE SB-1 MAKE IT SUITABLE FOR THE THERAPY OF PROSTHETIC JOINT INFECTIONS DUE TO STAPHYLOCOCCUS AUREUS: BIOFILM MATRIX DEGRADATION AND PERSISTER CELLS KILLING. Orthopaedic Proceedings Vol, 100. No SUPP_17.

Di Meo C, Panza L, Capitani D, Mannina L, Banzato A, Rondina M, Renier D, Rosato A and Crescenzi V 2007. Hyaluronan as carrier of carboranes for tumor targeting in boron neutron capture therapy. Biomacromolecules 8, 552–559. doi:10.1021/bm0607426.

Donlan RM and Costerton JW 2002. Biofilms: survival mechanisms of clinically relevant microorganisms. Clinical microbiology reviews 15, 167–193. doi:10.1128/cmr.15.2.167-193.2002.

Doyle SA 2009. High Throughput Protein Expression and Purification. Methods and Protocols. Humana Press, Totowa, NJ.

Dublanchet A and Bourne S 2007. The epic of phage therapy. The Canadian journal of infectious diseases & medical microbiology = Journal canadien des maladies infectieuses et de la microbiologie medicale 18, 15–18. doi:10.1155/2007/365761.

Dubois T, Tremblay YDN, Hamiot A, Martin-Verstraete I, Deschamps J, Monot M, Briandet R and Dupuy B 2019. A microbiota-generated bile salt induces biofilm formation in Clostridium difficile. NPJ biofilms and microbiomes 5, 14. doi:10.1038/s41522-019-0087-4.

Dunn NJH, Foley TT and Noid WG 2016. Van der Waals Perspective on Coarse-Graining: Progress toward Solving Representability and Transferability Problems. Accounts of chemical research 49, 2832–2840. doi:10.1021/acs.accounts.6b00498.

Dunsing V, Irmscher T, Barbirz S and Chiantia S 2019. Purely Polysaccharide-Based Biofilm Matrix Provides Size-Selective Diffusion Barriers for Nanoparticles and Bacteriophages. Biomacromolecules 20, 3842–3854. doi:10.1021/acs.biomac.9b00938.

Duran-Pinedo AE, Paster B, Teles R and Frias-Lopez J 2011. Correlation network analysis applied to complex biofilm communities. PloS one 6, e28438. doi:10.1371/journal.pone.0028438.

Dutkiewicz J, Mackiewicz B, Kinga Lemieszek M, Golec M and Milanowski J 2016. Pantoea agglomerans: a mysterious bacterium of evil and good. Part III. Deleterious effects: infections of humans, animals and plants. Annals of agricultural and environmental medicine : AAEM 23, 197–205. doi:10.5604/12321966.1203878.

Emsley P and Cowtan K 2004. Coot: model-building tools for molecular graphics. Acta crystallographica. Section D, Biological crystallography 60, 2126–2132. doi:10.1107/S0907444904019158.

Epstein AK, Pokroy B, Seminara A and Aizenberg J 2011. Bacterial biofilm shows persistent resistance to liquid wetting and gas penetration. Proceedings of the National Academy of Sciences of the United States of America 108, 995–1000. doi:10.1073/pnas.1011033108.

Errington J 2013. L-form bacteria, cell walls and the origins of life. Open biology 3, 120143. doi:10.1098/rsob.120143.

Estrela A, Heck M and Abraham W-R 2009. Novel Approaches to Control Biofilm Infections. Current Medicinal Chemistry 16, 1512–1530. doi:10.2174/092986709787909640.

Fan B and Maranas JK 2015. Coarse-grained simulation of cellulose Iβ with application to long fibrils. Cellulose 22, 31–44. doi:10.1007/s10570-014-0481-2.

Fang L and Catchmark JM 2015. Characterization of cellulose and other exopolysaccharides produced from Gluconacetobacter strains. Carbohydrate Polymers 115, 663–669. doi:10.1016/j.carbpol.2014.09.028.

Fennouri A, Daniel R, Pastoriza-Gallego M, Auvray L, Pelta J and Bacri L 2013. Kinetics of enzymatic degradation of high molecular weight polysaccharides through a nanopore: experiments and data-modeling. Analytical chemistry 85, 8488–8492. doi:10.1021/ac4020929.

Fennouri A, Przybylski C, Pastoriza-Gallego M, Bacri L, Auvray L and Daniel R 2012. Single molecule detection of glycosaminoglycan hyaluronic acid oligosaccharides and depolymerization enzyme activity using a protein nanopore. ACS nano 6, 9672–9678. doi:10.1021/nn3031047.

Fernandes S and São-José C 2018. Enzymes and Mechanisms Employed by Tailed Bacteriophages to Breach the Bacterial Cell Barriers. Viruses 10. doi:10.3390/v10080396.

Fleming D, Chahin L and Rumbaugh K 2017. Glycoside Hydrolases Degrade Polymicrobial Bacterial Biofilms in Wounds. Antimicrobial Agents and Chemotherapy 61. doi:10.1128/AAC.01998-16.

Fleming D and Rumbaugh K 2018. The Consequences of Biofilm Dispersal on the Host. Scientific reports 8, 10738. doi:10.1038/s41598-018-29121-2.

Flemming H-C 2011. The perfect slime. Colloids and surfaces. B, Biointerfaces 86, 251–259. doi:10.1016/j.colsurfb.2011.04.025.

Flemming H-C 2016. EPS-Then and Now. Microorganisms 4. doi:10.3390/microorganisms4040041.

Flemming H-C and Wingender J 2010. The biofilm matrix. Nature reviews. Microbiology 8, 623–633. doi:10.1038/nrmicro2415.

Flemming H-C, Wingender J, Szewzyk U, Steinberg P, Rice SA and Kjelleberg S 2016. Biofilms: an emergent form of bacterial life. Nature reviews. Microbiology 14, 563–575. doi:10.1038/nrmicro.2016.94.

Fokine A and Rossmann MG 2014. Molecular architecture of tailed double-stranded DNA phages. Bacteriophage 4, e28281. doi:10.4161/bact.28281.

Freeman ND and Pataky JK 2001. Levels of Stewart's Wilt Resistance Necessary to Prevent Reductions in Yield of Sweet Corn Hybrids. Plant Disease 85, 1278–1284. doi:10.1094/PDIS.2001.85.12.1278.

Freiberg A, Morona R, van den Bosch L, Jung C, Behlke J, Carlin N, Seckler R and Baxa U 2003. The tailspike protein of Shigella phage Sf6. A structural homolog of Salmonella phage P22 tailspike protein without sequence similarity in the beta-helix domain. The Journal of biological chemistry 278, 1542–1548. doi:10.1074/jbc.M205294200.

Freitas F, Alves VD and Reis MAM 2011. Advances in bacterial exopolysaccharides. From production to biotechnological applications. Trends in biotechnology 29, 388–398. doi:10.1016/j.tibtech.2011.03.008.

Freitas F, Alves VD and Reis MAM 2015. Bacterial Polysaccharides: Production and Applications in Cosmetic Industry. In Polysaccharides (eds KG Ramawat and J-M Mérillon), pp. 2017–2043. Springer International Publishing, Cham.

Fruciano DE and Bourne S 2007. Phage as an antimicrobial agent: d'Herelle's heretical theories and their role in the decline of phage prophylaxis in the West. The Canadian journal of infectious diseases & medical microbiology = Journal canadien des maladies infectieuses et de la microbiologie medicale 18, 19–26. doi:10.1155/2007/976850.

Fuchs A, Seiderer C and Seckler R 1991. In vitro folding pathway of phage P22 tailspike protein. Biochemistry 30, 6598–6604. doi:10.1021/bi00240a032.

Galván EM, Ielmini MV, Patel YN, Bianco MI, Franceschini EA, Schneider JC and Ielpi L 2013. Xanthan chain length is modulated by increasing the availability of the polysaccharide copolymerase protein GumC and the outer membrane polysaccharide export protein GumB. Glycobiology 23, 259–272. doi:10.1093/glycob/cws146.

Gandini A, Lacerda TM, Carvalho AJF and Trovatti E 2016. Progress of Polymers from Renewable Resources: Furans, Vegetable Oils, and Polysaccharides. Chemical Reviews 116, 1637–1669. doi:10.1021/acs.chemrev.5b00264.

Ganesan M, Knier S, Younger JG and Solomon MJ 2016. Associative and Entanglement Contributions to the Solution Rheology of a Bacterial Polysaccharide. Macromolecules 49, 8313–8321. doi:10.1021/acs.macromol.6b01598.

Ganesan M, Stewart EJ, Szafranski J, Satorius AE, Younger JG and Solomon MJ 2013. Molar mass, entanglement, and associations of the biofilm polysaccharide of Staphylococcus epidermidis. Biomacromolecules 14, 1474–1481. doi:10.1021/bm400149a.

García-González CA, Jin M, Gerth J, Alvarez-Lorenzo C and Smirnova I 2015. Polysaccharide-based aerogel microspheres for oral drug delivery. Carbohydrate Polymers 117, 797–806. doi:10.1016/j.carbpol.2014.10.045.

Gayk I 2012. Biochemische Charakterisierung des Proteins WceF aus dem Exopolysaccharidbiosynthese-Gencluster von Pantoea stewartii. Diploma Thesis.

Gaylord NG and Gibbs JH 1962. Physical chemistry of macromolecules. C. TANFORD. Wiley, New York, 1961. vii+7lOpp. $18.00. Journal of Polymer Science 62, S22-S23. doi:10.1002/pol.1962.1206217338.

Gest H 2004. The discovery of microorganisms by Robert Hooke and Antoni Van Leeuwenhoek, fellows of the Royal Society. Notes and records of the Royal Society of London 58, 187–201. doi:10.1098/rsnr.2004.0055.

Giese M, Blusch LK, Khan MK and MacLachlan MJ 2015. Functional materials from cellulose-derived liquid-crystal templates. Angewandte Chemie (International ed. in English) 54, 2888–2910. doi:10.1002/anie.201407141.

Gordon VD, Davis-Fields M, Kovach K and Rodesney CA 2017. Biofilms and mechanics. A review of experimental techniques and findings. Journal of Physics D: Applied Physics 50, 223002. doi:10.1088/1361-6463/aa6b83.

Götz F 2002. Staphylococcus and biofilms. Molecular microbiology 43, 1367–1378. doi:10.1046/j.1365-2958.2002.02827.x.

Grabowski CA and Mukhopadhyay A 2014. Size Effect of Nanoparticle Diffusion in a Polymer Melt. Macromolecules 47, 7238–7242. doi:10.1021/ma501670u.

Greenfield J, Shang X, Luo H, Zhou Y, Heselpoth RD, Nelson DC and Herzberg O 2019. Structure and tailspike glycosidase machinery of ORF212 from E. coli O157:H7 phage CBA120 (TSP3). Scientific reports 9, 7349. doi:10.1038/s41598-019-43748-9.

Guilbaud M, Piveteau P, Desvaux M, Brisse S and Briandet R 2015. Exploring the diversity of Listeria monocytogenes biofilm architecture by high-throughput confocal laser scanning microscopy and the predominance of the honeycomb-like morphotype. Applied and environmental microbiology 81, 1813–1819. doi:10.1128/AEM.03173-14.

Guo H, Bourret G, Lennox RB, Sutton M, Harden JL and Leheny RL 2012. Entanglement-controlled subdiffusion of nanoparticles within concentrated polymer solutions. Physical review letters 109, 55901. doi:10.1103/PhysRevLett.109.055901.

Gutiérrez D, Briers Y, Rodríguez-Rubio L, Martínez B, Rodríguez A, Lavigne R and García P 2015. Role of the Pre-neck Appendage Protein (Dpo7) from Phage vB_SepiS-phiIPLA7 as an Anti-biofilm Agent in Staphylococcal Species. Frontiers in microbiology 6, 1315. doi:10.3389/fmicb.2015.01315.

Guttman A, Cooke N and Starr CM 1994. Capillary electrophoresis separation of oligosaccharides: I. Effect of operational variables. Electrophoresis 15, 1518–1522. doi:10.1002/elps.11501501217.

Guvensen NC, Demir S and Ozdemir G 2013. Effects of magnesium and calcium cations on biofilm formation by Sphingomonas paucimobilis from an industrial environment. Current Opinion in Biotechnology 24, S68. doi:10.1016/j.copbio.2013.05.185.

Hakkarainen T, Koivuniemi R, Kosonen M, Escobedo-Lucea C, Sanz-Garcia A, Vuola J, Valtonen J, Tammela P, Mäkitie A, Luukko K, Yliperttula M and Kavola H 2016. Nanofibrillar cellulose wound dressing in skin graft donor site treatment. Journal of controlled release : official journal of the Controlled Release Society 244, 292–301. doi:10.1016/j.jconrel.2016.07.053.

Halder U, Banerjee A and Bandopadhyay R 2017. Structural and Functional Properties, Biosynthesis, and Patenting Trends of Bacterial Succinoglycan: A Review. Indian journal of microbiology 57, 278–284. doi:10.1007/s12088-017-0655-3.

Hall CW and Mah T-F 2017. Molecular mechanisms of biofilm-based antibiotic resistance and tolerance in pathogenic bacteria. FEMS microbiology reviews 41, 276–301. doi:10.1093/femsre/fux010.

Hall-Stoodley L, Costerton JW and Stoodley P 2004. Bacterial biofilms. From the natural environment to infectious diseases. Nature reviews. Microbiology 2, 95–108. doi:10.1038/nrmicro821.

Hansen LT and Vogel BF 2011. Desiccation of adhering and biofilm Listeria monocytogenes on stainless steel: Survival and transfer to salmon products. International journal of food microbiology 146, 88–93. doi:10.1016/j.ijfoodmicro.2011.01.032.

Harms A, Fino C, Sørensen MA, Semsey S and Gerdes K 2017. Prophages and Growth Dynamics Confound Experimental Results with Antibiotic-Tolerant Persister Cells. mBio 8. doi:10.1128/mBio.01964-17.

Harper D, Parracho H, Walker J, Sharp R, Hughes G, Werthén M, Lehman S and Morales S 2014. Bacteriophages and Biofilms. Antibiotics 3, 270–284. doi:10.3390/antibiotics3030270.

Harper RA, Carpenter GH, Proctor GB, Harvey RD, Gambogi RJ, Geonnotti AR, Hider R and Jones SA 2019. Diminishing biofilm resistance to antimicrobial nanomaterials through electrolyte screening of electrostatic interactions. Colloids and surfaces. B, Biointerfaces 173, 392–399. doi:10.1016/j.colsurfb.2018.09.018.

Hart JW, Waigh TA, Lu JR and Roberts IS 2019. Microrheology and Spatial Heterogeneity of Staphylococcus aureus Biofilms Modulated by Hydrodynamic Shear and Biofilm-Degrading Enzymes. Langmuir : the ACS journal of surfaces and colloids 35, 3553–3561. doi:10.1021/acs.langmuir.8b04252.

Hasnain MS and Nayak AK (Eds) 2019. Natural polysaccharides in drug delivery and biomedical applications. Academic Press, an imprint of Elsevier, London.

Heo Y and Larson RG 2005. The scaling of zero-shear viscosities of semidilute polymer solutions with concentration. Journal of Rheology 49, 1117–1128. doi:10.1122/1.1993595.

Herrera CM, Koutsoudis MD, Wang X and Bodman SB von 2008. Pantoea stewartii subsp. stewartii exhibits surface motility, which is a critical aspect of Stewart's wilt disease development on maize. Molecular plant-microbe interactions : MPMI 21, 1359–1370. doi:10.1094/MPMI-21-10-1359.

Hess B, Bekker H, Berendsen HJC and Fraaije JGEM 1997. LINCS: A linear constraint solver for molecular simulations. Journal of Computational Chemistry 18, 1463–1472. doi:10.1002/(SICI)1096-987X(199709)18:12<1463::AID-JCC4>3.0.CO;2-H.

Hess B, Kutzner C, van der Spoel D and Lindahl E 2008. GROMACS 4: Algorithms for Highly Efficient, Load-Balanced, and Scalable Molecular Simulation. Journal of chemical theory and computation 4, 435–447. doi:10.1021/ct700301q.

Hickman JW, Tifrea DF and Harwood CS 2005. A chemosensory system that regulates biofilm formation through modulation of cyclic diguanylate levels. Proceedings of the National Academy of Sciences of the United States of America 102, 14422–14427. doi:10.1073/pnas.0507170102.

Highsmith S, Garvin JH and Chipman DM 1975. Mechanism of action of bovine testicular hyaluronidase. Mapping of the active site. The Journal of biological chemistry 250, 7473–7480.

Hinze M, Köhl L, Kunz S, Weißhaupt S, Ernst M, Schmid A and Voegele RT 2016. Real-time PCR detection of Erwinia amylovora on blossoms correlates with subsequent fire blight incidence. Plant Pathology 65, 462–469. doi:10.1111/ppa.12429.

Hjerde T, Smidsrød O and Christensen BE 1996. The influence of the conformational state of κ- and τ-carrageenan on the rate of acid hydrolysis. Carbohydrate Research 288, 175–187. doi:10.1016/S0008-6215(96)90795-8.

Høiby N, Bjarnsholt T, Moser C, Jensen PØ, Kolpen M, Qvist T, Aanaes K, Pressler T, Skov M and Ciofu O 2017. Diagnosis of biofilm infections in cystic fibrosis patients. APMIS : acta pathologica, microbiologica, et immunologica Scandinavica 125, 339–343. doi:10.1111/apm.12689.

Høiby N, Ciofu O, Johansen HK, Song Z-j, Moser C, Jensen PØ, Molin S, Givskov M, Tolker-Nielsen T and Bjarnsholt T 2011. The clinical impact of bacterial biofilms. International journal of oral science 3, 55–65. doi:10.4248/IJOS11026.

Holyst R, Bielejewska A, Szymański J, Wilk A, Patkowski A, Gapiński J, Zywociński A, Kalwarczyk T, Kalwarczyk E, Tabaka M, Ziebacz N and Wieczorek SA 2009. Scaling form of viscosity at all length-scales in poly(ethylene glycol) solutions studied by fluorescence correlation spectroscopy and capillary electrophoresis. Physical chemistry chemical physics : PCCP 11, 9025–9032. doi:10.1039/b908386c.

Hoover WG 1985. Canonical dynamics: Equilibrium phase-space distributions. Physical Review A 31, 1695–1697. doi:10.1103/PhysRevA.31.1695.

Horn SJ, Sikorski P, Cederkvist JB, Vaaje-Kolstad G, Sørlie M, Synstad B, Vriend G, Vårum KM and Eijsink VGH 2006. Costs and benefits of processivity in enzymatic degradation of recalcitrant polysaccharides. Proceedings of the National Academy of Sciences of the United States of America 103, 18089–18094. doi:10.1073/pnas.0608909103.

Houry A, Gohar M, Deschamps J, Tischenko E, Aymerich S, Gruss A and Briandet R 2012. Bacterial swimmers that infiltrate and take over the biofilm matrix. Proceedings of the National Academy of Sciences of the United States of America 109, 13088–13093. doi:10.1073/pnas.1200791109.

http://glycam.org. Woods Group. (2005-2019). Complex Carbohydrate Research Center, University of Georgia, Athens, GA.

Hu J, Miyanaga K and Tanji Y 2012. Diffusion of bacteriophages through artificial biofilm models. Biotechnology progress 28, 319–326. doi:10.1002/btpr.742.

Hu L, Sun Y and Wu Y 2013. Advances in chitosan-based drug delivery vehicles. Nanoscale 5, 3103–3111. doi:10.1039/c3nr00338h.

Hughes G and Webber MA 2017. Novel approaches to the treatment of bacterial biofilm infections. British journal of pharmacology 174, 2237–2246. doi:10.1111/bph.13706.

Hunsucker KZ, Vora GJ, Hunsucker JT, Gardner H, Leary DH, Kim S, Lin B and Swain G 2018. Biofilm community structure and the associated drag penalties of a groomed fouling release ship hull coating. Biofouling 34, 162–172. doi:10.1080/08927014.2017.1417395.

Hynninen A-P, Matthews JF, Beckham GT, Crowley MF and Nimlos MR 2011. Coarse-Grain Model for Glucose, Cellobiose, and Cellotetraose in Water. Journal of chemical theory and computation 7, 2137–2150. doi:10.1021/ct200092t.

Ikuma K, Decho AW and Lau BLT 2015. When nanoparticles meet biofilms-interactions guiding the environmental fate and accumulation of nanoparticles. Frontiers in microbiology 6, 591. doi:10.3389/fmicb.2015.00591.

Ingólfsson HI, Lopez CA, Uusitalo JJ, Jong DH de, Gopal SM, Periole X and Marrink SJ 2014. The power of coarse graining in biomolecular simulations. Wiley interdisciplinary reviews. Computational molecular science 4, 225–248. doi:10.1002/wcms.1169.

Insulkar P, Kerkar S and Lele SS 2018. Purification and structural-functional characterization of an exopolysaccharide from Bacillus licheniformis PASS26 with in-vitro antitumor and wound healing activities. International Journal of Biological Macromolecules 120, 1441–1450. doi:10.1016/j.ijbiomac.2018.09.147.

Islam ST and Lam JS 2014. Synthesis of bacterial polysaccharides via the Wzx/Wzy-dependent pathway. Canadian journal of microbiology 60, 697–716. doi:10.1139/cjm-2014-0595.

Ivana Č, Marija Š, Jovanka L, Bojana K, Nevena B, Dubravka M and Ljiljana S 2015. Biofilm Forming Ability Of Salmonella Enteritidis In Vitro. Acta Veterinaria 65, 1493. doi:10.1515/acve-2015-0031.

Janczarek M, Rachwał K, Cieśla J, Ginalska G and Bieganowski A 2015. Production of exopolysaccharide by Rhizobium leguminosarum bv. trifolii and its role in bacterial attachment and surface properties. Plant and Soil 388, 211–227. doi:10.1007/s11104-014-2320-5.

Jang CH, Piao YL, Huang X, Yoon EJ, Park SH, Lee K, Zhan C-G and Cho H 2016. Modeling and Re-Engineering of Azotobacter vinelandii Alginate Lyase to Enhance Its Catalytic Efficiency for Accelerating Biofilm Degradation. PloS one 11, e0156197. doi:10.1371/journal.pone.0156197.

Jang HY, Zhang K, Chon BH and Choi HJ 2015. Enhanced oil recovery performance and viscosity characteristics of polysaccharide xanthan gum solution. Journal of Industrial and Engineering Chemistry 21, 741–745. doi:10.1016/j.jiec.2014.04.005.

Januschowski K, Schnichels S, Hurst J, Hohenadl C, Reither C, Rickmann A, Pohl L, Bartz-Schmidt K-U and Spitzer MS 2019. Ex vivo biophysical characterization of a hydrogel-based artificial vitreous substitute. PloS one 14, e0209217. doi:10.1371/journal.pone.0209217.

Jean-Gilles Beaubrun J, Tall BD, Flamer M-L, Patel I, Gopinath G, Auguste W, Jean C, George M, Tartera C, Ewing L and Hanes DE 2017. Increased secretion of exopolysaccharide and virulence potential of a mucoid variant of Salmonella enterica serovar Montevideo under environmental stress. Microbial pathogenesis 103, 107–113. doi:10.1016/j.micpath.2016.12.005.

Jeger M, Bragard C, Candresse T, Chatzivassiliou E, Dehnen-Schmutz K, Gilioli G, Grégoire J-C, Jaques Miret JA, MacLeod A, Navajas Navarro M, Niere B, Parnell S, Potting R, Rafoss T, Rossi V, Urek G, van Bruggen A, van der Werf W, West J, Winter S, Manceau C, Pautasso M and Caffier D 2018. Pest categorisation of Pantoea stewartii subsp. stewartii. EFSA Journal 16, 5575. doi:10.2903/j.efsa.2018.5356.

Jenkins J, Mayans O and Pickersgill R 1998. Structure and evolution of parallel beta-helix proteins. Journal of structural biology 122, 236–246. doi:10.1006/jsbi.1998.3985.

Jenkins J and Pickersgill R 2001. The architecture of parallel β-helices and related folds. Progress in Biophysics and Molecular Biology 77, 111–175. doi:10.1016/S0079-6107(01)00013-X.

Jenkins J, Shevchik VE, Hugouvieux-Cotte-Pattat N and Pickersgill RW 2004. The crystal structure of pectate lyase Pel9A from Erwinia chrysanthemi. Journal of Biological Chemistry 279, 9139–9145. doi:10.1074/jbc.M311390200.

Jin J, Han Y and Voth GA 2019. Coarse-graining involving virtual sites: Centers of symmetry coarse-graining. The Journal of Chemical Physics 150, 154103. doi:10.1063/1.5067274.

John ST and Csányi G 2017. Many-Body Coarse-Grained Interactions Using Gaussian Approximation Potentials. The journal of physical chemistry. B 121, 10934–10949. doi:10.1021/acs.jpcb.7b09636.

Jones CG, Lawton JH and Shachak M 1994. Organisms as Ecosystem Engineers. Oikos 69, 373. doi:10.2307/3545850.

Jones KM, Kobayashi H, Davies BW, Taga ME and Walker GC 2007. How rhizobial symbionts invade plants: the Sinorhizobium-Medicago model. Nature reviews. Microbiology 5, 619–633. doi:10.1038/nrmicro1705.

Kajava AV and Steven AC 2006. β-Rolls, β-Helices, and Other β-Solenoid Proteins. In Fibrous proteins. Amyloids, prions and beta proteins (eds A Kajava, J Squire and D Parry), pp. 55–96. Acad. Elsevier Press, Amsterdam.

Kamjunke N, Herzsprung P and Neu TR 2015. Quality of dissolved organic matter affects planktonic but not biofilm bacterial production in streams. The Science of the total environment 506-507, 353–360. doi:10.1016/j.scitotenv.2014.11.043.

Kamoshida G, Tansho-Nagakawa S, Kikuchi-Ueda T, Nakano R, Hikosaka K, Nishida S, Ubagai T, Higashi S and Ono Y 2016. A novel bacterial transport mechanism of Acinetobacter baumannii via activated human neutrophils through interleukin-8. Journal of leukocyte biology 100, 1405–1412. doi:10.1189/jlb.4AB0116-023RR.

Kamoun EA, Kenawy E-RS, Tamer TM, El-Meligy MA and Mohy Eldin MS 2015. Poly (vinyl alcohol)-alginate physically crosslinked hydrogel membranes for wound dressing applications: Characterization and bio-evaluation. Arabian Journal of Chemistry 8, 38–47. doi:10.1016/j.arabjc.2013.12.003.

Kang Y, Barbirz S, Lipowsky R and Santer M 2014. Conformational diversity of O-antigen polysaccharides of the Gram-negative bacterium Shigella flexneri serotype Y. The journal of physical chemistry. B 118, 2523–2534. doi:10.1021/jp4111713.

Kang Y, Gohlke U, Engström O, Hamark C, Scheidt T, Kunstmann S, Heinemann U, Widmalm G, Santer M and Barbirz S 2016. Bacteriophage Tailspikes and Bacterial O-Antigens as a Model System to Study Weak-Affinity Protein-Polysaccharide Interactions. Journal of the American Chemical Society 138, 9109–9118. doi:10.1021/jacs.6b00240.

Karatan E and Watnick P 2009. Signals, regulatory networks, and materials that build and break bacterial biofilms. Microbiology and molecular biology reviews : MMBR 73, 310–347. doi:10.1128/MMBR.00041-08.

Kavitake D, Delattre C, Devi PB, Pierre G, Michaud P, Shetty PH and Andhare P 2019. Physical and functional characterization of succinoglycan exopolysaccharide produced by Rhizobium radiobacter CAS from curd sample. International Journal of Biological Macromolecules 134, 1013–1021. doi:10.1016/j.ijbiomac.2019.05.050.

Kay MK, Erwin TC, McLean RJC and Aron GM 2011. Bacteriophage ecology in Escherichia coli and Pseudomonas aeruginosa mixed-biofilm communities. Applied and environmental microbiology 77, 821–829. doi:10.1128/AEM.01797-10.

Kim I-B, Wilson JN and Bunz UHF 2005. Mannose-substituted PPEs detect lectins: a model for Ricin sensing. Chemical communications (Cambridge, England), 1273–1275. doi:10.1039/b416587j.

Kim S-K and Lee J-H 2016. Biofilm dispersion in Pseudomonas aeruginosa. Journal of microbiology (Seoul, Korea) 54, 71–85. doi:10.1007/s12275-016-5528-7.

Kim W, Tengra FK, Young Z, Shong J, Marchand N, Chan HK, Pangule RC, Parra M, Dordick JS, Plawsky JL and Collins CH 2013. Spaceflight promotes biofilm formation by Pseudomonas aeruginosa. PloS one 8, e62437. doi:10.1371/journal.pone.0062437.

Kirschner KN, Yongye AB, Tschampel SM, González-Outeiriño J, Daniels CR, Foley BL and Woods RJ 2008. GLYCAM06: a generalizable biomolecular force field. Carbohydrates. Journal of computational chemistry 29, 622–655. doi:10.1002/jcc.20820.

Koeppen K, Hampton TH, Jarek M, Scharfe M, Gerber SA, Mielcarz DW, Demers EG, Dolben EL, Hammond JH, Hogan DA and Stanton BA 2016. A Novel Mechanism of Host-Pathogen Interaction through sRNA in Bacterial Outer Membrane Vesicles. PLoS pathogens 12, e1005672. doi:10.1371/journal.ppat.1005672.

Kohli I and Mukhopadhyay A 2012. Diffusion of Nanoparticles in Semidilute Polymer Solutions: Effect of Different Length Scales. Macromolecules 45, 6143–6149. doi:10.1021/ma301237r.

Kort DW de, Rombouts WH, Hoeben FJM, Janssen HM, van As H and van Duynhoven JPM 2015. Scaling Behavior of Dendritic Nanoparticle Mobility in Semidilute Polymer Solutions. Macromolecules 48, 7585–7591. doi:10.1021/acs.macromol.5b01530.

Kothari D, Das D, Patel S and Goyal A 2015. Dextran and Food Application. In Polysaccharides (eds KG Ramawat and J-M Mérillon), pp. 735–752. Springer International Publishing, Cham.

Koutsoudis MD, Tsaltas D, Minogue TD and Bodman SB von 2006. Quorum-sensing regulation governs bacterial adhesion, biofilm development, and host colonization in Pantoea stewartii subspecies stewartii. Proceedings of the National Academy of Sciences of the United States of America 103, 5983–5988. doi:10.1073/pnas.0509860103.

Kozlowska J, Prus W and Stachowiak N 2019. Microparticles based on natural and synthetic polymers for cosmetic applications. International Journal of Biological Macromolecules 129, 952–956. doi:10.1016/j.ijbiomac.2019.02.091.

Krause WE, Bellomo EG and Colby RH 2001. Rheology of sodium hyaluronate under physiological conditions. Biomacromolecules 2, 65–69. doi:10.1021/bm0055798.

Kreisberg JF, Betts SD, Haase-Pettingell C and King J 2002. The interdigitated beta-helix domain of the P22 tailspike protein acts as a molecular clamp in trimer stabilization. Protein science : a publication of the Protein Society 11, 820–830. doi:10.1110/ps.3440102.

Krstonošić V, Dokić L, Nikolić I and Milanović M 2015. Influence of xanthan gum on oil-in-water emulsion characteristics stabilized by OSA starch. Food Hydrocolloids 45, 9–17. doi:10.1016/j.foodhyd.2014.10.024.

Kumar K, Reddy G, Reddy BVR, Shekar P, Sumanthi J and Chandra KP 2012. Biological role of lectins: A review. Journal of Orofacial Sciences 4, 20. doi:10.4103/0975-8844.99883.

Kunstmann S, Gohlke U, Broeker NK, Roske Y, Heinemann U, Santer M and Barbirz S 2018a. Solvent Networks Tune Thermodynamics of Oligosaccharide Complex Formation in an Extended Protein Binding Site. Journal of the American Chemical Society 140, 10447–10455. doi:10.1021/jacs.8b03719.

Kunstmann S, Scheidt T, Buchwald S, Helm A, Mulard LA, Fruth A and Barbirz S 2018b. Bacteriophage Sf6 Tailspike Protein for Detection of Shigella flexneri Pathogens. Viruses 10. doi:10.3390/v10080431.

Kutateladze M and Adamia R 2008. Phage therapy experience at the Eliava Institute. Medecine et maladies infectieuses 38, 426–430. doi:10.1016/j.medmal.2008.06.023.

Kuttel MM, Jackson GE, Mafata M and Ravenscroft N 2015. Capsular polysaccharide conformations in pneumococcal serotypes 19F and 19A. Carbohydrate Research 406, 27–33. doi:10.1016/j.carres.2014.12.013.

Laemmli UK 1970. Cleavage of structural proteins during the assembly of the head of bacteriophage T4. Nature 227, 680–685.

Lafond PG and Izvekov S 2018. Multiscale Coarse-Graining with Effective Polarizabilities: A Fully Bottom-Up Approach. Journal of chemical theory and computation 14, 1873–1886. doi:10.1021/acs.jctc.7b00917.

Laganà P, Melcarne L and Delia S 2015. Acinetobacter baumannii and endocarditis, rare complication but important clinical relevance. International journal of cardiology 187, 678–679. doi:10.1016/j.ijcard.2015.04.019.

Lai Z, McCulloch J, Lashuel HA and Kelly JW 1997. Guanidine hydrochloride-induced denaturation and refolding of transthyretin exhibits a marked hysteresis: equilibria with high kinetic barriers. Biochemistry 36, 10230–10239. doi:10.1021/bi963195p.

Langlotz C, Schollmeyer M, Coplin DL, Nimtz M and Geider K 2011. Biosynthesis of the repeating units of the exopolysaccharides amylovoran from Erwinia amylovora and stewartan from Pantoea stewartii. Physiological and Molecular Plant Pathology 75, 163–169. doi:10.1016/j.pmpp.2011.04.001.

Larsson AM, Andersson R, Ståhlberg J, Kenne L and Jones TA 2003. Dextranase from Penicillium minioluteum. Structure 11, 1111–1121. doi:10.1016/S0969-2126(03)00147-3.

Lawrence JR, Swerhone GDW, Kuhlicke U and Neu TR 2007. In situ evidence for microdomains in the polymer matrix of bacterial microcolonies. Canadian journal of microbiology 53, 450–458. doi:10.1139/W06-146.

Lee I-M, Tu I-F, Yang F-L, Ko T-P, Liao J-H, Lin N-T, Wu C-Y, Ren C-T, Wang AH-J, Chang C-M, Huang K-F and Wu S-H 2017. Structural basis for fragmenting the exopolysaccharide of Acinetobacter baumannii by bacteriophage ΦAB6 tailspike protein. Scientific reports 7, 42711. doi:10.1038/srep42711.

Leiman PG, Battisti AJ, Bowman VD, Stummeyer K, Mühlenhoff M, Gerardy-Schahn R, Scholl D and Molineux IJ 2007. The structures of bacteriophages K1E and K1-5 explain processive degradation of polysaccharide capsules and evolution of new host specificities. Journal of molecular biology 371, 836–849. doi:10.1016/j.jmb.2007.05.083.

Leon AM, Aguilera JM and Park DJ 2019. Mechanical, rheological and structural properties of fiber-containing microgels based on whey protein and alginate. Carbohydrate Polymers 207, 571–579. doi:10.1016/j.carbpol.2018.11.094.

Li G, Qi L, Li A, Ding R and Zong M 2004. Study on the Kinetics for Enzymatic Degradation of a Natural Polysaccharide,Konjac Glucomannan. Macromolecular Symposia 216, 165–178. doi:10.1002/masy.200451216.

Li Y-H and Tian X 2012. Quorum sensing and bacterial social interactions in biofilms. Sensors (Basel, Switzerland) 12, 2519–2538. doi:10.3390/s120302519.

Li Z, Bian X, Yang X and Karniadakis GE 2016. A comparative study of coarse-graining methods for polymeric fluids: Mori-Zwanzig vs. iterative Boltzmann inversion vs. stochastic parametric optimization. The Journal of Chemical Physics 145, 44102. doi:10.1063/1.4959121.

Lin DM, Koskella B and Lin HC 2017. Phage therapy: An alternative to antibiotics in the age of multi-drug resistance. World journal of gastrointestinal pharmacology and therapeutics 8, 162–173. doi:10.4292/wjgpt.v8.i3.162.

Liston SD, McMahon SA, Le Bas A, Suits MDL, Naismith JH and Whitfield C 2018. Periplasmic depolymerase provides insight into ABC transporter-dependent secretion of bacterial capsular polysaccharides. Proceedings of the National Academy of Sciences of the United States of America 115, E4870-E4879. doi:10.1073/pnas.1801336115.

Liu K and Catchmark JM 2018. Effects of exopolysaccharides from Escherichia coli ATCC 35860 on the mechanical properties of bacterial cellulose nanocomposites. Cellulose 25, 2273–2287. doi:10.1007/s10570-018-1709-3.

Liu T, Angelo JM, Lin D-Q, Lenhoff AM and Yao S-J 2017. Characterization of dextran-grafted hydrophobic charge-induction resins: Structural properties, protein adsorption and transport. Journal of chromatography. A 1517, 44–53. doi:10.1016/j.chroma.2017.07.090.

Lu TK and Collins JJ 2007. Dispersing biofilms with engineered enzymatic bacteriophage. Proceedings of the National Academy of Sciences of the United States of America 104, 11197–11202. doi:10.1073/pnas.0704624104.

Lynch C, O'Connor JA, O'Brien D, Vaughan C, Bolton D, Coffey A and Lucey B 2019. First reported detection of biofilm formation by Campylobacter fetus during investigation of a case of prosthetic valve endocarditis. Journal of clinical pathology. doi:10.1136/jclinpath-2018-205677.

Ma L, Conover M, Lu H, Parsek MR, Bayles K and Wozniak DJ 2009. Assembly and development of the Pseudomonas aeruginosa biofilm matrix. PLoS pathogens 5, e1000354. doi:10.1371/journal.ppat.1000354.

Ma W and Suh WH 2019. Cost-Effective Cosmetic-Grade Hyaluronan Hydrogels for ReNcell VM Human Neural Stem Cell Culture. Biomolecules 9. doi:10.3390/biom9100515.

Maalej H, Hmidet N, Boisset C, Bayma E, Heyraud A and Nasri M 2016. Rheological and emulsifying properties of a gel-like exopolysaccharide produced by Pseudomonas stutzeri AS22. Food Hydrocolloids 52, 634–647. doi:10.1016/j.foodhyd.2015.07.010.

Majkowska-Skrobek G, Łątka A, Berisio R, Maciejewska B, Squeglia F, Romano M, Lavigne R, Struve C and Drulis-Kawa Z 2016. Capsule-Targeting Depolymerase, Derived from Klebsiella KP36 Phage, as a Tool for the Development of Anti-Virulent Strategy. Viruses 8. doi:10.3390/v8120324.

Malinova I, Mahlow S, Alseekh S, Orawetz T, Fernie AR, Baumann O, Steup M and Fettke J 2014. Double knockout mutants of Arabidopsis grown under normal conditions reveal that the plastidial phosphorylase isozyme participates in transitory starch metabolism. Plant physiology 164, 907–921. doi:10.1104/pp.113.227843.

Manning M and Colón W 2004. Structural basis of protein kinetic stability: resistance to sodium dodecyl sulfate suggests a central role for rigidity and a bias toward beta-sheet structure. Biochemistry 43, 11248–11254. doi:10.1021/bi0491898.

Mansell TJ, Linderman SW, Fisher AC and DeLisa MP 2010. A rapid protein folding assay for the bacterial periplasm. Protein science : a publication of the Protein Society 19, 1079–1090. doi:10.1002/pro.388.

Mansfield J, Genin S, Magori S, Citovsky V, Sriariyanum M, Ronald P, Dow M, Verdier V, Beer SV, Machado MA, Toth I, Salmond G and Foster GD 2012. Top 10 plant pathogenic bacteria in molecular plant pathology. Molecular plant pathology 13, 614–629. doi:10.1111/J.1364-3703.2012.00804.X.

Marczak M, Matysiak P, Kutkowska J and Skorupska A 2014. PssP2 is a polysaccharide co-polymerase involved in exopolysaccharide chain-length determination in Rhizobium leguminosarum. PloS one 9, e109106. doi:10.1371/journal.pone.0109106.

Markutsya S, Devarajan A, Baluyut JY, Windus TL, Gordon MS and Lamm MH 2013. Evaluation of coarse-grained mapping schemes for polysaccharide chains in cellulose. The Journal of Chemical Physics 138, 214108. doi:10.1063/1.4808025.

Marolda CL, Tatar LD, Alaimo C, Aebi M and Valvano MA 2006. Interplay of the Wzx translocase and the corresponding polymerase and chain length regulator proteins in the translocation and periplasmic assembly of lipopolysaccharide o antigen. Journal of Bacteriology 188, 5124–5135. doi:10.1128/JB.00461-06.

Mashayak SY, Jochum MN, Koschke K, Aluru NR, Rühle V and Junghans C 2015. Relative Entropy and Optimization-Driven Coarse-Graining Methods in VOTCA. PloS one 10, e0131754. doi:10.1371/journal.pone.0131754.

Masuko T, Minami A, Iwasaki N, Majima T, Nishimura S-I and Lee YC 2005. Carbohydrate analysis by a phenol-sulfuric acid method in microplate format. Analytical Biochemistry 339, 69–72. doi:10.1016/j.ab.2004.12.001.

McCoy AJ, Grosse-Kunstleve RW, Adams PD, Winn MD, Storoni LC and Read RJ 2007. Phaser crystallographic software. Journal of applied crystallography 40, 658–674. doi:10.1107/S0021889807021206.

McKay LL and Baldwin KA 1990. Applications for biotechnology: present and future improvements in lactic acid bacteria. FEMS microbiology reviews 7, 3–14. doi:10.1111/j.1574-6968.1990.tb04876.x.

Metzler R, Jeon J-H, Cherstvy AG and Barkai E 2014. Anomalous diffusion models and their properties: non-stationarity, non-ergodicity, and ageing at the centenary of single particle tracking. Physical chemistry chemical physics : PCCP 16, 24128–24164. doi:10.1039/c4cp03465a.

Miao M, Ma Y, Huang C, Jiang B, Cui SW and Zhang T 2015. Physicochemical properties of a water soluble extracellular homopolysaccharide from Lactobacillus reuteri SK24.003. Carbohydrate Polymers 131, 377–383. doi:10.1016/j.carbpol.2015.05.066.

Michel G, Helbert W, Kahn R, Dideberg O and Kloareg B 2003. The structural bases of the processive degradation of iota-carrageenan, a main cell wall polysaccharide of red algae. Journal of molecular biology 334, 421–433. doi:10.1016/j.jmb.2003.09.056.

Miller S, Schuler B and Seckler R 1998a. A reversibly unfolding fragment of P22 tailspike protein with native structure: the isolated beta-helix domain. Biochemistry 37, 9160–9168. doi:10.1021/bi980190e.

Miller S, Schuler B and Seckler R 1998b. Phage P22 tailspike protein: removal of head-binding domain unmasks effects of folding mutations on native-state thermal stability. Protein science : a publication of the Protein Society 7, 2223–2232. doi:10.1002/pro.5560071021.

Mishra R, Bhat R and Seckler R 2007. Chemical chaperone-mediated protein folding: stabilization of P22 tailspike folding intermediates by glycerol. Biological chemistry 388, 797–804. doi:10.1515/BC.2007.096.

Mitsumata T, Miura T, Takahashi N, Kawai M, Okajima MK and Kaneko T 2013. Ionic state and chain conformation for aqueous solutions of supergiant cyanobacterial polysaccharide. Physical review. E, Statistical, nonlinear, and soft matter physics 87, 42607. doi:10.1103/PhysRevE.87.042607.

Mittal H, Ray SS and Okamoto M 2016. Recent Progress on the Design and Applications of Polysaccharide-Based Graft Copolymer Hydrogels as Adsorbents for Wastewater Purification. Macromolecular Materials and Engineering 301, 496–522. doi:10.1002/mame.201500399.

Miyamoto S and Kollman PA 1992. Settle: An analytical version of the SHAKE and RATTLE algorithm for rigid water models. Journal of Computational Chemistry 13, 952–962. doi:10.1002/jcc.540130805.

Moelling K, Broecker F and Willy C 2018. A Wake-Up Call: We Need Phage Therapy Now. Viruses 10. doi:10.3390/v10120688.

Moore TC, Iacovella CR and McCabe C 2014. Derivation of coarse-grained potentials via multistate iterative Boltzmann inversion. The Journal of Chemical Physics 140, 224104. doi:10.1063/1.4880555.

Morrow BH, Payne GF and Shen J 2015. pH-Responsive Self-Assembly of Polysaccharide through a Rugged Energy Landscape. Journal of the American Chemical Society 137, 13024–13030. doi:10.1021/jacs.5b07761.

Mosier AC, Li Z, Thomas BC, Hettich RL, Pan C and Banfield JF 2015. Elevated temperature alters proteomic responses of individual organisms within a biofilm community. The ISME journal 9, 180–194. doi:10.1038/ismej.2014.113;

Mosquera-Fernández M, Sanchez-Vizuete P, Briandet R, Cabo ML and Balsa-Canto E 2016. Quantitative image analysis to characterize the dynamics of Listeria monocytogenes biofilms. International journal of food microbiology 236, 130–137. doi:10.1016/j.ijfoodmicro.2016.07.015.

Mota R, Rossi F, Andrenelli L, Pereira SB, Philippis R de and Tamagnini P 2016. Released polysaccharides (RPS) from Cyanothece sp. CCY 0110 as biosorbent for heavy metals bioremediation: interactions between metals and RPS binding sites. Applied microbiology and biotechnology 100, 7765–7775. doi:10.1007/s00253-016-7602-9.

Müller I, Lurz R, Kube M, Quedenau C, Jelkmann W and Geider K 2011. Molecular and physiological properties of bacteriophages from North America and Germany affecting the fire blight pathogen Erwinia amylovora. Microbial biotechnology 4, 735–745. doi:10.1111/j.1751-7915.2011.00272.x.

Müller JJ, Barbirz S, Heinle K, Freiberg A, Seckler R and Heinemann U 2008. An intersubunit active site between supercoiled parallel beta helices in the trimeric tailspike endorhamnosidase of Shigella flexneri Phage Sf6. Structure (London, England : 1993) 16, 766–775. doi:10.1016/j.str.2008.01.019.

Murshudov GN, Skubák P, Lebedev AA, Pannu NS, Steiner RA, Nicholls RA, Winn MD, Long F and Vagin AA 2011. REFMAC5 for the refinement of macromolecular crystal structures. Acta crystallographica. Section D, Biological crystallography 67, 355–367. doi:10.1107/S0907444911001314.

Nakamura A, Watanabe H, Ishida T, Uchihashi T, Wada M, Ando T, Igarashi K and Samejima M 2014. Trade-off between processivity and hydrolytic velocity of cellobiohydrolases at the surface of crystalline cellulose. Journal of the American Chemical Society 136, 4584–4592. doi:10.1021/ja4119994.

Nakauma M, Funami T, Fang Y, Nishinari K, Draget KI and Phillips GO 2017. Calcium binding and calcium-induced gelation of normal low-methoxyl pectin modified by low molecular-weight polyuronate fraction. Food Hydrocolloids 69, 318–328. doi:10.1016/j.foodhyd.2016.12.035.

Narayanasamy P 2011. Microbial Plant Pathogens-Detection and Disease Diagnosis. Bacterial and Phytoplasmal Pathogens, Vol.2. Springer Science+Business Media B.V, Dordrecht.

Nardini A, Salleo S and Jansen S 2011. More than just a vulnerable pipeline: xylem physiology in the light of ion-mediated regulation of plant water transport. Journal of Experimental Botany 62, 4701–4718. doi:10.1093/jxb/err208.

Nath P, Mangal R, Kohle F, Choudhury S, Narayanan S, Wiesner U and Archer LA 2018. Dynamics of Nanoparticles in Entangled Polymer Solutions. Langmuir : the ACS journal of surfaces and colloids 34, 241–249. doi:10.1021/acs.langmuir.7b03418.

Nayak AK, Pal D and Santra K 2016. Swelling and drug release behavior of metformin HCl-loaded tamarind seed polysaccharide-alginate beads. International Journal of Biological Macromolecules 82, 1023–1027. doi:10.1016/j.ijbiomac.2015.10.027.

Nielsen MM, Bozonnet S, Seo E-S, Mótyán JA, Andersen JM, Dilokpimol A, Abou Hachem M, Gyémánt G, Naested H, Kandra L, Sigurskjold BW and Svensson B 2009. Two secondary carbohydrate binding sites on the surface of barley alpha-amylase 1 have distinct functions and display synergy in hydrolysis of starch granules. Biochemistry 48, 7686–7697. doi:10.1021/bi900795a.

Nimtz M, Mort A, Wray V, Domke T, Zhang Y, Coplin DL and Geider K 1996. Structure of stewartan, the capsular exopolysaccharide from the corn pathogen Erwinia stewartii. Carbohydrate Research 288, 189–201.

Nobrega FL, Vlot M, Jonge PA de, Dreesens LL, Beaumont HJE, Lavigne R, Dutilh BE and Brouns SJJ 2018. Targeting mechanisms of tailed bacteriophages. Nature reviews. Microbiology 16, 760–773. doi:10.1038/s41579-018-0070-8.

Nockemann P, Thijs B, Parac-Vogt TN, van Hecke K, van Meervelt L, Tinant B, Hartenbach I, Schleid T, Ngan VT, Nguyen MT and Binnemans K 2008. Carboxyl-functionalized task-specific ionic liquids for solubilizing metal oxides. Inorganic chemistry 47, 9987–9999. doi:10.1021/ic801213z.

Nosé S and Klein ML 1983. Constant pressure molecular dynamics for molecular systems. Molecular Physics 50, 1055–1076. doi:10.1080/00268978300102851.

Nwodo UU, Green E and Okoh AI 2012. Bacterial exopolysaccharides: functionality and prospects. International journal of molecular sciences 13, 14002–14015. doi:10.3390/ijms131114002.

Nyström B, Kjøniksen A-L, Beheshti N, Zhu K and Knudsen KD 2009. Rheological and structural aspects on association of hydrophobically modified polysaccharides. Soft Matter 5, 1328. doi:10.1039/b817349d.

Obeng N, Pratama AA and van Elsas JD 2016. The Significance of Mutualistic Phages for Bacterial Ecology and Evolution. Trends in Microbiology 24, 440–449. doi:10.1016/j.tim.2015.12.009.

OEPP/EPPO. Pantoea stewartii subsp. stewartii. EPPO quarantine pest.

OEPP/EPPO 1978. Erwinia stewartii. OEPP/EPPO Bulletin 8.

Okshevsky M and Meyer RL 2015. The role of extracellular DNA in the establishment, maintenance and perpetuation of bacterial biofilms. Critical reviews in microbiology 41, 341–352. doi:10.3109/1040841X.2013.841639.

Okshevsky M, Regina VR and Meyer RL 2015. Extracellular DNA as a target for biofilm control. Current Opinion in Biotechnology 33, 73–80. doi:10.1016/j.copbio.2014.12.002.

Oliveira RRDS, Fermiano D, Feres M, Figueiredo LC, Teles FRF, Soares GMS and Faveri M 2016. Levels of Candidate Periodontal Pathogens in Subgingival Biofilm. Journal of dental research 95, 711–718. doi:10.1177/0022034516634619.

Olsen I, Chen T and Tribble GD 2018a. Genetic exchange and reassignment in Porphyromonas gingivalis. Journal of oral microbiology 10, 1457373. doi:10.1080/20002297.2018.1457373.

Olsen NMC, Thiran E, Hasler T, Vanzieleghem T, Belibasakis GN, Mahillon J, Loessner MJ and Schmelcher M 2018b. Synergistic Removal of Static and Dynamic Staphylococcus aureus Biofilms by Combined Treatment with a Bacteriophage Endolysin and a Polysaccharide Depolymerase. Viruses 10. doi:10.3390/v10080438.

Oniciuc E-A, Cerca N and Nicolau AI 2016. Compositional Analysis of Biofilms Formed by Staphylococcus aureus Isolated from Food Sources. Frontiers in microbiology 7, 390. doi:10.3389/fmicb.2016.00390.

Orgad O, Oren Y, Walker SL and Herzberg M 2011. The role of alginate in Pseudomonas aeruginosa EPS adherence, viscoelastic properties and cell attachment. Biofouling 27, 787–798. doi:10.1080/08927014.2011.603145.

P. Ruas-Madiedo and C.G. de los Reyes-Gavilán. Invited Review: Methods for the Screening, Isolation, and Characterization of Exopolysaccharides Produced by Lactic Acid Bacteria.

Palmer T and Berks BC 2012. The twin-arginine translocation (Tat) protein export pathway. Nature reviews. Microbiology 10, 483–496. doi:10.1038/nrmicro2814.

Panitz C, Frösler J, Wingender J, Flemming H-C and Rettberg P 2019. Tolerances of Deinococcus geothermalis Biofilms and Planktonic Cells Exposed to Space and Simulated Martian Conditions in Low Earth Orbit for Almost Two Years. Astrobiology 19, 979–994. doi:10.1089/ast.2018.1913.

Parrinello M and Rahman A 1981. Polymorphic transitions in single crystals: A new molecular dynamics method. Journal of Applied Physics 52, 7182–7190. doi:10.1063/1.328693.

Pataky JK 2003. Stewart's Wilt of Corn. APSnet Feature Articles. doi:10.1094/APSnetFeature-2003-0703.

Patel KK, Tripathi M, Pandey N, Agrawal AK, Gade S, Anjum MM, Tilak R and Singh S 2019. Alginate lyase immobilized chitosan nanoparticles of ciprofloxacin for the improved antimicrobial activity against the biofilm associated mucoid P. aeruginosa infection in cystic fibrosis. International journal of pharmaceutics 563, 30–42. doi:10.1016/j.ijpharm.2019.03.051.

Pedroso et al 2019. An innovative approach for the biotechnological production of succinoglycan from rice husks. Industrial Crops and Products 137, 615–627. doi:10.1016/j.indcrop.2019.05.052.

Peña C, Millán M and Galindo E 2008. Production of alginate by Azotobacter vinelandii in a stirred fermentor simulating the evolution of power input observed in shake flasks. Process Biochemistry 43, 775–778. doi:10.1016/j.procbio.2008.02.013.

Percival SL, Suleman L, Vuotto C and Donelli G 2015. Healthcare-associated infections, medical devices and biofilms: risk, tolerance and control. Journal of medical microbiology 64, 323–334. doi:10.1099/jmm.0.000032.

Petersen TN, Kauppinen S and Larsen S 1997. The crystal structure of rhamnogalacturonase A from Aspergillus aculeatus: a right-handed parallel beta helix. Structure (London, England : 1993) 5, 533–544.

Peterson BW, He Y, Ren Y, Zerdoum A, Libera MR, Sharma PK, van Winkelhoff A-J, Neut D, Stoodley P, van der Mei HC and Busscher HJ 2015. Viscoelasticity of biofilms and their recalcitrance to mechanical and chemical challenges. FEMS microbiology reviews 39, 234–245. doi:10.1093/femsre/fuu008.

Petrásek Z and Schwille P 2008. Precise measurement of diffusion coefficients using scanning fluorescence correlation spectroscopy. Biophysical journal 94, 1437–1448. doi:10.1529/biophysj.107.108811.

Petri DFS 2015. Xanthan gum: A versatile biopolymer for biomedical and technological applications. Journal of Applied Polymer Science 132, n/a-n/a. doi:10.1002/app.42035.

Pfeilmeier S, Caly DL and Malone JG 2016. Bacterial pathogenesis of plants: future challenges from a microbial perspective: Challenges in Bacterial Molecular Plant Pathology. Molecular plant pathology 17, 1298–1313. doi:10.1111/mpp.12427.

Piercey MJ, Ells TC, Macintosh AJ and Truelstrup Hansen L 2017. Variations in biofilm formation, desiccation resistance and Benzalkonium chloride susceptibility among Listeria monocytogenes strains isolated in Canada. International journal of food microbiology 257, 254–261. doi:10.1016/j.ijfoodmicro.2017.06.025.

Pijning T, van Pouderoyen G, Kluskens L, van der Oost J and Dijkstra BW 2009. The crystal structure of a hyperthermoactive exopolygalacturonase from Thermotoga maritima reveals a unique tetramer. FEBS letters 583, 3665–3670. doi:10.1016/j.febslet.2009.10.047.

Piqué N, Miñana-Galbis D, Merino S and Tomás JM 2015. Virulence Factors of Erwinia amylovora: A Review. International journal of molecular sciences 16, 12836–12854. doi:10.3390/ijms160612836.

Pires DP, Oliveira H, Melo LDR, Sillankorva S and Azeredo J 2016. Bacteriophage-encoded depolymerases: their diversity and biotechnological applications. Applied microbiology and biotechnology 100, 2141–2151. doi:10.1007/s00253-015-7247-0.

Plattner M, Sheider MM and Leiman PG 2018. Crystal structure of Bacteriophage CBA120 tailspike protein 2 enzymatically active domain (TSP2dN, orf211).

Poinot T, Govin A and Grosseau P 2014. Importance of coil-overlapping for the effectiveness of hydroxypropylguars as water retention agent in cement-based mortars. Cement and Concrete Research 56, 61–68. doi:10.1016/j.cemconres.2013.11.005.

Pol-Fachin L, Serrato RV and Verli H 2010. Solution conformation and dynamics of exopolysaccharides from Burkholderia species. Carbohydrate Research 345, 1922–1931. doi:10.1016/j.carres.2010.06.010.

Prado Acosta M, Valdman E, Leite SGF, Battaglini F and Ruzal SM 2005. Biosorption of Copper by Paenibacillus polymyxa Cells and their Exopolysaccharide. World Journal of Microbiology and Biotechnology 21, 1157–1163. doi:10.1007/s11274-005-0381-6.

Qin Y, Jiang J, Zhao L, Zhang J and Wang F 2018. Applications of Alginate as a Functional Food Ingredient. In Biopolymers for Food Design, pp. 409–429. Elsevier.

Racicot K, Kwon JY, Aldo P, Abrahams V, El-Guindy A, Romero R and Mor G 2016. Type I Interferon Regulates the Placental Inflammatory Response to Bacteria and is Targeted by Virus: Mechanism of Polymicrobial Infection-Induced Preterm Birth. American journal of reproductive immunology (New York, N.Y. : 1989) 75, 451–460. doi:10.1111/aji.12501.

Rederstorff E, Rethore G, Weiss P, Sourice S, Beck-Cormier S, Mathieu E, Maillasson M, Jacques Y, Colliec-Jouault S, Fellah BH, Guicheux J and Vinatier C 2017. Enriching a cellulose hydrogel with a biologically active marine exopolysaccharide for cell-based cartilage engineering. Journal of tissue engineering and regenerative medicine 11, 1152–1164. doi:10.1002/term.2018.

Reich L, Becker M, Seckler R and Weikl TR 2009. Invivo folding efficiencies for mutants of the P22 tailspike beta-helix protein correlate with predicted stability changes. Biophysical chemistry 141, 186–192. doi:10.1016/j.bpc.2009.01.015.

Rigouin C, Ladrat CD, Sinquin C, Colliec-Jouault S and Dion M 2009. Assessment of biochemical methods to detect enzymatic depolymerization of polysaccharides. Carbohydrate Polymers 76, 279–284. doi:10.1016/j.carbpol.2008.10.022.

Rochex A, Godon J-J, Bernet N and Escudié R 2008. Role of shear stress on composition, diversity and dynamics of biofilm bacterial communities. Water research 42, 4915–4922. doi:10.1016/j.watres.2008.09.015.

Rodesney CA, Roman B, Dhamani N, Cooley BJ, Katira P, Touhami A and Gordon VD 2017. Mechanosensing of shear by Pseudomonas aeruginosa leads to increased levels of the cyclic-di-GMP signal initiating biofilm development. Proceedings of the National Academy of Sciences of the United States of America 114, 5906–5911. doi:10.1073/pnas.1703255114.

Ropartz D, Bodet PE, Przybylski C, Gonnet F, Daniel R, Fer M, Helbert W, Bertrand D, Rogniaux H 2011 Performance evalutation on a wide set of matrix-assisted laser desorption ionization matrices for the detection of oligosaccharides in a high-throughput mass spectrometric screening of carbohydrate depolymerizing enzymes. Rapid Communications in Mass Spectrometry 14, 2059-70. doi:10.1002/rcm.5060

Roper MC 2011. Pantoea stewartii subsp. stewartii. Lessons learned from a xylem-dwelling pathogen of sweet corn. Molecular plant pathology 12, 628–637. doi:10.1111/j.1364-3703.2010.00698.x.

Ruas-Madiedo P, Hugenholtz J and Zoon P 2002. An overview of the functionality of exopolysaccharides produced by lactic acid bacteria. International Dairy Journal 12, 163–171. doi:10.1016/S0958-6946(01)00160-1.

Ruas-Madiedo P, de los Reyes-Gavilán CG 2005. Invited Review: Methods for the Screening, Isolation, and Characterization of Exopolysaccharides Produced by Lactic Acid Bacteria. Journal of Dairy Science 88, 843-856. doi:10.3168/jds.S0022-0302(05)72750-8

Rühle V, Junghans C, Lukyanov A, Kremer K and Andrienko D 2009. Versatile Object-Oriented Toolkit for Coarse-Graining Applications. Journal of chemical theory and computation 5, 3211–3223. doi:10.1021/ct900369w.

Rwei S-P, Nguyen T-A, Chien-Jung Lee J and Chiang W-Y 2015. Liquid crystal formation and rheological study in aqueous blends of xanthan/acacia gum. Food Hydrocolloids 46, 52–58. doi:10.1016/j.foodhyd.2014.12.013.

Rybtke M, Hultqvist LD, Givskov M and Tolker-Nielsen T 2015. Pseudomonas aeruginosa Biofilm Infections: Community Structure, Antimicrobial Tolerance and Immune Response. Journal of molecular biology 427, 3628–3645. doi:10.1016/j.jmb.2015.08.016.

Sajayan A, Seghal Kiran G, Priyadharshini S, Poulose N and Selvin J 2017. Revealing the ability of a novel polysaccharide bioflocculant in bioremediation of heavy metals sensed in a Vibrio bioluminescence reporter assay. Environmental pollution (Barking, Essex : 1987) 228, 118–127. doi:10.1016/j.envpol.2017.05.020.

Sandai D, Tabana YM, Ouweini AE and Ayodeji IO 2016. Resistance of Candida albicans Biofilms to Drugs and the Host Immune System. Jundishapur journal of microbiology 9, e37385. doi:10.5812/jjm.37385.

Santos ALSD, Galdino ACM, Mello TP de, Ramos LdS, Branquinha MH, Bolognese AM, Columbano Neto J and Roudbary M 2018. What are the advantages of living in a community? A microbial biofilm perspective! Memorias do Instituto Oswaldo Cruz 113, e180212. doi:10.1590/0074-02760180212.

Sauter J and Grafmüller A 2016. Predicting the Chemical Potential and Osmotic Pressure of Polysaccharide Solutions by Molecular Simulations. Journal of chemical theory and computation 12, 4375–4384. doi:10.1021/acs.jctc.6b00295.

Sauter J and Grafmüller A 2017. Procedure for Transferable Coarse-Grained Models of Aqueous Polysaccharides. Journal of chemical theory and computation 13, 223–236. doi:10.1021/acs.jctc.6b00613.

Saxton MJ and Jacobson K 1997. Single-particle tracking: applications to membrane dynamics. Annual review of biophysics and biomolecular structure 26, 373–399. doi:10.1146/annurev.biophys.26.1.373.

Schindelin J, Arganda-Carreras I, Frise E, Kaynig V, Longair M, Pietzsch T, Preibisch S, Rueden C, Saalfeld S, Schmid B, Tinevez J-Y, White DJ, Hartenstein V, Eliceiri K, Tomancak P and Cardona A 2012. Fiji: an open-source platform for biological-image analysis. Nature methods 9, 676–682. doi:10.1038/nmeth.2019.

Schmid J and Sieber V 2015. Enzymatic transformations involved in the biosynthesis of microbial exo-polysaccharides based on the assembly of repeat units. Chembiochem : a European journal of chemical biology 16, 1141–1147. doi:10.1002/cbic.201500035.

Schmid J, Sieber V and Rehm B 2015. Bacterial exopolysaccharides. Biosynthesis pathways and engineering strategies. Frontiers in microbiology 6, 496. doi:10.3389/fmicb.2015.00496.

Schneible JD, Singhal A, Lilova RL, Hall CK, Grafmüller A and Menegatti S 2019. Tailoring the Chemical Modification of Chitosan Hydrogels to Fine-Tune the Release of a Synergistic Combination of Chemotherapeutics. Biomacromolecules 20, 3126–3141. doi:10.1021/acs.biomac.9b00707.

Schollmeyer M, Langlotz C, Huber A, Coplin DL and Geider K 2012. Variations in the molecular masses of the capsular exopolysaccharides amylovoran, pyrifolan and stewartan. International Journal of Biological Macromolecules 50, 518–522. doi:10.1016/j.ijbiomac.2012.01.003.

Schuler B, Fürst F, Osterroth F, Steinbacher S, Huber R and Seckler R 2000. Plasticity and steric strain in a parallel beta-helix: rational mutations in the P22 tailspike protein. Proteins 39, 89–101.

Schulz EC, Schwarzer D, Frank M, Stummeyer K, Mühlenhoff M, Dickmanns A, Gerardy-Schahn R and Ficner R 2010. Structural basis for the recognition and cleavage of polysialic acid by the bacteriophage K1F tailspike protein EndoNF. Journal of molecular biology 397, 341–351. doi:10.1016/j.jmb.2010.01.028.

Schuster E, Lundin L and Williams MAK 2012. Investigating the Relationship between Network Mechanics and Single-Chain Extension Using Biomimetic Polysaccharide Gels. Macromolecules 45, 4863–4869. doi:10.1021/ma300724n.

Schwarczinger I, Kolozsváriné Nagy J, Künstler A, Szabó L, Geider K, Király L and Pogány M 2017. Characterization of Myoviridae and Podoviridae family bacteriophages of Erwinia amylovora from Hungary - potential of application in biological control of fire blight. European Journal of Plant Pathology 149, 639–652. doi:10.1007/s10658-017-1214-9.

Schwarzer D, Browning C, Stummeyer K, Oberbeck A, Mühlenhoff M, Gerardy-Schahn R and Leiman PG 2015. Structure and biochemical characterization of bacteriophage phi92 endosialidase. Virology 477, 133–143. doi:10.1016/j.virol.2014.11.002.

Schwarzer D, Stummeyer K, Haselhorst T, Freiberger F, Rode B, Grove M, Scheper T, Itzstein M von, Mühlenhoff M and Gerardy-Schahn R 2009. Proteolytic release of the intramolecular chaperone domain confers processivity to endosialidase F. The Journal of biological chemistry 284, 9465–9474. doi:10.1074/jbc.M808475200.

Sekhohola-Dlamini L and Tekere M 2019. Microbiology of municipal solid waste landfills: a review of microbial dynamics and ecological influences in waste bioprocessing. Biodegradation. doi:10.1007/s10532-019-09890-x.

Serra DO, Klauck G and Hengge R 2015. Vertical stratification of matrix production is essential for physical integrity and architecture of macrocolony biofilms of Escherichia coli. Environmental microbiology 17, 5073–5088. doi:10.1111/1462-2920.12991.

Serra DO, Richter AM and Hengge R 2013a. Cellulose as an architectural element in spatially structured Escherichia coli biofilms. Journal of Bacteriology 195, 5540–5554. doi:10.1128/JB.00946-13.

Serra DO, Richter AM, Klauck G, Mika F and Hengge R 2013b. Microanatomy at cellular resolution and spatial order of physiological differentiation in a bacterial biofilm. mBio 4, e00103-13. doi:10.1128/mBio.00103-13.

Seul A, Müller JJ, Andres D, Stettner E, Heinemann U and Seckler R 2014. Bacteriophage P22 tailspike. Structure of the complete protein and function of the interdomain linker. Acta crystallographica. Section D, Biological crystallography 70, 1336–1345. doi:10.1107/S1399004714002685.

Seviour T, Malde AK, Kjelleberg S, Yuan Z and Mark AE 2012. Molecular dynamics unlocks atomic level self-assembly of the exopolysaccharide matrix of water-treatment granular biofilms. Biomacromolecules 13, 1965–1972. doi:10.1021/bm3005808.

Sharon N 2007. Lectins: carbohydrate-specific reagents and biological recognition molecules. Journal of Biological Chemistry 282, 2753–2764. doi:10.1074/JBC.X600004200.

Sheppard DC and Howell PL 2016. Biofilm Exopolysaccharides of Pathogenic Fungi. Lessons from Bacteria. The Journal of biological chemistry 291, 12529–12537. doi:10.1074/jbc.R116.720995.

Shi X and Zhu X 2009. Biofilm formation and food safety in food industries. Trends in Food Science & Technology 20, 407–413. doi:10.1016/j.tifs.2009.01.054.

Singh A, Arya SK, Glass N, Hanifi-Moghaddam P, Naidoo R, Szymanski CM, Tanha J and Evoy S 2010. Bacteriophage tailspike proteins as molecular probes for sensitive and selective bacterial detection. Biosensors & bioelectronics 26, 131–138. doi:10.1016/j.bios.2010.05.024.

Singh R, Sahore S, Kaur P, Rani A and Ray P 2016. Penetration barrier contributes to bacterial biofilm-associated resistance against only select antibiotics, and exhibits genus-, strain- and antibiotic-specific differences. Pathogens and disease 74. doi:10.1093/femspd/ftw056.

Singhvi G, Hans N, Shiva N and Kumar Dubey S 2019. Chapter 5 - Xanthan gum in drug delivery applications. In Natural polysaccharides in drug delivery and biomedical applications (eds MS Hasnain and AK Nayak), pp. 121–144. Academic Press, an imprint of Elsevier, London.

Sørbotten A, Horn SJ, Eijsink VGH and Vårum KM 2005. Degradation of chitosans with chitinase B from Serratia marcescens. Production of chito-oligosaccharides and insight into enzyme processivity. The FEBS journal 272, 538–549. doi:10.1111/j.1742-4658.2004.04495.x.

Sorin EJ and Pande VS 2005. Exploring the helix-coil transition via all-atom equilibrium ensemble simulations. Biophysical journal 88, 2472–2493. doi:10.1529/biophysj.104.051938.

Sparta KM, Krug M, Heinemann U, Mueller U and Weiss MS 2016. XDSAPP2.0. Journal of Applied Crystallography 49, 1085–1092. doi:10.1107/S1600576716004416.

Staggs JEJ 2002. Modelling random scission of linear polymers. Polymer Degradation and Stability 76, 37–44. doi:10.1016/S0141-3910(01)00263-4.

Steinbacher S, Seckler R, Miller S, Steipe B, Huber R and Reinemer P 1994. Crystal structure of P22 tailspike protein: interdigitated subunits in a thermostable trimer. Science (New York, N.Y.) 265, 383–386. doi:10.1126/science.8023158.

Steinbacher Sea. Phage P22 Tailspike Protein: Crystal Structure of the Head-binding Domain at 2.3 A , Fully Refined Structure of the Endorhamnosidase at 1.56 A Resolution, and the Molecular Basis of O-Antigen Recognition and Cleavage.

Stewart EJ, Ganesan M, Younger JG and Solomon MJ 2015. Artificial biofilms establish the role of matrix interactions in staphylococcal biofilm assembly and disassembly. Scientific reports 5, 13081. doi:10.1038/srep13081.

Stewart EJ, Satorius AE, Younger JG and Solomon MJ 2013. Role of environmental and antibiotic stress on Staphylococcus epidermidis biofilm microstructure. Langmuir : the ACS journal of surfaces and colloids 29, 7017–7024. doi:10.1021/la401322k.

Stewart FC 1897. A bacterial disease of sweet corn. N. Y. Agric. Exp. Sta. Bull. 130, 422–439.

Stewart PS, Davison WM and Steenbergen JN 2009. Daptomycin rapidly penetrates a Staphylococcus epidermidis biofilm. Antimicrobial Agents and Chemotherapy 53, 3505–3507. doi:10.1128/AAC.01728-08.

Strohalm M, Kavan D, Novák P, Volný M and Havlícek V 2010. mMass 3: a cross-platform software environment for precise analysis of mass spectrometric data. Analytical chemistry 82, 4648–4651. doi:10.1021/ac100818g.

Stummeyer K, Schwarzer D, Claus H, Vogel U, Gerardy-Schahn R and Mühlenhoff M 2006. Evolution of bacteriophages infecting encapsulated bacteria: lessons from Escherichia coli K1-specific phages. Molecular microbiology 60, 1123–1135. doi:10.1111/j.1365-2958.2006.05173.x.

Sutherland I 2001a. Biofilm exopolysaccharides: a strong and sticky framework. Microbiology (Reading, England) 147, 3–9. doi:10.1099/00221287-147-1-3.

Sutherland I 2001b. The biofilm matrix – an immobilized but dynamic microbial environment. Trends in Microbiology 9, 222–227. doi:10.1016/S0966-842X(01)02012-1.

Svircev A, Roach D and Castle A 2018. Framing the Future with Bacteriophages in Agriculture. Viruses 10. doi:10.3390/v10050218.

Tako M and Nakamura S 1985. Synergistic interaction between xanthan and guar gum. Carbohydrate Research 138, 207–213. doi:10.1016/0008-6215(85)85104-1.

Tako M and Nakamura S 1986. D-Mannose-specific interaction between xanthan and D-galacto-D-mannan. FEBS letters 204, 33–36. doi:10.1016/0014-5793(86)81382-5.

Tao K, Kelly S and Radutoiu S 2019. Microbial associations enabling nitrogen acquisition in plants. Current opinion in microbiology 49, 83–89. doi:10.1016/j.mib.2019.10.005.

Tayal A, Kelly RM and Khan SA 1999. Rheology and Molecular Weight Changes during Enzymatic Degradation of a Water-Soluble Polymer. Macromolecules 32, 294–300. doi:10.1021/ma980773w.

Terwilliger TC, Adams PD, Read RJ, McCoy AJ, Moriarty NW, Grosse-Kunstleve RW, Afonine PV, Zwart PH and Hung LW 2009. Decision-making in structure solution using Bayesian estimates of map quality: the PHENIX AutoSol wizard. Acta crystallographica. Section D, Biological crystallography 65, 582–601. doi:10.1107/S0907444909012098.

Thomsen MS, Wernberg T, Altieri A, Tuya F, Gulbransen D, McGlathery KJ, Holmer M and Silliman BR 2010. Habitat cascades: the conceptual context and global relevance of facilitation cascades via habitat formation and modification. Integrative and comparative biology 50, 158–175. doi:10.1093/icb/icq042.

Tielen P, Kuhn H, Rosenau F, Jaeger K-E, Flemming H-C and Wingender J 2013. Interaction between extracellular lipase LipA and the polysaccharide alginate of Pseudomonas aeruginosa. BMC microbiology 13, 159. doi:10.1186/1471-2180-13-159.

Tielen P, Rosenau F, Wilhelm S, Jaeger K-E, Flemming H-C and Wingender J 2010. Extracellular enzymes affect biofilm formation of mucoid Pseudomonas aeruginosa. Microbiology (Reading, England) 156, 2239–2252. doi:10.1099/mic.0.037036-0.

Tinevez J-Y, Perry N, Schindelin J, Hoopes GM, Reynolds GD, Laplantine E, Bednarek SY, Shorte SL and Eliceiri KW 2017. TrackMate: An open and extensible platform for single-particle tracking. Methods (San Diego, Calif.) 115, 80–90. doi:10.1016/j.ymeth.2016.09.016.

Tironi IG, Sperb R, Smith PE and van Gunsteren WF 1995. A generalized reaction field method for molecular dynamics simulations. The Journal of Chemical Physics 102, 5451–5459. doi:10.1063/1.469273.

Tischler AH, Lie L, Thompson CM and Visick KL 2018. Discovery of Calcium as a Biofilm-Promoting Signal for Vibrio fischeri Reveals New Phenotypes and Underlying Regulatory Complexity. Journal of Bacteriology 200. doi:10.1128/JB.00016-18.

Tkhilaishvili T, Lombardi L, Klatt A-B, Trampuz A and Di Luca M 2018. Bacteriophage Sb-1 enhances antibiotic activity against biofilm, degrades exopolysaccharide matrix and targets persisters of Staphylococcus aureus. International journal of antimicrobial agents 52, 842–853. doi:10.1016/j.ijantimicag.2018.09.006.

Tømmeraas K and Melander C 2008. Kinetics of hyaluronan hydrolysis in acidic solution at various pH values. Biomacromolecules 9, 1535–1540. doi:10.1021/bm701341y.

Torelli R, Cacaci M, Papi M, Paroni Sterbini F, Martini C, Posteraro B, Palmieri V, Spirito M de, Sanguinetti M and Bugli F 2017. Different effects of matrix degrading enzymes towards biofilms formed by E. faecalis and E. faecium clinical isolates. Colloids and surfaces. B, Biointerfaces 158, 349–355. doi:10.1016/j.colsurfb.2017.07.010.

Torres CAV, Ferreira ARV, Freitas F, Reis MAM, Coelhoso I, Sousa I and Alves VD 2015. Rheological studies of the fucose-rich exopolysaccharide FucoPol. International Journal of Biological Macromolecules 79, 611–617. doi:10.1016/j.ijbiomac.2015.05.029.

Touchon M, Moura de Sousa JA and Rocha EP 2017. Embracing the enemy: the diversification of microbial gene repertoires by phage-mediated horizontal gene transfer. Current opinion in microbiology 38, 66–73. doi:10.1016/j.mib.2017.04.010.

Toyofuku M, Inaba T, Kiyokawa T, Obana N, Yawata Y and Nomura N 2016. Environmental factors that shape biofilm formation. Bioscience, biotechnology, and biochemistry 80, 7–12. doi:10.1080/09168451.2015.1058701.

Truhlar SME, Cunningham EL and Agard DA 2004. The folding landscape of Streptomyces griseus protease B reveals the energetic costs and benefits associated with evolving kinetic stability. Protein science : a publication of the Protein Society 13, 381–390. doi:10.1110/ps.03336804.

Tseng BS, Majerczyk CD, Passos da Silva D, Chandler JR, Greenberg EP and Parsek MR 2016. Quorum Sensing Influences Burkholderia thailandensis Biofilm Development and Matrix Production. Journal of Bacteriology 198, 2643–2650. doi:10.1128/JB.00047-16.

Tseng BS, Zhang W, Harrison JJ, Quach TP, Song JL, Penterman J, Singh PK, Chopp DL, Packman AI and Parsek MR 2013. The extracellular matrix protects Pseudomonas aeruginosa biofilms by limiting the penetration of tobramycin. Environmental microbiology 15, 2865–2878. doi:10.1111/1462-2920.12155.

Tsereteli L and Grafmüller A 2017. An accurate coarse-grained model for chitosan polysaccharides in aqueous solution. PloS one 12, e0180938. doi:10.1371/journal.pone.0180938.

Tu J, Park T, Morado DR, Hughes KT, Molineux IJ and Liu J 2017. Dual host specificity of phage SP6 is facilitated by tailspike rotation. Virology 507, 206–215. doi:10.1016/j.virol.2017.04.017.

Tuinier R, van Casteren WHM, Looijesteijn PJ, Schols HA, Voragen AGJ and Zoon P 2001. Effects of structural modifications on some physical characteristics of exopolysaccharides from Lactococcus lactis. Biopolymers 59, 160–166. doi:10.1002/1097-0282(200109)59:3<160::AID-BIP1015>3.0.CO;2-V.

Ullah H, Santos HA and Khan T 2016. Applications of bacterial cellulose in food, cosmetics and drug delivery. Cellulose 23, 2291–2314. doi:10.1007/s10570-016-0986-y.

van der Spoel D, Lindahl E, Hess B, Groenhof G, Mark AE and Berendsen HJC 2005. GROMACS: fast, flexible, and free. Journal of Computational Chemistry 26, 1701–1718. doi:10.1002/jcc.20291.

van Gunsteren WF and Berendsen HJC 1988. A Leap-frog Algorithm for Stochastic Dynamics. Molecular Simulation 1, 173–185. doi:10.1080/08927028808080941.

van Ieperen W 2007. Ion-mediated changes of xylem hydraulic resistance in planta: fact or fiction? Trends in plant science 12, 137–142. doi:10.1016/j.tplants.2007.03.001.

van Wolferen M, Orell A and Albers S-V 2018. Archaeal biofilm formation. Nature reviews. Microbiology 16, 699–713. doi:10.1038/s41579-018-0058-4.

Vanneste JL 2000. Fire blight: the disease and its causative agent, *Erwinia amylovora*. CABI Publishing, Wallingford.

Varrot A, Frandsen TP, Ossowski I von, Boyer V, Cottaz S, Driguez H, Schülein M and Davies GJ 2003. Structural Basis for Ligand Binding and Processivity in Cellobiohydrolase Cel6A from Humicola insolens. Structure 11, 855–864. doi:10.1016/S0969-2126(03)00124-2.

Vidakovic L, Singh PK, Hartmann R, Nadell CD and Drescher K 2018. Dynamic biofilm architecture confers individual and collective mechanisms of viral protection. Nature microbiology 3, 26–31. doi:10.1038/s41564-017-0050-1.

Vuong C, Kocianova S, Voyich JM, Yao Y, Fischer ER, DeLeo FR and Otto M 2004. A crucial role for exopolysaccharide modification in bacterial biofilm formation, immune evasion, and virulence. Journal of Biological Chemistry 279, 54881–54886. doi:10.1074/jbc.M411374200.

Walterson AM and Stavrinides J 2015. Pantoea. Insights into a highly versatile and diverse genus within the Enterobacteriaceae. FEMS microbiology reviews 39, 968–984. doi:10.1093/femsre/fuv027.

Wang C, Saito M, Ogawa M and Yoshida S-I 2016a. Colony types and virulence traits of Legionella feeleii determined by exopolysaccharide materials. FEMS microbiology letters 363. doi:10.1093/femsle/fnw098.

Wang H, Wei C-X, Min L and Zhu L-Y 2018. Good or bad: gut bacteria in human health and diseases. Biotechnology & Biotechnological Equipment 32, 1075–1080. doi:10.1080/13102818.2018.1481350.

Wang HM, Loganathan D and Linhardt RJ 1991. Determination of the pKa of glucuronic acid and the carboxy groups of heparin by 13C-nuclear-magnetic-resonance spectroscopy. The Biochemical journal 278 (Pt 3), 689–695. doi:10.1042/bj2780689.

Wang X, Yang F and Bodman SB von 2012. The genetic and structural basis of two distinct terminal side branch residues in stewartan and amylovoran exopolysaccharides and their potential role in host adaptation. Molecular microbiology 83, 195–207. doi:10.1111/j.1365-2958.2011.07926.x.

Wang Y, Han G, Guo B and Huang J 2016b. Hyaluronan oligosaccharides promote diabetic wound healing by increasing angiogenesis. Pharmacological reports : PR 68, 1126–1132. doi:10.1016/j.pharep.2016.07.001.

Waseh S, Hanifi-Moghaddam P, Coleman R, Masotti M, Ryan S, Foss M, MacKenzie R, Henry M, Szymanski CM and Tanha J 2010. Orally administered P22 phage tailspike protein reduces salmonella colonization in chickens. Prospects of a novel therapy against bacterial infections. PloS one 5, e13904. doi:10.1371/journal.pone.0013904.

Wehle M, Vilotijevic I, Lipowsky R, Seeberger PH, Silva DV and Santer M 2012. Mechanical compressibility of the glycosylphosphatidylinositol (GPI) anchor backbone governed by independent glycosidic linkages. Journal of the American Chemical Society 134, 18964–18972. doi:10.1021/ja302803r.

Weiss M, Elsner M, Kartberg F and Nilsson T 2004. Anomalous subdiffusion is a measure for cytoplasmic crowding in living cells. Biophysical journal 87, 3518–3524. doi:10.1529/biophysj.104.044263.

Weller-Stuart T, Maayer P de and Coutinho T 2017. Pantoea ananatis. Genomic insights into a versatile pathogen. Molecular plant pathology 18, 1191–1198. doi:10.1111/mpp.12517.

Werner WE, Demorest DM, Stevens J and Wiktorowicz JE 1993. Size-dependent separation of proteins denatured in SDS by capillary electrophoresis using a replaceable sieving matrix. Analytical Biochemistry 212, 253–258. doi:10.1006/abio.1993.1319.

Wessman M, Bjarnsholt T, Eickhardt-Sørensen SR, Johansen HK and Homøe P 2015. Mucosal biofilm detection in chronic otitis media: a study of middle ear biopsies from Greenlandic patients. European archives of oto-rhino-laryngology : official journal of the European Federation of Oto-Rhino-Laryngological Societies (EUFOS) : affiliated with the German Society for Oto-Rhino-Laryngology - Head and Neck Surgery 272, 1079–1085. doi:10.1007/s00405-014-2886-9.

Whitfield C 2006. Biosynthesis and assembly of capsular polysaccharides in Escherichia coli. Annual review of biochemistry 75, 39–68. doi:10.1146/annurev.biochem.75.103004.142545.

Wilking JN, Zaburdaev V, Volder M de, Losick R, Brenner MP and Weitz DA 2013. Liquid transport facilitated by channels in Bacillus subtilis biofilms. Proceedings of the National Academy of Sciences of the United States of America 110, 848–852. doi:10.1073/pnas.1216376110.

Wilkinson J, Abd-Elaziz K, den Daas I, Wemer J, van Haastert M, Hodgkinson V, Foster M and Coyle C 2019. Two placebo-controlled crossover studies in healthy subjects to evaluate gastric acid neutralization by an alginate-antacid formulation (Gaviscon Double Action). Drug development and industrial pharmacy 45, 430–438. doi:10.1080/03639045.2018.1546314.

Williams S.D., M.J., Hand, F.P. 2019. https://ohioline.osu.edu/factsheet/plpath-gen-6. Accessed: 24.09.2019.

Witten J and Ribbeck K 2017. The particle in the spider's web. Transport through biological hydrogels. Nanoscale 9, 8080–8095. doi:10.1039/c6nr09736g.

Wu Z, Cui Q and Yethiraj A 2010. A new coarse-grained model for water: the importance of electrostatic interactions. The journal of physical chemistry. B 114, 10524–10529. doi:10.1021/jp1019763.

Wyatt NB and Liberatore MW 2009. Rheology and viscosity scaling of the polyelectrolyte xanthan gum. Journal of Applied Polymer Science 114, 4076–4084. doi:10.1002/app.31093.

Xiang Y and Rossmann MG 2011. Crystal structure of the pre-mature bacteriophage phi29 gene product 12.

Xiao J and Koo H 2010. Structural organization and dynamics of exopolysaccharide matrix and microcolonies formation by Streptococcus mutans in biofilms. Journal of applied microbiology 108, 2103–2113. doi:10.1111/j.1365-2672.2009.04616.x.

Yamasaki M, Ogura K, Hashimoto W, Mikami B and Murata K 2005. A structural basis for depolymerization of alginate by polysaccharide lyase family-7. Journal of molecular biology 352, 11–21. doi:10.1016/j.jmb.2005.06.075.

Yang J, Chen S and Fang Y 2009. Viscosity study of interactions between sodium alginate and CTAB in dilute solutions at different pH values. Carbohydrate Polymers 75, 333–337. doi:10.1016/j.carbpol.2008.07.037.

Yang Y, Feng F, Zhou Q, Zhao F, Du R, Zhou Z and Han Y 2018. Isolation, purification and characterization of exopolysaccharide produced by Leuconostoc pseudomesenteroides YF32 from soybean paste. International Journal of Biological Macromolecules 114, 529–535. doi:10.1016/j.ijbiomac.2018.03.162.

Yang Y, Sun Q, Xu X, Yang X, Gao Y, Sun X, Zhao Y, Ding Z, Ge W, Cheng R and Zhang J 2019. Oral Administration of Succinoglycan Riclin Improves Diet-Induced Hypercholesterolemia in Mice. Journal of agricultural and food chemistry 67, 13307–13317. doi:10.1021/acs.jafc.9b06034.

Yi L, Ouyang Y, Sun X, Xu N, Linhardt RJ and Zhang Z 2015. Qualitative and quantitative analysis of branches in dextran using high-performance anion exchange chromatography coupled to quadrupole time-of-flight mass spectrometry. Journal of chromatography. A 1423, 79–85. doi:10.1016/j.chroma.2015.10.064.

York GM and Walker GC 1997. The Rhizobium meliloti exoK gene and prsD/prsE/exsH genes are components of independent degradative pathways which contribute to production of low-molecular-weight succinoglycan. Molecular microbiology 25, 117–134. doi:10.1046/j.1365-2958.1997.4481804.x.

Yu L, Xu X, Zhou J, Lv G and Chen J 2017. Chain conformation and rheological behavior of exopolysaccharide from Bacillus mucilaginosus SM-01. Food Hydrocolloids 65, 165–174. doi:10.1016/j.foodhyd.2016.11.013.

Yu S, Su T, Wu H, Liu S, Di Wang, Zhao T, Jin Z, Du W, Zhu M-J, Chua SL, Yang L, Zhu D, Gu L and Ma LZ 2015. PslG, a self-produced glycosyl hydrolase, triggers biofilm disassembly by disrupting exopolysaccharide matrix. Cell research 25, 1352–1367. doi:10.1038/cr.2015.129;

Yu Y, Singh H, Tsitrin T, Kwon K, Bekele S, Eguez RV, Lin Y-H, Sikorski P, Moncera KJ, Torralba MG, Morrow L, Wolcott R, Nelson KE and Pieper R 2019. Nutritional Immunity and Antibiotic Drug Treatments Influence Microbial Composition but Fail to Eliminate Urethral Catheter Biofilms in Recurrently Catheterized Patients.

Zakariassen H, Eijsink VGH and Sørlie M 2010. Signatures of activation parameters reveal substrate-dependent rate determining steps in polysaccharide turnover by a family 18 chitinase. Carbohydrate Polymers 81, 14–20. doi:10.1016/j.carbpol.2010.01.048.

Zeng G, Vad BS, Dueholm MS, Christiansen G, Nilsson M, Tolker-Nielsen T, Nielsen PH, Meyer RL and Otzen DE 2015. Functional bacterial amyloid increases Pseudomonas biofilm hydrophobicity and stiffness. Frontiers in microbiology 6, 1099. doi:10.3389/fmicb.2015.01099.

Zhang P, Guo J-S, Shen Y, Yan P, Chen Y-P, Wang H, Yang J-X, Fang F and Li C 2015. Microbial communities, extracellular proteomics and polysaccharides: A comparative investigation on biofilm and suspended sludge. Bioresource technology 190, 21–28. doi:10.1016/j.biortech.2015.04.058.

Zhang Y, Rossi F, Papa S, Violatto MB, Bigini P, Sorbona M, Redaelli F, Veglianese P, Hilborn J and Ossipov DA 2016. Non-invasive in vitro and in vivo monitoring of degradation of fluorescently labeled hyaluronan hydrogels for tissue engineering applications. Acta biomaterialia 30, 188–198. doi:10.1016/j.actbio.2015.11.053.

Zhao T, Tashiro Y and Sonomoto K 2019. Smart fermentation engineering for butanol production: designed biomass and consolidated bioprocessing systems. Applied microbiology and biotechnology 103, 9359–9371. doi:10.1007/s00253-019-10198-2.

Zheng Y, Monty J and Linhardt RJ 2015. Polysaccharide-based nanocomposites and their applications. Carbohydrate Research 405, 23–32. doi:10.1016/j.carres.2014.07.016.

8. Supplementary

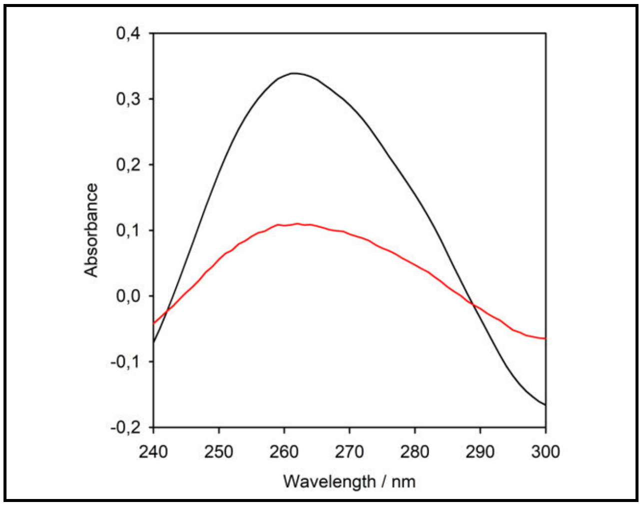

Figure S1: Purification of labeled P22 bacteriophages

The absorbance spectra of P22 phages are shown after incubation with Yo-Pro (black) or after purification over a PD-10 Desalting Column (red).

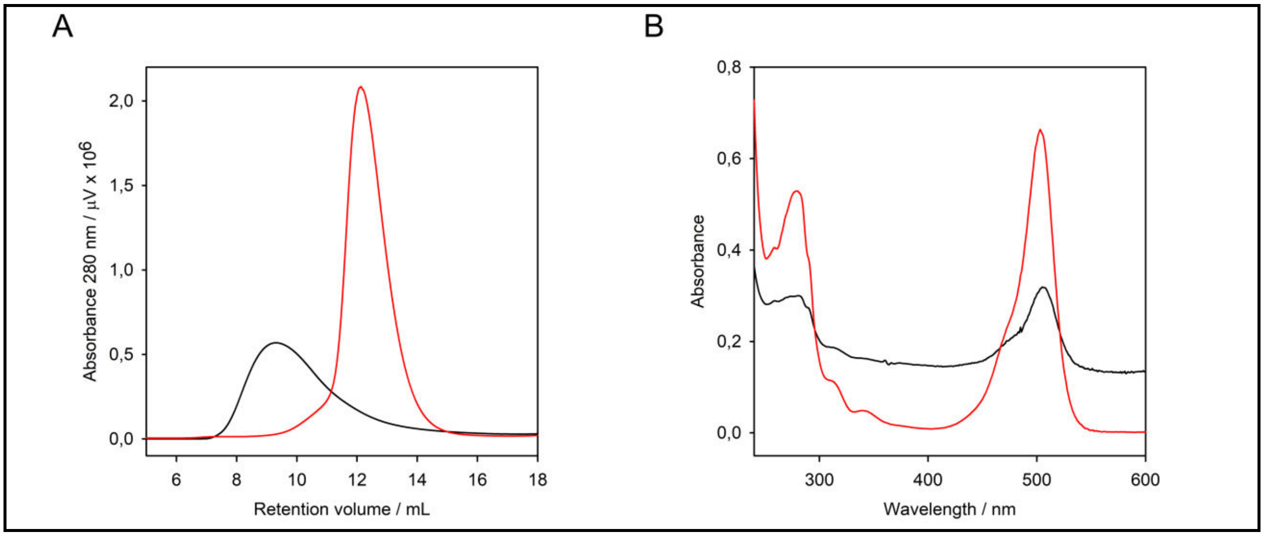

Figure S2: Purification of fluorescently labeled proteins

(A) WceF (black) or ΦEa1h TSP (red) were fluorescently labeled with ATTO 488 and separated from free dye by size-exclusion chromatography (Superdex^{TM} S200 10/300). (B) The protein concentration was determined from each absorbance spectra by comparing the absorption at 280 and 550 nm.

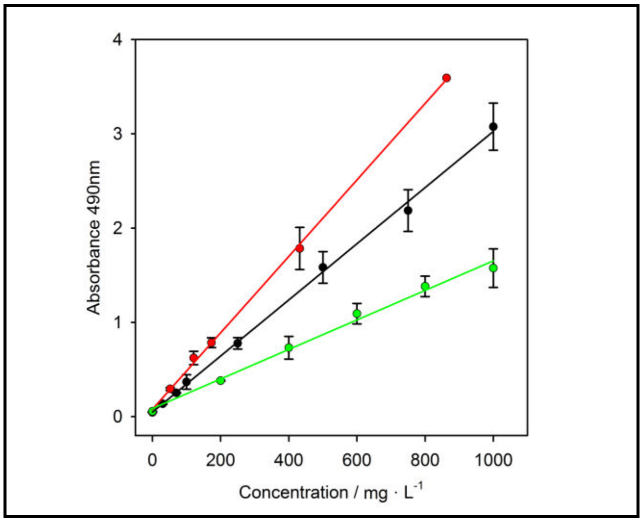

Figure S3: Phenol sulfuric acid calibration curves

The linearity of the phenol sulfuric acid method was tested at different glucose (black), sucrose (red) and stewartan concentrations (green).

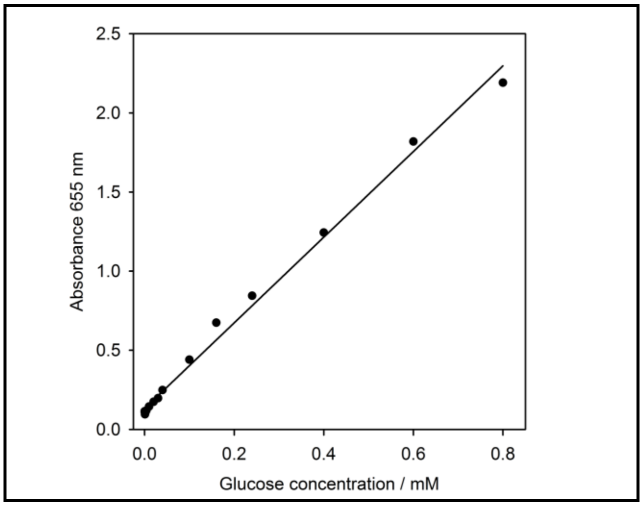

Figure S4: MBTH-Test calibration curve

The linearity of the MBTH-Test was tested at different glucose concentrations.

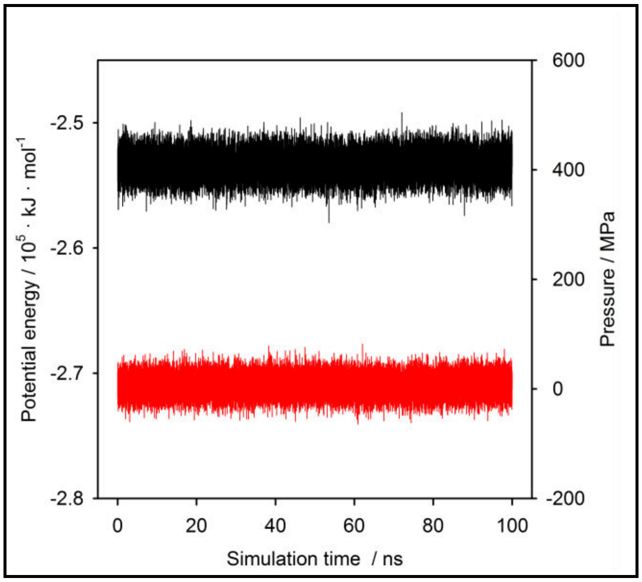

Figure S5: MD run of the atomistic simulation of 3 RU stewartan

An atomistic system of stewartan was equilibrated in NPT and NVT ensembles. Here, the potential energy (black) and the pressure (red) of the final 100 ns MD run is shown.

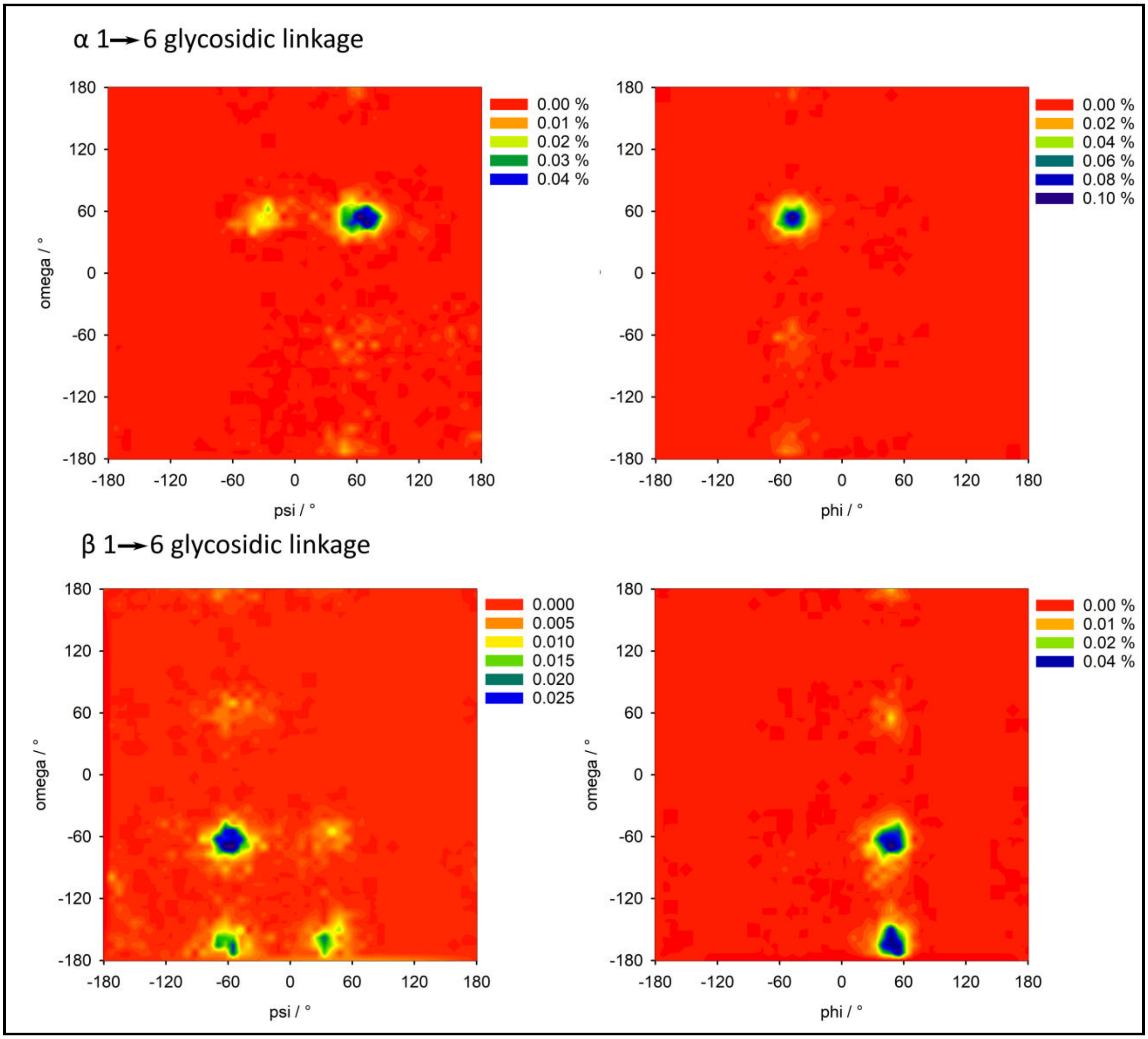

Figure S6: Heat maps of the torsion angle omega ω in dependence to psi ψ and phi ϕ of 1-6 linkages in 3 RU stewartan Conformations of the stewartan torsion angles were taken from the 100 ns MD run of the atomistic stewartan reference system.

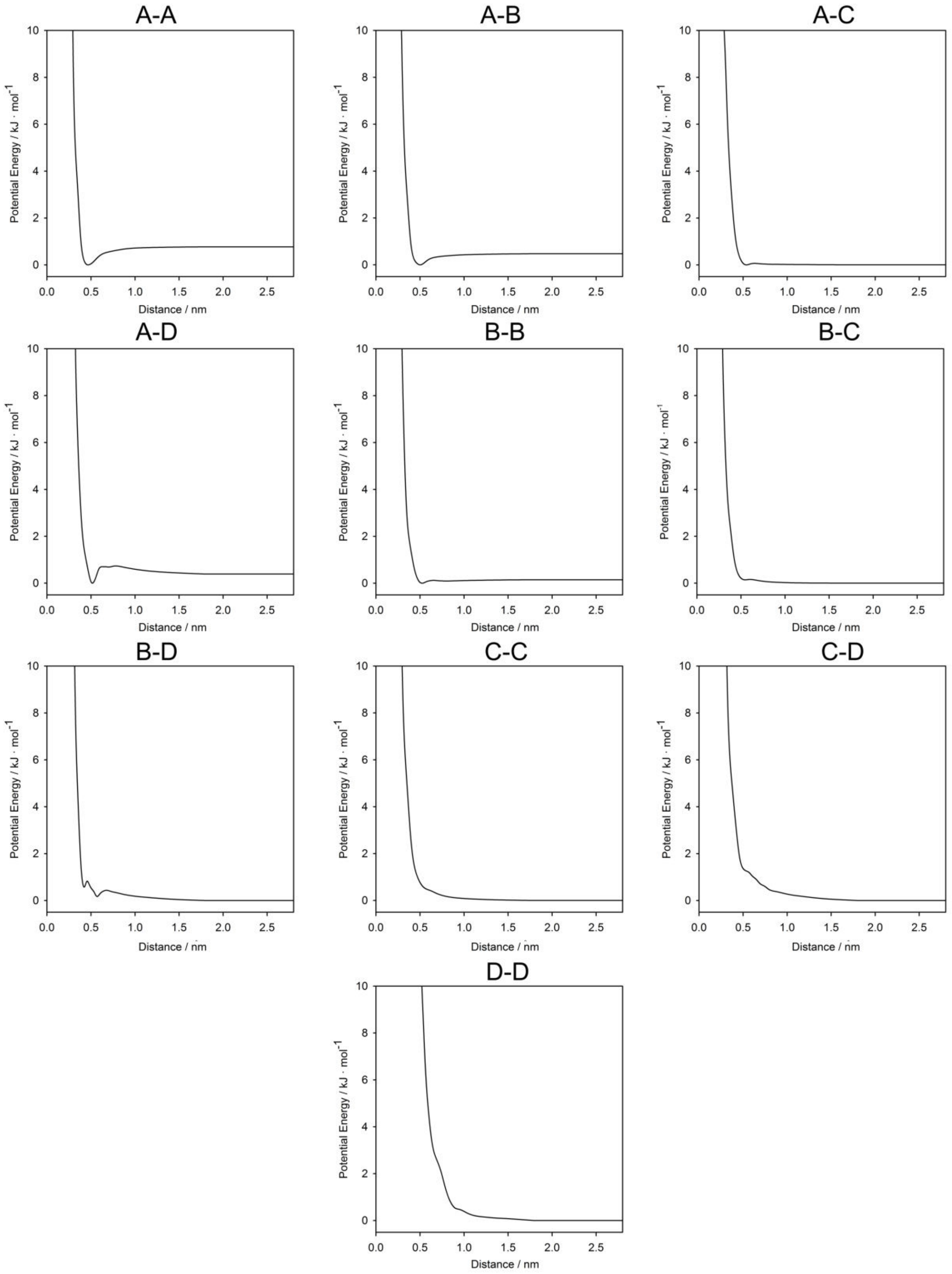

Figure S7: All nonbonded interactions used in the coarse-grained stewartan systems

The nonbonded potentials between the coarse-grained beads of the stewartan model were obtained from the atomistic reference structure using the force matching method. The coarse-grained mapping of the stewartan structure is shown in Figure 9.

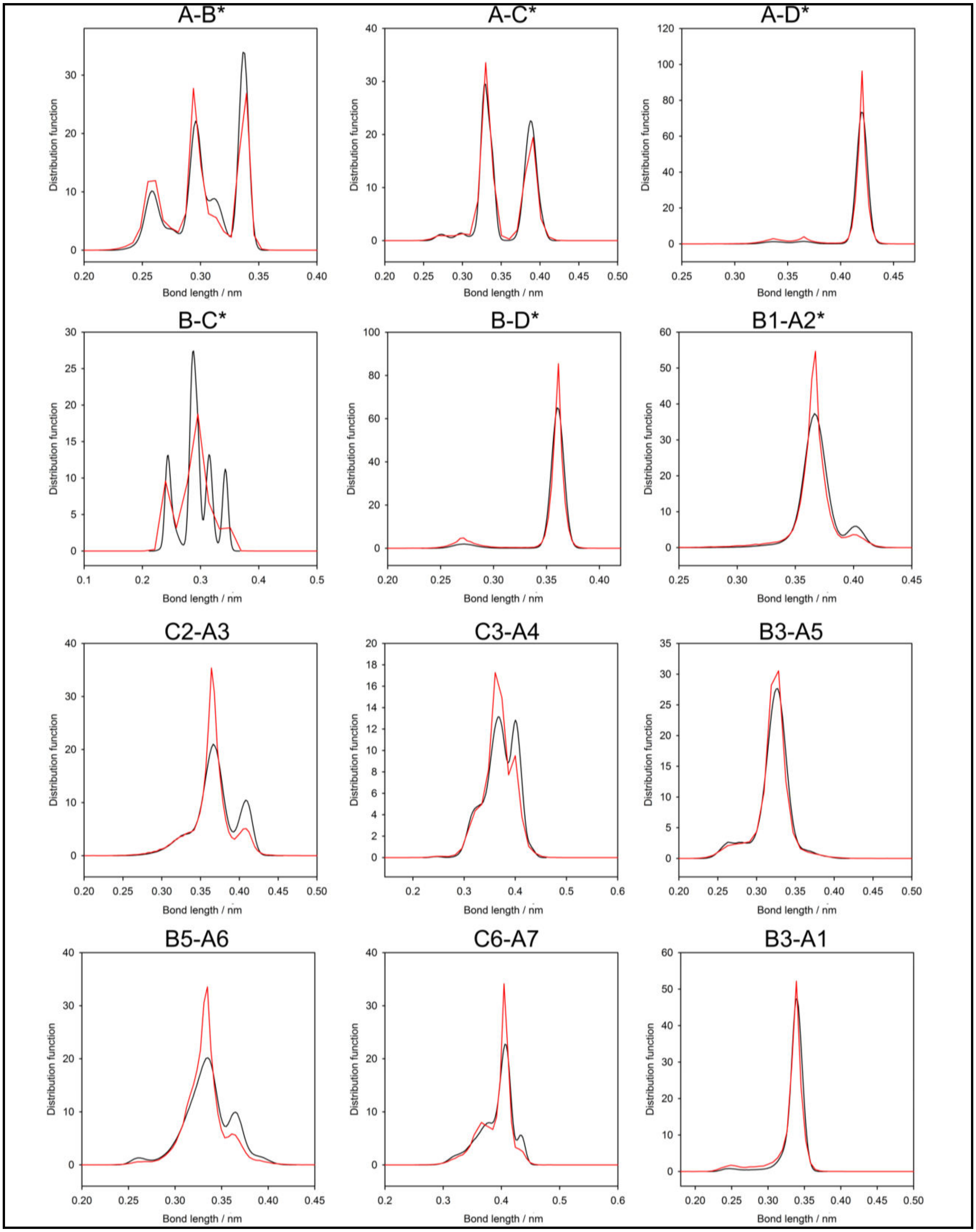

Figure S8: Bonded distribution functions of the atomistic and coarse-grained stewartan simulations

The reproduction of the atomistic configurations by the coarse-grained model was analyzed by comparing the bond distribution functions of the atomistic (black) and coarse-grained simulations (red). Bonded potentials were derived from the atomistic reference structure using Boltzmann inversion. The coarse-grained mapping of the stewartan structure is shown in Figure 9.

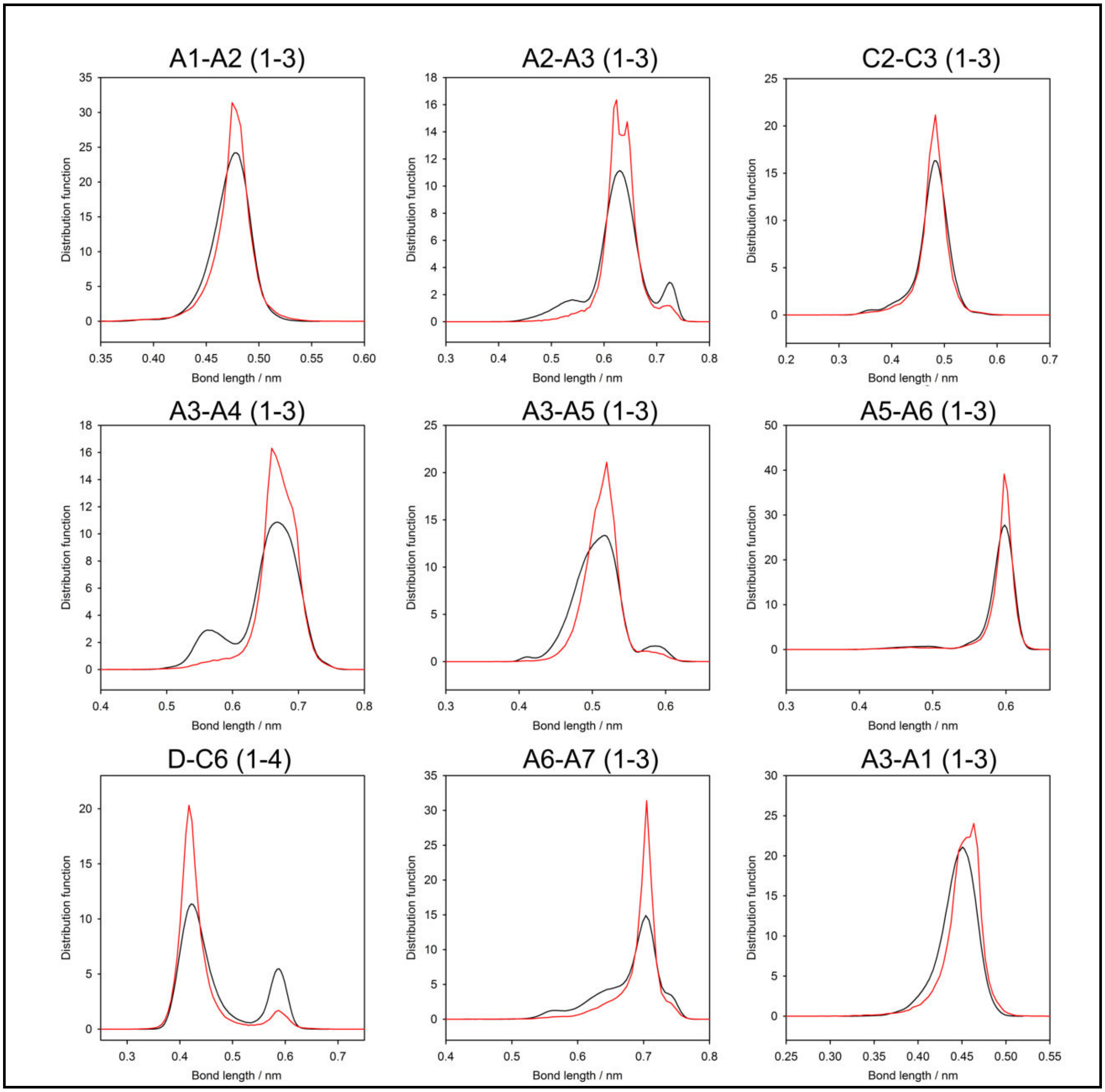

Figure S9: Distribution functions of virtual bonds functions of the atomistic and coarse-grained stewartan simulations (I)
The reproduction of the atomistic configurations by the coarse-grained model was analyzed by comparing the bond distribution functions of the atomistic (black) and coarse-grained simulations (red). Bonded potentials were derived from the atomistic reference structure using Boltzmann inversion. Virtual bonds, either 1-3 or 1-4, are indicated. The coarse-grained mapping of the stewartan structure is shown in Figure 9.

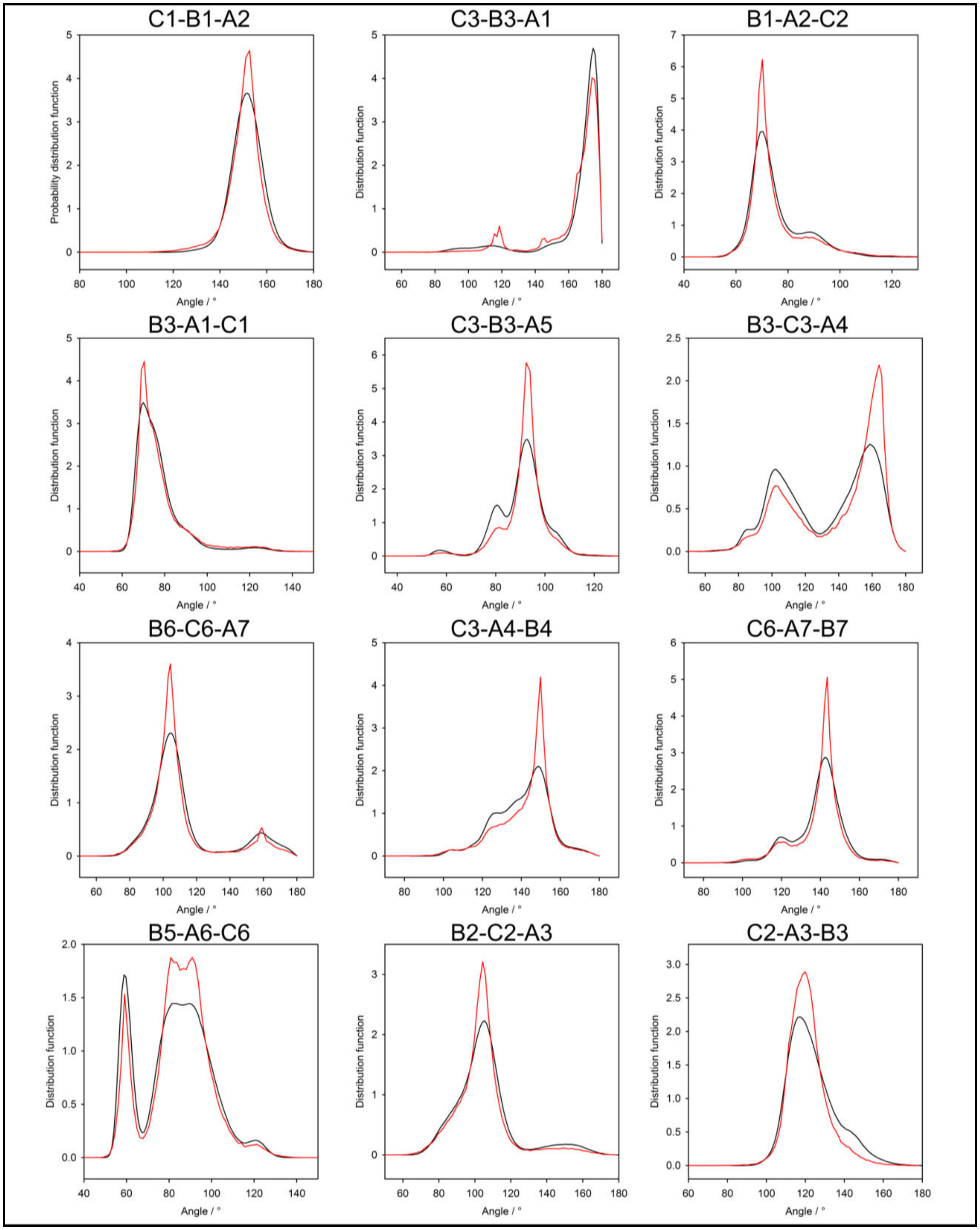

Figure S10: Angular distribution functions of the atomistic and coarse-grained stewartan simulations (I)

The reproduction of the atomistic configurations by the coarse-grained model was analyzed by comparing the bond distribution functions of the atomistic (black) and coarse-grained simulations (red). Angular potentials were derived from the atomistic reference structure using Boltzmann inversion. The coarse-grained mapping of the stewartan structure is shown in Figure 9.

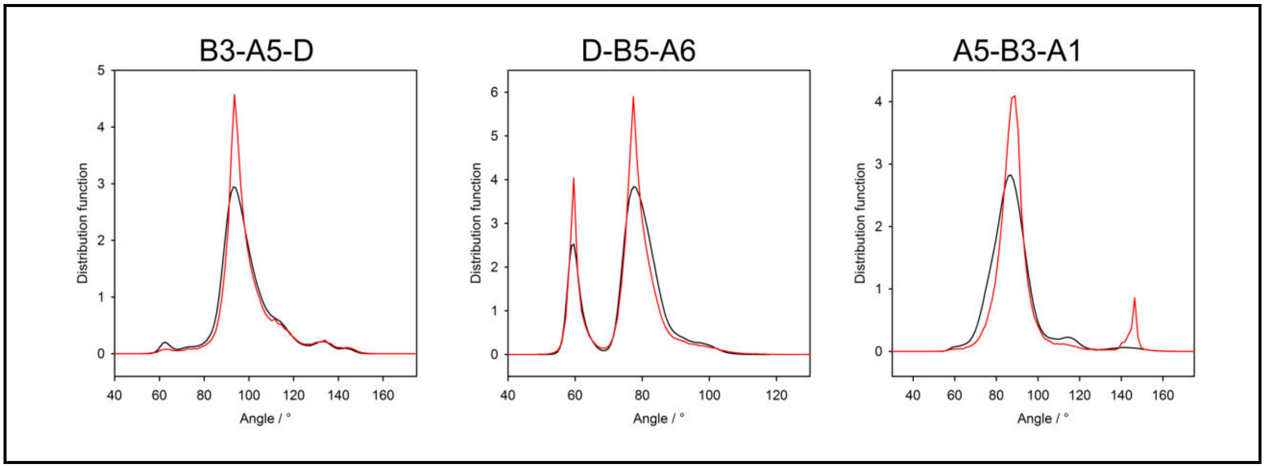

Figure S11: Angular distribution functions of the atomistic and coarse-grained stewartan simulations (II)

The reproduction of the atomistic configurations by the coarse-grained model was analyzed by comparing the bond distribution functions of the atomistic (black) and coarse-grained simulations (red). Angular potentials were derived from the atomistic reference structure using Boltzmann inversion. The coarse-grained mapping of the stewartan structure is shown in Figure 9.

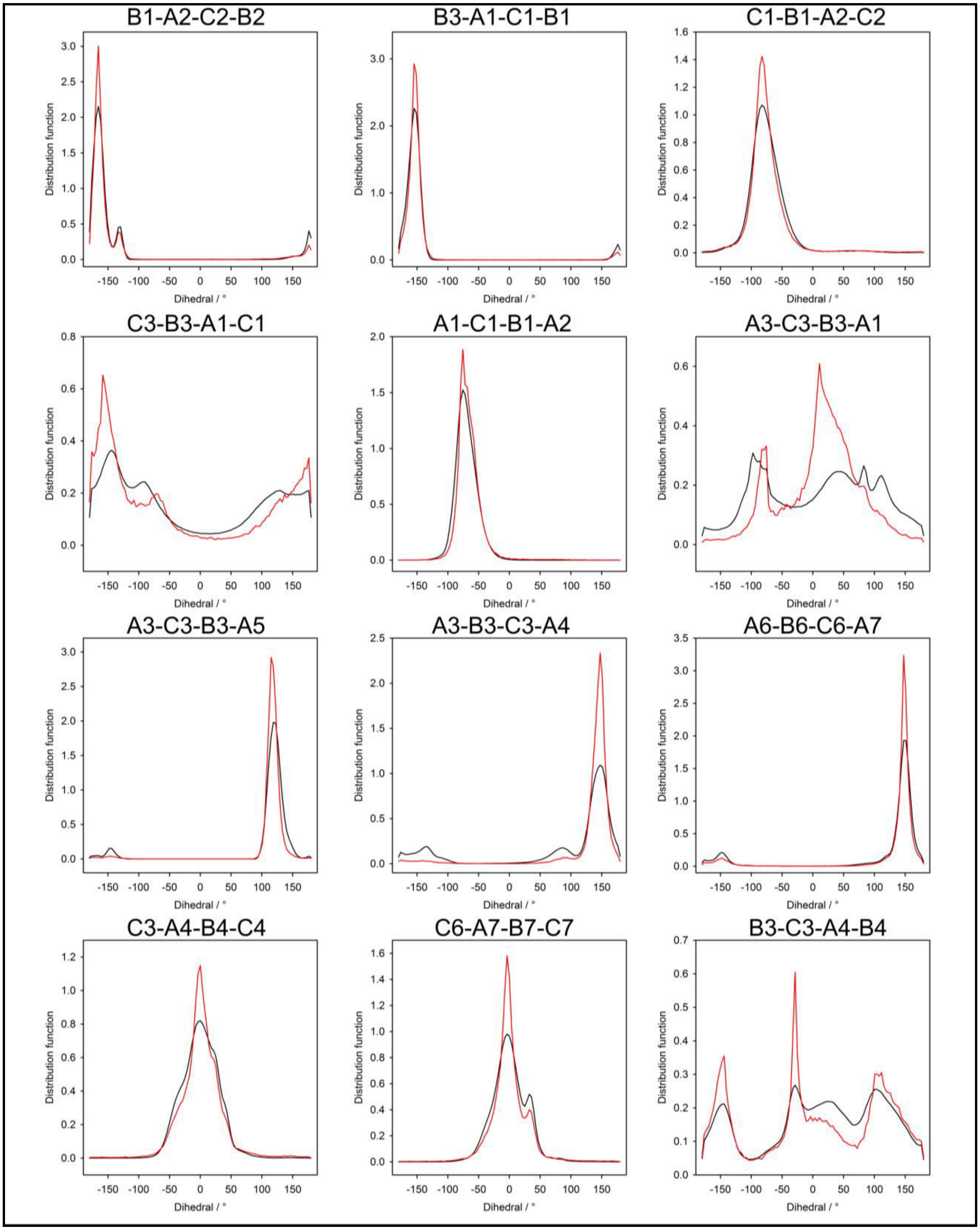

B1-A2-C2-B2

B3-A1-C1-B1

C1-B1-A2-C2

C3-B3-A1-C1

A1-C1-B1-A2

A3-C3-B3-A1

A3-C3-B3-A5

A3-B3-C3-A4

A6-B6-C6-A7

C3-A4-B4-C4

C6-A7-B7-C7

B3-C3-A4-B4

Figure S12: Dihedral distribution functions of the atomistic and coarse-grained stewartan simulations (I)

The reproduction of the atomistic configurations by the coarse-grained model was analyzed by comparing the bond distribution functions of the atomistic (black) and coarse-grained simulations (red). Dihedral potentials were derived from the atomistic reference structure using Boltzmann inversion. The coarse-grained mapping of the stewartan structure is shown in Figure 9.

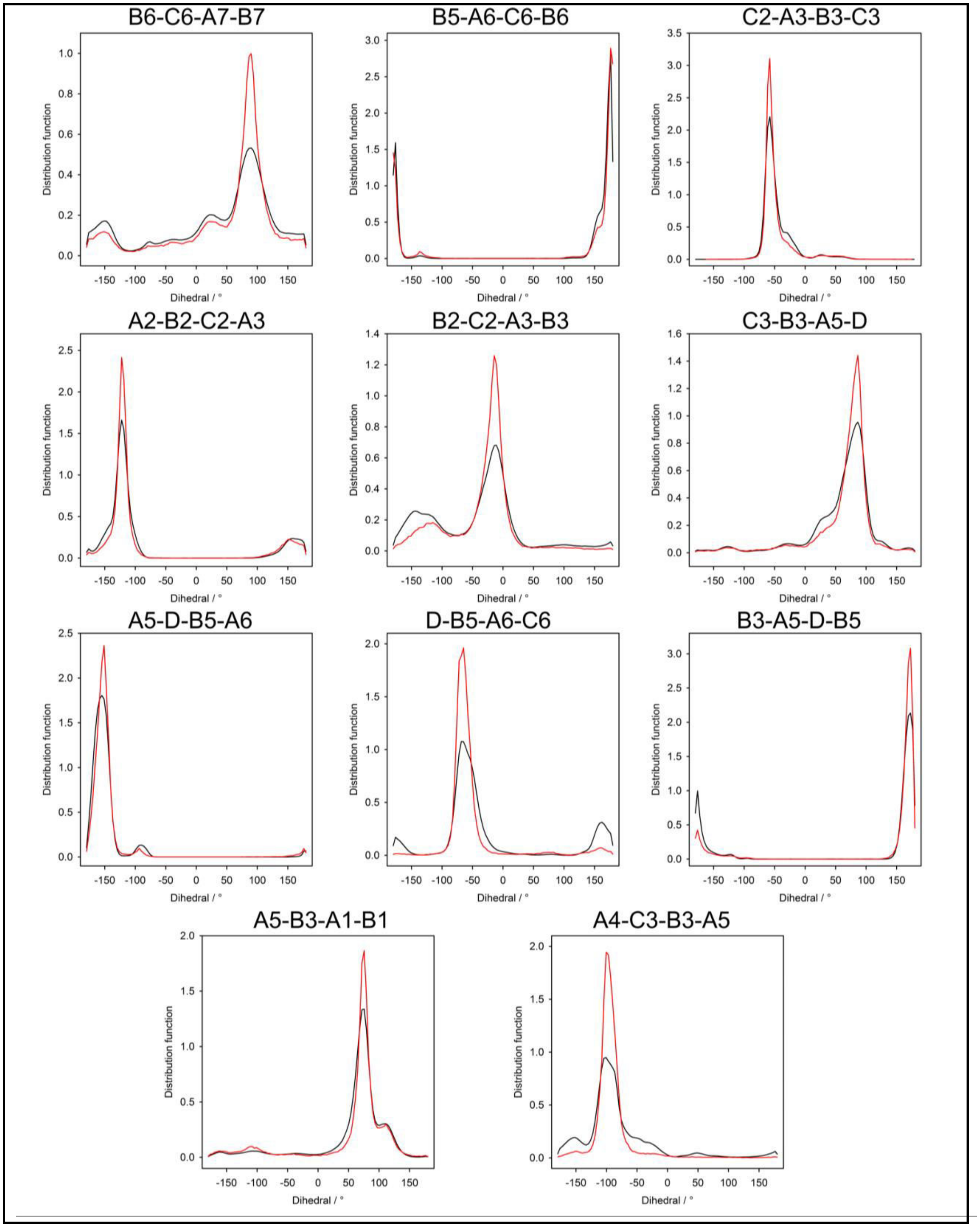

Figure S13: Dihedral distribution functions of the atomistic and coarse-grained stewartan simulations (II)

The reproduction of the atomistic configurations by the coarse-grained model was analyzed by comparing the bond distribution functions of the atomistic (black) and coarse-grained simulations (red). Dihedral potentials were derived from the atomistic reference structure using Boltzmann inversion. The coarse-grained mapping of the stewartan structure is shown in Figure 9.

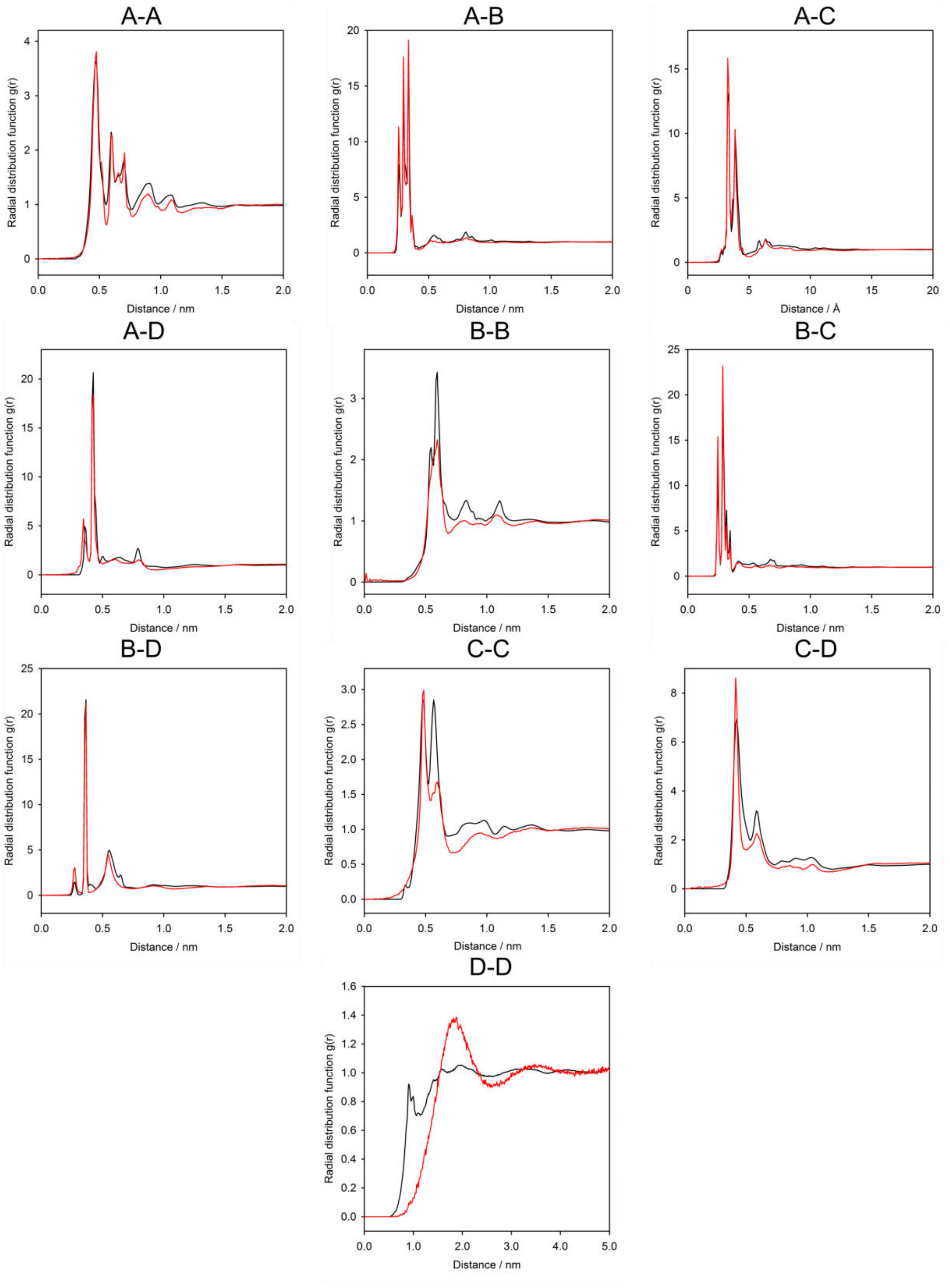

Figure S14: Radial distribution functions of the simulation of atomistic and coarse-grained 3 RU stewartan

The reproduction of the atomistic configurations by the coarse-grained model was analyzed by comparing the radial distribution functions of the atomistic simulation (black) and coarse-grained simulations (red). The coarse-grained mapping of the stewartan structure is shown in Figure 9.

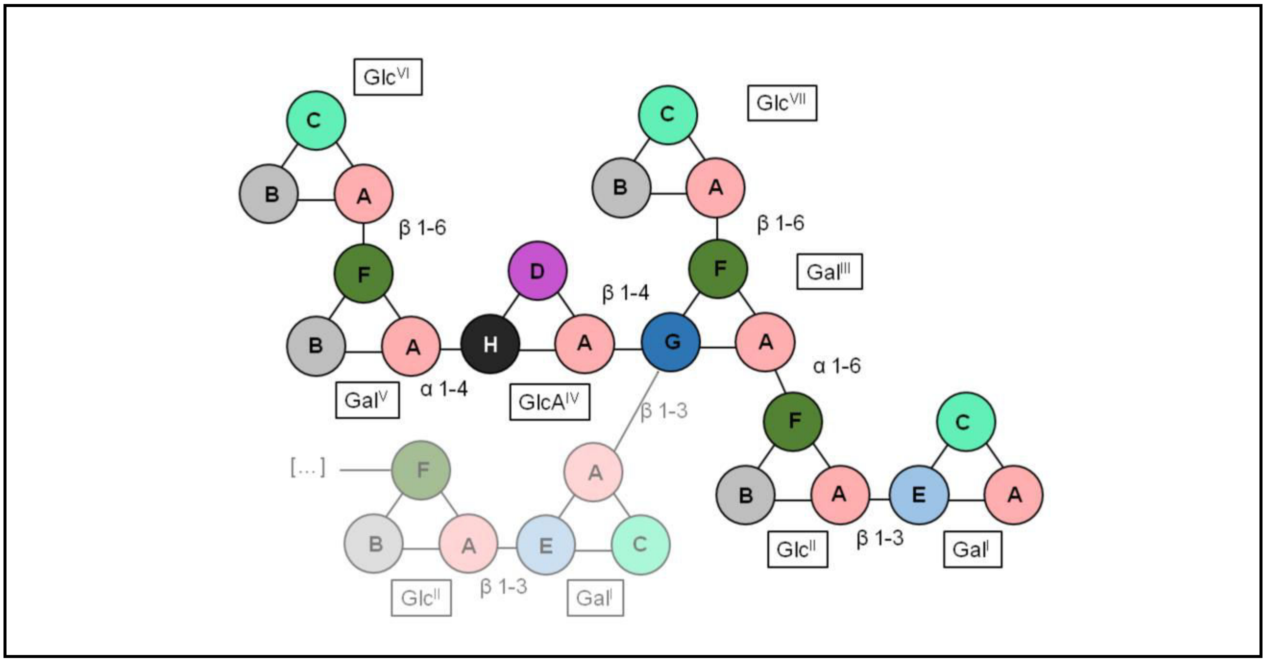

Figure S15: Eight bead coarse-grain mapping scheme for stewartan

The atomistic stewartan was coarse-grained using the eight bead types A, B, C, D, E, F and G. Here, the coarse-grain mapping scheme is shown for one RU with labels describing the monosaccharide unit and linkage type. The beginning of the next RU is suggested by a shaded structure.

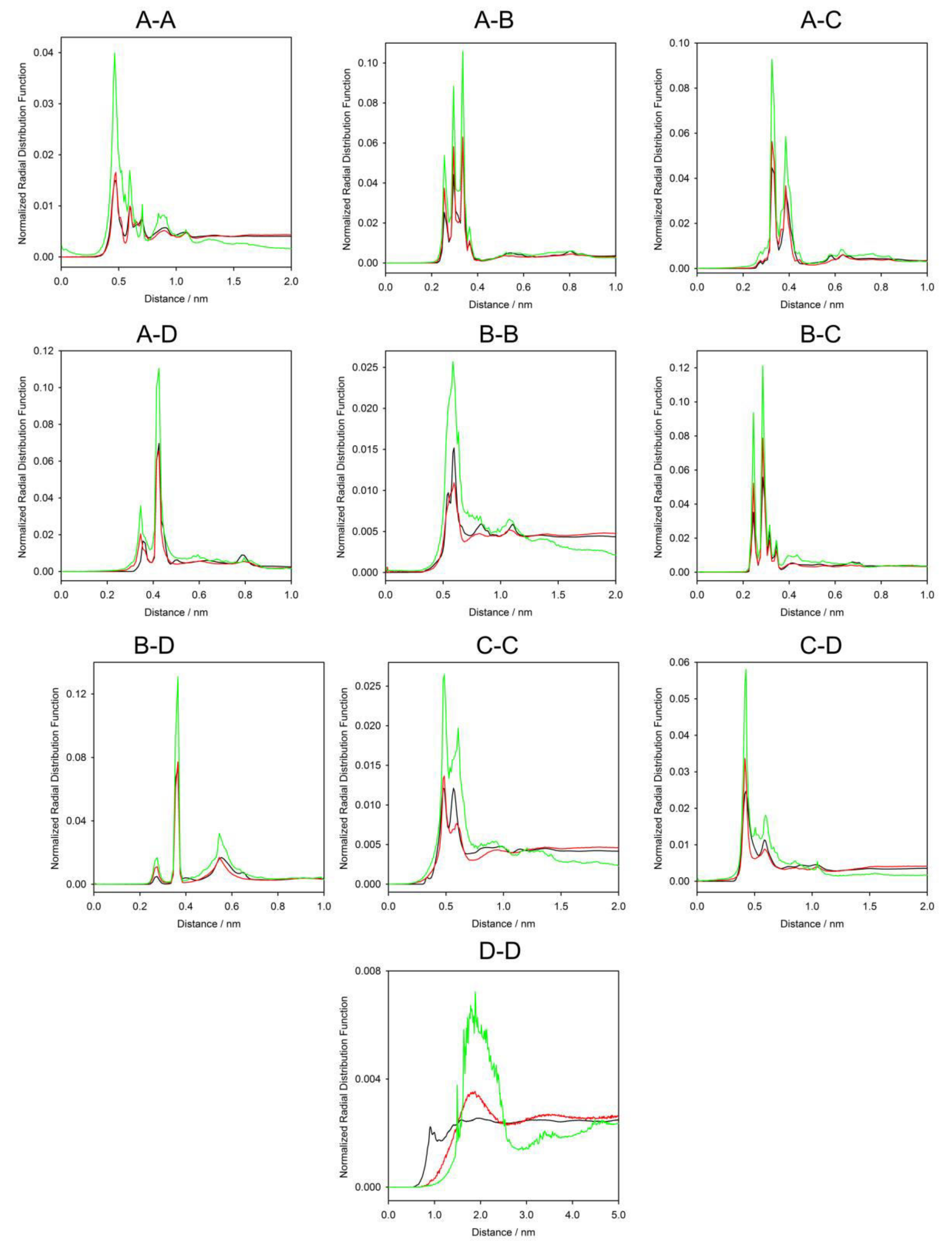

Figure S16: Radial distribution functions of the simulation of coarse-grained 20 RU stewartan

The radial distribution functions of coarse-grained 20 RU stewartan system (green) were compared to the 3 RU stewartan systems (atomistic -black, coarse-grained -red). The coarse-grained mapping of the stewartan structure is shown in Figure 9.

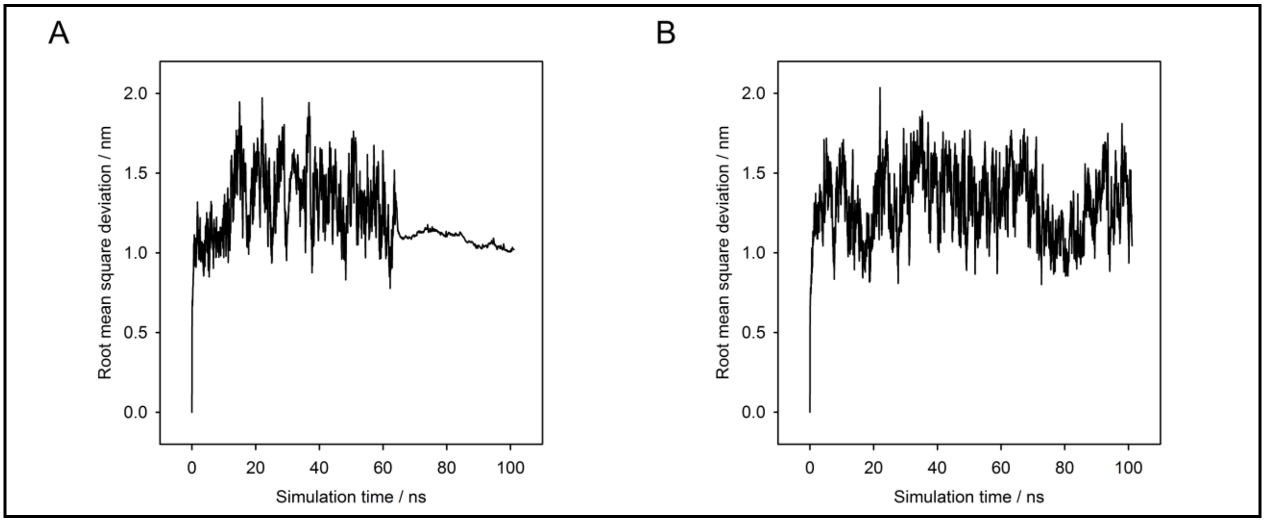

Figure S17: Coarse-grained 20 RU stewartan chains effectively freeze during the coarse-grained simulations

A population of stewartan molecules (15 %) stopped vibrating during the 100 ns simulation of coarse-grained 20 RU stewartan. This effect is here exemplified with a stewartan system with a RU concentration of 86 mM. The root mean square deviation of an (A) example chain which froze and (B) of one chain of the other 85 % is shown.

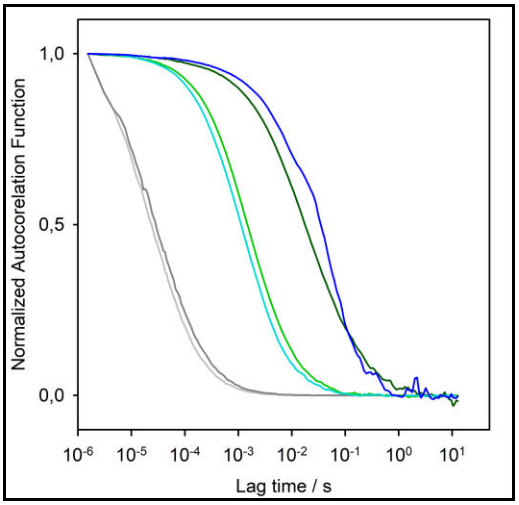

Figure S18: Examples of normalized autocorrelation functions from fluorescence correlation spectroscopy measurements

The diffusion time τ_D and anomaly exponent α for the diffusion of Alexa Fluor® 488 (gray), 46 nm microspheres (green) and 194 nm microspheres (blue) were determined from fitting the normalized autocorrelation functions obtained from fluorescence correlation spectroscopy measurements. Diffusion studies were done in buffer (light colors) or in 10 mg · mL^{-1} stewartan (dark colors).

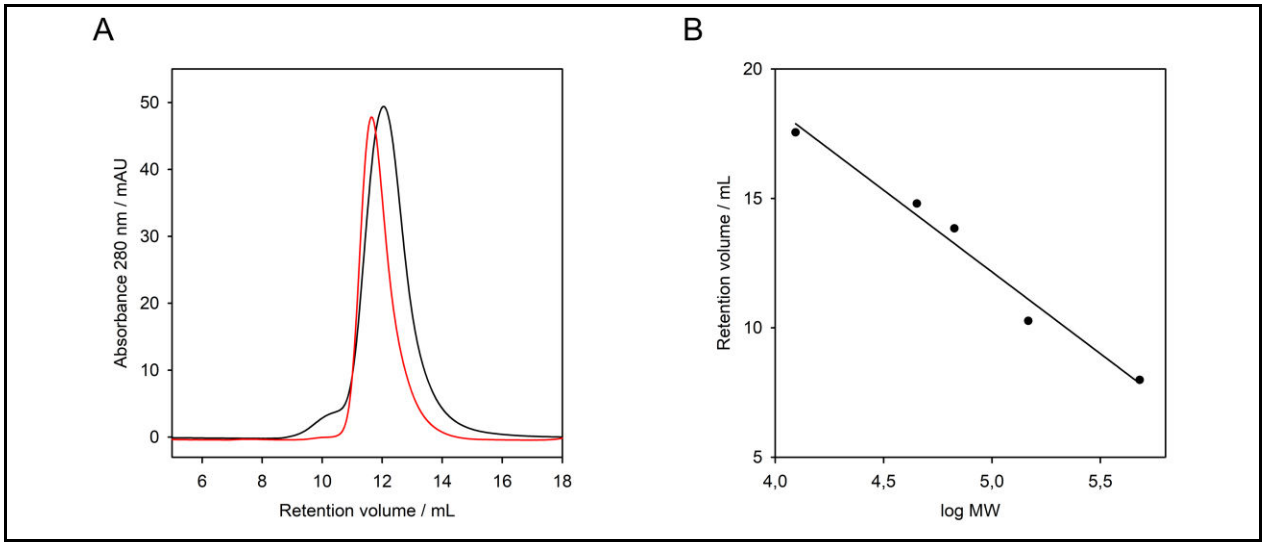

Figure S19: Oligomeric state analysis of WceF and ΦEa1h TSP

(A) The oligomeric states of WceF (black) and ΦEa1h TSP (red) were obtained by size-exclusion chromatography (Superdex^{TM} 200 10/30). (B) The apparent molecular mass was determined from a linear fit of the calibration data points. Here, the used standards were: Ferritin (Horse, 480 kDa), Aldolase (Rabbit, 147 kDa), Albumin (Bovine, 67 kDa), Albumin (chicken, 45 kDa) and Cytochrom C (Horse, 12.4 kDa).

Table S1: Types of inward oriented amino acid stacks in the WceF β-helix (amino acids: 250-522)

stacking type	amino acid number
Cystein	C365, C398, C422, C443
Isoleucin	I269, I303
Phenylalanine	F308, F339
Valin	V369, V403
Mixed	F267, V301, F332, C355, I388
	F294, L321
	L322, L347, I370, L404
	L337, W360, F393
	I357, L390, I414, I435
	L406, I428

Table S2: Biophysical characterization of the interfaces of WceF and TSPs

The interface between the amino acid sequences of the C-terminal fragment (polypeptide chain from the β-helix to the C-terminus) or full-length protein for P22 (pdb: 2XC1) and ϕAB6 (pdb:5JS4) were compared to WceF. Here the interface is defined as the area between two adjacent subunits.

	Interface of C-terminal fragments			**Full-length**		
	WceF	**P22 TSP**	**ϕAB6 TSP**	**WceF**	**P22 TSP**	**ϕAB6 TSP**
amino acids	250-735	126-666	98-565	38-527	7-546	19-405
Chains forming the interface	E-F	A-B	A-C	E-F	A-B	A-C
Interface area / Å	4998	4170	4241	5147	5747	5429
Number of residues in interface	140	115	118	148	155	164
Number of hydrogen bonds	86	65	64	88	84	85
Number of salt bridges	25	11	11	25	18	13
Solvation free energy ΔG	-42.1	-36.2	-40.1	-40.5	-52.1	-49.1

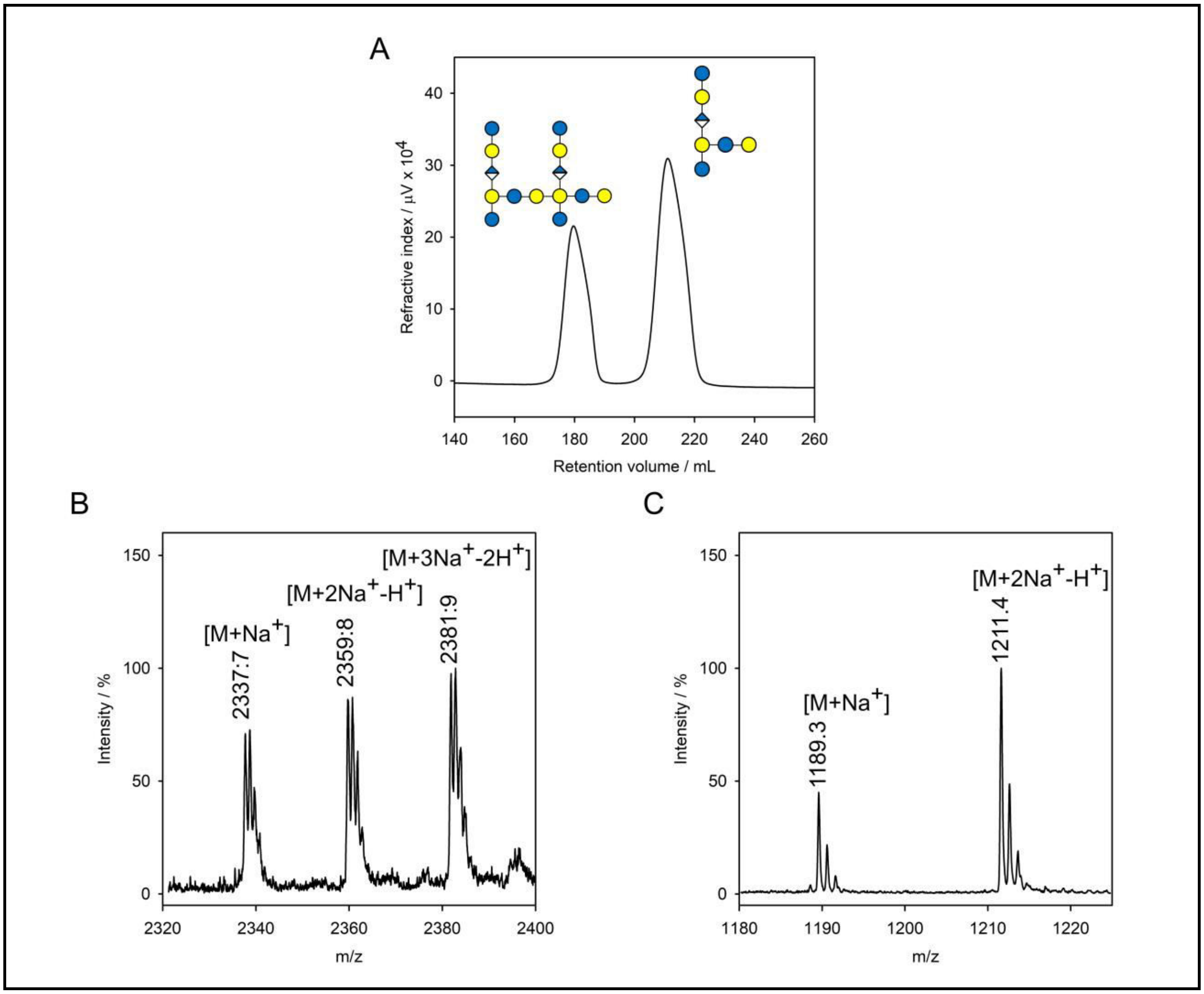

Figure S20: Characterization of the oligosaccharide fragments which were used as standards in capillary electrophoresis
12.5 mg · mL^{-1} stewartan was digested with ΦEa1h TSP for 24 h at 37°C. (A) Two oligosaccharide fragments were purified in size-exclusion chromatography which eluted at (B) 210 mL and (C) 180 mL retention volume. (B), (C) Mass spectrometric analysis of the oligosaccharide fragments.

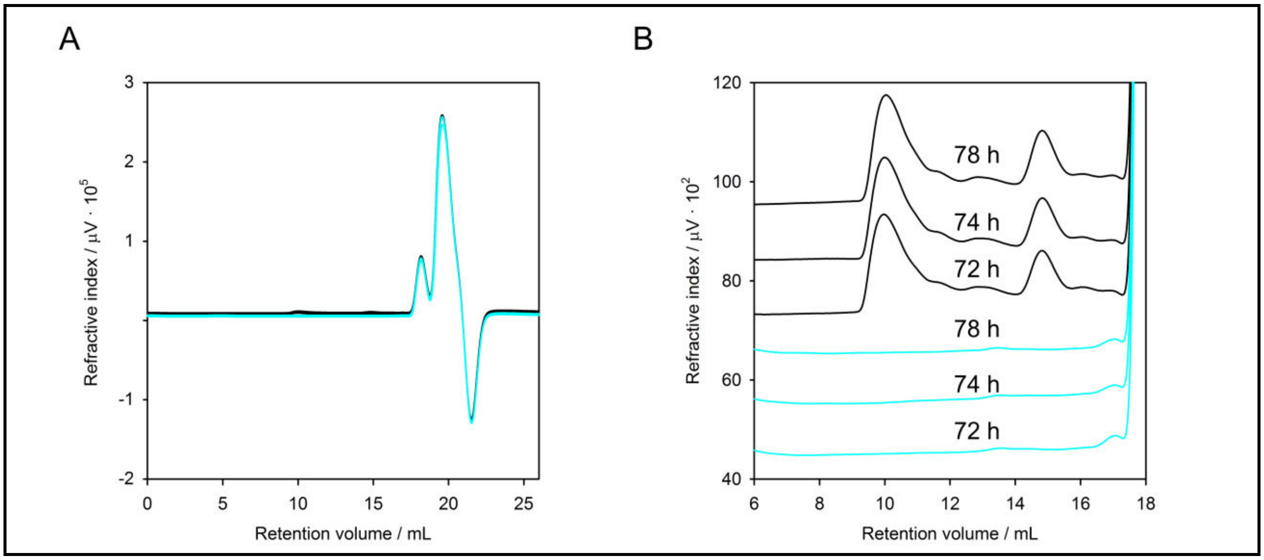

Figure S21: Size-exclusion chromatography analysis of a stewartan hydrolysis by WceF

1 mg · ml^{-1} stewartan was digested with WceF at 30°C (black) or incubated without WceF (cyan). (A) NaOH stopped reactions at the indicated time points were subjected to size-exclusion chromatography (Superdex^{TM} peptide 10/300). (B) Stacked chromatograms in the retention volume regime of 6-18 mL are shown.

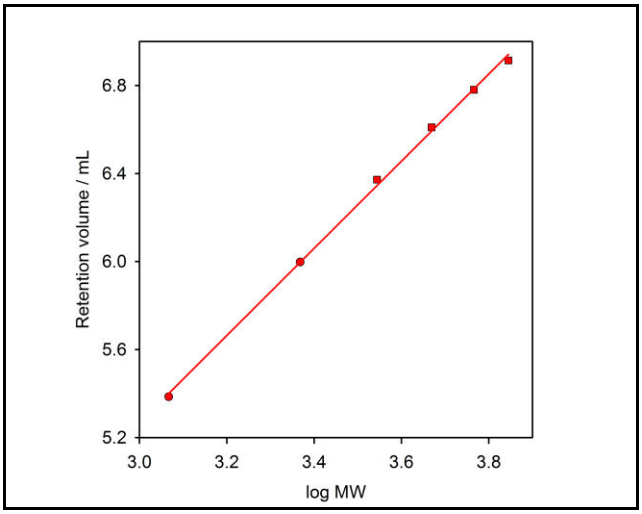

Figure S22: Capillary electrophoresis analysis of a stewartan digestion by Ea1h TSP

1 mg · mL^{-1} stewartan was digested with ΦEa1h TSP for 0.5 h and oligosaccharide fragments were fluorescently labeled to enable the analysis of the oligosaccharide hydrolysis products using capillary electrophoresis. The retention volumes of each oligosaccharide species in the capillary electrophoresis was determined and plotted against the logarithm of its molecular weight (one and two RU, circles) or the molecular weight was assumed to be three, four and five RU (squares). Finally, all oligosaccharide species were fitted linearly.

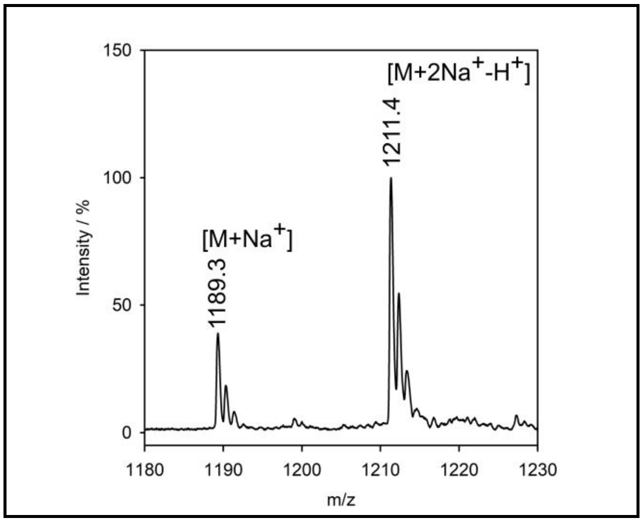

Figure S23: Mass spectrometric analysis of the oligosaccharide fragment produced during the stewartan digestion by WceF

1 mg · mL^{-1} stewartan was digested with WceF for 197 h at 30°C and an oligosaccharide fragment eluting around 15 mL retention time was purified in size-exclusion chromatography and analyzed in mass spectrometry.

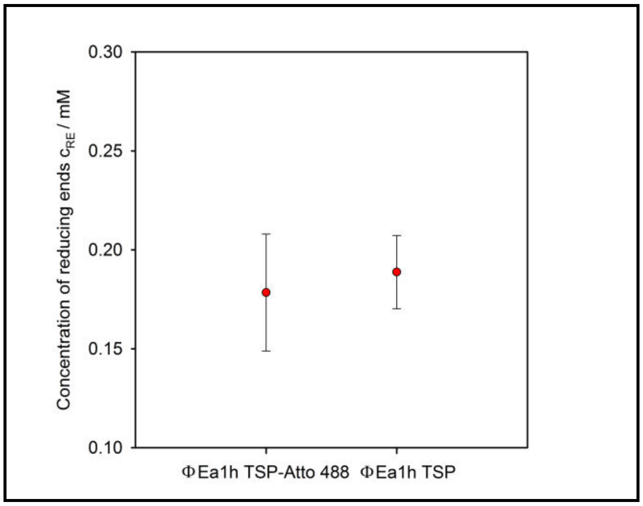

Figure S24: Comparison of stewartan glycosidase activity of labeled and unlabeled ΦEa1h TSP

10 mg · mL^{-1} stewartan was digested with the fluorescent labeled ΦEa1h TSP (ΦEa1h TSP-Atto 488) or with the unlabeled ΦEa1h TSP. The concentration of reducing ends was determined after 30 min using the MBTH-test.

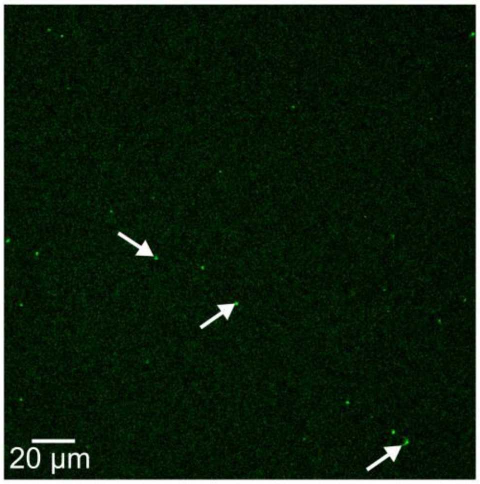

Figure S25: Aggregation behavior of WceF in pure buffer
An image of fluorescently labeled WceF in the buffer solution is shown (50 mM MES, pH 5, 50 mM NaCl). Examples of WceF aggregates are denoted with white arrows.

VI. Acknowledgement

Eine ganze Menge Freunde und Kollegen haben mich in den letzen fast dreieinhalb Jahren unterstützt, ohne die diese Arbeit nicht möglich gewesen wäre. Ihnen gebühren diese Zeilen!

Zuallererst möchte ich mich zutiefst bei Stefanie Barbirz bedanken, die mich bei diesem Projekt von dem ersten Bewerbungsschreiben bis hin zu dieser Arbeit begleitet hat. Ihre Fragen und Anregungen haben mich zu dem Biochemiker gemacht der ich heute bin. Sie hat mir die große, weite Forscherwelt gezeigt und mir es ermöglicht mich mit den großen Wissenschaftlern aus der Szene auszutauschen. Danke auch für die unglaubliche Geduld und Hilfsbereitschaft bei der Ausarbeitung von diversen Vorträgen und Berichten.

Interimstrainerin Andrea Grafmüller danke ich für die Möglichkeit die MD Simulation durchzuführen. Die Beantwortung von unzähligen Fragen und die Analysen meiner Stewartan Simulationen haben das *coarse grain* Model von Stewartan immer wieder vorangetrieben.

Robert Seckler gebührt natürlich auch ein riesiges Dankeschön dafür, dass er als Erster die Hauptbetreuerverantwortung übernahm und somit den Grundstein eines angenehmen und erfolgreichen Verlaufs meiner Doktorarbeit legte.

Ich bedanke mich bei Thomas Weikl und Lothar Elling, dass sie nicht zögerten als Gutachter für diese Arbeit zu fungieren.

Valentin Dunsing, ohne deine Ideen und Experimente wäre diese Arbeit nie auf dieses Niveau angehoben worden. Dein Anteil an dieser Arbeit steht außer Frage.

To Ankush Singhal, Nina Bröker, Tobias Rindfleisch, Mandy Schietke, Jana Kramer, Simone Brockmann, Sonja Kunstmann, Mareike Stephan, Martin Wolff, Melanie Anding, Andreas Schmidt, Patrick Knox-Brown, Anja Thalhammer, Angelo Valleriani, Pallavi Banerjee, Ankansha Moga, Isabell Tunn and many, many more... you helped me with all kinds of protocols, script writing, strange air bubbles in the simulations, melted plastic bins, annoying instruments, finding of highly hidden chemicals, intense football trainings session in Italy and reading of this work. Thank you for just having all this fun during this work.

Ankush and Swapnil... I am going to really miss our lunch talks! I wished we could have finished your side project, Anki!

Dankeschön auch an Yvette Roske, die meine ständigen Fragen zu der WceF Struktur und dem PISA Server beantworten musste.

Susan Weber, ich habe am Anfang gar nicht erahnt, wie viel Papierkram und Organisationsarbeit während der Doktorarbeit und dem Elterndasein auf einem zukommt. Du hast aber alles mit unglaublichem Enthusiasmus aufgefangen und bearbeitet...

Vielen Dank auch an Jörg Fettke und Antje Völkel, die mir die massenspektrometrischen, kapillarelektrophoretischen und makroviskosimetrischen Analysen möglich gemacht haben.

Zu guter Letzt: ein Dankeschön an alle Freunde und Verwandte, die mich schon viel länger begleitet haben und immer Verständnis hatten, wenn ich die SMS und Whatsapp Nachrichten nicht sofort beantwortet habe. Ich würde gerne sagen, nach dieser Arbeit wird es besser... hoffen wir es mal. Peter, ohne dich wäre ich niemals in Potsdam gelandet!

Liebe Anni, du musstest viel aushalten in den letzten Jahren und besonders in den letzten Monaten. Ich weiß, dass ich mich immer auf dich verlassen kann!

Und du kleiner Mann, der mit seinen kleinen Grabbelfingern ständig an die Tür geklopft und mich vom Arbeiten abgehalten hat. Vielleicht sogar absichtlich hast du mich immer wieder, selbst in den größten Stressphasen, geerdet und meine Gedanken auf das wirklich Wichtige im Leben gelenkt.